

Ontwerp van metaalorganische roosters
voor toepassingen in de katalyse van fijnchemicaliën:
een gecombineerd experimenteel en computationeel onderzoek

Design of Metal Organic Frameworks
for the Catalytic Production of Fine Chemicals:
a Combined Experimental and Computational Investigation

Thomas Bogaerts

Promotoren: prof. dr. ir. V. Van Speybroeck, prof. dr. P. Van Der Voort
Proefschrift ingediend tot het behalen van de graad van
Doctor in de Ingenieurswetenschappen: Chemische Technologie

Vakgroep Toegepaste Fysica
Voorzitter: prof. dr. ir. C. Leys
Faculteit Ingenieurswetenschappen en Architectuur
Academiejaar 2015 - 2016



ISBN 978-90-8578-832-4
NUR 913, 928
Wettelijk depot: D/2015/10.500/76



This research has been conducted at the Center for Molecular Modelling and the Center for Ordered Materials, Organometallics and Catalysis

PREFACE

Het uitvoeren van een doctoraatsonderzoek en het schrijven van een thesis is een echt huzarenstukje dat uiteraard niet alleen geklaard kan worden. Daarom wil ik dit manuscript graag starten met enkele dankwoordjes.

Om te beginnen wil ik graag mijn promotoren, Veronique Van Speybroeck en Pascal Van Der Voort, bedanken voor het vertrouwen dat ze in mij hadden. Ze boden mij de kans om experimenteel en theoretisch onderzoek te combineren. Zonder die kans was ik waarschijnlijk nooit aan deze uitdaging begonnen.

Verder wil ik ook mijn verloofde, Sarah, bedanken voor alle steun tijdens deze laatste jaren, zelfs als ik niet kon uitleggen wat ik juist aan het doen was. Ook mijn ouders ben ik dankbaar om mij, net als tijdens mijn opleiding te blijven motiveren. Daarnaast wil ik ook Matthias en Iwein bedanken, ik ken jullie al sinds we twaalf waren en ik ben blij jullie nog steeds goede vrienden te mogen noemen

Ook mijn collega's verdienen een extra woordje van dank voor alle hulp en inzichten op wetenschappelijk vlak, maar ook voor een regelmatige leuke babbel. Van het CMM wil ik dan vooral Thierry, Lennart en Kristof bedanken, met wie ik ook het plezier had om samen te studeren. Ook mijn collega's bij COMOC hebben mij enorm geholpen, ik ben mijn doctoraat begonnen zonder noemenswaardige kennis van experimenteel werk, alles wat ik in deze vier jaar geleerd heb is dankzij jullie. *I especially want to thank Ying-Ya, who guided me into the wondrous world of metal-organic*

Preface

frameworks and got me started on this path. Daarnaast wil ik ook Els bedanken voor de hilarische momenten op de bureau, ik hoop dat je al je dromen kan realiseren. Tot slot wil ik aan de 'jonge garde' nog veel succes toewensen en ik hoop dat zij binnen enkele jaren ook in deze positie kunnen staan en terugkijken op alle aangename momenten.

Om af te sluiten wil ik ook alle medewerkers van het secretariaat en de rest van het ATP bedanken. Claudine, An, Pierre, Wim, Bart, Tom, Pat en Danny, al jullie hulp met administratieve en technische problemen wordt erg op prijs gesteld.

Thomas Bogaerts
25/09/2015

Leden Van De examencommissie

Voorzitter

Prof. dr. ir. Patrick De Baets (Universiteit Gent)

Leescomissie

Prof. dr. ir. Veronique Van Speybroeck (Universiteit Gent, promotor)

Prof. dr. ir. An Verberckmoes (Universiteit Gent)

Prof. dr. Patrick Bultinck (Universiteit Gent)

Prof. dr. Martin Hartmann (Friedrich-Alexander-Universität Erlangen-Nürnberg)

Overige leden

Prof. dr. Pascal Van Der Voort (Universiteit Gent, promotor)

Prof. dr. ir. Karen Hemelsoet (Universiteit Gent)

Prof. dr. ir. Chris Stevens (Universiteit Gent)

Prof. dr. Jorge Gascon (Technische Universiteit Delft)

Prof. dr. Frank De Proft (Vrije Universiteit Brussel)

CONTENTS

PREFACE	I
ACRONYMS	XVII
SYMBOLS	XIX
SAMENVATTING	XXI
SUMMARY	XXVII

PART I: DESIGN OF METAL ORGANIC FRAMEWORKS FOR THE CATALYTIC PRODUCTION OF FINE CHEMICALS

1

CHAPTER 1. INTRODUCTION	3
1.1 Catalysis	3
General	3
Catalysis in fine chemistry	4
Design of catalysts	6
1.2 Salen complexes for enantioselective oxidation catalysis	7
Epoxidation	7
Discovery of the chiral salen complex	8
Mechanistic considerations from experimental studies	13
Mechanistic considerations from computational studies	16

Salen complexes: recent advances and practical applicability.....	19
1.3 Metal Organic Frameworks	21
Synthesis and nomenclature	21
Applications	24
Chiral salen catalysts in MOFs	27
The MIL-101 framework	28
1.4 Outline of the remaining chapters	29
1.5 References	29
CHAPTER 2. GOAL AND METHODOLOGY	41
2.1 Goal of the research presented in this thesis.....	41
2.2 Molecular modeling.....	42
General	42
Electronic structure methods	42
Van der Waals interactions	44
Excited states: Time dependent density functional theory (TDDFT)....	44
Thermodynamics from ab initio data	45
Software used for the research	46
2.3 Experimental methods	47
General	47
Powder X-ray Diffraction	47
Structure refinement.....	48
2.4 References	49
CHAPTER 3. MAJOR RESEARCH RESULTS	53
3.1 Computational description of the salen complex	53
General	53

High-level reference data	53
Benchmark of various DFT methods compared to the high level reference data	55
3.2 Unraveling mechanistic details for a small model salen complex	56
Model.....	56
The radical intermediate	57
Alternative intermediates	58
3.3 Radical probe experiments.....	59
Ring opening versus epoxidation reaction on the manganese-acacen' complex	59
3.4 Modelling the selectivity	64
Overview.....	64
The symmetrical salen complex	65
The asymmetrical salen complex	66
3.5 Experimental design of heterogeneous salen catalysts	68
Strategies employed for the immobilization.....	68
Grafting of the complex.....	69
Sixth coordination site as anchoring point.....	71
Ship in a bottle encapsulation	73
Summary.....	75
3.6 Comparing a modeled structure of a material to experiments via measured and modeled XRD diffractograms	76
General	76
Methodology	77
Case study: detailed structure of MIL-47(V).....	78
3.7 Contributions to other papers: Computer assisted interpretation of spectroscopy	81
General	81

The UV/Vis modelling of a gallium-bipyridine MOF (COMOC-4).....	81
Using COMOC-4 as a basis for a bimetallic MOF	84
Immobilization of TiO(acac) ₂ on NH ₂ -MIL-47(V), characterization via IR spectroscopy.....	86
3.8 References	87
 CHAPTER 4. CONCLUSIONS AND PERSPECTIVES	 93

PART II: PUBLISHED PAPERS **101**

Paper I: Communication: DMRG-SCF study of the singlet, triplet, and quintet states of oxo-Mn(Salen).....	103
Paper II: Mechanistic investigation on the oxygen transfer with the manganese-salen complex	111
Paper III: The enantioselectivity of the manganese-salen complex in the epoxidation of unfunctionalized olefins and the influence of grafting.....	123
Paper IV: Covalent immobilization of the Jacobsen catalyst on mesoporous phenolic polymer: a highly enantioselective and stable asymmetric epoxidation catalyst.....	133
Paper V: Mn-salen@MIL101(Al) a heterogeneous, enantioselective catalyst using a ‘bottle around the ship’ approach	141
Paper VI: Fine-tuning the ab initio modeled structure of MIL-47(V) with the aid of powder X-ray diffraction	151
Paper VII: Bipyridine-Based Nanosized Metal–Organic Framework with Tunable Luminescence by a Postmodification with Eu(III): An Experimental and Theoretical Study	167
Paper VIII: Bimetallic–Organic Framework as a Zero-Leaching Catalyst in the Aerobic Oxidation of Cyclohexene	187

Paper IX: Ti-functionalized NH₂-MIL-47: an effective and stable epoxidation catalyst205

APPENDIX A. PUBLICATION LIST 221

APPENDIX B. ACKNOWLEDGEMENTS 227

LIST OF FIGURES

Figure 1.1. Schematic representation of a catalyzed reaction.....	4
Figure 1.2. Selection of possible reactions with epoxides by exploiting the high ring strain of the three-membered ring	9
Figure 1.3. Different mechanisms for the epoxidation of olefins with peroxides as a model oxidant. The radical chain mechanism (a) , oxirane pathway (b) , oxygen rebound mechanism (c)	10
Figure 1.4. Example of an enantioselective epoxidation reaction with an unfunctionalized olefin as substrate.	10
Figure 1.5. Variants of the salen complex, with a chiral diamine backbone (a) and a chiral biphenyl backbone (b)	11
Figure 1.6. Numbering to denote substituent positions on salen ligands. ..	11
Figure 1.7. Bulky ruthenium-salen catalyst for enantioselective aziridination reactions.	12
Figure 1.8. Mn ^V -oxo intermediate of the Jacobsen complex.	13
Figure 1.9. General reaction scheme of olefin epoxidation catalyzed by the Mn-salen complex.	13
Figure 1.10. Reaction scheme with a radical intermediate (parts of the structure are omitted for simplicity).	14
Figure 1.11. Trans-2-phenyl-1-vinylcyclopropane as radical probe	15
Figure 1.12. Radical probes proposed by Akermark et al.	15
Figure 1.13. Schematic representation of various approach vectors to the salen complex, adapted from Norrby et al. and Cavallo et al.	17
Figure 1.14. Different mechanisms proposed for the oxygen transfer.	19

List of figures

Figure 1.15. Possible non-radical intermediates found in different computational studies..... 19

Figure 1.16. MIL-53 (left) and MIL-101 (right) topologies. Both MOFs can be made by combining a Cr-salt and terephthalic acid linkers, this illustrate the versatile structures that can be obtained with metal organic frameworks, Reprinted (adapted) with permission from. Copyright 2015 American Chemical Society..... 22

Figure 1.17. Example of isorecticular MOF design by linker variation. Reproduced from with permission of The Royal Society of Chemistry..... 24

Figure 1.18. Overview of different ways to introduce active sites in a MOF. Adapted with permission from. Copyright 2015 American Chemical Society and The Royal Society of Chemistry. 26

Figure 1.19. Two different salen linkers designed for building into a MOF. 28

Figure 2.1. Schematic representation of powder X-ray diffraction..... 48

Figure 3.1. Mn-acacen' model used for the benchmark calculations. 54

Figure 3.2. Behavior of different functionals compared to the DMRGSCF reference values. 56

Figure 3.3. Possible mechanisms that were originally proposed for the epoxidation with a Mn-salen complex. 57

Figure 3.4. Energy diagram for the oxygen transfer relative to the reactants on the spin 0 plane. 58

Figure 3.5. Radical probes utilized in the experiments from Akermark et al. the phenylic groups are added to allow for an unbiased position of the radical. 60

Figure 3.6. Epoxidation versus ring-opening pathway, free energy diagram for probe **(1)** on the left and probe **(2)** on the right (nomenclature in Table 3.3). Free energies are relative to the reactants on spin 1. 61

Figure 3.7. Free energy diagrams for the competitive ring-opening and epoxidation reaction for probe **(1)**..... 63

Figure 3.8. Free energy diagrams for the competitive ring-opening and epoxidation reaction for probe **(2)**..... 63

Figure 3.9. Geometry for the epoxidation reaction for the different probes. 64

Figure 3.10. Pathway for the epoxidation of dihydronaphthalene, the first transition state determines the enantioselectivity of this reaction..... 65

Figure 3.11. The transition state for the two approaches with the closest distances denoted (\AA).....	66
Figure 3.12. Possible transition states and relative energies for the asymmetrical salen catalysts, the steric interactions are shown (in \AA).	67
Figure 3.13. Model with a substitution to mimic grafting.....	68
Figure 3.14. Buildup of the salen complex on MIL-101(Cr) (represented by M0).	70
Figure 3.15. IR spectra of the different steps in the modification process. .	71
Figure 3.16. Results for the different runs in the epoxidation with the grafted salen catalyst.	71
Figure 3.17. Immobilization procedure on a phenolic resin via the sixth coordination site. Reprinted with permission from Elsevier.....	72
Figure 3.18. Results for the different runs in the epoxidation with the catalyst immobilized on the phenolic resin.....	73
Figure 3.19. Schematic overview of the encapsulation procedure.....	74
Figure 3.20. Drifts spectra for the encapsulation of the Jacobsen complex in $\text{NH}_2\text{-MIL-101(Al)}$. Reproduced with permission from The Royal Society of Chemistry.....	75
Figure 3.21. Results for the different runs in the epoxidation with the catalyst immobilized by encapsulation in $\text{NH}_2\text{-MIL-101}$. Reproduced with permission from The Royal Society of Chemistry.....	75
Figure 3.22. Comparison of the MIL-47(V) structure without (on the left) and with (on the right) displaced vanadium chains.	78
Figure 3.23. Example of a qualitative comparisons between a measured spectrum and different models, the main differences are denoted.....	79
Figure 3.24. Measured UV/Vis spectra of COMOC-4 as a methanol suspension. Reprinted with permission from. Copyright 2015 American Chemical Society.....	82
Figure 3.25. Models for COMOC-4, the linker reference (a),the small model where only two linkers are present and the metal chain consists of two Ga atoms (b), and the large model that consists of four linkers and three gallium atoms in the chain (c) Reprinted with permission from. Copyright 2015 American Chemical Society..	83

List of figures

Figure 3.26. Overview of measured and calculated results for the neutral and cationic model. Reprinted with permission from. Copyright 2015 American Chemical Society. 84

Figure 3.27. Calculated spectra of the linker and linker CuCl_2 chelated on the linker. Reprinted with permission from Wiley-VCH Verlag. 86

Figure 3.28. Contribution of grafted metal on the excitations calculated from a single snapshot that makes up the average spectrum. Reprinted with permission from Elsevier. 87

LIST OF TABLES

Table 1.1. Production and waste generation in the different segments of the chemical industry.	6
Table 1.2. results of the radical probe experiments.....	16
Table 3.1. Energies relative to spin 0 for the different spin states calculated by the DMRG-SCF method for the basis sets considered (kJ/mol).	55
Table 3.2. Free energies of different intermediates relative to the reactants on the spin 0 plain (X=Cl).....	59
Table 3.3. Amount of epoxide product compared to ring opening products with the radical probe experiments.	60
Table 3.4. Summary of the different catalytic systems and grafting procedures.....	76
Table 3.5. Relative energies of different calculated geometries.....	79
Table 3.6. Quantitative comparison for different structures in different 2θ ranges.	80

ACRONYMS

%ee	Enantiomeric Excess
CASSCF	Complete Active Space Self-Consistent Field
CI	Configuration Interaction
DFT	Density Functional Theory
DMRG	Density Matrix Renormalization Group
DRIFT	Diffuse Reflectance Infrared Fourier Transform spectroscopy
FMR	Five Membered Ring
GC	Gas Chromatography
HF	Hartree Fock
HPLC	High Performance Liquid Chromatography
LOT	Level of Theory
MAS	Magic Angle Spinning
MCPBA	Meta-Chloroperoxybenzoic Acid
MM	Molecular Mechanics
MOF	Metal Organic Framework
NMA	Normal Mode Analysis
NMR	Nuclear Magnetic Resonance
POM	Polyoxometalate
PSM	Post Synthetic Modification
(P)XRD	(Powder) X-Ray Diffractometry
QM	Quantum Mechanics

Acronyms

SCF

Self-Consistent Field

TDDFT

Time Dependent Density Functional Theory

UV/Vis

Ultra Violet and Visible

SYMBOLS

ΔG^\ddagger	kJ/mol	Transition State Free Energy Difference
E_a	kJ/mol	Activation Energy
G	kJ/mol	Gibbs Free Energy
H	kJ/mol	Enthalpy
S	J/mol.K	Entropy
h	J.s	Planck Constant
k_b	J/K	Boltzmann Constant
R	J/mol.K	Universal Gas Constant
Q		Partition Function
T	K	Temperature
N		Number of Atoms
S_F		Scale Factor
L_k		Lorentz Polarization Factor
$F_{k,j}$		Structure Factor
S_j		Profile Shape Function
$P_{k,j}$		Texture Factor
A_j		The Absorption Factor
f_n		Atomic Scattering Factor
B_n		Temperature Factor
I^{calc}	cps	Calculated intensity
λ	nm	Wavelength

SAMENVATTING

Nanoporeuze materialen worden veelvuldig gebruikt in tal van toepassingen. Het ontwerp van deze materialen is dan ook een actueel onderwerp. Deze materialen vinden vooral een toepassing in katalyse en adsorptie. Ook meer niche applicaties waar poreuze materialen goed presteren, komen op de voorgrond. Voorbeelden zijn toepassingen in micro-elektronica of als sensor. Het ontwerpproces van deze materialen bestaat nog voor een groot deel uit *“trial and error”* hoewel er recent veel vooruitgang gemaakt is in een meer gestructureerde aanpak, onder andere met de introductie van *“high throughput”* technieken. Ab initio modellering heeft in de laatste jaren zijn plaats gevonden binnen het domein van de chemie, chemische technologie en materiaalkunde. Het gebruik van computationele modelleringstechnieken kan leiden tot een beter begrip van bestaande processen waardoor die geoptimaliseerd kunnen worden. Door de toenemende rekenkracht en krachtige numerieke algoritmes kan modellering ook meer en meer ingezet worden in het ontwerp van nieuwe materialen en processen.

In de fijnchemie en de productie van farmaceutische stoffen speelt katalyse een belangrijke rol. Veel reacties vertonen een erg lage selectiviteit, of zijn helemaal onmogelijk zonder de juiste katalysator. In dit domein wordt nog veelvuldig gebruik gemaakt van homogene katalysatoren. Binnen dergelijke processen moeten de katalysatoren achteraf van de producten gescheiden worden wat altijd leidt tot een verlies. Binnen de fijnchemie weegt de toegevoegde waarde van het product meestal op tegen dat verlies. Recent is er echter meer aandacht om een zo groen mogelijke chemische industrie

te creëren, waarbij de afvalgeneratie geminimaliseerd wordt. In deze optiek wordt er onderzoek verricht naar het vervangen van de bestaande homogene katalysatoren door heterogene varianten. Deze heterogene katalysator moet zo veel mogelijk eigenschappen van het homogene materiaal bewaren, zoals de hoge selectiviteit. In vele processen in de fijnchemie is de vorming nevenproducten namelijk ongewenst en gevaarlijk.

In deze thesis wordt een gecombineerde experimentele en theoretische aanpak gevolgd voor het ontwerp van een heterogene katalysator voor de enantioselectieve epoxidatie van ongefunctionaliseerde olefinen. Deze reactie werd reeds geoptimaliseerd op een chiraal salen complex en vormt dus een ideaal uitgangspunt voor het ontwerp van heterogene materialen als alternatief voor homogene processen. Om gestructureerd naar een methode te zoeken waarbij het salen complex geïmmobiliseerd wordt, is er eerst meer inzicht nodig in het mechanisme en de oorzaken van de hoge enantioselectiviteit van het complex. Vroegere pogingen om dit computationeel te onderzoeken faalden omdat het niet duidelijk was welke elektronische structuurmethode de voorkeur had. Rekening houdende met de grootte van de onderzochte systemen dient de finaal geselecteerde theoretische methode ook computationeel aantrekkelijk te zijn. In het kader hiervan werd in een eerste stap van dit doctoraatsonderzoek gezocht naar een geschikte dichtheidsfunctionaal methode om de elektronische structuur van het salencomplex te beschrijven. Hiervoor werd een computationele benchmarkstudie verricht waarbij werd vergeleken met een nauwkeurige “*multi-reference*” methode.

In het tweede deel van dit doctoraatsonderzoek werd vervolgens het reactiemechanisme van de epoxidatiereactie met het salencomplex onderzocht. Het bleek het meest waarschijnlijk dat zuurstof van het Mn^V -oxo complex naar het olefine wordt overgedragen via een radicalair intermediair. Dit mechanisme werd vroeger al voorgesteld voor deze reactie, maar experimenten met ‘radicalaire probes’, die gevormde radicalen irreversibel zouden vangen via de vorming van zijproducten, spraken dit tegen. In dit werk werd de interactie van deze probes bestudeerd met computationele methoden om het mechanisme te ontrafelen. Er werd gevonden dat er inderdaad zijproducten kunnen

gevormd worden uit het radicalair intermediair, maar dat deze reacties systematisch hoger geactiveerd zijn dan de vorming van de epoxiden zelf. Dit kan verklaren dat, ondanks het radicalaire intermediair, deze substraten toch aanleiding geven tot de vorming van epoxiden.

Eens het mechanisme gekend is, kan de stap geïsoleerd worden die bepalend is voor de selectiviteit. Op die manier kan ook de enantioselectiviteit gemodelleerd worden. Bij een initiële studie met het klassieke, symmetrische salen complex met *tert*-butyl substituenten op salicylaldehyde werden er twee mogelijke oriëntaties van het substraat ten opzichte van het complex gevonden. Deze resultaten toonden het belang aan van de sterisch grote groepen, aangezien deze één van de twee oriëntaties voor nadering van het olefine bevoordelen. Het belang van de *tert*-butyl groepen is een directe indicatie dat een covalente grafting inherent voor een verlaging van de selectiviteit zal zorgen. Bij deze manier van immobiliseren worden die substituenten vaak achterwege gelaten om de verankering te vereenvoudigen. Meestal worden de groepen enkel vervangen aan één kant van het complex, waardoor het verankerde materiaal asymmetrisch gesubstitueerd is. De theoretische berekeningen tonen aan dat de asymmetrische variant een lagere selectiviteit vertoont en bijgevolg kan gesteld worden dat grafting niet de gewenste techniek voor verankering zal zijn. Dit werd inderdaad experimenteel bevestigd.

Met de kennis van het selectiviteitsmechanisme wordt het mogelijk om de beste verankeringsprocedure voor te stellen. Hierbij werden twee dragermaterialen gebruikt: een fenolhars en een MIL-101 metaalorganisch rooster. Om de resultaten van het computationeel model te bevestigen, werd een asymmetrisch salen complex stapsgewijs opgebouwd op een MIL-101(Cr) drager. De resulterende katalysator vertoont een lagere selectiviteit, zoals verwacht uit het computationeel model. Daarnaast werd ook een lagere activiteit waargenomen. Aangezien deze resultaten nogmaals het belang van de substituenten op de vleugels van het complex aantonen, werd er gezocht naar een verankeringsmethode waar deze behouden bleven. Eén mogelijkheid is het koppelen van het complex aan een fenolhars via de zesde coördinatie-site van het complex. Deze verankeringsprocedure behield de selectiviteit van het homogene complex

maar de activiteit daalde significant. Als meest succesvolle immobilisatieprocedure werd het commerciële complex in de poriën van een NH₂-MIL-101(Al) framework gevangen tijdens de synthese van het materiaal, met vorming van een zogenaamde “ship-in-a-bottle” katalysator. Een katalytische test met dit laatste materiaal leidde tot een behoud van de selectiviteit en het grootste deel van de activiteit. De resultaten zoals hierboven samengevat, tonen de synergie aan tussen experimenteel en computationeel onderzoek bij het ontwerp van nieuwe katalysatoren.

Naast het ontwerpen van nieuwe heterogene katalysatoren, vormt karakterisatie van de structuur van het materiaal een belangrijk aandachtspunt bij elke synthese en ook voor computationeel materiaalonderzoek. In deze thesis werd een methode voorgesteld om de kwaliteit van een computationeel model te verifiëren. Het is mogelijk berekende structuren rechtstreeks te vergelijken met experimentele data via het x-straal diffractogram. Hierbij kan zowel een kwalitatieve aanpak, waarbij een gesimuleerd diffractogram visueel vergeleken wordt met het experimentele, als een kwantitatieve aanpak, waarbij een geometrie via een Rietveld model ‘gefit’ wordt aan een diffractogram, gevolgd worden. Met deze methode kon de meest gepaste structuur voor een MIL-47(V) MOF bepaald worden uit een set van vooropgestelde berekende geometrieën met een gelijkaardige energie. Er kon zelfs onderscheid gemaakt worden tussen de kleine geometrierverschillen die een gevolg zijn van het opleggen van een andere elektronische structuur (ferro- of anti-ferromagnetisch).

Karakterisatie van poreuze materialen en andere vaste stoffen kan erg moeilijk zijn. Veel technieken zoals infrarood en UV/Vis spectroscopie vertonen een slechtere resolutie vergeleken met analyses van vloeistoffen of gassen. Daarom werden er binnen het raam van dit onderzoek ook computationele methoden aangewend om gemeten spectra van materialen te analyseren en te interpreteren op de nanoschaal. In eerste instantie werden UV/Vis spectra berekend van een metaalorganisch rooster bestaande uit gallium en 2,2'-bipyridine-5,5'-dicarboxylaat linkers. In het UV/Vis spectrum van dit materiaal als suspensie in methanol waren twee banden aanwezig. Met behulp van berekende spectra werd het mogelijk

om de verschillende waargenomen banden toe te wijzen. Naast een excitatie van het onveranderde kristalrooster bleek de tweede band een gevolg te zijn van kationische defecten in de structuur. De aanwezigheid van een bipyridine groep leent zich ook tot het verankeren van andere metaalcentra die actief kunnen zijn in katalyse, in dit geval werd CuCl_2 geselecteerd om te gebruiken in een aerobe oxidatiereactie. Het verankeren van dit centrum gaf aanleiding tot veranderingen in het UV/Vis spectrum. Om een goede overeenkomst met de waargenomen spectra te vinden, werden geavanceerde moleculaire dynamica simulaties uitgevoerd. Hiermee konden nauwkeurige modelspectra berekend worden. Door een vergelijking met deze berekeningen bleken de waargenomen veranderingen inderdaad overeen te komen met de verwachte verankering.

Het onderzoek zoals voorgesteld in dit doctoraat toont aan dat gecombineerd experimenteel en computationeel onderzoek vernieuwende inzichten kan geven in het rationeel ontwerp van nieuwe materialen. Dit werd in eerste instantie aangetoond door de heterogenisatie van een homogene, chirale katalysator. Door de kennis van het reactiemechanisme werd inzicht verkregen in mogelijke methoden voor verankering van het homogeen complex. Hiernaast werd aangetoond dat computationele methoden een belangrijke bijdrage kunnen leveren in de karakterisatie van materialen. Het domein van de computationele spectroscopie is inderdaad volop in beweging en grote interacties tussen theorie en experiment zullen ongetwijfeld ontstaan. Uit dit werk kan besloten worden dat een nauwe samenwerking tussen experimenteel en computationeel werk zeer interessante resultaten kan opleveren bij het gestructureerd ontwerpen van nieuwe, poreuze materialen.

SUMMARY

Nanoporous materials are used in a large number of applications, making the design of these materials an important topic in current research. For large-scale applications within catalysis and adsorption these materials are widely applied. For more high-tech niche applications such as sensors and electronics there is also much interest towards porous solids. However the design of these compounds generally involves a high degree of trial and error. Recently much progress has been made towards a more structured approach with the popularity of high throughput synthesis. In the last few decades, *ab initio* modelling has found its place in the field of chemistry, chemical engineering and material science. The use of computational modeling can lead to a better understanding of existing processes, allowing these to be further optimized. With the increasing computational power and more sophisticated numerical algorithms, these modeling studies can also be used in the design of new materials and processes.

In the field of fine chemistry and pharmaceuticals, catalysis plays a very important role. Many transformations are unfeasible or possess a very low selectivity when the correct catalyst is not applied. In this field, homogeneous catalysis is still the method of choice for most applications. In these processes the homogeneous catalyst should be separated from the products afterwards which leads to a significant loss of catalyst. Although this economic loss is limited compared to the added values in the fine chemical industry, the increased incentive for the reduction of waste generation and energy consumption has sparked the interest for the use of heterogeneous catalysts in this field as well. Since for most processes in this field an

Summary

optimized homogeneous catalyst is already available, the new heterogeneous variant should provide the same properties. Especially the high selectivity is very important since in many fine chemistry processes side products are unwanted or even dangerous.

In this work, a combined experimental and theoretical approach is used in the design of a heterogeneous catalyst for the enantioselective epoxidation of unfunctionalized olefins. This reaction has been optimized on the homogeneous, chiral salen complex, making this the ideal starting point for the design of a heterogeneous material for this process. In order to allow a computationally aided design that would lead to a heterogeneous catalyst that maintains the selectivity of the salen catalyst, firstly the mechanism of epoxidation had to be unraveled. Previous attempts to tackle this problem computationally were unsuccessful due to uncertainties on the electronic structure method to be used for this system. Therefore it was decided to compare a broad series of density functionals to high level multireference calculations in order to isolate the best-suited method. It was important to use a DFT model since high-level wavefunction methods, although very accurate, are computationally too demanding to apply on the large system which is under investigation here.

In the second part of this research the mechanism of the epoxidation reaction with the salen complex was unraveled. A pathway with a radical intermediate appeared to be the most plausible. However, this mechanism was contradicted earlier by experiments with radical probes that would 'capture' any radical intermediate in non-epoxide side products. Our model allowed to conclude that this formation of side products was, contrary to chemical intuition, higher activated than the formation of epoxides. The difference in product distribution between several variants of the radical probes could also be explained, confirming that the radical mechanism remained the most probable for this reaction.

The knowledge of the mechanism could be used to isolate in which step the selectivity of the complex was determined which, in turn, allowed the modelling of this enantioselectivity. The study of the symmetrical salen complex with relatively bulky *tert*-butyl groups on both salicylaldehyde

moieties allowed to rationalize the important influence of these bulky groups. It was shown that two approaches of the olefin to the complex leading to the two enantiomers were dominant and one of those approaches was hindered by the bulky groups. One possibility for the immobilization of chiral salen complexes in a porous material is covalently grafting them to a support. In order to facilitate this process, the bulky groups on the wings are mostly replaced to reduce the steric hindrance in the grafting and to introduce a functional group to allow the coupling. This modification can be done on a single side of the complex leading to a so-called asymmetric salen complex. Theoretical calculations showed that the asymmetric variant shows an inherently lower selectivity, implying that this immobilization technique was not the preferred approach. This was also observed in the experiments.

With the knowledge on the selectivity behavior that was found from the computational modeling study, a rational design of an immobilized salen catalyst could be proposed. As a carrier material two supports were chosen: a MIL-101 metal organic framework and a phenolic resin. As a first step, the results from the modelling calculation were verified and an asymmetric salen complex was grafted on MIL-101(Cr). This led to a decrease in selectivity, as was expected, but also to a decrease in activity. Since our models showed the importance of using the symmetrical complex with bulky substituents, another immobilization procedure was proposed. In this approach the complex was anchored to a phenolic resin via a substitution on the sixth coordination side. While this grafting method allowed the retention of selectivity it was detrimental for the activity. This was attributed to the change in electronic properties of the manganese center. In the most successful immobilization approach, the commercial salen complex was immobilized by building an $\text{NH}_2\text{-MIL101(Al)}$ material around it, forming a ship-in-a-bottle catalyst. A catalytic test with this material showed that the selectivity was maintained and the loss of activity was limited. These results show the possible synergy between experimental and computational research in the design of new catalysts.

Other applications of the computational modeling of materials were also explored, more specifically the verification of calculated crystal structures. When modelling nanoporous, crystalline materials such as metal organic

Summary

frameworks it can be interesting to have a method to verify the quality of the model. It was shown to be possible to directly compare calculated geometries to experiments via x-ray diffractograms. Both a qualitative approach, where simulated diffractograms are compared to experimental ones, as a quantitative approach, where calculated geometries were fit to the measured diffractogram using a Rietveld model have shown their value in this exercise. This method was applied on a MIL-47(V) structure, where the most suitable geometry was found from a set of calculated possibilities with similar energies. Even subtle geometrical differences between structures with different electronic structures (ferro- or anti-ferromagnetic) could be distinguished from each other.

As a third part of this work, the use of theoretical modelling in the interpretation of spectra was investigated. During the development of a new material the characterization can in many cases be non-trivial. Many spectroscopic techniques suffer from a low resolution in the analysis of solids. Within the framework of this research calculations were used to assist in the interpretation of UV/Vis and IR spectra. This procedure was applied on the development of a gallium MOF with 2,2'-bipyridine-5,5'-dicarboxylate linkers. In the UV/VIS spectrum, two absorption bands were present and only one could be attributed to the pristine material. With the aid of the calculated spectra, the second band was assigned to cationic defects in the crystal structure. The presence of a bipyridine moiety in the structure opens the possibility for further modifications with metal centers that could serve as an active site for catalysis. In this case a modification with CuCl_2 was proposed to use in the aerobic epoxidation of olefins. Attempts to graft the active site induced an effect in the UV/Vis spectrum. To achieve a good agreement between the calculated and measured spectra, advanced molecular dynamic calculations were done. With this approach, accurate model spectra could be calculated. By comparing these to the measured spectra the observed changes in the UV/Vis spectrum could indeed be attributed to a successful grafting.

The research as shown in this work indicates that a combined experimental and computational research can provide innovating insights in the rational design of new materials. This was firstly shown by the heterogenation of a

homogeneous, chiral catalyst. The knowledge of the reaction mechanism provided insight in how the immobilization methods would influence the selectivity of the material. Besides the design of catalysts it was shown that computational models can provide an important contribution to the characterization of materials. The domain of computational spectroscopy is growing continuously and fruitful complementary efforts between theoretical and experimental research are to be expected. To conclude, this thesis shows that a close collaboration between experimental and theoretical research can provide very interesting results in the targeted design of nanoporous materials.

Part I: Design of metal organic frameworks for the catalytic production of fine chemicals

CHAPTER 1. INTRODUCTION

1.1 CATALYSIS

General

The textbook definition of a catalyst is a compound that accelerates a chemical reaction without being consumed in the process. This is represented in an energy diagram as shown in Figure 1.1. However, for practical applications, a catalyst has a much larger impact than only accelerating the reaction. A crucial function is also increasing the selectivity of a process. Indeed, inhibiting the production of unwanted or even dangerous side products can be achieved by choosing the appropriate catalyst. In general, the use of catalyzed reactions has two functions: an economic one, with the aim to produce the desired products more efficiently, and an environmental one, with the aim of reducing the energy requirements and waste production of a process.

The field of catalysis can be divided in two main divisions: heterogeneous catalysis, where the catalyst is in a different phase from the reactants, or homogeneous catalysis where the catalyst is in the same phase^[1-6]. Examples of heterogeneous catalysts are (acid) zeolites that are currently workhorses in the petrochemical industry^[7, 8], but also deposited metals in porous materials^[9] and grafted homogeneous complexes belong to this category of catalysis. The latter catalysts have received an increased interest in the last decade^[10, 11], but their industrial applications have been limited. Heterogeneous catalysis currently dominates the petrochemical and bulk chemical industry but has also found its way in fine chemistry

applications^[6, 12]. The examples of homogeneous catalysis are even more numerous, the range goes from very simple systems such as sulfuric acid, that are used in bulk chemistry, to large metal complexes typically found in fine chemistry processes. An emerging class of homogeneous catalysts are enzymes^[13]. With the goal of using chemical processes that have been 'optimized' by nature, an exploration to employ these highly complex but very active and selective substances in the chemical industry is currently ongoing.

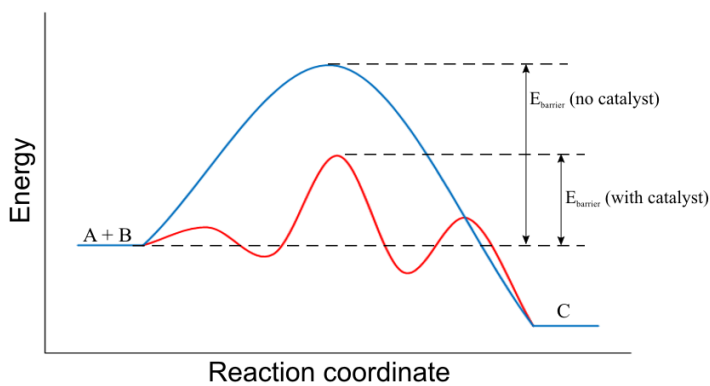


Figure 1.1. Schematic representation of a catalyzed reaction.

Catalysis in fine chemistry

To provide a more detailed picture of the use of catalysis in the chemical industry it is interesting to divide industrial processes into four distinctive groups; oil refining, bulk chemistry, fine chemistry and the production of pharmaceuticals. This division is mostly made on the basis of yearly production scale (see Table 1.1). In each of these segments catalysis plays a crucial role but mostly for different reasons and the catalyst takes different shapes, i.e. homogeneous, heterogeneous, zeolites, deposited metal clusters.

Oil refining and bulk chemistry use a catalyst to reduce the energy requirements and increase the speed of a process. Some conversions are even unfeasible without the right catalyst. Selectivity is relatively less important compared to other segments in the industry. In a majority of the

processes from this category, heterogeneous catalysts are employed. This allows the use of continuous processes, that are crucial for the production of chemicals on a large scale. The production of fine chemicals and pharmaceuticals on the other hand, is mostly done with the help of homogeneous catalysts. These are in most cases very selective compounds to avoid undesired side products or induce the formation of products that would not be formed in an uncatalyzed reaction. Since the cost of the separation of these catalysts from the reaction mixture is in most cases low compared to the added value on the products, little effort has been done on finding heterogeneous catalysts with the same function as the homogeneous one. On top of that, it is mostly a difficult challenge to find a heterogeneous catalyst that has the same selectivity as the best homogeneous system for a certain reaction. However, there is a growing incentive to replace the current generation of homogeneous systems by heterogeneous variants. The main reason for this are environmental concerns^[14, 15].

An objective way of measuring the impact of a process is the E-factor, first introduced by Sheldon^[16-18]. The most basic definition of this factor is:

$$E = \frac{\text{waste produced (kg)}}{\text{product produced (kg)}} \quad (1.1)$$

For practical applications the waste produced is multiplied by a factor involving the toxicity of the waste^[19]. For example, the production of water as a 'waste' product is far less invasive as the production of methanol waste. When analyzing the average E-factors for the different segments of the industry it becomes apparent that the large-scale industries have significantly reduced the generation of waste products compared to the small-scale industries (Table 1.1). The difference has become so large that the absolute amount of waste produced in fine chemistry and pharmaceutical chemistry is of the same order of magnitude as in oil refining although the production quantities are significantly lower. A part of this effect is due to the use of homogeneous catalysts. The steps needed to separate the catalyst from the products generate unwanted compounds and mostly a significant fraction of the catalyst is lost in the process. These

disadvantages could be avoided when using a heterogeneous catalyst. Another important effect is the generation of side-products in a process. When these products cannot be valorized they are also considered as waste. This means that an important factor in the design of a good catalyst will be maximizing the selectivity of the material towards the desired products.

Table 1.1. Production and waste generation in the different segments of the chemical industry^[16].

Segment	Production (ton/year)	E-factor
Oil refining	10^6 - 10^8	<0.1
Bulk Chemistry	10^4 - 10^6	1-5
Fine Chemistry	10^2 - 10^4	5-50
Pharmaceuticals	10 - 10^3	25-100

Design of catalysts

An important goal in this thesis is to design a heterogeneous catalyst for the well-known process of chiral olefin epoxidation. This task may be achieved using various approaches. The easiest way is to look in a pool of existing materials for a candidate that has similar chemical properties compared to the currently used materials and catalysts for the process. For example when there is a reaction that requires acid catalysis, one could look for an acid zeolite and use that as a candidate. While this answer seems very straightforward, there is a whole range of acid zeolites available and not every candidate will have the appropriate properties for the process under investigation^[20]. Thus, there are more advanced tools necessary for the design of a heterogeneous catalyst.

A common technique is an extended design of experiments, by an investigation where different parameters of the catalyst and reaction setup are modified, the mechanism of a reaction can be discovered. This method is referred to as (experimental) microkinetic modelling^[21, 22]. With the knowledge of the mechanism, a list of important features that the material should have to be usable in the process, can be compiled^[23]. In a next phase

of the design, the catalytic material is synthesized to contain those features. This requires a profound insight in material chemistry and a class of materials that has enough flexibility to allow the needed modification. As with any good design process the knowledge from the first steps is used to further improve the material by repeating this procedure several times.

In the development of a microkinetic model as described above, gaining mechanistic insight is done by a kinetic analysis. There are of course several other ways to achieve this. For example in situ spectroscopic studies or prior knowledge on the considered type of reaction. With the increase in computational power of the last decades it has become feasible to use molecular simulations to assess the behavior of a chemical reaction. This methodology describes a chemical system from basic physical principles and allows an atomic-scale insight into the parameters that control the behavior of a catalyst, and overall the chemical reaction. The advantage of this technique is the possibility to test a multitude of different variants of a system in a relatively short time. Moreover it is possible to simulate conditions that are not achievable in a laboratory. The main disadvantage of this approach is that the results are not necessarily immediately applicable and sometimes not experimentally achievable. Thus using molecular modeling in rational design of catalyst, requires a close interaction between the results obtained from the computational research, the synthesis of the material and experimental validation of the behavior of the material in the chemical reaction under investigation.

1.2 SALEN COMPLEXES FOR ENANTIOSELECTIVE OXIDATION CATALYSIS

Epoxidation

Epoxides are valuable intermediates in numerous chemical reactions. The high ring-strain in the three-membered ring allows for a facile transformation to a whole range of different products, i.e. diols, ethers, carboxylic acids,...^[24, 25] (Figure 1.2). These epoxides can be produced in different ways, but the most direct route seems to be the oxidation of

olefins. The oxygen is transferred from a whole range of oxidants to the double bond of the substrate, a straightforward example of this is the oxidation of olefins with meta-chloroperbenzoic acid (MCPBA)^[26]. Unlike the latter example, many transformations of olefins to epoxides require some sort of catalyst. A good way to classify a catalyst for the epoxidation of olefins is via the mechanism at work^[27] (Figure 1.3). The first possible process involves a radical chain mechanism where the oxidant forms a radical intermediate that is active for the epoxidation. This process is mostly done with metal catalysts that can undergo a one-electron redox step (i.e. $\text{Cu}^{\text{II}}/\text{Cu}^{\text{I}}$ or $\text{Co}^{\text{III}}/\text{Co}^{\text{II}}$). It is not surprising that, due to the radical character of this system, this mechanism is the least selective^[28]. The second, industrially most relative mechanism is the so-called oxirane pathway^[29, 30]. This reaction is catalyzed by metal complexes of Ti(IV), V(V) or Mo(VI). The coordination chemistry of these complexes is most often of huge importance for the activity and selectivity. The third scheme is the oxygen-rebound mechanism^[31, 32], this mechanism is catalyzed by metal complexes that can undergo a two-electron redox step (i.e. $\text{Cr}^{\text{III}}/\text{Cr}^{\text{V}}$ or $\text{Mn}^{\text{III}}/\text{Mn}^{\text{V}}$). In this pathway, the oxygen atom is firstly transferred from the oxidant to the catalyst and then passed on to the substrate.

Discovery of the chiral salen complex

We will consider the oxygen rebound mechanism more in-depth. This mechanism is well known in porphyrin systems^[31, 32] and is thus an important mechanism in nature. For synthetic chemistry the approach also seems very attractive, some very active catalysts operate via this pathway^[33, 34]. Another type of complexes that are used in this type of oxygen transfer are compounds of Mn, Cr or V with salen ligands. A salen ligand is a chelating ligand consisting of two salicylaldehyde moieties connected by, in its simplest form, an ethylenediamine bridge. Although these chelating compounds are already in use for a long time^[35], since the late 80's there has been a significant increase in the academic interest in the use of salen complexes for oxidation reactions.

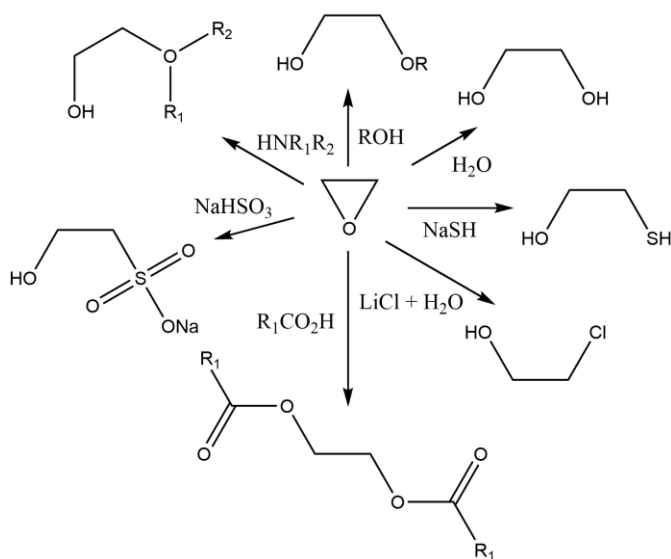
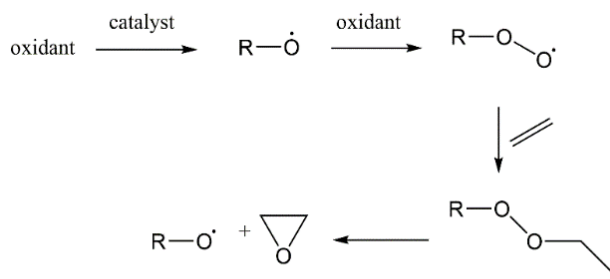


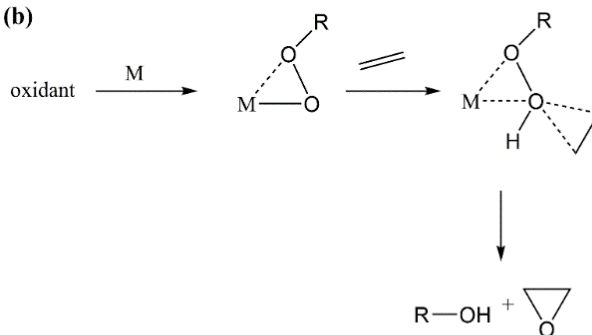
Figure 1.2. Selection of possible reactions with epoxides by exploiting the high ring strain of the three-membered ring.

In 1990 Katsuki^[36] and Jacobsen^[37] reported, independently of each other, a chiral variant of the manganese salen complex (simply referred to as 'chiral salen complex'). This meant a great leap forward in the popularity of salen complexes. Since epoxides are very reactive it could prove very interesting to be able to make chiral epoxides from unfunctionalized olefins (Figure 1.4). These intermediates can transfer their chirality in subsequent steps and can thus introduce a chiral center during a synthesis procedure. The value of chiral epoxides is indicated by the large previous interest in a catalyst that could successfully generate these compounds, being the titanium tartrate or Sharpless complex^[38, 39]. This system was very active and selective, but its main disadvantage was that it required an allylic alcohol as substrate for epoxidation and unfunctionalized olefins could not be oxidized enantioselectively. Despite these disadvantages, the value of this catalyst in the field of organic chemistry was recognized with a nobel prize in 2001^[40].

(a)



(b)



(c)

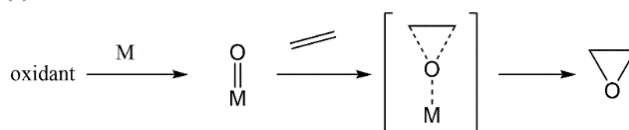


Figure 1.3. Different mechanisms for the epoxidation of olefins with peroxides as a model oxidant. The radical chain mechanism (a), oxirane pathway (b) and oxygen rebound mechanism (c).

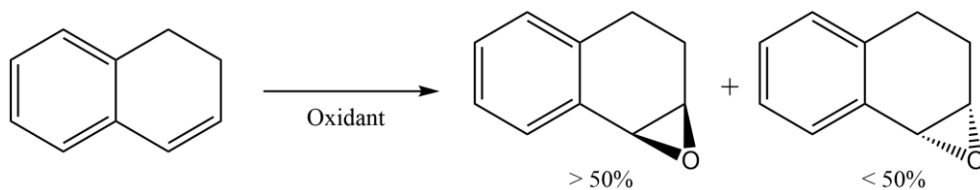


Figure 1.4. Example of an enantioselective epoxidation reaction with an unfunctionalized olefin as substrate.

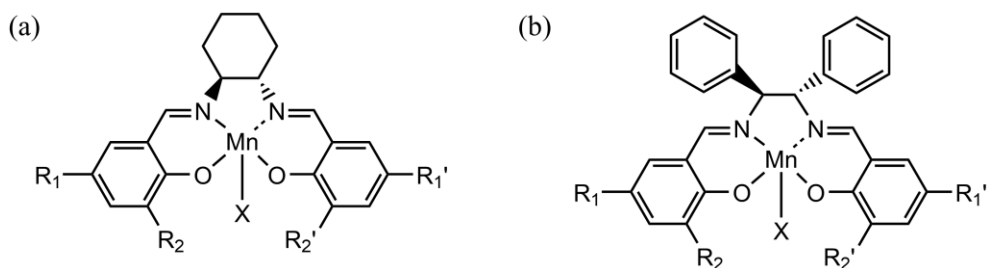


Figure 1.5. Variants of the salen complex, with a chiral diamine backbone (a) and a chiral biphenyl backbone (b)

The first class of chiral salen complexes had a chiral 1,2-diphenylethenediamine backbone (Figure 1.5 (b)). Later on, Jacobsen proposed a variant that was built from a chiral cyclohexanediamine (Figure 1.5 (a))^[41]. The main advantage of the latter is that the chiral diamine used is very easily obtainable by a recrystallization with tartaric acid from a racemic mixture^[42]. Early on, it became apparent that substituents on the salicylaldehyde moieties could significantly increase the selectivity^[36] and activity^[43]. By introducing extra chiral groups on the C3/C3' positions (see Figure 1.6 for the numbering) the selectivity of the catalyst could be largely improved^[44, 45]. However, this increases the complexity of synthesizing the ligands. The more simple variant has *tert*-butyl groups on the C3/C3' and the C5/C5' positions. This complex consists of relatively simple and cheap building blocks and can be produced easily on a large scale,^[46] while still maintaining a very good selectivity for a wide range of substrates. All those features, together with the commercial availability, make this variant of the chiral salen complex (often denoted as the Jacobsen (salen) complex) the choice for many applications.

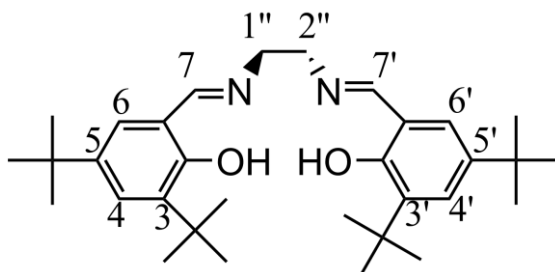


Figure 1.6. Numbering to denote substituent positions on salen ligands.

The high potency of the chiral salen ligand loaded with manganese in enantioselective epoxidation reactions has led to much research on the application of this system for other reactions. The first example of this is the asymmetric aziridination. This use of the salen complex is again based on the prior knowledge that porphyrins are a viable catalyst for this reaction^[47]. Although initial results were poor,^[48, 49] much effort was done with the use of very advanced and bulky salen ligands (for example Figure 1.7) to improve the selectivity. The use of a Ru-salen type catalyst allowed to obtain very high selectivities in a good yield^[50]. However the ligands used are much harder and more expensive to synthesize than the commercial Jacobsen catalyst (Figure 1.5 (a)) making it a less attractive catalyst for this reaction as Mn-salen complexes are in the epoxidation of olefins.

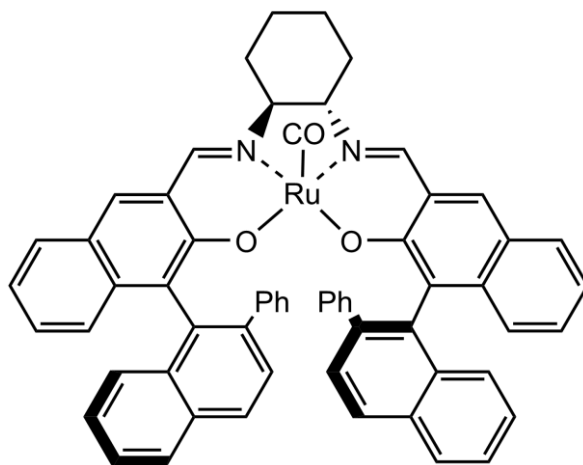


Figure 1.7. Bulky ruthenium-salen catalyst for enantioselective aziridination reactions.

Another application is the use of salen-type catalysts for enantioselective sulfoxidation reactions of thioethers. This application is driven by the fact that many asymmetric epoxidation catalysts are also successful in selective sulfoxidation reactions. With this idea in mind Fujita *et al.*^[51] employed the vanadium-loaded salen complex even before the breakthrough of salen catalysts for asymmetric olefin epoxidation. However the resulting selectivity was relatively disappointing. The use of the di- μ -oxo (Ti)salen complex provided a much better selectivity as was shown by Katsuki *et al.*^[52, 53] Other reactions using iron variants and the classical manganese system also led to decent results^[54, 55]. But since the scope of possible

substrates is still limited, the search for a catalyst with a broad range of applicability and the capability to avoid overoxidation in the sulfoxidation process still continues.

Mechanistic considerations from experimental studies

The mechanism of olefin epoxidation with Mn-salen complexes has been contested for many years. Although the oxygen rebound mechanism was assumed to be valid on the Mn-salen complex, the Mn^V-oxo intermediate (Figure 1.8) could not be easily isolated as was the case with the chromium variant^[56]. An important breakthrough was the discovery of this intermediate using mass spectroscopy^[57]. This observation suggested that the oxygen rebound mechanism is indeed the most likely pathway for this variant.

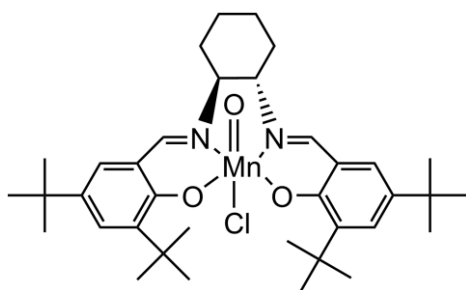


Figure 1.8. Mn^V-oxo intermediate of the Jacobsen complex.

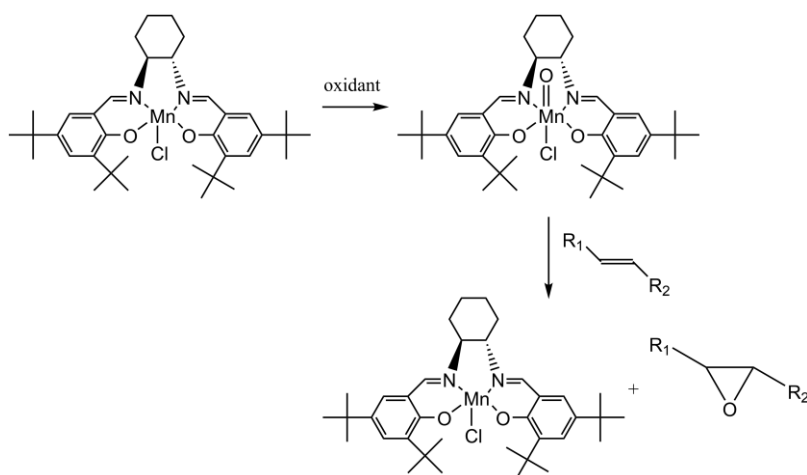


Figure 1.9. General reaction scheme of olefin epoxidation catalyzed by the Mn-salen complex.

The main mechanistic question concerning this reaction is what happens after the oxygen is transferred to the manganese complex. How does it transfer from the catalyst to the olefin? Very early, the observation was made that *cis* olefins led to a mixture of both *cis* and *trans* epoxides (Figure 1.9)^[36]. Moreover, the reaction rate is much higher when the substrate is a conjugated olefin. These two facts lead to the conclusion that the reaction should occur via a radical intermediate (Figure 1.10). This radical allows for a free rotation between the olefin C-C bond, that would explain the isomerization leading to a mixture of *cis* and *trans* epoxides. The theory is further supported by the observation that conjugated olefins are converted faster than the unconjugated variants. The radical is stabilized by resonance, thus providing a more stable intermediate and a faster reaction.

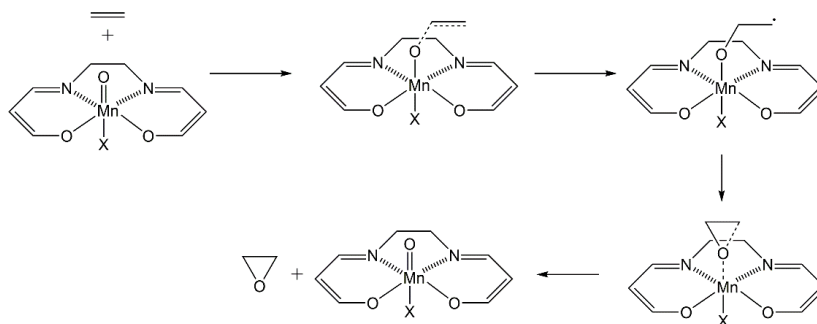


Figure 1.10. Reaction scheme with a radical intermediate (parts of the structure are omitted for simplicity).

However, this straightforward explanation was quickly questioned by experimental results from Wong *et al.*^[58] They proposed to investigate the mechanism further using a radical probe. These radical probes are molecules that quickly form a specific product when a radical center is present. For example *trans*-2-phenyl-1-vinylcyclopropane (Figure 1.11) has a three-membered propane ring vicinal to the double bond. When a radical is formed, the cyclopropane ring would open and a series of ring-opening products would be formed. Thus, the hypothesis was formulated that when the radical intermediate exists, a majority of ring opening products would be observed, since this step is supposed to be very lowly activated. The authors concluded that, depending on the exact substituents on the probe, different mechanisms for the oxygen transfer were at work.

Next to the originally proposed radical pathway a concerted route was assumed.

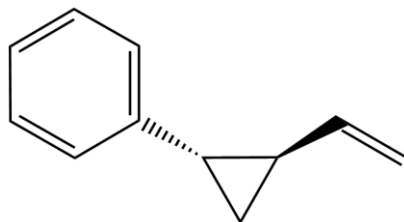
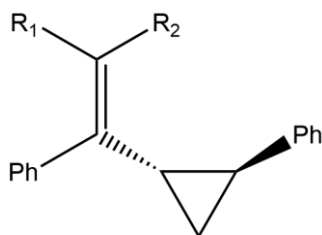


Figure 1.11. *Trans-2-phenyl-1-vinylcyclopropane as radical probe*

Akermark *et al.*^[59] optimized this procedure by proposing modifications on the original probe that would not introduce any bias to the position of the radical (Figure 1.12 and Table 1.2). Again, different substituents on the probe were considered. The results from these tests were similar to the previous work, a mixture of epoxide and ring-opening products was present. The ratio of the products was shown to be dependent on both the exact substrates and the oxidant used. Again the conclusion was that a radical mechanism could not support these observations and thus it was proposed that the epoxidation takes place via a metallaoxetane mechanism Figure 1.14(C).



- (1) $R_1 = H, R_2 = H$
- (2) $R_1 = H, R_2 = CH_3$
- (3) $R_1 = CH_3, R_2 = H$

Figure 1.12. *Radical probes proposed by Akermark et al.*^[59]

The metallaoxetane pathway has already obtained significant support as a viable alternative for the radical intermediate mechanism^[60]. A later set of experiments calculating Hammett relations when modifying the electronic

effects on the substrates by changing functional groups on cis-stilbenes led to similar conclusions^[61]. Despite many experimental approaches pointing to alternative mechanisms at work, none of the proposed alternatives can explain the observed cis/trans isomerization and rate acceleration for conjugated olefins very well. An interesting summary of the research on the mechanisms was provided by Linker^[62].

Table 1.2. Results of the radical probe experiments.

	NaOCl/ CH ₂ Cl ₂ (a)	Iodosylbenzene/ benzene (b)
(1)	100%	57%
(2)	100%	83%
(3)	56%	54%

Next to the mechanism of the oxygen transfer, the effects that control the enantioselectivity are also not unraveled yet. Several experiments have been conducted to probe the approach vectors^[41, 63, 64]. Experiments with styrene derivatives featuring different substituents^[63] have led to the conclusion that the so called distal, side-on approach (schematically shown in Figure 1.13), where the substrate approaches from the side and the most bulky group is pointed away from the complex is preferred, except for some tri-substituted variants. However, an experiment where different substituents were introduced on the salen ligand^[41] seemed to point to an approach via the backbone (diamine).

Mechanistic considerations from computational studies

The elusiveness of the mechanism for olefin epoxidation with Mn-salen complexes has triggered much computational research on this topic. A pioneering work in this field is the study of Svensson *et al.*^[65] They were the first to use a simplified model for the Mn^V-oxo-salen complex and employed ethene as a model for the olefin. Although this model omits many steric effects of the complex it was the only way to reduce the system to a size that was feasible for the computational resources at that time. Using ethene as a probe molecule does not allow to provide any conclusions on the enantioselective behavior of the catalyst, but it certainly provides a

good model to unravel the mechanism. One of the important conclusions of this study was the observation that the oxygen transfer could take place on different spin planes with zero, two or four unpaired electrons (spin 0, spin 1 or spin 2). This report suggested a spin transfer during the reaction and the metallaoxetane intermediate was discarded for being too unstable.

The main criticism on this methodology was the use of a cationic model system. As shown in Figure 1.5, there is a counter ion on the manganese center, in the most common case this is a chloride anion. In the apolar solvents that are used for this reaction it is likely that the counter ion stays coordinated to the complex and has a significant influence on its electronic configuration. Jacobsen *et al.*^[66] recognized this and proposed the neutral model for the complex, including the counter ion. Moreover they employed a BP86 DFT functional instead of a B3LYP functional, which led to a different ordering of the spin states. They concluded that the reaction occurred via a radical intermediate and that it was most favorable on the spin 1 plane. A pathway on the spin 0 system occurring via a concerted mechanism was also found, but was shown to be far less stable.

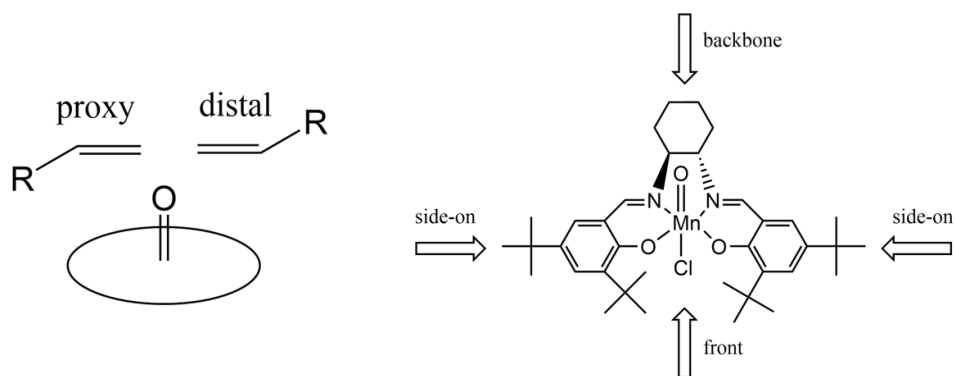


Figure 1.13. Schematic representation of various approach vectors to the salen complex, adapted from Norrby *et al.*^[63], and Cavallo *et al.*^[67]

The possibility of the reaction taking place on different spin planes led to yet another discussion. The results from the pure DFT functional (BP86) were shown to be in agreement with high level CCSD(T) calculations by Burt *et al.*^[68] This led to the use of pure DFT functionals being favored over hybrid functionals for this system. More research on this topic by Jacobsen

et al.^[69-72] discovered possible alternatives for the radical intermediate. Most significantly, the metallaoxetane structure was found to be very stable with the cationic model for the salen complex. Burt *et al.*^[73] proposed another intermediate: the five-membered ring (FMR) and showed the epoxidation via this intermediate being plausible on all different spin planes. All these discoveries culminated in the modeling of the full catalytic cycle with sodiumhypochloride as oxidant. The hypochloride anion was proposed to be the preferred counter ion, and the reaction would take place via a phase transfer from the aqueous to the organic phase^[69].

The main problem with the B3LYP functional was identified to be the HF exchange part. A modified B3LYP functional with only 15% HF exchange was shown to possess a qualitative agreement with the BLYP and BP86 functionals^[74]. Despite the interesting results many groups recognized that there was still much effort needed to find a good electronic structure method to describe the Mn-salen type complexes. Therefore, high-level post-HF methods were employed to find the correct electronic configuration^[75] and several benchmarks were set up to find which DFT functional succeeded the best in reproducing these results^[76-79]. In this work a suitable DFT functional will be chosen by comparing results from a broad range of functionals to high level electronic structure methods. Following this procedure, the long-standing question on how oxygen is transferred to the olefin can be answered.

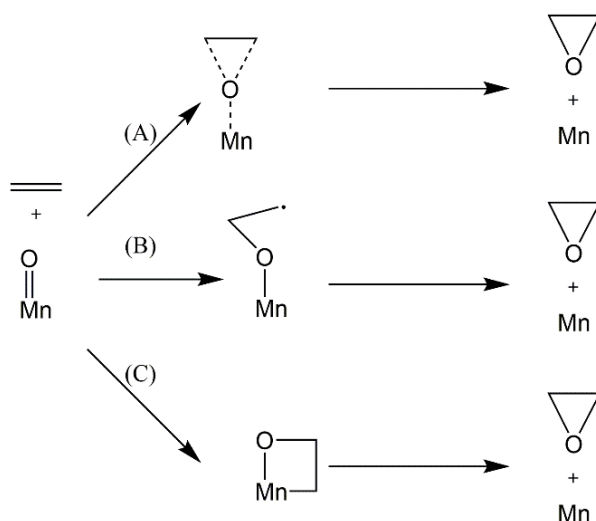


Figure 1.14. Different mechanisms proposed for the oxygen transfer.

Next to the mechanism for the oxygen transfer, the origin of the enantioselectivity of the salen complex was studied computationally, but the number of computational studies on the selectivity are limited. The research on the selectivity has always been performed with molecular mechanics methods due to the size of the system^[67]. Although there is some empirical insight in the mechanisms governing the selectivity of this catalyst a fundamental understanding is still missing. By using the full complex as a model many interactions contributing to the enantioselectivity can be identified.

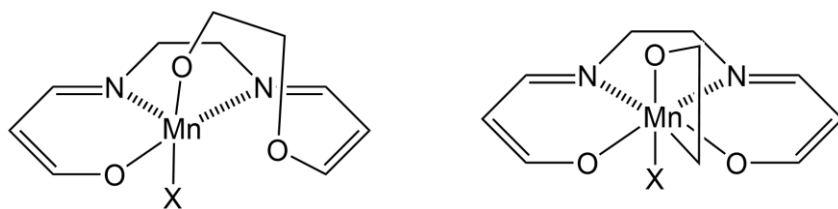


Figure 1.15. Possible non-radical intermediates found in different computational studies.

Salen complexes: recent advances and practical applicability

Finding variants of the homogeneous salen complexes for olefin oxidations is still a research topic that attracts much attention. But the complexity of these more bulky systems make that the industrial relevance of these

catalysts will be limited to some very specific cases. Thus an in-depth discussion of this will be omitted. Arguably the most important advancement in the application of chiral salen complexes is the ability to use sodiumhypochloride as an oxidant^[64]. Since this substance is cheap, easily available and provides only a harmless salt (NaCl) as byproduct, it is an ideal oxidizing agent in this reaction. A second advancement that was important for the practical applicability of this system is the method for a straight-forward and easily upscalable synthesis procedure of the Jacobsen complex, including the purification of the chiral backbone^[46].

Next to the use in chiral olefin epoxidation, the scope of salen-type ligands has widened in the recent years, mostly by exploring different metal centers or ligand modifications. An application that has raised much interest in the recent years is the valorization of CO₂ by copolymerization with epoxides^[80, 81]. Other applications are the catalysis of Mizoroki–Heck and Hiyama cross-coupling reactions^[82], non-enantioselective oxidations^[83], kinetic resolution of alcohols^[84] and many more. This broad scale of possibilities is due to the flexibility in modification of these complexes, both in metal center as in functional groups on the ligand.

As with any homogeneous catalyst, the applicability could be improved with the design of a heterogeneous analogue that maintains the activity and selectivity of the original material. A solid material can easily be separated from a liquid or gaseous phase, thus allowing a good recycling of the (expensive) catalyst. Another reason to heterogenize catalytic complexes is to avoid the pollution of the end-product. In many fine-chemical applications any contamination of the products is detrimental for the application and an easy, quantitative separation is very important. Given the many benefits, there has been a lot of research on the design of heterogeneous salen catalysts. A covalent grafting seems the most straightforward route to achieve this. As a carrier material for this approach resins are proposed due to their ease of modification^[85-87]. Most of these materials succeeded in the catalytic epoxidation but the enantioselectivity was significantly lower than the homogeneous variants. Other reports use the sixth coordination side on the manganese center to anchor the complex^[88, 89]. Generally this method leads to a more selective catalyst.

These methods and many others have been reviewed by Duan *et al.*^[90] While several immobilization procedures have been proposed, a method that maintains both the selectivity and activity of a complex would be very valuable and could prove a large step forward in the industrial applicability of this complex.

1.3 METAL ORGANIC FRAMEWORKS

While the first reference to what one might call a Metal Organic Framework (MOF) dates from 1965^[91] the big interest in this topic however, was sparked by the report from Yaghi *et al.*^[92] in 1999. The design and applications of these materials has been summarized in several interesting books^[93, 94], reviews and themed journals^[95-97]. Many definitions of a MOF are proposed, they can be summarized as: hybrid crystalline materials consisting of metal nodes and organic linkers and possessing inherent porosity. When analyzing this definition one can see why there are such a huge amount of MOF structures known. There is an almost infinite amount of combinations between different metals and linkers. This leads to a whole spectrum of MOFs with various shapes and connectivities, the only limitation on a metal-linker combination is its ability to form a 3D network (or stacked 2D sheets). These networks can have different pore sizes and shapes ranging from 1D channels or large cages with smaller windows (illustrated in Figure 1.16).

Synthesis and nomenclature

Although the goal of this thesis is not the design of new MOF structures, many previously reported materials are applied, making it interesting to take a look on how these materials are synthesized. From a fundamental point of view the growth of a MOF is no different than that of another crystalline material. The first step is the nucleation, where a small amount of components meet to form a starting center for the crystal. After this first step there is a growth phase where the nuclei grow to full crystals. This is a constant exchange between components from the solution that couple on the solid phase and vice versa. This two-way process is crucial to provide a well-defined crystal structure since it is an internal correction of structural

defects^[98]. From a practical perspective the most applied synthesis procedure is a solvothermal system. Here the metal salts and organic linkers are mixed in a solvent and heated, sometimes under pressure if the synthesis temperature is higher than the boiling point of the solvent.

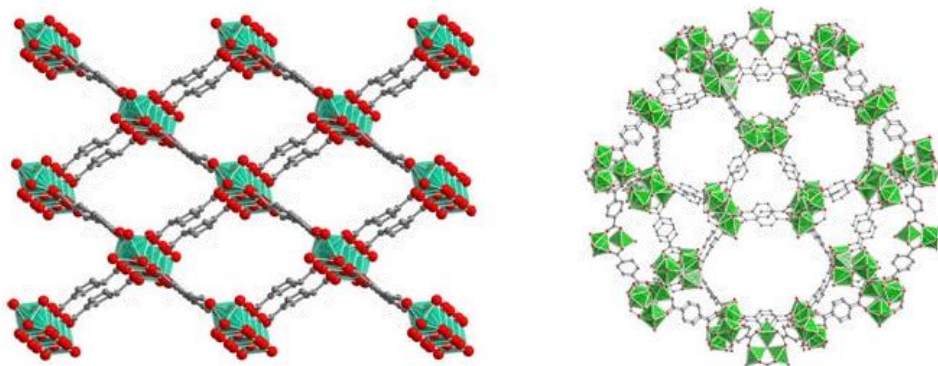


Figure 1.16. MIL-53 (left) and MIL-101 (right) topologies. Both MOFs can be made by combining a Cr-salt and terephthalic acid linkers, this illustrates the versatile structures that can be obtained with metal organic frameworks, Reprinted (adapted) with permission from^[99]. Copyright 2015 American Chemical Society.

Other synthesis approaches are for example an electrochemical synthesis, where the crystals are formed on an electrode with the help of an electrical current. The latter procedure has the most promise as an industrial synthesis route since it can be operated continuously. BASF produces a series of MOFs for commercial applications such as separation, adsorption and catalysis via this procedure^[100, 101].

Another procedure that has attracted much attention is the microwave-assisted synthesis. The use of microwaves to enhance reaction rates or to enable reactions that were previously unfeasible is already well-established in synthetic chemistry^[102]. The same methodologies have been applied on the synthesis of MOFs^[103]. Here the main advantage is that synthesis times could be shortened significantly. As an example the synthesis of MIL-100(Cr) can be considered, the classical solvothermal synthesis procedure takes multiple days while the microwave-assisted method provides the same yield in four hours^[104]. Next to this first report, numerous other materials can be produced more efficiently with the microwave approach.

Compared to other synthesis pathways, microwave-assisted synthesis procedures yield tiny crystals mostly of 100 nm to a few micrometers. Although the use of microwave-assisted synthesis procedures is widespread, the physical principles behind this methodology are not well-known. The most accepted theory is the presence of a beneficial local heating effect when irradiating polar solvents.

The previous examples are arguably the most applied procedures to synthesize a metal organic framework. When single crystals are required for a structural analysis by XRD, low temperature methods are preferred^[98]. All of these methods provide a relatively low yield of highly crystalline and large crystals. Another method worth mentioning is the mechanochemical synthesis where the material is formed in a solvent-free (or solvent-poor) medium by ball milling^[105, 106]. This procedure generally yields a material with a poorer crystallinity than can be obtained via other procedures. The main advantages of this methodology are the short reaction times and the ease of upscaling.

Due to the absence of a standardized method for the nomenclature of metal organic frameworks the system has become complex. Generally a MOF is named in two parts; firstly there is a series of letters that most of the time refer to the institute or group that first reported the material. Some examples are HKUST (Hong Kong university of science and technology), MIL (*matériaux de l'institut Lavoisier*). The second part of the name is a number denoting how many MOFs have been previously reported by that group. Due to the nature of MOFs, series of similar combinations of metals and linkers can be designed, this is called isorecticular synthesis (Figure 1.17)^[107, 108]. Mostly these variants are named by using their parent name with the modification on the linker or metal center noted, i.e. MIL-53, MIL-53(Cr), MIL-53(Ga), NH₂-MIL-53^[109]. The nomenclature presented here is the one used in this work, but since there are many different systems, other types of names can be found in literature.

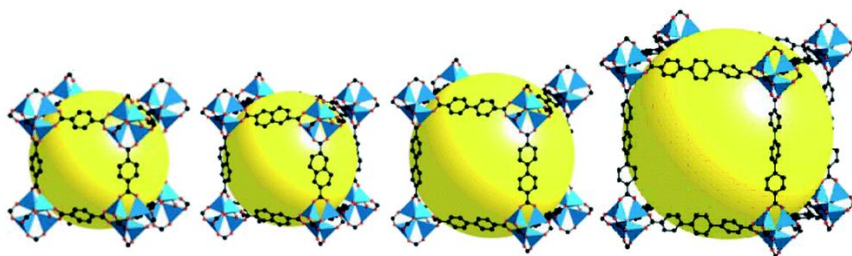


Figure 1.17. Example of isorecticular MOF design by linker variation. Reproduced from^[110] with permission of The Royal Society of Chemistry.

Applications

As with every porous material an important application of MOFs is gas adsorption and separation. In this area the largest research efforts have gone to the design of metal organic frameworks for hydrogen storage^[111, 112]. The application of hydrogen as a clean fuel in cars and other mobile systems has been hindered by the amount of fuel that can be stored in a limited space, therefore there is a need for adsorbents to be loaded in a fuel tank in order to increase the amount of gas that can be stored in a volume under a certain pressure. The main features a material should have to be a good adsorbent in this application is a low weight, high surface area and a good affinity for hydrogen. In this application the versatility in the design of MOFs shines, an isorecticular series of structures can be made to select the best candidate and to assess the influence of the linker^[113]. Despite much interest in this field a readily applicable material that can increase the stored amount of hydrogen to a sufficient height for practical applications has not been proposed. However the sheer number of structures that have been designed for this application shows the versatility of MOFs and the opportunities for the design of novel materials^[114].

This work however focusses on the application of MOFs within the field of catalysis and more attention will be given to this area of application. Opportunities of using MOFs in catalysis have been reviewed extensively^[115, 116]. Unlike many other porous materials such as silica's, resins, PMOs or all-silica zeolites, MOFs have an inherent metal center in their structure that could serve as an active site for catalysis. For example the vanadium sites in MIL-47 structures are very suitable for olefin epoxidation reactions^[117, 118].

Sometimes the MOF is not catalytically active as such due to adsorption of water on the free metal sites, blocking their catalytic activity. This effect was shown by De Vos *et al.*^[119] with the use of a dehydrated HKUST-1 as a Lewis acid catalyst. In the case of Lewis acid catalysis the hybrid nature of metal organic frameworks can be exploited by tuning the electronic interactions between the linker and metal site by modifying the former^[120]. Despite many opportunities with this approach, sometimes the metal site is not available for catalysis since its complete coordination shell is occupied^[121]. In that case one has to look to incorporate other active sites in the structure, for example by building them into the material by the linkers. As an example some MOFs have been designed with advanced transition metal complexes as linkers such as metalloporphyrins^[122] or salen complexes^[123]. While sometimes the approach of building catalytic complexes in the structure as linkers can lead to a huge success^[124], the activity or selectivity of the homogeneous catalyst can rarely be matched. When the aim is to heterogenize complex homogeneous catalysts, a more successful approach can be an encapsulation procedure where the structure fits in the cages of a MOF but cannot leave through the windows. While examples of this approach are rare, a successful encapsulation was presented by Eddaoudi *et al.*^[125] The catalytic applications of MOFs are much more numerous than presented in this short overview and several reviews are available on this topic for further information^[116, 126, 127].

When, despite the large amount of metal and linker combinations that may form a MOF, there is no proper material available that is suitable for the target application, one can exploit the presence of organic linkers or unsaturated metal sites as a platform for further modification^[128]. All of these modifications take place after the framework is formed and are therefore mostly called 'post synthetic modifications' (PSM). The most straightforward approach to a postmodification is the chemical modification of functional groups present in the linker, called covalent PSM. Some nice covalent PSM platforms have been proposed^[129-131] including systems based on 'click' chemistry^[132, 133]. Most of the covalent PSM procedures require some sort of functional group being present in the material. Since many MOFs are based on simple terephthalate linkers, in

most cases there is no such anchor point available. To expand the scope of covalent PSM methods a functional group can be introduced by a Friedel-Crafts alkylation providing a terminal chloride atom which is a good leaving group^[134]. Several ways to modify MOFs for catalytic applications are shown in the overview in Figure 1.18.

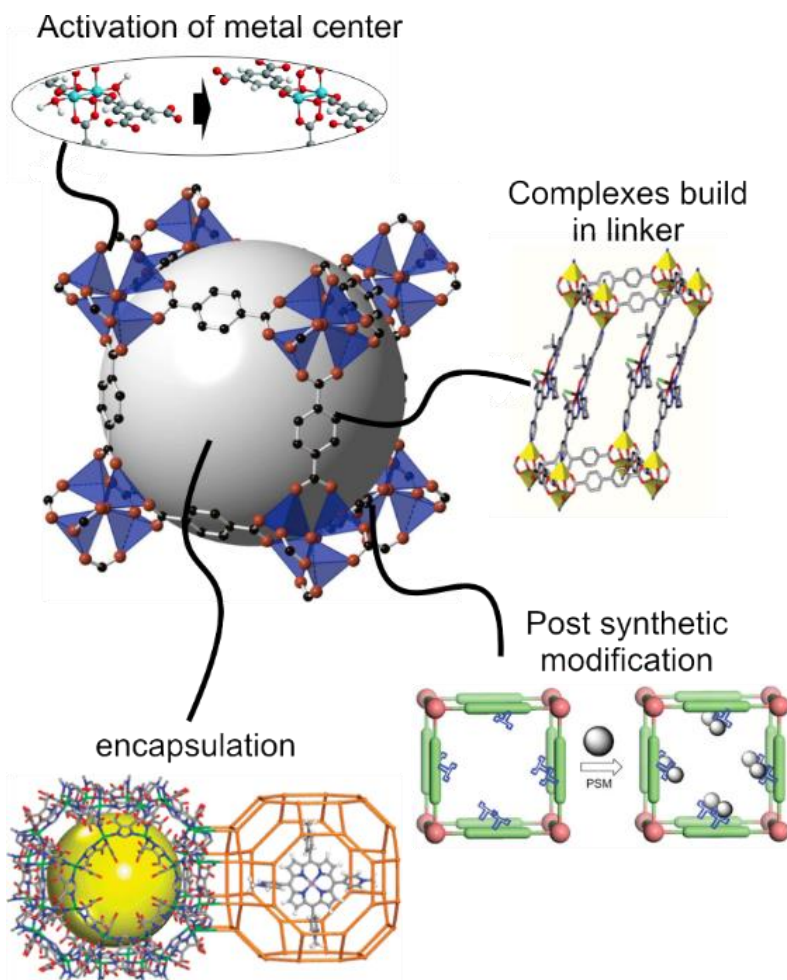


Figure 1.18. Overview of different ways to introduce active sites in a MOF. Adapted with permission from^[119, 125, 135]. Copyright 2015 American Chemical Society and The Royal Society of Chemistry.

Next to catalysis, another useful property of MOFs that can be important in some advanced niche applications is their luminescence behavior. When excited by (UV-)light many metal organic frameworks exhibit some sort of

fluorescence behavior^[136, 137]. Intuitively, one can assume this is a consequence of an electronic interplay between the linkers and the metal node. This property has sparked the interest for some high-end applications, most of them including the sensing of toxic, explosive or otherwise dangerous compounds^[138, 139]. The presence of guest molecules in the MOF host changes the electronic structure of the material and thus the fluorescence color. Since MOFs generally have a high surface area, many guest molecules can be adsorbed leading to a high local concentration and a more significant color change than would be the case with a non-porous material.

Chiral salen catalysts in MOFs

As was pointed out in a previous section there has been much interest in the heterogenation of chiral salen complexes to improve their practical applicability. When considering the possible approaches to make catalytically active MOF materials, the use of variations on this type of complex as a linker comes into mind as a feasible strategy. Some linkers that have been designed for this are shown in Figure 1.19. A first report uses the synthesis strategy where two types of linkers form a framework, when the salen-shape linker is directed vertically in the structure, a biphenyldicarboxylate linker was directed horizontally on the metal cluster containing zinc centers^[135]. This MOF was very active and reasonable enantioselectivities were obtained in the epoxidation of chromene. The framework is an example of an interpenetrated MOF, where two crystal structures are grown inside each other so that the linkers of one crystal are in the pores of another crystal. The effect of this interpenetration on the selectivity was studied by molecular mechanics calculations^[140]. In another approach a salen linker with a diol modification was built in a Cu-based framework, which also led to enantioselectivities that were good but slightly lower than the homogeneous complex^[122]. Another group reported an interesting study where the chiral salen linkers were postmodified with other metal centers, opening the way for new types of chiral reactions but no catalytic tests were done with this material^[141].

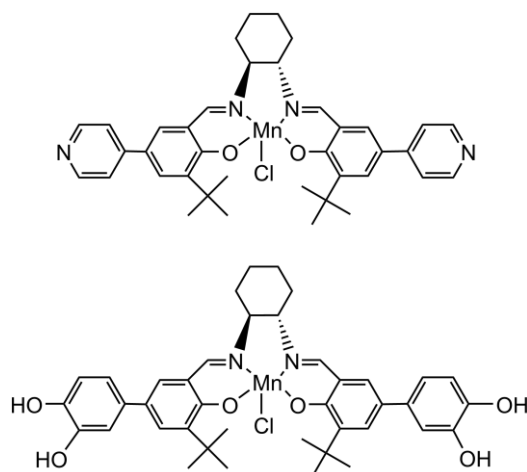


Figure 1.19. Two different salen linkers designed for building into a MOF^[135, 141].

The MIL-101 framework

One example of a metal organic framework will be studied more in depth since it is used extensively in this work. The original MIL-101 structure (Figure 1.16) is a chromium terephthalate MOF that was discovered by Férey *et al.*^[142] This remarkable material has an unusual pore size for a crystalline compound, with two types of cages of 12700 Å³ and 20600 Å³ respectively. Due to the high interest for this material many variants have been synthesized. An example is the exchange of the chromium cation for vanadium or iron^[143, 144]. Also linker modifications on this material were reported to introduce -NO₂ and -NH₂ functionalities^[145]. A postmodification process was required since direct synthesis of MIL-101(Cr) structures with the modified linkers was found to be impossible. Another important variant was the NH₂-MIL-101(Al) material, which was synthesized because combining an aluminum salt with pristine terephthalic did not yield a material with a MIL-101 topology^[146, 147].

Several catalytic applications of MIL-101 type of materials were reported, as reviewed by Kholdeeva *et al.*^[148]. Also the aluminium variant of the catalyst with -NH₂ groups was proposed to be active for applications in basic catalysis^[147]. The specific structure of MIL-101 frameworks has also been used to improve existing catalytic systems. The encapsulation of polyoxometalates (POMs) by adsorption allowed to increase the reusability

of this system^[149, 150]. Also large organic complexes, such as phthalocyanine complexes were reported to be trapped in the pores of the MOF and maintained their catalytic activity^[151].

1.4 OUTLINE OF THE REMAINING CHAPTERS

In the next chapter an overview of the general research goal of this thesis is presented. In addition, a brief overview of the used computational and advanced experimental techniques used in this work will be given.

In the third chapter all major research results obtained in this thesis will be discussed, divided in the three subtopics: immobilization of the salen complex by combining computational studies with experiments, use of diffractograms to resolve differences between theoretically obtained structures for MOFs and the modelling of experimental spectra, with special focus on UV/Vis spectroscopy.

In the fourth chapter a summary will be provided together with an outlook on how these methods could be applied further.

1.5 REFERENCES

- [1] Ross, J. R. H., *Heterogeneous Catalysis: Fundamentals and Applications*. Elsevier: 2012.
- [2] Xamena, F. L.; Gascon, J., *Metal Organic Frameworks as Heterogeneous Catalysts*. Royal Society of Chemistry: 2013.
- [3] Mortreux, A.; Petit, F., *Industrial Applications of Homogeneous Catalysis*. Springer Netherlands: 2012.
- [4] Behr, A.; Neubert, P., *Applied Homogeneous Catalysis*. Wiley: 2012.
- [5] Ali, M. E.; Rahman, M. M.; Sarkar, S. M.; Hamid, S. B. A., Heterogeneous Metal Catalysts for Oxidation Reactions. *Journal of Nanomaterials* **2014**, *2014*, 23.
- [6] Barbaro, P.; Liguori, F., *Heterogenized Homogeneous Catalysts for Fine Chemicals Production: Materials and Processes*. Springer Netherlands: 2010.
- [7] Kulprathipanja, S., *Zeolites in Industrial Separation and Catalysis*. Wiley: 2010.
- [8] Smit, B.; Maesen, T. L. M., Towards a molecular understanding of shape selectivity. *Nature* **2008**, *451* (7179), 671-678.

- [9] Corain, B.; Schmid, G.; Toshima, N., *Metal Nanoclusters in Catalysis and Materials Science: The Issue of Size Control: The Issue of Size Control*. Elsevier Science: 2011.
- [10] Zhao, X. S.; Bao, X. Y.; Guo, W.; Lee, F. Y., Immobilizing catalysts on porous materials. *Materials Today* **2006**, *9* (3), 32-39.
- [11] Kirschning, A., *Immobilized Catalysts: Solid Phases, Immobilization and Applications*. Springer: 2004.
- [12] Blaser, H. U.; Baiker, A.; Prins, R., *Heterogeneous Catalysis and Fine Chemicals IV*. Elsevier Science: 1997.
- [13] Drauz, K.; Gröger, H.; May, O., *Enzyme Catalysis in Organic Synthesis: A Comprehensive Handbook*. Wiley-VCH: 2012.
- [14] Cybulski, A., *Fine Chemicals Manufacture: Technology and Engineering*. Elsevier: 2001.
- [15] Hagen, J., *Industrial Catalysis: A Practical Approach*. Wiley: 2006.
- [16] Sheldon, R. A., The E Factor: fifteen years on. *Green Chemistry* **2007**, *9* (12), 1273-1283.
- [17] Sheldon, R. A., Catalysis: The Key to Waste Minimization. *Journal of Chemical Technology & Biotechnology* **1997**, *68* (4), 381-388.
- [18] Sheldon, R. A., Consider the environmental quotient. *CHEMTECH; (United States); Journal Volume: 24:3* **1994**, 38-46.
- [19] Lapkin, A.; Constable, D., *Green Chemistry Metrics: Measuring and Monitoring Sustainable Processes*. Wiley: 2008.
- [20] Van der Mynsbrugge, J.; De Ridder, J.; Hemelsoet, K.; Waroquier, M.; Van Speybroeck, V., Enthalpy and Entropy Barriers Explain the Effects of Topology on the Kinetics of Zeolite-Catalyzed Reactions. *Chemistry – A European Journal* **2013**, *19* (35), 11568-11576.
- [21] Pignataro, B., *New Strategies in Chemical Synthesis and Catalysis*. Wiley: 2012.
- [22] Toch, K.; Thybaut, J. W.; Marin, G. B., A systematic methodology for kinetic modeling of chemical reactions applied to n-hexane hydroisomerization. *AIChE Journal* **2015**, *61* (3), 880-892.
- [23] Saliccioli, M.; Stamatakis, M.; Caratzoulas, S.; Vlachos, D. G., A review of multiscale modeling of metal-catalyzed reactions: Mechanism development for complexity and emergent behavior. *Chem. Eng. Sci.* **2011**, *66* (19), 4319-4355.
- [24] Ager, D., *Handbook of Chiral Chemicals, Second Edition*. CRC Press: 2005.
- [25] Siemel, G.; Rieth, R.; Rowbottom, K. T., Epoxides. In *Ullmann's Encyclopedia of Industrial Chemistry*, Wiley-VCH Verlag GmbH & Co. KGaA: 2000.
- [26] Oyama, S. T., *Mechanisms in Homogeneous and Heterogeneous Epoxidation Catalysis*. Elsevier Science: 2011.
- [27] Srinivasan, K.; Perrier, S.; Kochi, J. K., Dual pathways for manganese catalysis of olefin oxidation with alkyl hydroperoxides. *Journal of Molecular Catalysis* **1986**, *36* (3), 297-317.
- [28] Allen, S. E.; Walvoord, R. R.; Padilla-Salinas, R.; Kozłowski, M. C., Aerobic Copper-Catalyzed Organic Reactions. *Chem. Rev.* **2013**, *113* (8), 6234-6458.

- [29] Sharpless, K. B.; Verhoeven, T., Metal-catalyzed, highly selective oxygenations of olefins and acetylenes with *tert*-butyl hydroperoxide. Practical considerations and mechanisms. *Aldrichimica acta* **1979**, *12* (4), 63-74.
- [30] Gould, E. S.; Hiatt, R. R.; Irwin, K. C., Metal ion catalysis of oxygen transfer reactions. I. Vanadium catalysis of the epoxidation of cyclohexene. *J. Am. Chem. Soc.* **1968**, *90* (17), 4573-4579.
- [31] Groves, J. T., Key elements of the chemistry of cytochrome P-450: The oxygen rebound mechanism. *Journal of Chemical Education* **1985**, *62* (11), 928.
- [32] Groves, J. T.; McClusky, G. A., Aliphatic hydroxylation via oxygen rebound - oxygen-transfer catalyzed by iron. *J. Am. Chem. Soc.* **1976**, *98* (3), 859-861.
- [33] Meunier, B., Metalloporphyrins as versatile catalysts for oxidation reactions and oxidative DNA cleavage. *Chem. Rev.* **1992**, *92* (6), 1411-1456.
- [34] Wang, D.; Groves, J. T., Efficient water oxidation catalyzed by homogeneous cationic cobalt porphyrins with critical roles for the buffer base. *Proceedings of the National Academy of Sciences* **2013**, *110* (39), 15579-15584.
- [35] Hill, H. A. O.; Morallee, K. G.; Pellizer, G.; Mestroni, G.; Costa, G., Electronic transmission in some organometallic derivatives of cobalt (3) bae and salen complexes. *Journal of Organometallic Chemistry* **1968**, *11* (1), 167-&.
- [36] Irie, R.; Noda, K.; Ito, Y.; Matsumoto, N.; Katsuki, T., Catalytic asymmetric epoxidation of unfunctionalized olefins. *Tetrahedron Lett.* **1990**, *31* (50), 7345-7348.
- [37] Zhang, W.; Loebach, J. L.; Wilson, S. R.; Jacobsen, E. N., Enantioselective epoxidation of unfunctionalized olefins catalyzed by (salen)manganese complexes. *J. Am. Chem. Soc.* **1990**, *112* (7), 2801-2803.
- [38] Katsuki, T.; Sharpless, K. B., The 1st practical method for asymmetric epoxidation. *J. Am. Chem. Soc.* **1980**, *102* (18), 5974-5976.
- [39] Gao, Y.; Hanson, R. M.; Klunder, J. M.; Ko, S. Y.; Masamune, H.; Sharpless, K. B., Catalytic asymmetric epoxidation and kinetic resolution - modified procedures including insitu derivatization. *J. Am. Chem. Soc.* **1987**, *109* (19), 5765-5780.
- [40] Ahlberg, P., *Chemistry, 2001-2005*. World Scientific: 2008.
- [41] Jacobsen, E. N.; Zhang, W.; Muci, A. R.; Ecker, J. R.; Deng, L., Highly enantioselective epoxidation catalysts derived from 1,2-diaminocyclohexane. *J. Am. Chem. Soc.* **1991**, *113* (18), 7063-7064.
- [42] Larrow, J. F.; Jacobsen, E. N., (R,R)-N,N '-bis(3,5-di-*tert*-butylsalicylidene)-1,2-cyclohexanediaminomanganese(III) chloride, a highly enantioselective epoxidation catalyst. *Organic Syntheses, Vol 75* **1998**, *75*, 1-11.
- [43] Chang, S.; Heid, R. M.; Jacobsen, E. N., Enantioselective epoxidation of cyclic 1,3-dienes catalyzed by a sterically and electronically optimized (salen)mn complex. *Tetrahedron Lett.* **1994**, *35* (5), 669-672.

- [44] Irie, R.; Noda, K.; Ito, Y.; Katsuki, T., Enantioselective epoxidation of unfunctionalized olefins using chiral (salen)manganese(III) complexes. *Tetrahedron Lett.* **1991**, *32* (8), 1055-1058.
- [45] Sasaki, H.; Irie, R.; Katsuki, T., Catalytic asymmetric epoxidation with (salen)manganese(III) complex bearing binaphthyl groups of axial chirality. *Synlett* **1993**, (4), 300-302.
- [46] Larrow, J. F.; Jacobsen, E. N.; Gao, Y.; Hong, Y. P.; Nie, X. Y.; Zepp, C. M., A practical method for the large-scale preparation of n,n'-bis(3,5-di-tert-butylsalicylidene)1,2-cyclohexanediaminato(2-) manganese(III) chloride, a highly enantioselective epoxidation catalyst. *J. Org. Chem.* **1994**, *59* (7), 1939-1942.
- [47] Groves, J. T.; Takahashi, T., Activation and transfer of nitrogen from a nitridomanganese(V) porphyrin complex - the aza analog of epoxidation. *J. Am. Chem. Soc.* **1983**, *105* (7), 2073-2074.
- [48] O'Connor, K. J.; Wey, S.-J.; Burrows, C. J., Alkene aziridination and epoxidation catalyzed by chiral metal salen complexes. *Tetrahedron Lett.* **1992**, *33* (8), 1001-1004.
- [49] Li, Z.; Conser, K. R.; Jacobsen, E. N., Asymmetric alkene aziridination with readily available chiral diimine-based catalysts. *J. Am. Chem. Soc.* **1993**, *115* (12), 5326-5327.
- [50] Kim, C.; Uchida, T.; Katsuki, T., Asymmetric olefin aziridination using a newly designed Ru(CO)(salen) complex as the catalyst. *Chem. Commun.* **2012**, *48* (57), 7188-7190.
- [51] Nakajima, K.; Kojima, M.; Fujita, J., Asymmetric Oxidation of Sulfides to Sulfoxides by Organic Hydroperoxides with Optically Active Schiff Base-Oxovanadium(IV) Catalysts. *Chem. Lett.* **1986**, *15* (9), 1483-1486.
- [52] Saito, B.; Katsuki, T., Ti(salen)-catalyzed enantioselective sulfoxidation using hydrogen peroxide as a terminal oxidant. *Tetrahedron Lett.* **2001**, *42* (23), 3873-3876.
- [53] Saito, B.; Katsuki, T., Mechanistic consideration of Ti(salen)-catalyzed asymmetric sulfoxidation. *Tetrahedron Lett.* **2001**, *42* (47), 8333-8336.
- [54] Choi, A. Y.; Hwang, G. S.; Senapati, B. K.; Ryu, D. H., Efficient Asymmetric Sulfoxidation of Prochiral Sulfides Catalyzed by Chiral Salen-Mn(III) Complexes. *Bull. Korean Chem. Soc.* **2008**, *29* (10), 1879-1880.
- [55] Egami, H.; Katsuki, T., Fe(salen)-catalyzed asymmetric oxidation of sulfides with hydrogen peroxide in water. *J. Am. Chem. Soc.* **2007**, *129* (29), 8940-8941.
- [56] Samsel, E. G.; Srinivasan, K.; Kochi, J. K., Mechanism of the chromium-catalyzed epoxidation of olefins - role of oxochromium(V) cations. *J. Am. Chem. Soc.* **1985**, *107* (25), 7606-7617.
- [57] Plattner, D. A.; Feichtinger, D.; El-Bahraoui, J.; Wiest, O., Coordination chemistry of manganese-salen complexes studied by electrospray tandem mass spectrometry: the significance of axial ligands. *Int. J. Mass Spectrom.* **2000**, *195*, 351-362.
- [58] Fu, H.; Look, G. C.; Zhang, W.; Jacobsen, E. N.; Wong, C. H., Mechanistic study of a synthetically useful monooxygenase model using the hypersensitive probe trans-2-phenyl-1-vinylcyclopropane. *J. Org. Chem.* **1991**, *56* (23), 6497-6500.

- [59] Linde, C.; Arnold, M.; Norrby, P. O.; Akermark, B., Is there a radical intermediate in the (salen)Mn-catalyzed epoxidation of alkenes? *Angew. Chem.-Int. Edit. Engl.* **1997**, *36* (16), 1723-1725.
- [60] Hamada, T.; Fukuda, T.; Imanishi, H.; Katsuki, T., Mechanism of one oxygen atom transfer from oxo (salen)manganese(V) complex to olefins. *Tetrahedron* **1996**, *52* (2), 515-530.
- [61] Linde, C.; Koliai, N.; Norrby, P. O.; Akermark, B., Experimental evidence for multiple oxidation pathways in the (salen)Mn-catalyzed epoxidation of alkenes. *Chem.-Eur. J.* **2002**, *8* (11), 2568-2573.
- [62] Linker, T., The Jacobsen-Katsuki epoxidation and its controversial mechanism. *Angew. Chem.-Int. Edit. Engl.* **1997**, *36* (19), 2060-2062.
- [63] Fristrup, P.; Dideriksen, B. B.; Tanner, D.; Norrby, P. O., Probing competitive enantioselective approach vectors operating in the Jacobsen-Katsuki epoxidation: A kinetic study of methyl-substituted Styrenes. *J. Am. Chem. Soc.* **2005**, *127* (39), 13672-13679.
- [64] Zhang, W.; Jacobsen, E. N., Asymmetric olefin epoxidation with sodium-hypochlorite catalyzed by easily prepared chiral Mn(III) salen complexes. *J. Org. Chem.* **1991**, *56* (7), 2296-2298.
- [65] Linde, C.; Akermark, B.; Norrby, P. O.; Svensson, M., Timing is critical: Effect of spin changes on the diastereoselectivity in Mn(salen)-catalyzed epoxidation. *J. Am. Chem. Soc.* **1999**, *121* (21), 5083-5084.
- [66] Cavallo, L.; Jacobsen, H., Radical Intermediates in the Jacobsen - Katsuki Epoxidation. *Angewandte Chemie International Edition* **2000**, *39* (3), 589-592.
- [67] Jacobsen, H.; Cavallo, L., A Possible Mechanism for Enantioselectivity in the Chiral Epoxidation of Olefins with [Mn(salen)] Catalysts. *Chemistry - A European Journal* **2001**, *7* (4), 800-807.
- [68] Abashkin, Y. G.; Collins, J. R.; Burt, S. K., (Salen)Mn(III)-catalyzed epoxidation reaction as a multichannel process with different spin states. Electronic tuning of asymmetric catalysis: A theoretical study. *Inorg. Chem.* **2001**, *40* (16), 4040-4048.
- [69] Cavallo, L.; Jacobsen, H., Toward a catalytic cycle for the Mn-salen mediated alkene epoxidation: A computational approach. *Inorg. Chem.* **2004**, *43* (6), 2175-2182.
- [70] Cavallo, L.; Jacobsen, H., Manganese-salen complexes as oxygen-transfer agents in catalytic epoxidations - A density functional study of mechanistic aspects. *Eur. J. Inorg. Chem.* **2003**, (5), 892-902.
- [71] Cavallo, L.; Jacobsen, H., Transition metal mediated epoxidation as test case for the performance of different density functionals: A Computational Study. *J. Phys. Chem. A* **2003**, *107* (28), 5466-5471.
- [72] Cavallo, L.; Jacobsen, H., Electronic effects in (salen)Mn-based epoxidation catalysts. *J. Org. Chem.* **2003**, *68* (16), 6202-6207.
- [73] Abashkin, Y. G.; Burt, S. K., (Salen)Mn-catalyzed epoxidation of alkenes: A two-zone process with different spin-state channels as suggested by DFT study. *Org. Lett.* **2004**, *6* (1), 59-62.
- [74] Jacobsen, H.; Cavallo, L., Re-evaluation of the Mn(salen) mediated epoxidation of alkenes by means of the B3LYP* density functional. *Phys. Chem. Chem. Phys.* **2004**, *6* (13), 3747-3753.

- [75] Sears, J. S.; Sherrill, C. D., The electronic structure of oxo-Mn(salen): Single-reference and multireference approaches. *J. Chem. Phys.* **2006**, *124* (14), 144314.
- [76] Takatani, T.; Sears, J. S.; Sherrill, C. D., Assessing the Performance of Density Functional Theory For the Electronic Structure of Metal-Salens: The M06 Suite of Functionals and the d(4)-Metals. *J. Phys. Chem. A* **2010**, *114* (43), 11714-11718.
- [77] Takatani, T.; Sears, J. S.; Sherrill, C. D., Assessing the Performance of Density Functional Theory for the Electronic Structure of Metal-Salens: The d(6)-Metals. *J. Phys. Chem. A* **2009**, *113* (32), 9231-9236.
- [78] Sears, J. S.; Sherrill, C. D., Assessing the performance of density functional theory for the electronic structure of metal-salens: The d(2)-metals. *J. Phys. Chem. A* **2008**, *112* (29), 6741-6752.
- [79] Sears, J. S.; Sherrill, C. D., Assessing the performance of density functional theory for the electronic structure of metal-salens: The 3d(0)-metals. *J. Phys. Chem. A* **2008**, *112* (15), 3466-3477.
- [80] Wang, Y.; Qin, Y.; Wang, X.; Wang, F., Trivalent Titanium Salen Complex: Thermally Robust and Highly Active Catalyst for Copolymerization of CO₂ and Cyclohexene Oxide. *ACS Catalysis* **2015**, *5* (1), 393-396.
- [81] Darensbourg, D. J.; Yeung, A. D., Kinetics of the (salen)Cr(III)- and (salen)Co(III)-catalyzed copolymerization of epoxides with CO₂, and of the accompanying degradation reactions. *Polymer Chemistry* **2015**, *6* (7), 1103-1117.
- [82] Movassagh, B.; Parvis, F. S.; Navidi, M., Pd(II) salen complex covalently anchored to multi-walled carbon nanotubes as a heterogeneous and reusable precatalyst for Mizoroki-Heck and Hiyama cross-coupling reactions. *Appl. Organomet. Chem.* **2015**, *29* (1), 40-44.
- [83] Modi, C. K.; Chudasama, J. A.; Nakum, H. D.; Parmar, D. K.; Patel, A. L., Catalytic oxidation of limonene over zeolite-Y entrapped oxovanadium (IV) complexes as heterogeneous catalysts. *Journal of Molecular Catalysis A: Chemical* **2014**, *395* (0), 151-161.
- [84] Zhang, Y.; Gao, B.; Zhou, Q.; Zhao, J., Oxidative Kinetic Resolution of Secondary Alcohols with Salen-Mn(III)/NBS/NaClO System. *Catal. Lett.* **2014**, *144* (11), 1797-1802.
- [85] Angelino, M. D.; Laibinis, P. E., Polymer-supported salen complexes for heterogeneous asymmetric synthesis: Stability and selectivity. *Journal of Polymer Science Part A: Polymer Chemistry* **1999**, *37* (21), 3888-3898.
- [86] Angelino, M. D.; Laibinis, P. E., Synthesis and Characterization of a Polymer-Supported Salen Ligand for Enantioselective Epoxidation. *Macromolecules* **1998**, *31* (22), 7581-7587.
- [87] Canali, L.; Sherrington, D. C.; Deleuze, H., Synthesis of resins with pendently-bound chiral manganese-salen complexes and use as heterogeneous asymmetric alkene epoxidation catalysts. *React. Funct. Polym.* **1999**, *40* (2), 155-168.
- [88] Zhang, H.; Xiang, S.; Li, C., Enantioselective epoxidation of unfunctionalised olefins catalyzed by Mn(salen) complexes

- immobilized in porous materials via phenyl sulfonic group. *Chem. Commun.* **2005**, (9), 1209-1211.
- [89] Das, P.; Silva, A. R.; Carvalho, A. P.; Pires, J.; Freire, C., Enantioselective Epoxidation of Alkenes by Jacobsen Catalyst Anchored onto Aminopropyl-functionalised Laponite, MCM-41 and FSM-16. *Catal. Lett.* **2009**, *129* (3-4), 367-375.
- [90] Shi, Z. H.; Li, N. G.; Shi, Q. P.; Tang, Y. P.; Tang, H.; Shen, M. Z.; Duan, J. A., Immobilization of Chiral Manganese(III)-salen Complexes for Enantioselective Epoxidation of Unfunctionalised Olefins. *Curr. Org. Synth.* **2014**, *11* (2), 204-243.
- [91] Tomic, E. A., Thermal stability of coordination polymers. *Journal of Applied Polymer Science* **1965**, *9* (11), 3745-3752.
- [92] Li, H.; Eddaoudi, M.; O'Keeffe, M.; Yaghi, O. M., Design and synthesis of an exceptionally stable and highly porous metal-organic framework. *Nature* **1999**, *402* (6759), 276-279.
- [93] MacGillivray, L. R., *Metal-Organic Frameworks: Design and Application*. Wiley: 2010.
- [94] Farrusseng, D., *Metal-Organic Frameworks: Applications from Catalysis to Gas Storage*. Wiley: 2011.
- [95] Zhou, H.-C.; Long, J. R.; Yaghi, O. M., Introduction to Metal-Organic Frameworks. *Chem. Rev.* **2012**, *112* (2), 673-674.
- [96] Zhou, H. C.; Kitagawa, S., Metal-Organic Frameworks (MOFs). *Chem. Soc. Rev.* **2014**, *43* (16), 5415-5418.
- [97] Lee, Y.-R.; Kim, J.; Ahn, W.-S., Synthesis of metal-organic frameworks: A mini review. *Korean J. Chem. Eng.* **2013**, *30* (9), 1667-1680.
- [98] Stock, N.; Biswas, S., Synthesis of Metal-Organic Frameworks (MOFs): Routes to Various MOF Topologies, Morphologies, and Composites. *Chem. Rev.* **2012**, *112* (2), 933-969.
- [99] O'Keeffe, M.; Yaghi, O. M., Deconstructing the Crystal Structures of Metal-Organic Frameworks and Related Materials into Their Underlying Nets. *Chem. Rev.* **2012**, *112* (2), 675-702.
- [100] Czaja, A. U.; Trukhan, N.; Muller, U., Industrial applications of metal-organic frameworks. *Chem. Soc. Rev.* **2009**, *38* (5), 1284-1293.
- [101] Mueller, U.; Puetter, H.; Hesse, M.; Schubert, M.; Wessel, H.; Huff, J.; Guzman, M., Method for electrochemical production of a crystalline porous metal organic skeleton material. Google Patents: 2011.
- [102] Mingos, D. M. P.; Baghurst, D. R., Applications of microwave dielectric heating effects to synthetic problems in chemistry. *Chem. Soc. Rev.* **1991**, *20* (1), 1-47.
- [103] Klinowski, J.; Paz, F. A. A.; Silva, P.; Rocha, J., Microwave-Assisted Synthesis of Metal-Organic Frameworks. *Dalton Trans.* **2011**, *40* (2), 321-330.
- [104] Jhung, S. H.; Lee, J. H.; Chang, J. S., Microwave synthesis of a nanoporous hybrid material, chromium trimesate. *Bull. Korean Chem. Soc.* **2005**, *26* (6), 880-881.
- [105] Friscic, T., New opportunities for materials synthesis using mechanochemistry. *Journal of Materials Chemistry* **2010**, *20* (36), 7599-7605.

- [106] Pichon, A.; Lazuen-Garay, A.; James, S. L., Solvent-free synthesis of a microporous metal-organic framework. *Crystengcomm* **2006**, *8* (3), 211-214.
- [107] Furukawa, H.; Cordova, K. E.; O'Keeffe, M.; Yaghi, O. M., The Chemistry and Applications of Metal-Organic Frameworks. *Science* **2013**, *341* (6149).
- [108] Furukawa, H.; Go, Y. B.; Ko, N.; Park, Y. K.; Uribe-Romo, F. J.; Kim, J.; O'Keeffe, M.; Yaghi, O. M., Isorecticular Expansion of Metal-Organic Frameworks with Triangular and Square Building Units and the Lowest Calculated Density for Porous Crystals. *Inorg. Chem.* **2011**, *50* (18), 9147-9152.
- [109] Ferey, G.; Latroche, M.; Serre, C.; Millange, F.; Loiseau, T.; Percheron-Guegan, A., Hydrogen adsorption in the nanoporous metal-benzenedicarboxylate $M(OH)(O_2C-C_6H_4-CO_2)$ ($M = Al^{3+}, Cr^{3+}$), MIL-53. *Chem. Commun.* **2003**, (24), 2976-2977.
- [110] Shen, K.; Zhang, M.; Zheng, H., Critical factors influencing the structures and properties of metal-organic frameworks. *CrystEngComm* **2015**, *17* (5), 981-991.
- [111] Langmi, H. W.; Ren, J.; North, B.; Mathe, M.; Bessarabov, D., Hydrogen Storage in Metal-Organic Frameworks: A Review. *Electrochimica Acta* **2014**, *128* (0), 368-392.
- [112] Murray, L. J.; Dinca, M.; Long, J. R., Hydrogen storage in metal-organic frameworks. *Chem. Soc. Rev.* **2009**, *38* (5), 1294-1314.
- [113] Rowsell, J. L. C.; Millward, A. R.; Park, K. S.; Yaghi, O. M., Hydrogen Sorption in Functionalized Metal-Organic Frameworks. *J. Am. Chem. Soc.* **2004**, *126* (18), 5666-5667.
- [114] Chung, Y. G.; Camp, J.; Haranczyk, M.; Sikora, B. J.; Bury, W.; Krungleviciute, V.; Yildirim, T.; Farha, O. K.; Sholl, D. S.; Snurr, R. Q., Computation-Ready, Experimental Metal-Organic Frameworks: A Tool To Enable High-Throughput Screening of Nanoporous Crystals. *Chemistry of Materials* **2014**, *26* (21), 6185-6192.
- [115] Farrusseng, D.; Aguado, S.; Pinel, C., Metal-Organic Frameworks: Opportunities for Catalysis. *Angew. Chem.-Int. Edit.* **2009**, *48* (41), 7502-7513.
- [116] Lee, J.; Farha, O. K.; Roberts, J.; Scheidt, K. A.; Nguyen, S. T.; Hupp, J. T., Metal-organic framework materials as catalysts. *Chem. Soc. Rev.* **2009**, *38* (5), 1450-1459.
- [117] Leus, K.; Vandichel, M.; Liu, Y.-Y.; Muylaert, I.; Musschoot, J.; Pyl, S.; Vrielinck, H.; Callens, F.; Marin, G. B.; Detavernier, C.; Wiper, P. V.; Khimiyak, Y. Z.; Waroquier, M.; Van Speybroeck, V.; Van Der Voort, P., The coordinatively saturated vanadium MIL-47 as a low leaching heterogeneous catalyst in the oxidation of cyclohexene. *J. Catal.* **2012**, *285* (1), 196-207.
- [118] Leus, K.; Muylaert, I.; Vandichel, M.; Marin, G. B.; Waroquier, M.; Van Speybroeck, V.; Van der Voort, P., The remarkable catalytic activity of the saturated metal organic framework V-MIL-47 in the cyclohexene oxidation. *Chem. Commun.* **2010**, *46* (28), 5085-5087.

- [119] Alaerts, L.; Seguin, E.; Poelman, H.; Thibault-Starzyk, F.; Jacobs, P. A.; De Vos, D. E., Probing the Lewis acidity and catalytic activity of the metal-organic framework Cu-3(btc)(2) (BTC = benzene-1,3,5-tricarboxylate). *Chem.-Eur. J.* **2006**, *12* (28), 7353-7363.
- [120] Vermoortele, F.; Vandichel, M.; Van de Voorde, B.; Ameloot, R.; Waroquier, M.; Van Speybroeck, V.; De Vos, D. E., Electronic Effects of Linker Substitution on Lewis Acid Catalysis with Metal-Organic Frameworks. *Angewandte Chemie International Edition* **2012**, n/a-n/a.
- [121] Vandichel, M.; Hajek, J.; Vermoortele, F.; Waroquier, M.; De Vos, D. E.; Van Speybroeck, V., Active site engineering in UiO-66 type metal-organic frameworks by intentional creation of defects: a theoretical rationalization. *CrystEngComm* **2015**, *17* (2), 395-406.
- [122] Shultz, A. M.; Farha, O. K.; Hupp, J. T.; Nguyen, S. T., A Catalytically Active, Permanently Microporous MOF with Metalloporphyrin Struts. *J. Am. Chem. Soc.* **2009**, *131* (12), 4204-+.
- [123] Shultz, A. M.; Sarjeant, A. A.; Farha, O. K.; Hupp, J. T.; Nguyen, S. T., Post-Synthesis Modification of a Metal-Organic Framework To Form Metallosalen-Containing MOF Materials. *J. Am. Chem. Soc.* **2011**, *133* (34), 13252-13255.
- [124] Ma, L.; Falkowski, J. M.; Abney, C.; Lin, W., A series of isorecticular chiral metal-organic frameworks as a tunable platform for asymmetric catalysis. *Nat Chem* **2010**, *2* (10), 838-846.
- [125] Alkordi, M. H.; Liu, Y. L.; Larsen, R. W.; Eubank, J. F.; Eddaoudi, M., Zeolite-like metal-organic frameworks as platforms for applications: On metalloporphyrin-based catalysts. *J. Am. Chem. Soc.* **2008**, *130* (38), 12639-+.
- [126] Gascon, J.; Corma, A.; Kapteijn, F.; Llabrés i Xamena, F. X., Metal Organic Framework Catalysis: Quo vadis? *ACS Catalysis* **2013**, *4* (2), 361-378.
- [127] Liu, J.; Chen, L.; Cui, H.; Zhang, J.; Zhang, L.; Su, C.-Y., Applications of metal-organic frameworks in heterogeneous supramolecular catalysis. *Chem. Soc. Rev.* **2014**, *43* (16), 6011-6061.
- [128] Cohen, S. M., Postsynthetic Methods for the Functionalization of Metal-Organic Frameworks. *Chem. Rev.* **2012**, *112* (2), 970-1000.
- [129] Ingleson, M. J.; Barrio, J. P.; Guilbaud, J. B.; Khimyak, Y. Z.; Rosseinsky, M. J., Framework functionalisation triggers metal complex binding. *Chem. Commun.* **2008**, (23), 2680-2682.
- [130] Lescouet, T.; Vitillo, J. G.; Bordiga, S.; Canivet, J.; Farrusseng, D., An alternative pathway for the synthesis of isocyanato- and urea-functionalised metal-organic frameworks. *Dalton Trans.* **2013**, *42* (23), 8249-8258.
- [131] Aguado, S.; Canivet, J.; Farrusseng, D., Engineering structured MOF at nano and macroscales for catalysis and separation. *Journal of Materials Chemistry* **2011**, *21* (21), 7582-7588.
- [132] Goto, Y.; Sato, H.; Shinkai, S.; Sada, K., "Clickable" Metal-Organic Framework. *J. Am. Chem. Soc.* **2008**, *130* (44), 14354-+.
- [133] Savonnet, M.; Bazer-Bachi, D.; Bats, N.; Perez-Pellitero, J.; Jeanneau, E.; Lecocq, V.; Pinel, C.; Farrusseng, D., Generic Postfunctionalization

- Route from Amino-Derived Metal-Organic Frameworks. *J. Am. Chem. Soc.* **2010**, *132* (13), 4518-+.
- [134] Goesten, M. G.; Sai Sankar Gupta, K. B.; Ramos-Fernandez, E. V.; Khajavi, H.; Gascon, J.; Kapteijn, F., Chloromethylation as a functionalisation pathway for metal-organic frameworks. *CrystEngComm* **2012**, *14* (12), 4109-4111.
- [135] Cho, S.-H.; Ma, B.; Nguyen, S. T.; Hupp, J. T.; Albrecht-Schmitt, T. E., A metal-organic framework material that functions as an enantioselective catalyst for olefin epoxidation. *Chem. Commun.* **2006**, *0* (24), 2563-2565.
- [136] Hu, Z.; Deibert, B. J.; Li, J., Luminescent metal-organic frameworks for chemical sensing and explosive detection. *Chem. Soc. Rev.* **2014**, *43* (16), 5815-5840.
- [137] Allendorf, M. D.; Bauer, C. A.; Bhakta, R. K.; Houk, R. J. T., Luminescent metal-organic frameworks. *Chem. Soc. Rev.* **2009**, *38* (5), 1330-1352.
- [138] Rieter, W. J.; Taylor, K. M. L.; Lin, W., Surface Modification and Functionalization of Nanoscale Metal-Organic Frameworks for Controlled Release and Luminescence Sensing. *J. Am. Chem. Soc.* **2007**, *129* (32), 9852-9853.
- [139] Buso, D.; Jasieniak, J.; Lay, M. D. H.; Schiavuta, P.; Scopece, P.; Laird, J.; Amenitsch, H.; Hill, A. J.; Falcaro, P., Highly Luminescent Metal-Organic Frameworks Through Quantum Dot Doping. *Small* **2012**, *8* (1), 80-88.
- [140] Oxford, G. A. E.; Dubbeldam, D.; Broadbelt, L. J.; Snurr, R. Q., Elucidating steric effects on enantioselective epoxidation catalyzed by (salen)Mn in metal-organic frameworks. *J. Mol. Catal. A-Chem.* **2011**, *334* (1-2), 89-97.
- [141] Cho, S. H.; Gadzikwa, T.; Afshari, M.; Nguyen, S. T.; Hupp, J. T., Bis(catechol)salen Mn-III coordination polymers as support-free heterogeneous asymmetric catalysts for epoxidation. *Eur. J. Inorg. Chem.* **2007**, (31), 4863-4867.
- [142] Ferey, G.; Mellot-Draznieks, C.; Serre, C.; Millange, F.; Dutour, J.; Surble, S.; Margiolaki, I., A chromium terephthalate-based solid with unusually large pore volumes and surface area. *Science* **2005**, *309* (5743), 2040-2042.
- [143] Biswas, S.; Couck, S.; Grzywa, M.; Denayer, J. F. M.; Volkmer, D.; Van Der Voort, P., Vanadium Analogues of Nonfunctionalized and Amino-Functionalized MOFs with MIL-101 Topology – Synthesis, Characterization, and Gas Sorption Properties. *Eur. J. Inorg. Chem.* **2012**, *2012* (15), 2481-2486.
- [144] Taylor-Pashow, K. M. L.; Della Rocca, J.; Xie, Z. G.; Tran, S.; Lin, W. B., Postsynthetic Modifications of Iron-Carboxylate Nanoscale Metal-Organic Frameworks for Imaging and Drug Delivery. *J. Am. Chem. Soc.* **2009**, *131* (40), 14261-+.
- [145] Bernt, S.; Guillerme, V.; Serre, C.; Stock, N., Direct covalent post-synthetic chemical modification of Cr-MIL-101 using nitrating acid. *Chem. Commun.* **2011**, *47* (10), 2838-2840.
- [146] Serra-Crespo, P.; Ramos-Fernandez, E. V.; Gascon, J.; Kapteijn, F., Synthesis and Characterization of an Amino Functionalized MIL-

- 101(Al): Separation and Catalytic Properties. *Chemistry of Materials* **2011**, *23* (10), 2565-2572.
- [147] Hartmann, M.; Fischer, M., Amino-functionalized basic catalysts with MIL-101 structure. *Microporous Mesoporous Mat.* **2012**, *164*, 38-43.
- [148] Maksimchuk, N. V.; Zalomaeva, O. V.; Skobelev, I. Y.; Kovalenko, K. A.; Fedin, V. P.; Kholdeeva, O. A., *Metal-organic frameworks of the MIL-101 family as heterogeneous single-site catalysts*. 2012; Vol. 468, p 2017-2034.
- [149] Maksimchuk, N. V.; Timofeeva, M. N.; Melgunov, M. S.; Shmakov, A. N.; Chesalov, Y. A.; Dybtsev, D. N.; Fedin, V. P.; Kholdeeva, O. A., Heterogeneous selective oxidation catalysts based on coordination polymer MIL-101 and transition metal-substituted polyoxometalates. *J. Catal.* **2008**, *257* (2), 315-323.
- [150] Saedi, Z.; Tangestaninejad, S.; Moghadam, M.; Mirkhani, V.; Mohammadpoor-Baltork, I., The effect of encapsulated Zn-POM on the catalytic activity of MIL-101 in the oxidation of alkenes with hydrogen peroxide. *J. Coord. Chem.* **2012**, *65* (3), 463-473.
- [151] Kockrick, E.; Lescouet, T.; Kudrik, E. V.; Sorokin, A. B.; Farrusseng, D., Synergistic effects of encapsulated phthalocyanine complexes in MIL-101 for the selective aerobic oxidation of tetralin. *Chem. Commun.* **2011**, *47* (5), 1562-1564.

CHAPTER 2. GOAL AND METHODOLOGY

2.1 GOAL OF THE RESEARCH PRESENTED IN THIS THESIS

In this thesis a combined experimental and theoretical approach will be used to design nanoporous materials for catalysis. More specifically, attention is given to find a heterogeneous equivalent for a well-known, selective, homogeneously catalyzed process: the enantioselective epoxidation of unfunctionalized olefins with salen-type catalysts. For this design process we will present a heterogenation procedure of the Jacobsen salen catalyst. In a first step we will try to find the epoxidation mechanism with *ab initio* techniques. Starting from those results the selectivity can be determined with the same techniques. With that knowledge, a heterogenation procedure that maintains the selectivity of the homogeneous catalyst will be designed experimentally.

A second part of this work, focusses on the structure characterization of nanoporous materials. To that end experimentally very well resolved X-ray diffractograms will be used to discriminate between various obtained theoretical structures for the MIL-47(V) type of material.

The third part of this work consists of various contributions that were given to assist in the characterization of new materials and more in particular to resolve features obtained from various spectroscopic techniques. Both UV/Vis and IR spectra of metal organic frameworks are calculated and compared with spectra of modified metal organic frameworks with the aim of assisting in the experimental design process.

2.2 MOLECULAR MODELING

General

The term molecular modeling is used to refer to a set of tools that enable the computational prediction and study of the behavior of materials. In this work we will mostly use ab initio modeling techniques, for which the electronic structure of the systems under investigation is described from first principles, thus using no empirical input. The electronic structure of a molecule is found by solving the Schrödinger equation for the electrons at fixed positions of the nuclei. The latter is a consequence of the Born-Oppenheimer approximation, which relies on the fact that the nuclei are much heavier than the electrons^[1, 2]. Generally the goal of computational modeling techniques is finding the most stable geometry of a molecule or solid. This requires a minimization of the energy, calculated by numerically solving the eigenvalue problem of Schrödinger's equation, as a function of the atomic coordinates. By imposing certain constraints during this optimization one can also find structures for the transition states of a chemical reaction. With the knowledge of the energy for equilibria and transition states on the potential energy surface, it is possible to analyze the mechanism of a reaction on the nanoscale. Next to an analysis of the reaction pathway, the knowledge of the electronic structure of a molecule allows for the calculation of other experimental observables. An example of this are electronic excitation spectra, such as a UV/VIS spectrum.

The key issue in this approach is the solution of the Schrödinger equation. This equation cannot be solved exactly, except for the hydrogen atom or other one-electron systems. Within this framework a variety of models and approximations have been developed to solve the electronic structure problem. A short overview is given hereafter. It is not the intention to give a complete review on this topic, for more detailed explanations we refer to dedicated textbooks on the subject^[3-5].

Electronic structure methods

Although the Hartree-Fock method will not be used extensively in this work, it is important to introduce it briefly as it is one of the corner stones within

the field of many body physics. The theory is based on the description of an N-body system with a single Slater determinant. As a result of this hypothesis a set of equations is found in which the electrons move in a so-called mean-field, without considering other electrons. The explicit detailed interaction between the particles is not included anymore. In that sense, electron correlation is not included in this method, apart of course from the exchange interaction imposed by the Pauli exclusion principle.

A single Slater determinant description might be quite troublesome for systems in which various states are energetically close to each other. Where the influence of static correlation became important, a DMRG-adapted (density matrix renormalization group) CAS electronic method was used, referred to as DMRG-SCF^[6]. By writing the CAS wavefunction as a matrix product state, the DMRG algorithm can be applied in the solution. This very efficient algorithm allows for large active spaces to be modeled with a high accuracy in a feasible timeframe^[7].

Other post-HF methods that are worth mentioning are configuration interaction (CI) and Møller-Plesset perturbation theory, which are thoroughly explained in numerous textbooks on the topic^[8, 9]

A major revolution within computational chemistry was introduced by the extensive usage of density functional theory (DFT)^[10, 11]. This methodology offers a good trade-off between accuracy and computational efficiency. The large influence of the development of this method on the field of quantum chemistry was rewarded with a Nobel prize in 1998 to Kohn and Pople^[12]. While mostly classified as an ab initio method, density functional theory may contain some empirical input depending on the choice of the exchange correlation functional. The key point within DFT consists in describing the properties of the system using the electron density. It was proven by Hohenberg and Kohn that the electron density gives all properties of the system in the ground state^[11]. This was later expanded to include degenerate states with the Levy-Lieb constrained search^[13]. While the scheme of DFT is formally exact, a good choice for the exchange and correlation functional has to be made. Generally these functionals can be classified in several categories: local, non-local and hybrid, and the amount

of various functionals proposed to date is very large^[14]. Some key functionals that will be used in this work are OPBE^[15-17], B3LYP^[18, 19] and CAM-B3LYP^[20]. A rationale on why a certain functional is used for a set of calculations will be provided when it is applicable.

Van der Waals interactions

One of the major shortcomings with many currently available functionals is their incapability to describe the long-range electron correlation effects that are known as dispersive Van der Waals interactions^[21, 22]. Although one could neglect these contributions as being weak interactions, they play a crucial role in the behavior of a catalyst if it is sufficiently bulky (solid state or large organometallic complex). The structure and energy of a system is thus partially determined by non-covalent interactions. In the last years a lot of attention has been given to the incorporation of these interactions in the DFT framework, for example by developing new functionals that are able to describe long-range interactions^[23]. Another approach that has become very popular is the DFT-D method introduced by Grimme^[22]. Grimme *et al.* proposed a damped energy term that can be added to DFT results in order to correct the energy. This term is parameterized for each functional. The importance of Van der Waals contributions in heterogeneous zeolite catalysis was recently reviewed^[24]. In this work a term was added after the optimization via the so-called DFTD-D3 method^[25].

Excited states: Time dependent density functional theory (TDDFT)

DFT can only be used to calculate ground state properties of a molecule. However UV/Vis spectra are a consequence of electron excitation and a methodology to calculate excitation energies, and thus the visual spectra is required. Time dependent density functional theory (TDDFT) is such a method^[26, 27]. TDDFT is a general method that solves the time-dependent Schrödinger equation, the excitation energies can be derived by isolating the resonance frequencies from the frequency decomposition of the time dependent density. With the use of the linear response formalism proposed by Casida^[28, 29] these resonance frequencies can be found directly by solving

an eigenvalue problem. This latter formulation is mostly applied, since the majority of TDDFT studies have the calculation of excitation energies as a goal.

Thermodynamics from *ab initio* data

All methods previously discussed provide solutions for the electronic structure of the system under consideration. Using various algorithms, minimal energy states and transition states can be found. However, if we want to find a reaction pathway that allows us to deduce information on the reaction behavior, information on the entropy and enthalpy of the reaction is also required. This would allow the generation of free energy profiles which provides the most complete picture of a reaction.

The electronic energy is calculated with the aid of the electronic structure methods described above. Via the molecular partition function this electronic energy is connected to the internal energy. This molecular partition function consists of various contributions such as the translational, rotational and vibrational part:

$$Q = q_{\text{electronic}} \cdot q_{\text{translation}} \cdot q_{\text{rotational}} \cdot q_{\text{vibrational}} \quad (2.1)$$

The electronic part of the partition function is only dependent on a single energy state due to the Born-Oppenheimer approximation. The translational and rotational part result from the global motion of the molecule and are dependent on the mass and moments of inertia of the molecule. In order to separate the rotational part from the vibrational part the assumption is made that a molecule is a rigid rotor with the bond distances frozen in equilibrium^[30]. The vibrational part is found by describing the internal motions of the molecule as a set of independent harmonic oscillators. This is called normal mode analysis (NMA)^[31]. In practice the mass-weighted hessian matrix is diagonalized which allows obtaining the eigenvalues and eigenvectors, representing frequencies and vibrational modes. The internal energy is calculated using following expression, where Q represents the molecular partition function of the

system. For more explanation on the topic we refer to standard textbooks^[30].

$$U = E_{DFT} + k_b T^2 \cdot \left(\frac{\partial \ln(Q)}{\partial T} \right)_V \quad (2.2)$$

With the internal energy, the enthalpy can be calculated easily when assuming an ideal gas behavior

$$H = U + pV = U + k_b T \quad (2.3)$$

The entropy in turn is determined as a function of the partition function:

$$S = k_b \ln(Q) + T \cdot \left(\frac{\partial \ln(Q)}{\partial T} \right)_V \quad (2.4)$$

To conclude, the Gibbs free energy can be determined as:

$$G = H - TS \quad (2.5)$$

Next to determining thermodynamic properties, the normal modes can also be used to model the infrared spectrum. The vibrational frequencies are the center of the IR absorption bands which are represented by gaussian peaks. However, to achieve a more accurate comparison with an experimental spectrum the wavenumbers should be shifted, depending on the used HF/DFT methodology and proportional to the calculated value of the wavenumber^[32].

Software used for the research

Most ab initio calculations are done with the Gaussian suite of programs.^[33] All optimizations are accompanied by a frequency calculation to verify whether the structure is a local minimum (no imaginary frequencies) or a real transition state (a single imaginary frequency). The DMRG SCF calculations were done with the in-house code CheMPS2^[7]. NMA and free

energy calculations were executed with the help of the TAMkin^[34, 35] python library.

2.3 EXPERIMENTAL METHODS

General

Most experimental techniques used in this work such as nitrogen sorption, UV/Vis, DRIFT, GC and HPLC are already discussed in numerous textbooks^[36, 37] and will not be described here. However, more attention will be given to the structure determination of crystalline materials. The determination of a solid state structure is a challenging problem. The texture, porosity or morphology of a material can be visualized with microscopy or simple experimental techniques. The atomic structure however is less obvious to unravel, and this is mostly achieved with the aid of powder X-ray diffraction.

Powder X-ray Diffraction

An important technique to assist in the application of structure determination via X-ray diffraction are Rietveld refinements. For the case of solids where sufficiently large single crystals can be isolated, structure determination is relatively straightforward^[38]. However for materials such as MOFs or zeolites this is more complicated, as they do not occur as a single crystal but rather as a powder. A powder XRD provides less information than a single crystal diffractogram since the small crystals are randomly oriented. This leads to diffraction cones (Figure 2.1) instead of a 2D diffraction pattern. A one dimensional scan of those cones leads to the typical powder diffractogram.

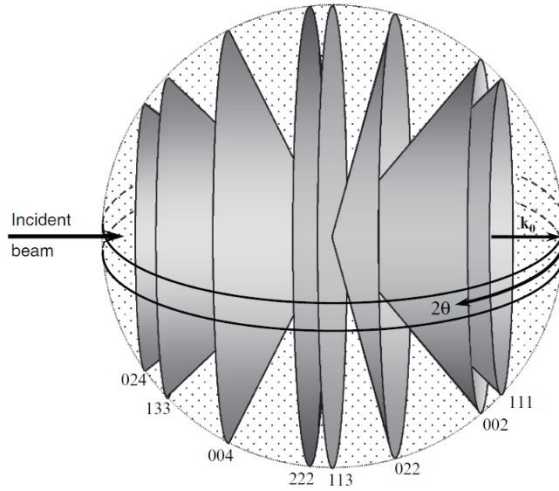


Figure 2.1. Schematic representation of powder X-ray diffraction^[39].

Structure refinement

Since a powder XRD pattern is a projection of 3D structure information on a 1D pattern some information can be lost. The refinement of a diffractogram is a topic that sparked much interest during the last decades^[40]. One of the most significant evolutions in powder pattern refinement is the Rietveld analysis^[41-44]. Hugo Rietveld single-handedly revolutionized the field of powder diffraction with his mathematical model for the diffractogram, including a whole range of experimental influences on the peak shapes:

$$I_i^{calc} = S_F \sum_{k=1}^{N_{peaks}} L_k |F_{k,j}|^2 S_j(2\theta_i - 2\theta_{k,j}) P_{k,j} A_j + bkg \quad (2.6)$$

$$|F_{k,j}|^2 = m_k \left| \sum_{n=1}^N f_n e^{-B_n \frac{\sin^2 \theta}{\lambda^2}} (e^{2\pi i(hx_n + ky_n + lz_n)}) \right|^2 \quad (2.7)$$

With S_F the scale factor, L_k the Lorentz polarization factor, S_j the shape of the peak in function of 2θ , $P_{k,j}$ the texture factor of the phase and A_j the absorption factor of the phase. $F_{k,j}$ is the peak intensity as a function of the

geometry. N is the number of atoms, f_n the atomic scattering factor and B_n the temperature factor.

With this model it becomes possible to fit the equation to the measured diffractogram, thus finding the atomic coordinates^[45] (a measure for this fit is shown in equation 2.6). In modern studies this fit is done in two steps. Firstly a profile-only fit is done to assess the experimental parameters, examples are Pawley or Le Bail^[46-48] refinements. From this first step the calculated intensities are used in the complete Rietveld method to find the structure of the material under investigation.

$$Rwp = \sqrt{\frac{\sum_{i=1}^N w_i (I_i^{exp} - I_i^{calc})^2}{\sum_{i=1}^N w_i (I_i^{exp})^2}} \cdot 100\% \quad (2.8)$$

The Rietveld model is used in this research to investigate the correspondence between experimental data and calculated structures of MOFs.

2.4 REFERENCES

- [1] Koch, W.; Holthausen, M. C., *A Chemist's Guide to Density Functional Theory*. Wiley: 2001.
- [2] Kozłowski, P. M.; Adamowicz, L., Equivalent quantum approach to nuclei and electrons in molecules. *Chem. Rev.* **1993**, 93 (6), 2007-2022.
- [3] Hinchliffe, A., *Molecular Modelling for Beginners*. Wiley: 2011.
- [4] Brazdova, V.; Bowler, D. R., *Atomistic Computer Simulations: A Practical Guide*. Wiley: 2013.
- [5] Leach, A. R., *Molecular Modelling: Principles and Applications*. Prentice Hall: 2001.
- [6] Wouters, S.; Van Neck, D., The density matrix renormalization group for ab initio quantum chemistry. *Eur. Phys. J. D* **2014**, 68 (9), 1-20.
- [7] Wouters, S.; Poelmans, W.; Ayers, P. W.; Van Neck, D., CheMPS2: A free open-source spin-adapted implementation of the density matrix renormalization group for ab initio quantum chemistry. *Computer Physics Communications* **2014**, 185 (6), 1501-1514.
- [8] Cramer, C. J., *Essentials of Computational Chemistry: Theories and Models*. Wiley: 2005.
- [9] Szabo, A.; Ostlund, N. S., *Modern Quantum Chemistry: Introduction to Advanced Electronic Structure Theory*. Dover Publications: 2012.

- [10] Kohn, W.; Sham, L. J., Self-Consistent Equations Including Exchange and Correlation Effects. *Physical Review* **1965**, *140* (4A), A1133-A1138.
- [11] Hohenberg, P.; Kohn, W., Inhomogeneous Electron Gas. *Physical Review* **1964**, *136* (3B), B864-B871.
- [12] Grenthe, I., *Chemistry, 1996-2000*. World Scientific: 2003.
- [13] Kaplan, I. G., Problems in DFT with the total spin and degenerate states. *International Journal of Quantum Chemistry* **2007**, *107* (14), 2595-2603.
- [14] Perdew, J. P.; Ruzsinszky, A.; Tao, J.; Staroverov, V. N.; Scuseria, G. E.; Csonka, G. I., Prescription for the design and selection of density functional approximations: More constraint satisfaction with fewer fits. *The Journal of Chemical Physics* **2005**, *123* (6), 062201.
- [15] Handy, N. C.; Cohen, A. J., Left-right correlation energy. *Mol. Phys.* **2001**, *99* (5), 403-412.
- [16] Hoe, W.-M.; Cohen, A. J.; Handy, N. C., Assessment of a new local exchange functional OPTX. *Chemical Physics Letters* **2001**, *341* (3-4), 319-328.
- [17] Perdew, J. P.; Burke, K.; Ernzerhof, M., Generalized gradient approximation made simple. *Phys. Rev. Lett.* **1996**, *77* (18), 3865-3868.
- [18] Becke, A. D., Density-functional thermochemistry .3. The role of exact exchange. *J. Chem. Phys.* **1993**, *98* (7), 5648-5652.
- [19] Lee, C. T.; Yang, W. T.; Parr, R. G., Development of the colle-salvetti correlation-energy formula into a functional of the electron-density. *Phys. Rev. B* **1988**, *37* (2), 785-789.
- [20] Yanai, T.; Tew, D. P.; Handy, N. C., A new hybrid exchange–correlation functional using the Coulomb-attenuating method (CAM-B3LYP). *Chemical Physics Letters* **2004**, *393* (1-3), 51-57.
- [21] Grimme, S.; Antony, J.; Schwabe, T.; Muck-Lichtenfeld, C., Density functional theory with dispersion corrections for supramolecular structures, aggregates, and complexes of (bio)organic molecules. *Organic & Biomolecular Chemistry* **2007**, *5* (5), 741-758.
- [22] Grimme, S., Accurate description of van der Waals complexes by density functional theory including empirical corrections. *J. Comput. Chem.* **2004**, *25* (12), 1463-1473.
- [23] Zhao, Y.; Truhlar, D. G., Density Functionals with Broad Applicability in Chemistry. *Accounts Chem. Res.* **2008**, *41* (2), 157-167.
- [24] Van Speybroeck, V.; De Wispelaere, K.; Van der Mynsbrugge, J.; Vandichel, M.; Hemelsoet, K.; Waroquier, M., First principle chemical kinetics in zeolites: the methanol-to-olefin process as a case study. *Chem. Soc. Rev.* **2014**, *43* (21), 7326-7357.
- [25] Grimme, S.; Antony, J.; Ehrlich, S.; Krieg, H., A consistent and accurate ab initio parametrization of density functional dispersion correction (DFT-D) for the 94 elements H-Pu. *J. Chem. Phys.* **2010**, *132* (15).
- [26] Marques, M. A. L.; Maitra, N. T.; Nogueira, F. M. S.; Gross, E. K. U.; Rubio, A., *Fundamentals of Time-Dependent Density Functional Theory*. Springer: 2012.

- [27] Dreuw, A.; Head-Gordon, M., Single-reference ab initio methods for the calculation of excited states of large molecules. *Chem. Rev.* **2005**, *105* (11), 4009-4037.
- [28] Ullrich, C., *Time-Dependent Density-Functional Theory: Concepts and Applications*. OUP Oxford: 2012.
- [29] Casida, M. E., Time-dependent density-functional theory for molecules and molecular solids. *Journal of Molecular Structure: THEOCHEM* **2009**, *914* (1-3), 3-18.
- [30] McQuarrie, D. A.; Simon, J. D., *Molecular Thermodynamics*. University Science Books: 1999.
- [31] Lucas, K., *Applied Statistical Thermodynamics*. Springer Berlin Heidelberg: 2013.
- [32] Merrick, J. P.; Moran, D.; Radom, L., An evaluation of harmonic vibrational frequency scale factors. *J. Phys. Chem. A* **2007**, *111* (45), 11683-11700.
- [33] M. J. Frisch, G. W. T., H. B. Schlegel, G. E. Scuseria, M. A. Robb, J. R. Cheeseman, G. Scalmani, V. Barone, B. Mennucci, G. A. Petersson, H. Nakatsuji, M. Caricato, X. Li, H. P. Hratchian, A. F. Izmaylov, et al. *Gaussian 09*, Revision D.01, Gaussian, Inc., Wallingford CT; 2009.
- [34] Ghysels, A.; Verstraelen, T.; Hemelsoet, K.; Waroquier, M.; Van Speybroeck, V., TAMkin: A Versatile Package for Vibrational Analysis and Chemical Kinetics. *J. Chem Inf. Model.* **2010**, *50* (9), 1736-1750.
- [35] CMM software. <http://molmod.ugent.be/software>.
- [36] Delannay, F., *Characterization of heterogeneous catalysts*. M. Dekker: 1984.
- [37] Heftmann, E., *Chromatography: Fundamentals and applications of chromatography and related differential migration methods - Part A: Fundamentals and techniques*. Elsevier Science: 2004.
- [38] Chasman, D., *Protein Structure: Determination, Analysis, and Applications for Drug Discovery*. Taylor & Francis: 2003.
- [39] Pecharsky, V.; Zavalij, P., *Fundamentals of Powder Diffraction and Structural Characterization of Materials, Second Edition: 33 Tab.* Springer: 2009.
- [40] David, W. I. F.; Shankland, K.; McCusker, L. B.; Bärlocher, C., *Structure Determination from Powder Diffraction Data*. OUP Oxford: 2006.
- [41] Rietveld, H. M., The Rietveld method. *Phys. Scr.* **2014**, *89* (9), 6.
- [42] Rietveld, H., A profile refinement method for nuclear and magnetic structures. *Journal of Applied Crystallography* **1969**, *2* (2), 65-71.
- [43] Rietveld, H. M., Line profiles of neutron powder-diffraction peaks for structure refinement. *Acta Crystallographica* **1967**, *22*, 151-&.
- [44] Rietveld, H. M., A method for including line profiles of neutron powder diffraction peaks in determination of crystal structures. *Acta Crystallographica* **1966**, *S 21*, A228-&.
- [45] Jansen, E.; Schafer, W.; Will, G., R values in analysis of powder diffraction data using Rietveld refinement. *Journal of Applied Crystallography* **1994**, *27* (4), 492-496.

- [46] Le Bail, A.; Duroy, H.; Fourquet, J. L., Abinitio structure determination of *lisbwo6* by x-ray-powder diffraction. *Mater. Res. Bull.* **1988**, *23* (3), 447-452.
- [47] Le Bail, A., Whole powder pattern decomposition methods and applications: A retrospection. *Powder Diffraction* **2005**, *20* (4), 316-326.
- [48] Jansen, J.; Peschar, R.; Schenk, H., On the determination of accurate intensities from powder diffraction data .1. Whole-pattern fitting with a least-squares procedure. *Journal of Applied Crystallography* **1992**, *25*, 231-236.

CHAPTER 3. MAJOR RESEARCH RESULTS

3.1 COMPUTATIONAL DESCRIPTION OF THE SALEN COMPLEX

General

As explained before, there has been some dispute on the best computational methodology for ab initio calculations on epoxidation reactions with the salen complex. The use of different DFT models yields different conclusions on the mechanism and the spin state of the system^[1-3]. This is due to the high multireference character of this system, as was reported in previous studies^[4, 5]. To tackle the multireference character, the use of post-HF (fullCI, CASSCF) methodologies could be a valid approach. However, since we aim to use a large model for the salen complex in order to assess selectivity and the influence of steric effects on the catalyst behavior it becomes impossible to use these high level methodologies due to computational limitations. This means we have to revert to the use of DFT to model this system and a benchmark will be required to choose the correct functional.

High-level reference data

Before a benchmark can be done, a quantity has to be defined that that should be reproduced accurately by the DFT calculations. For this quantity high level reference data should be produced. Since the spin state of the Mn^V-oxo salen complex is one of the main areas of dispute, the relative energies of the spin 0,1 and 2 state (multiplicity of 1, 3 or 5) can be used as a good benchmark quantity. The second task is to define the methodology to obtain this reference data. Since the Mn-salen complex has a high

multireference character the chosen methodology has to be able to cope with this. The most applicable post-HF methodology seems to be a CASSCF calculation. These types of calculations can only be done on a relatively small model system, shown in Figure 3.1, while previous work has shown that a very large active space would be required to obtain an accurate result^[5]. Recently Van Neck *et al.*^[6] proposed a software package using the DMRG-SCF methodology for multireference calculations. By writing the exact wavefunction in an active space with the help of a matrix product state, it becomes possible to increase the size of this active space efficiently. As a consequence, relatively large model systems can be used.

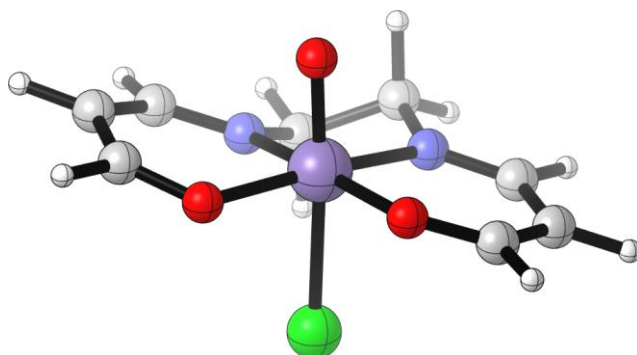


Figure 3.1. Mn-acacen' model used for the benchmark calculations.

With this methodology a simulation with an active space of 28 electrons in 22 orbitals was performed for the different spin states using the Mn-acacen' model (Figure 3.1). These results are shown in **Paper I**. The energy ordering of the spin states found by Van Neck *et al.*^[7] was proven to be independent of the applied basis set and it was shown that more orbitals were required for an accurate description than was proposed earlier by Burt *et al.*^[4] and Sherrill *et al.*^[5] The relative energies compared to the spin 0 state are shown in Table 3.1. This shows that no matter what the basis set is, the spin 1 state is favored and the spin 2 state is highly unfavored.

Table 3.1. Energies relative to spin 0 for the different spin states calculated by the DMRG-SCF method for the basis sets considered (kJ/mol).

	6-31G*	cc-pVDZ	ANODZ
Spin 1	-20.9	-22.2	-16.7
Spin 2	60.7	50.6	60.7

Benchmark of various DFT methods compared to the high level reference data

These reference data allows us to create a benchmark for a whole series of DFT functionals. It was attempted to take into account a very broad spectrum of candidates, from functionals that are considered workhorses in the field (such as B3LYP or MO6-2X) to relatively unknown exchange correlation functionals (Figure 3.2). The results are discussed in **paper II**. This benchmark allowed the proposition of some trends. Firstly functionals containing pure HF exchange tend to overestimate the stability of the spin 2 state. This effect can be explained by the fact that the pairing of electrons in an orbital is mostly stabilized by correlation effects. If different spin states are energetically very close to each other, the high spin state variant will always be preferred by functionals containing a majority of HF exchange contribution such as B3LYP. On the other hand some pure DFT functionals such as BP86 overestimate the stability of the spin 0 state.

Although not a single of the tested functionals succeeds in reproducing the reference results quantitatively, several of them managed to reproduce the spin ordering qualitatively. The best results seem to come from the functionals containing Handy's^[8, 9] modification of the Becke exchange functional (OPTX). In further calculations the OPBE functional will be used.

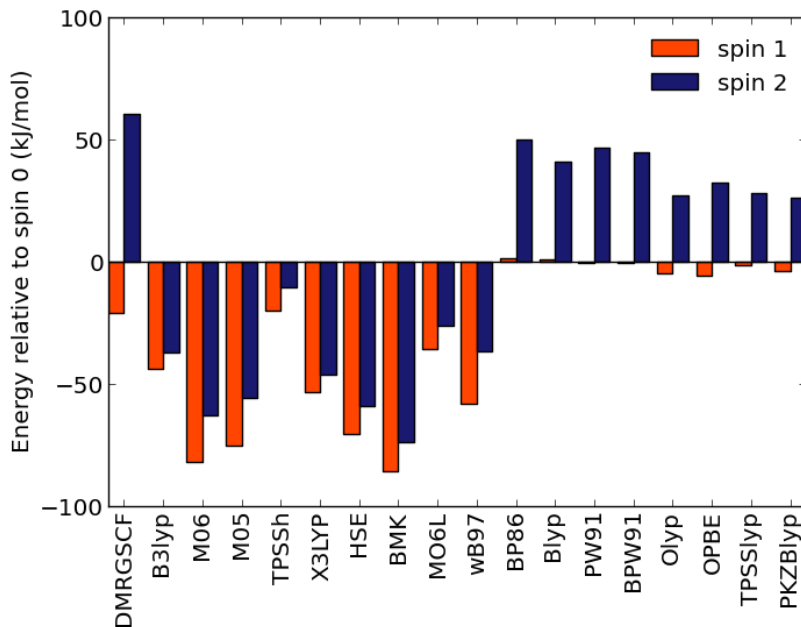


Figure 3.2. Behavior of different functionals compared to the DMRGSCF reference values^[10].

3.2 UNRAVELING MECHANISTIC DETAILS FOR A SMALL MODEL SALEN COMPLEX

Model

The original computational studies of the salen complex were done on the Mn-acacen' model, omitting the backbone and aromatic parts of the salicylaldehyde wings. Ethene was used as a substrate. This model does not allow for any study of the selectivity of the reaction. The substrate has no prochiral center and the complex is too small to include any steric effects that would induce selectivity. From this model we aim to learn the mechanism for the transfer of activated oxygen from the complex to the substrate. The first hypothesis is the existence of a radical intermediate, another possibility is the concerted oxygen transfer (mechanisms shown in Figure 3.3). Other possibilities that were proposed are a pathway that occurs via a manganaoxetane intermediate or one via a five membered ring. The comparison between these pathways is shown in **Paper II**.

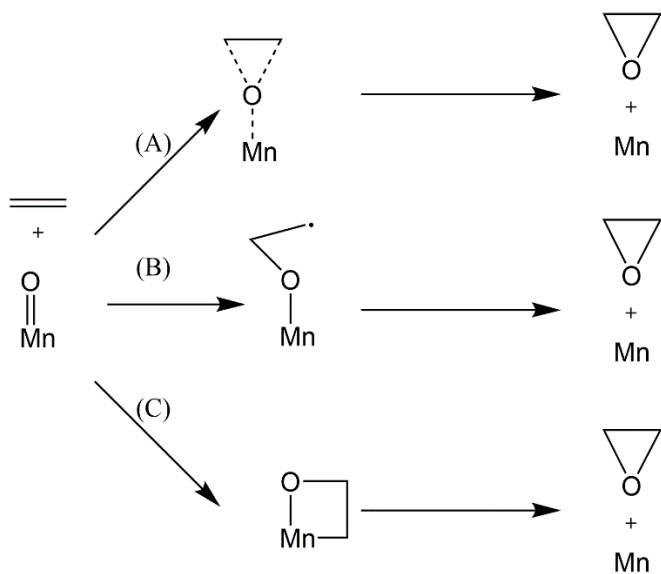


Figure 3.3. Possible mechanisms that were originally proposed for the epoxidation with a Mn-salen complex^[11].

The radical intermediate

The oxygen transfer via a radical intermediate is shown in Figure 3.4. On the spin 0 plane this transfer was not found possible, on the spin 1 and spin 2 plane this mechanism is feasible. It was shown before that the Mn^V-oxo complex should have a spin 1 state. During the oxygen transfer there would be a spin transfer to the spin 2 plane. The formation of the first C-O bond has the highest barrier: 45.5 kJ/mol on the spin 1 plane. The collapse of the radical with the formation of the second C-O bond is very lowly activated, and seems to be favored on the spin 2 plane.

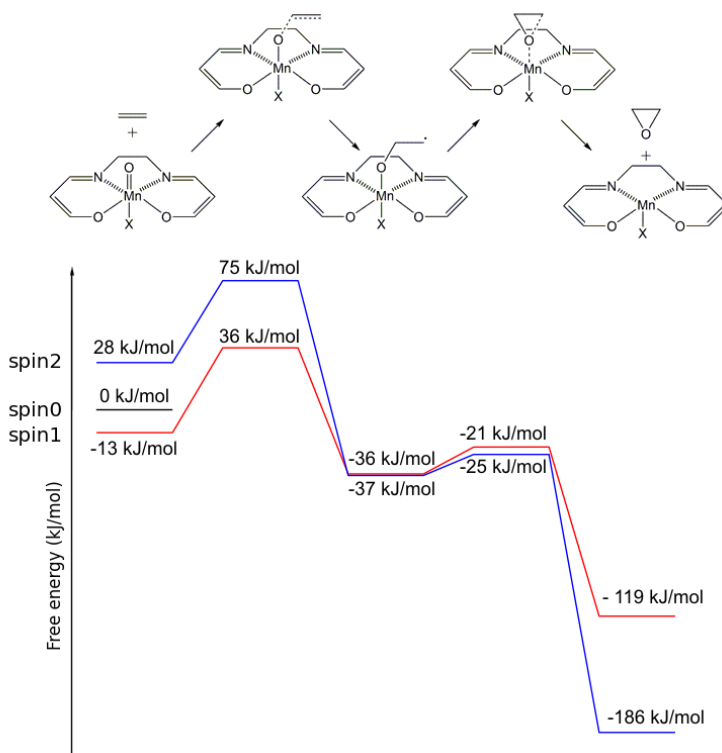


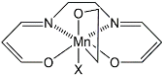
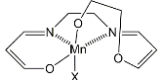
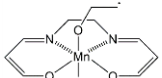
Figure 3.4. Energy diagram for the oxygen transfer relative to the reactants on the spin 0 plane^[10].

Alternative intermediates

The existence of a radical intermediate was contested by several experimental studies^[11-14] and alternative mechanisms were proposed. The first possibility is a concerted pathway where both C-O bonds are formed simultaneously. With the selected methodology no such pathway could be found despite extensive searches. Other possible intermediates that were suggested are the manganooxetane intermediate and the formation of a five-membered ring consisting of the manganese, oxygen, the two substrate carbons and the oxygen of the ligand (Table 3.2). This latter intermediate was proposed from an earlier computational study^[15]. Table 3.2 shows a comparison between all different intermediates on the spin planes where they could be identified. The manganooxetane intermediate could only be identified on the spin 0 plane but was found to be very unstable. While the FMR intermediate on the spin 1 plane was more stable than the radical

intermediates, the formation of this compound can only occur via a collapse of the radical intermediate. Moreover a direct pathway from the five-membered ring to the epoxide could not be found.

Table 3.2. Free energies of different intermediates relative to the reactants on the spin 0 plain (X=Cl)^[10].

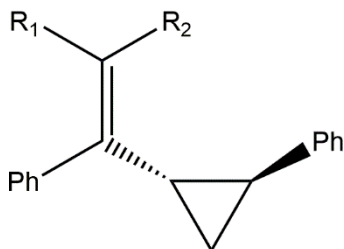
	Structure	Spin state occurrence	Free energy
Manganoaxetane		Spin 0	119.0 kJ/mol
Five-membered ring		Spin 0	-4.1 kJ/mol
		Spin 1	-71.3 kJ/mol
Radical intermediate		Spin 1	-36.6 kJ/mol
		Spin 2	-37.5 kJ/mol

These results suggest that the radical intermediate is the only possible route for epoxidation reactions with this complex. Therefore further research is needed to justify the experiments that seem to contradict the existence of a radical pathway.

3.3 RADICAL PROBE EXPERIMENTS

Ring opening versus epoxidation reaction on the manganese-acacen' complex

An important set of experiments that point to the existence of a non-radical intermediate are the ones using a radical probe that would capture any radical formed during the reaction. These substrates contain a labile three-membered ring vicinal to the double bond, this ring would be easily opened by the existence of a radical and would thus capture all radicals as ring opening products. This approach was first proposed by Wong *et al.*^[11] and was further optimized by Akermark *et al.*^[12] Their most important results are summarized in Table 3.3 and Figure 3.5.



(1) $R_1 = \text{H}$, $R_2 = \text{CH}_3$

(2) $R_1 = \text{CH}_3$, $R_2 = \text{H}$

Figure 3.5. Radical probes utilized in the experiments from Akermark et al. the phenylic groups are added to allow for an unbiased position of the radical.

Table 3.3. Amount of epoxide product compared to ring opening products with the radical probe experiments.

	NaOCl/ CH_2Cl_2 (a)	Iodosylbenzene/ benzene (b)
(1)	100%	83%
(2)	56%	54%

Firstly the behavior of the probes was modelled on the small system. On the model, with ethene as a substrate, it already became apparent that the formation of a second C-O bond from the radical intermediate had a very low barrier. This reaction could thus compete with the ring opening of the radical probe. To take into account the different oxidant systems, we modified the sixth coordination side of the complex, with a hypochlorite oxidant the hypochlorite anions will replace the chloride anions, while in the iodosyl system these anions are maintained. The results from the first case are summarized in Figure 3.6 and are further elaborated in **Paper II**.

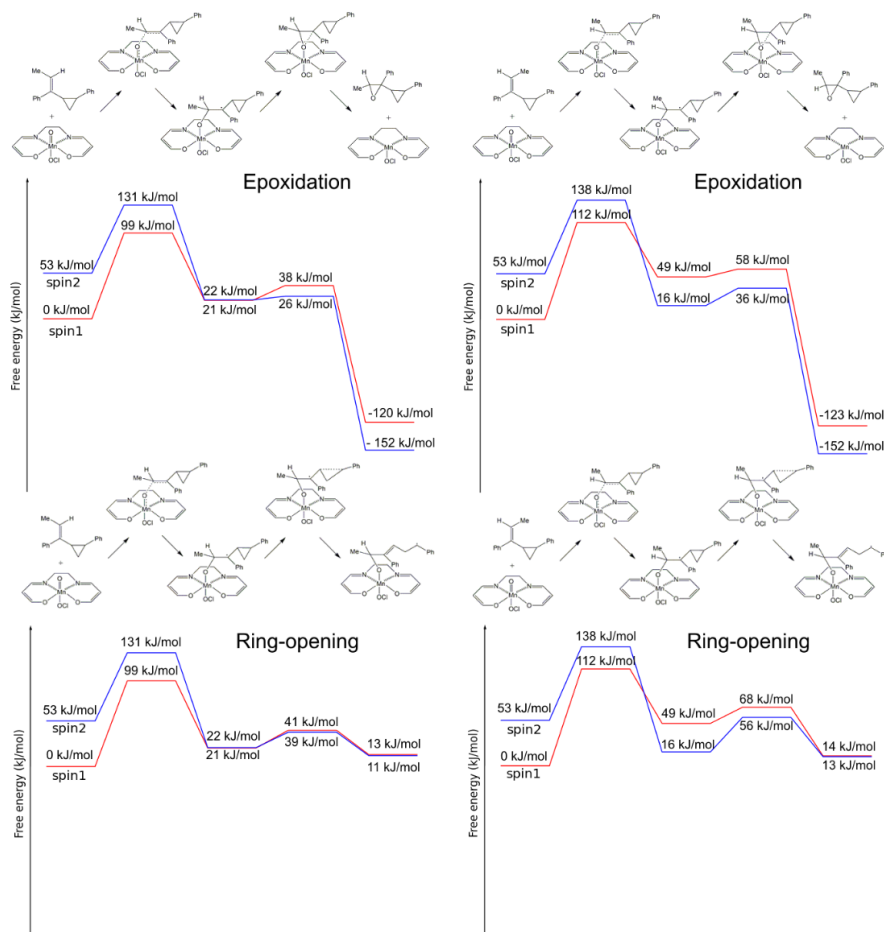


Figure 3.6. Epoxidation versus ring-opening pathway, free energy diagram for probe (1) on the left and probe (2) on the right (nomenclature in Table 3.3). Free energies are relative to the reactants on spin 1^[10]. Reproduced with permission from Wiley.

From this limited model it is clear that the barriers for epoxidation with probe (1) are generally lower than those for ring-opening, leading to the thermodynamically favored epoxide being favored. These results are more or less consistent with the experimental observation that probe (1) yields a majority of epoxide product. For probe (2) the same conclusion seems valid, however experimentally a 50-50 distribution between epoxide and ring-opening products is found. These discrepancies could be attributed to the small system size, because the probes are relatively bulky and a big part of

complex is omitted, many steric effects will not be included. Thus, since the limited model does not suffice, the full salen complex has to be considered.

Ring-opening versus epoxidation on the full Jacobsen complex

Because it can be assumed that the steric surroundings of the complex are important for the selectivity behavior, the last step of the reaction (ring opening or epoxidation) was modelled with the full complex. Because of the system size, some sacrifices have to be made on the basis set size, where a double zeta was used for C,H,N and O, the heavier Cl and Mn atoms were still modeled with a triple zeta basis set. Including all steric influences of the ligand greatly clarifies the effects at work. With probe **(2)** the barrier for epoxidation is higher than the one for the ring-opening (Figure 3.8) which probably explains the observed distribution between thermodynamically favored epoxide and kinetically favored ring opening products. Probe **(1)** has similar barriers for the ring opening reaction leading to the thermodynamically more favored product being formed (Figure 3.7).

This effect can also be seen by studying the geometry of the transition states. In the ring-opening step the substrate is positioned relatively far from the ligand, avoiding any unfavorable interaction. The epoxidation takes place with the reactant closer to the ligand, opening the way for steric effects that influence the resulting product distribution. With probe **(1)** there are no unfavorable interactions present. For probe **(2)** the methyl group (marked orange in Figure 3.9 **(2)**) would be hindered by the *tert*-butyl group of the complex, forcing the probe to twist during the transition state. This twist appears to be unfavorable, significantly increasing the barrier (Figure 3.8).

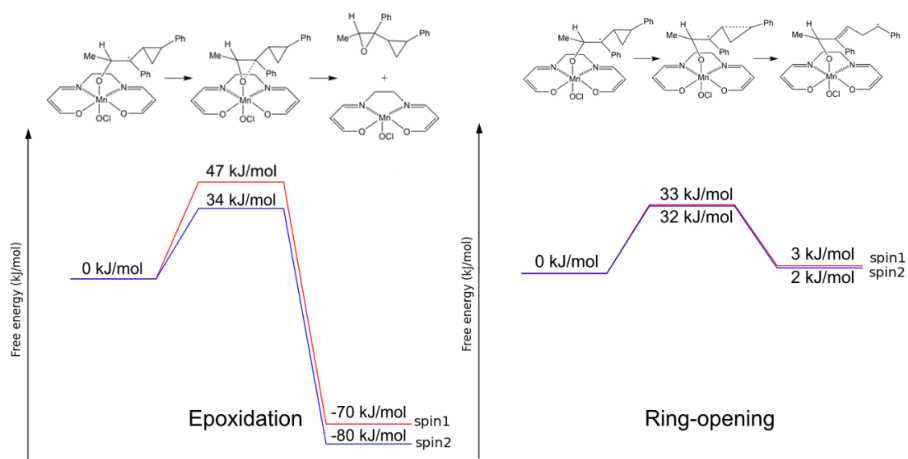


Figure 3.7. Free energy diagrams for the competitive ring-opening and epoxidation reaction for probe **(1)**^[10]. Reproduced with permission from Wiley.

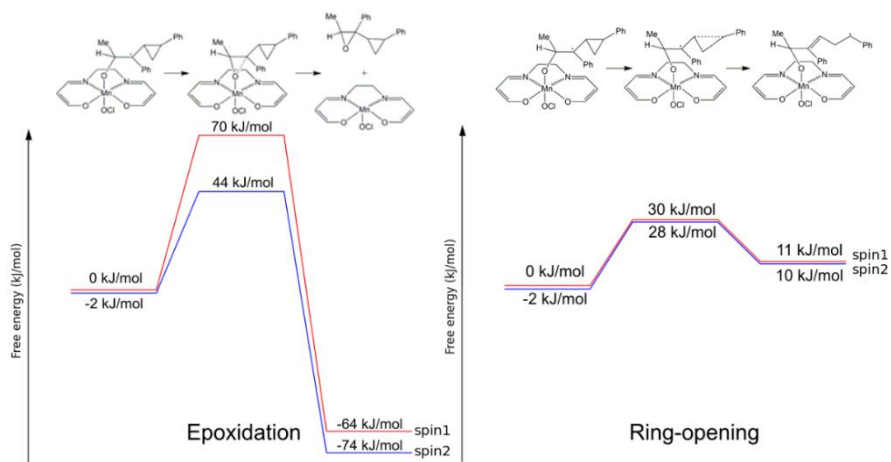


Figure 3.8. Free energy diagrams for the competitive ring-opening and epoxidation reaction for probe **(2)**^[10]. Reproduced with permission from Wiley.

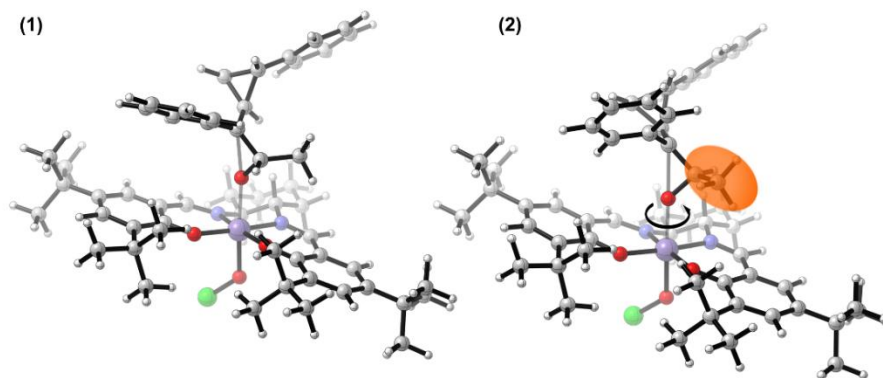


Figure 3.9. Geometry for the epoxidation reaction for the different probes. Reproduced with permission from Wiley.

3.4 MODELLING THE SELECTIVITY

Overview

With the results from the previous parts we can assure ourselves that the two-step mechanism is the most probable. This has an important implication for the selectivity, namely that the formation of the first C-O bond determines the enantiomer that will be formed (Figure 3.10). To model this selectivity we will consider dihydronaphthalene as a probe molecule, since this is also the substrate used in further experimental tests. The variant of the salen complex that is used will be the (1S,2S)-complex and as the counter ion chlorine is chosen. In what follows we will thus consider the transition state of the first step (top line in Figure 3.10). Since the enantioselectivity is determined there, an accurate description of this step will allow us to provide much insight in the selectivity. These results are shown in **paper III** and **paper IV**.

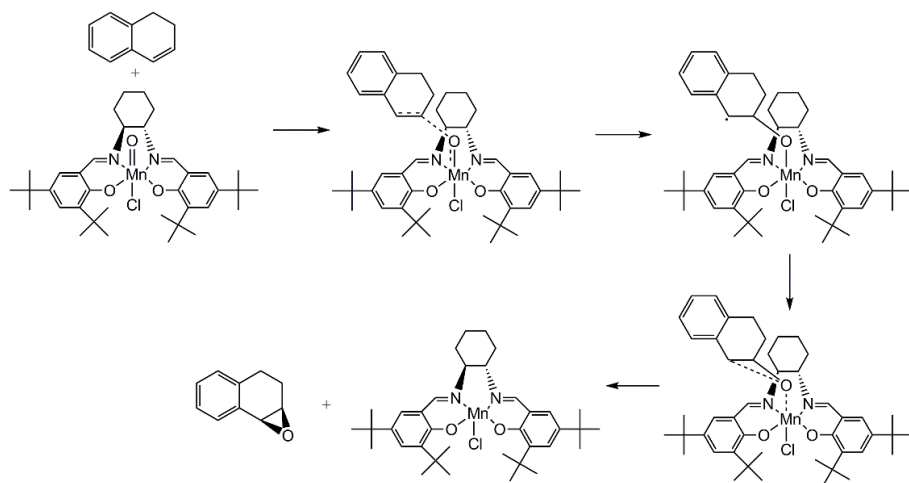


Figure 3.10. Pathway for the epoxidation of dihydronaphthalene, the first transition state determines the enantioselectivity of this reaction.

The symmetrical salen complex

In homogeneous phase reactions, the Jacobsen variant of the salen complex is most widely accepted and we will also use this as model. This variant has two identical salicylaldehyde ‘wings’ with *tert*-butyl groups on the C3/C3’ and C5/C5’ positions. Since both sides of the complex are identical, these complexes are called symmetrical salen complexes. In this case there are two approaches possible, one leading to (1R,2S)-dihydronaphthaleneoxide and one leading to (1S,2R)-dihydronaphthaleneoxide (in short the RS-approach and the SR-approach). A rotational scan on full QM level for the transition state shows there is one minimum for each approach. This is in contradiction with previous results from Cavallo *et al.*^[16] who found several local minima when using MM calculations. These two approaches were optimized and the free energy difference was calculated to be about 10 kJ/mol.

While the geometry of the transition state does not provide conclusive information on the approach of the substrate to the catalyst, one can deduce from these results that a distal approach from the front seems to be most likely for this substrate. The importance of the substituents on the C3/C3’ positions becomes clear from this model. Most of the unfavorable interactions of the RS-approach come from these substituents. This can be seen by the close distance of the substrate to the C3 substituents of the

complex shown in Figure 3.11. With dihydronaphthalene as a test case, there is only one close interaction between the C5 substituent, indicating that this moiety is less important for the selectivity. This is in agreement with the experimental observation that the absence of C3/C3' substituents drastically reduces the selectivity of this catalyst. The C5/C5' positions are of less importance for the selectivity^[17, 18].

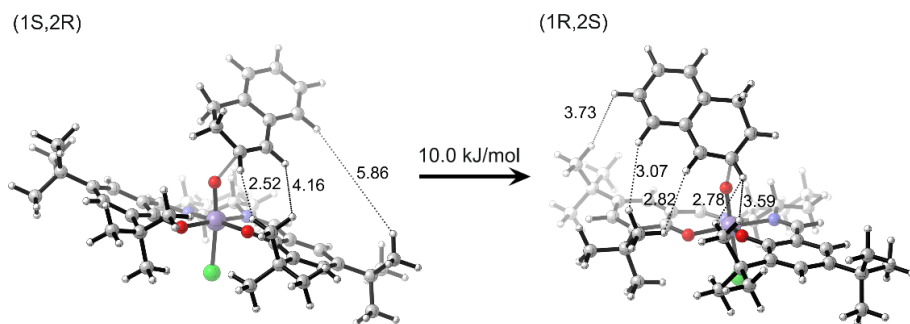


Figure 3.11. The transition state for the two approaches with the closest distances denoted (Å)^[19]. Reprinted with permission from Elsevier.

The asymmetrical salen complex

Many authors have suggested the grafting of a modified salen complex as a possible approach to find a heterogeneous analogue for this homogeneous system^[20-22]. To achieve the grafting, they propose a modification on one or both of the salicylaldehyde moieties to introduce a functional group that can be used to anchor the catalyst to a carrier material. To allow an easy grafting and to accommodate the groups needed for coupling, the bulky *tert*-butyl groups are often times omitted. In order to keep as much as possible the effect of the *tert*-butyl groups, an asymmetric complex, where only one of the two salicylaldehyde wings is modified, is used here. This leads to an increase in the possible transition state geometries. The general RS- and SR-approaches are maintained but the substituents can be on both sides for each approach, leading to four possible transition states (as indicated in Figure 3.12). The specific case shown here is the complex with the introduction of a hydroxyl group that can be used to form an ether bridge with the carrier material. For each of those four combinations a rotational scan showed a single minimum, as was the case for the symmetrical complex. The further optimized structures of these minima are shown in Figure 3.12.

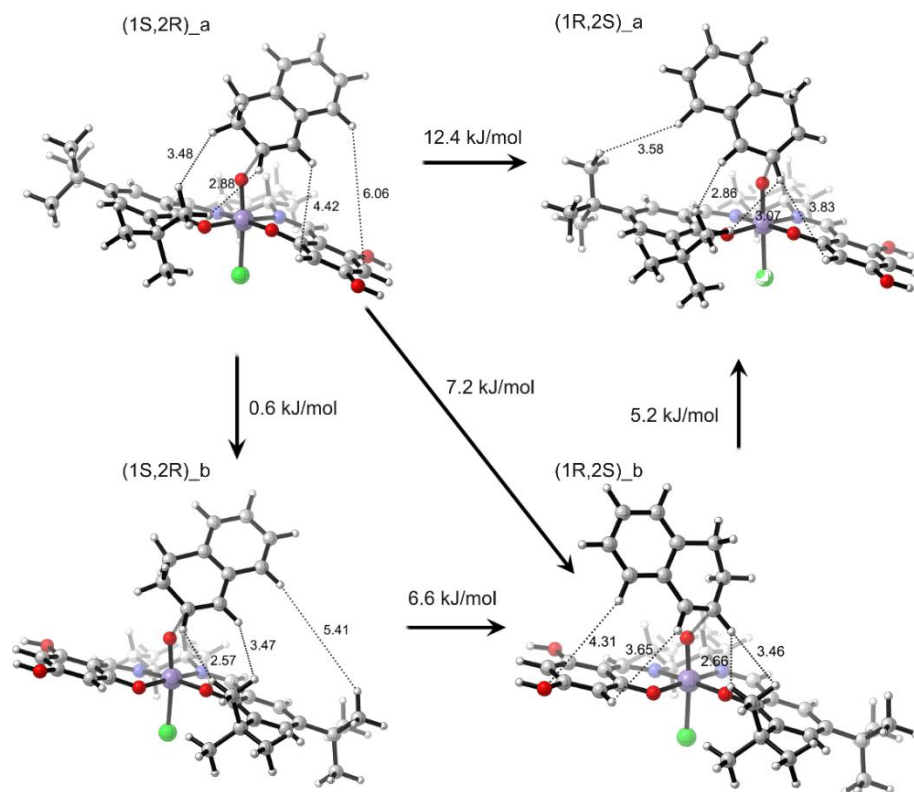


Figure 3.12. Possible transition states and relative energies for the asymmetrical salen catalysts, the steric interactions are shown (in Å)^[19]. Reprinted with permission from Elsevier.

These results show that when the *tert*-butyl groups are located on the hindering side of the complex (upward facing wing) there is almost no difference in energy with the symmetrical salen complex (difference between (1S,2R)_a and (1R,2S)_a). The energy difference is even a bit larger (12.4 kJ/mol) due to the absence of hindering steric effects on the downwards facing wing. However the energy difference between the most stable SR-approach and the most stable RS-approach is smaller (7.2 kJ/mol between (1R,2S)_a and (1S,2R)_b in Figure 3.12). The lower energy difference is a consequence of the lack of steric hindrance on the C3 position in the RS-approach. This effect again shows the paramount importance of the *tert*-butyl groups on the C3/C3' positions for obtaining a high selectivity. This effect is shown in the papers of Bajaj *et al.*^[23] and Zheng *et al.*^[24] They proposed a grafting approach that did not modify the C3/C3' substituents. Although the presence of these substituents made the covalent grafting

harder, due to the occurrence of steric effects, the enantioselectivity of these materials was significantly improved in comparison with previous results^[20-22].

The model with hydroxyl groups on one side of the complex is of course not complete when considering a grafted salen catalyst. To provide insight in the behavior of the complex once it is bound to the support, a variation of the model is used where a methylbenzene group is attached to one of the hydroxyl groups via an ether bridge. Only the substitution on the C4 position is considered since this is the most available position for a connection with the carrier material (Figure 3.13). Although this modification is quite bulky, it is relatively far from the active site and it may be anticipated to have a limited effect on the selectivity behavior, except maybe for the largest substrates. The simulations confirm this theory, since the energy differences between the four transition states are not significantly different from the original model.

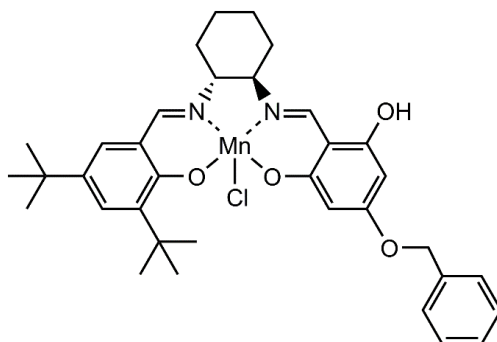


Figure 3.13. Model with a substitution to mimic grafting.

3.5 EXPERIMENTAL DESIGN OF HETEROGENEOUS SALEN CATALYSTS

Strategies employed for the immobilization

From the modelling of the selectivity behavior for different variants of the salen complex we can gain significant insight in the feasible procedures to heterogenize this complex. The most important lesson is that for a covalent grafting approach with an asymmetric complex it will be hard to find an

analogue that maintains the selectivity of the Jacobsen variant. In order to verify this, we will analyze a grafting procedure where the complex is built up step by step in the cages of a MIL-101(Cr) MOF (**Paper III**). Next to the covalent grafting approach different alternatives are explored that would allow to maintain as much of the steric environment of the complex as possible. The first possibility is anchoring the complex via the sixth coordination site of manganese. When the carrier material can possess a negatively charged ion, this site can form an ionic bound with the positively charged salen complex. This way of grafting has been proposed by Freire *et al.*^[25] and is further explored in **Paper IV**. The last method that is tested in this work is an immobilization procedure where the interactions between the complex and the host material are minimal. In **Paper V** the commercial variant of the salen complex is heterogenized by trapping it in the cages of a MIL-101 structure forming a so-called ship-in-a-bottle catalyst.

Grafting of the complex

Since the postmodification of a metal organic framework has proven to be an interesting tool to design heterogeneous catalysts, this strategy was also tested in the immobilization of the salen complex. As a carrier material the MIL-101(Cr) was chosen because this is a very stable material and possesses sufficiently large pores to contain the salen complex^[26]. The method used for this grafting is a piece-by-piece buildup of the complex in the pores (Figure 3.14). In order to do that, an anchoring point must be introduced in the MOF since the pristine MIL-101 variant contains no available functional groups. To achieve this, a chloromethylation^[27] is done to introduce a good leaving group that can serve for further reaction. Afterwards the active complex is built up on the carrier in a series of postmodification steps, as first proposed by Laibinis *et al.*^[28] This is an example of the asymmetric variant of a salen complex since the salicylaldehyde moiety that is connected to the carrier needs to contain substituents other than the *tert*-butyl groups.

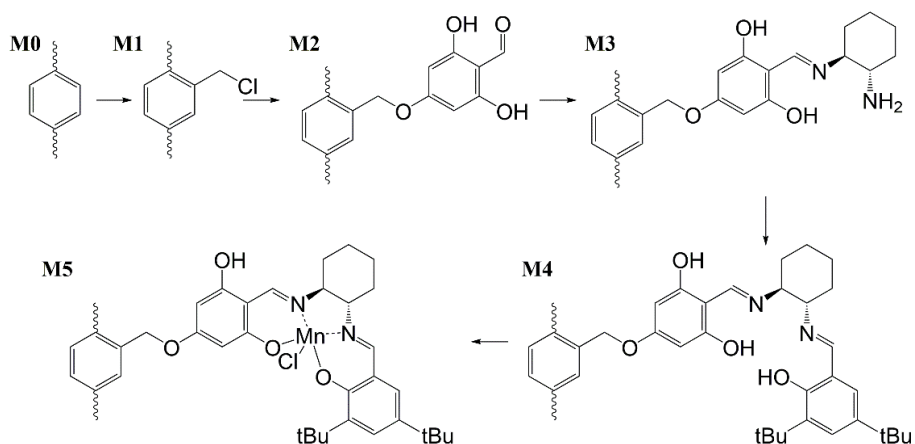


Figure 3.14. Buildup of the salen complex on MIL-101(Cr) (represented by M0).

The different steps in the modification process were characterized by various techniques, with the most clarifying being DRIFTS analysis (Figure 3.15). The chloromethylation is indicated by slightly visible peaks around 900 cm^{-1} . The C=O stretching vibration becomes visible at 1686 cm^{-1} and is indicative of the presence of the first benzaldehyde group. At 2852 cm^{-1} and 2919 cm^{-1} two peaks that are indicative of the cyclohexane backbone appear. The presence of manganese is quantified via XRF and is shown to be 0.38 mmol/g .

Using MCPBA as an oxidizing agent with dichloromethane as a solvent allowed for the enantioselective epoxidation of dihydronaphthalene with an enantiomeric excess of 62.5% and conversion of 48% after two hours. The Jacobsen complex in homogeneous phase led to 85% conversion with 70% enantiomeric excess under the same conditions. Moreover, the catalyst can be reused for three consecutive times (Figure 3.16). This corresponds with the modelling result that a grafted complex leads to a lower selectivity when the crucial bulky groups are not present. The lower conversion is probably due to the high loading of the complex on the MOF. In both the heterogeneous and in the homogeneous system the same amount of manganese was used but the high grade of substitution in the heterogeneous system could block some active sites leading to a lower observed activity.

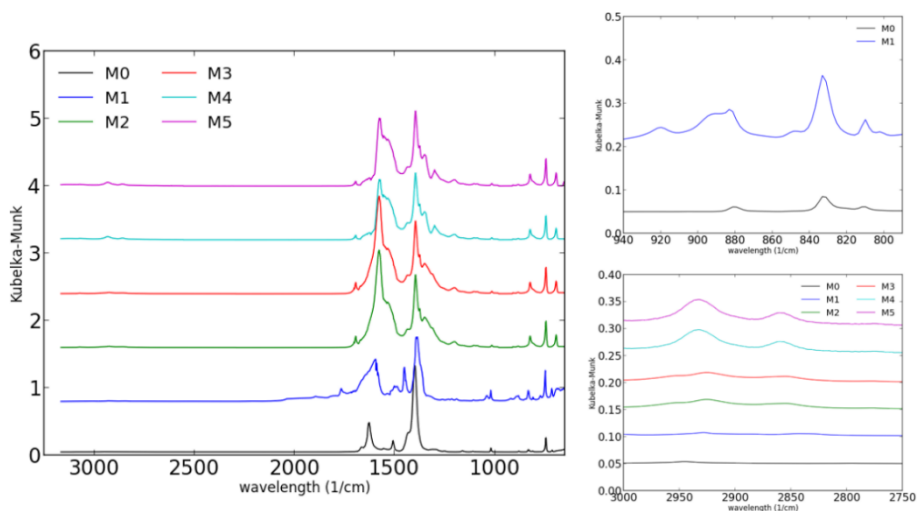


Figure 3.15. IR spectra of the different steps in the modification process^[19]. Reprinted with permission from Elsevier.

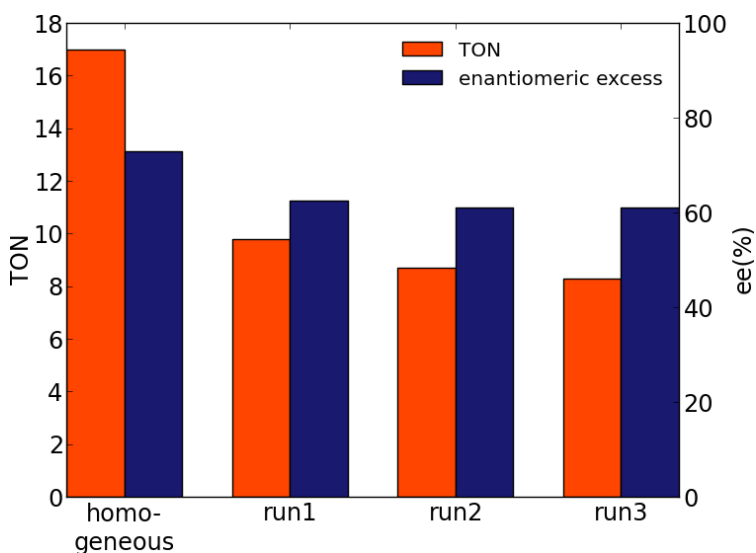


Figure 3.16. Results for the different runs in the epoxidation with the grafted salen catalyst^[19]. %ee determined by chiral HPLC. Reprinted with permission from Elsevier.

Sixth coordination site as anchoring point

In **paper IV** another approach for the grafting of the salen complex was used. Here the commercial variant of the complex was anchored on a phenolic resin via an ion exchange procedure. In this way the carrier acts as a sixth coordination site for the salen complex. The main advantage of using a

phenolic resin as a carrier material is the availability of many hydroxyl groups as anchor points for the modification. In a two-step ion exchange procedure the hydroxyl groups on the surface were modified to NaO-R groups by the addition of sodiumhydroxide. Sodium could then be exchanged with the salen complex in order to immobilize it (Figure 3.17).

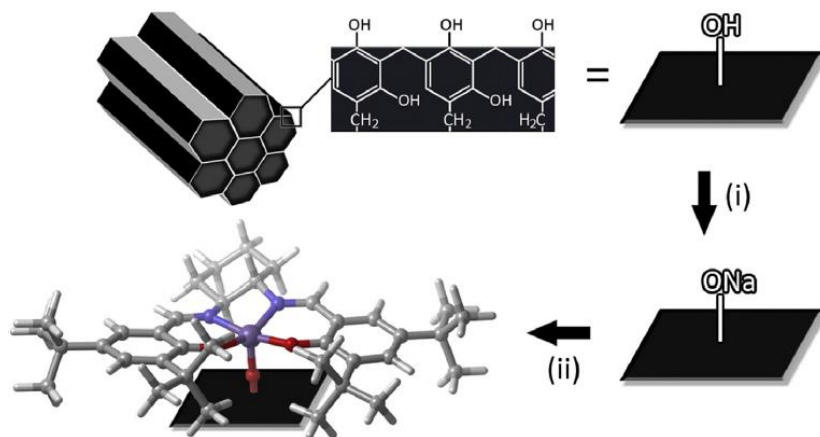


Figure 3.17. Immobilization procedure on a phenolic resin via the sixth coordination site.
Reprinted with permission from Elsevier^[29].

In this case the epoxidation of dihydronaphthalene was done with NaOCl as oxidizing agent. Homogeneously, the Jacobsen complex yielded a conversion of 90% after 24h with an enantiomeric excess of 80% using this medium. The heterogenized variant provided the same selectivity with a conversion of 62%. This material can also be used in several runs while maintaining the selectivity and activity (Figure 3.18). Here the conversion of the immobilized catalyst is lower than the homogeneous variant but the selectivity is maintained, showing the retention of the *tert*-butyl group has the desired effect. The reduction in conversion could have several reasons: Generally, an immobilized catalyst has a lower conversion than its homogeneous variant due to diffusion limitations or unwanted steric effects. In this case the method of grafting can have a significant influence on the activity of the material. The nature of the sixth coordination site has an influence on the behavior of the catalyst^[30], in our system the connection between the resin and the complex could induce electronic effects that reduce the activity of the catalyst.

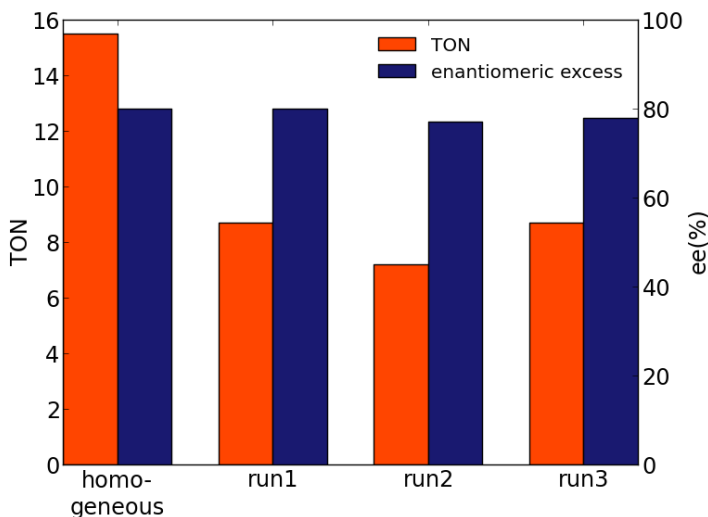


Figure 3.18. Results for the different runs in the epoxidation with the catalyst immobilized on the phenolic resin. %ee determined with chiral HPLC.

Ship in a bottle encapsulation

The previous two examples show there is still room for optimization in the design of a heterogenized salen catalyst. We aim to design a system where the steric environment of the complex is maintained and there is minimal interaction between the carrier and the complex. The methodology for this is presented in **paper V**. The typical cage structure of the MIL-101 framework has a sufficient size to contain the Jacobsen complex, but the windows are small enough to avoid migration of this complex out of the cages. Therefore the goal in this part will be the immobilization by trapping the commercial Jacobsen complex in the cages of a MIL-101 structure. The approach chosen to obtain this result was a procedure where the MOF is synthesized around the complex (Figure 3.19). This limits the choices of host structures as the complex must be resistant to the synthesis conditions of the MOF. Since the MIL-101(Cr) is synthesized in water (in which the complex is not soluble) and at high temperature, this material cannot be used for our goal. Therefore a variant of this MOF is used, the NH₂-MIL-101(Al). The MOF is synthesized via a method reported by Fisher *et al.*^[31] The reaction occurs in DMF at 110°C with a slow addition of AlCl₃ which should allow the salen complex to remain stable.

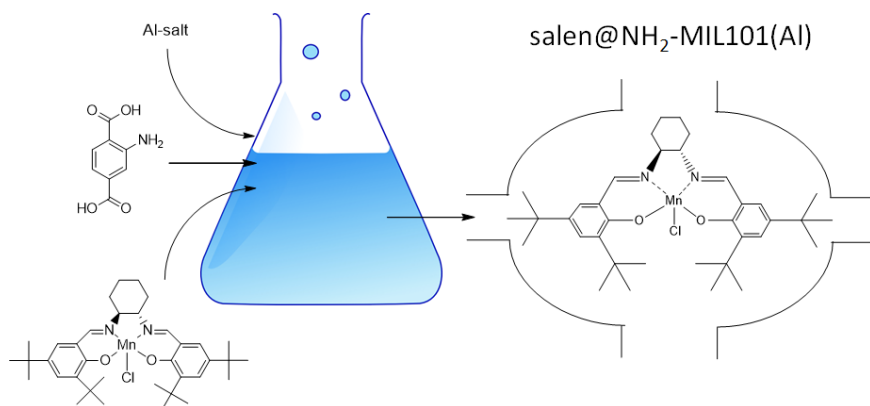


Figure 3.19. Schematic overview of the encapsulation procedure.

The presence of the salen complex in the host can be shown by DRIFTS measurements. The cyclohexanediamine backbone vibrations at 2852 cm^{-1} and 2919 cm^{-1} are the main indication of a successful encapsulation (Figure 3.20). Those vibrations remain present even after a soxhlet extraction, showing the complex cannot easily diffuse out of the carrier. An analysis of the amount of manganese allows us to conclude the loading is 0.02 mmol/g .

This catalyst was tested with the same oxidant system as the grafted salen catalyst. The conversion was shown to be 70% with an enantiomeric excess of 70%. This means the selectivity of the homogeneous complex was maintained while the conversion is slightly decreased (Figure 3.21), probably as a consequence of the diffusion in the pores of the host structure. From these data we can conclude that the influence of the host on the complex is limited, as we hoped to achieve. By this absence of interactions and the use of the same complex as in homogenous phase the selectivity could be maintained.

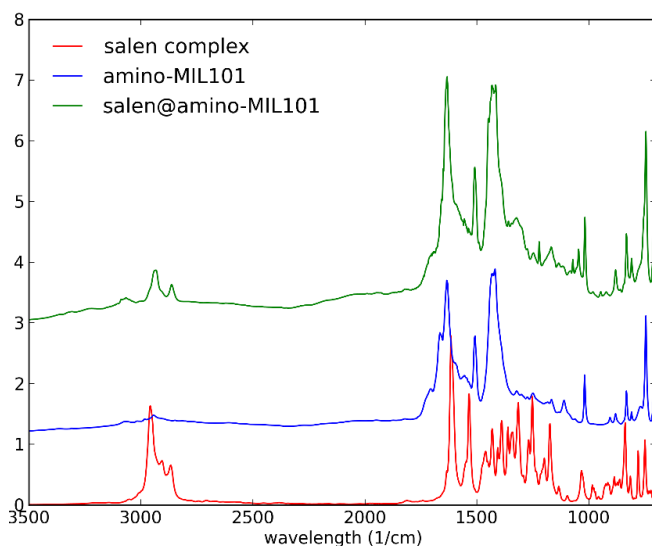


Figure 3.20. Drifts spectra for the encapsulation of the Jacobsen complex in $\text{NH}_2\text{-MIL-101(Al)}$ [32]. Reproduced with permission from The Royal Society of Chemistry.

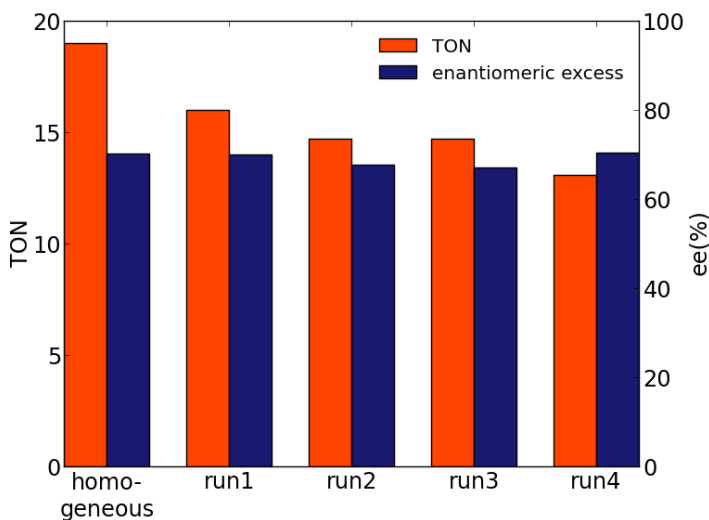


Figure 3.21. Results for the different runs in the epoxidation with the catalyst immobilized by encapsulation in $\text{NH}_2\text{-MIL-101}$ [32]. %ee values were obtained with chiral HPLC. Reproduced with permission from The Royal Society of Chemistry.

Summary

These experimental results are in good correspondence with the findings obtained from ab initio modelling studies. When employing an asymmetric

salen complex, the selectivity decreases, however the use of a MIL-101(Cr) host structure seems to give rise to a better selectivity than reported with other carrier structures. This could be due to the open structure of the MOF. Contrary to silicas or resins, that have very dense pore walls, the MIL-101(Cr) structure has significantly more free space around the anchoring points. Allowing the grafted complex to assume its most favorable shape.

With immobilization methods that maintain the geometry of the original complex, especially the *tert*-butyl groups, the selectivity of the homogeneous catalyst could also be conserved. When using the sixth coordination site as an anchoring point, the change in electronic effects could explain the reduced activity. The ship in a bottle encapsulation minimizes the interactions between the carrier and the complex, thus keeping the selectivity and still providing a good activity compared to the homogeneous system. An overview of the results, without considering the subsequent runs is shown in Table 3.4.

Table 3.4. Summary of the different catalytic systems and grafting procedures.

System	Conversion	Selectivity (%ee)
<i>Homogeneous with MCPBA</i>	85% (2h)	70%
Grafting in MIL-101(Cr)	48% (2h)	62.5%
Encapsulation NH ₂ -MIL-101(Al)	70% (2h)	70%
<i>Homogeneous with NaOCl</i>	90% (24h)	80%
Anchoring on a phenolic resin	62% (24h)	80%

3.6 COMPARING A MODELED STRUCTURE OF A MATERIAL TO EXPERIMENTS VIA MEASURED AND MODELED XRD DIFFRACTOGRAMS

General

Next to the main topic of the design of a heterogeneous salen catalyst some work on the interpretation of various characterization techniques was done in the frame of this thesis. Using computational models to assist in structure determination has been common practice. For example the structure of MIL-

101(Cr) could be unraveled only with the aid of computational structure modeling^[26]. However, doing this the other way around, using experimental data to validate the accuracy of the computational geometry is much less common. A straightforward way to approach this for crystalline materials is the refinement of the geometry from a powder XRD diffractogram and comparing that to the calculated geometry. However, this is not necessarily a good methodology as the refinement of a PXRD pattern to a 3D geometry is a statistical process and there can be other possible geometries fitting the XRD pattern. An alternative way to approach the comparison is to calculate the diffractogram from the computational model and compare that directly to the measured data. This approach is followed here and is applied on the MIL-47(V) framework

Methodology

To evaluate the similarity between structures one can use a qualitative or a quantitative approach. From any geometry an idealized XRD pattern can be calculated by determining the 2θ values of the diffractions and representing them by Gaussian peaks. The intensity can be estimated from the nature and positions of the atoms in the structure (equation (3.1)). This can provide a qualitative comparison between modelled geometries and a measured diffractogram^[33-36].

$$|F_{k,j}|^2 = \left| \sum_{n=1}^N f_n (e^{2\pi i(hx_n + ky_n + lz_n)}) \right|^2 \quad (3.1)$$

Providing a quantitative comparison can be done via procedures similar to a Rietveld refinement. The aim is here to take into account the experimental influence on peak-broadening, asymmetry, etc. which is modeled via a fit of the Rietveld equation. Those parameters, combined with the atomic coordinates, can be used to calculate the X-ray diffractogram (equation 2.5 and 2.6) and the agreement with the experimental result can be found (equation 2.7). The result from this method is a number that denotes how well the simulated diffractogram (including parameters for line broadening asymmetry,...) fits the measured one, a so-called goodness of fit. When

conducting a quantitative comparison, care has to be taken to avoid biases to a certain geometry, as is explained in **Paper VI**.

Case study: detailed structure of MIL-47(V)

As a case study for this methodology the MIL-47(V) system is considered and different models are proposed for this system. Corresponding vanadium atoms in different chains can be displaced relative to each other (shown in Figure 3.22) and the material can have a ferromagnetic or antiferromagnetic electronic structure, this leads to four possibilities denoted as A^{FM} , A^{AF} , B^{FM} , B^{AF} . These models were optimized with the periodic VASP code^[37-39] using the projector augmented wave (PAW) method^[40] and the generalized gradient approximation functional, as constructed by Perdew, Burke and Ernzerhof (PBE)^[41]. A basic requirement for an in depth computational study of this material is the availability of a good model, normally being the structure with the minimal energy. However, the energy of the four candidates was found to be close to each another (Table 3.5), and previous theoretical studies showed that the calculated mechanical properties are highly dependent on the used model^[42]. The methodology proposed here to compare these structures directly to experimental results can provide more insight in this problem and will assist in the selection of the most accurate model.

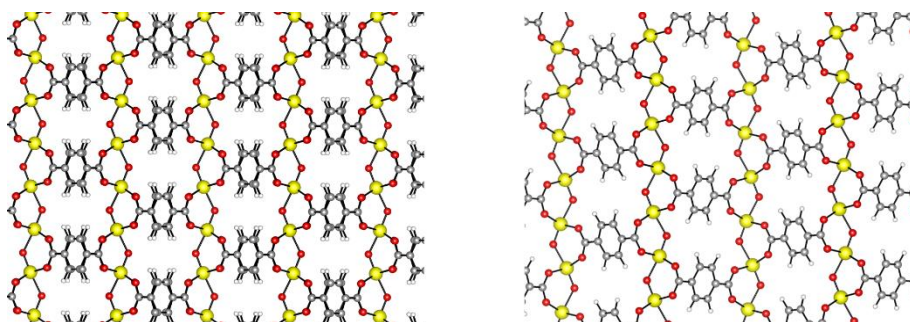


Figure 3.22. Comparison of the MIL-47(V) structure without (on the left) and with (on the right) displaced vanadium chains.

Table 3.5. Relative energies of different calculated geometries.

		Spin configuration			
		Ferromagnetic		Anti-ferromagnetic	
Crystal structure	not displaced	A^{FM}	0	A^{AF}	-278.38
	displaced	B^{FM}	-53.26	B^{AF}	-329.09

From a qualitative comparison of the calculated diffractograms, it becomes clear that the structures with displaced vanadium chains correspond significantly better to the experimentally measured diffractogram (Figure 3.23). However a distinction between the different electronic structures could not be made. In order to allow this distinction a quantitative method is used. To avoid any bias, a profile only fit is done with the Le Bail method to determine the experimental parameters in the Rietveld equation. After this step the geometry is introduced and the measure of fit is calculated (equation 2.5, 2.6 and 2.7). The results from such an approach are shown in Table 3.6.

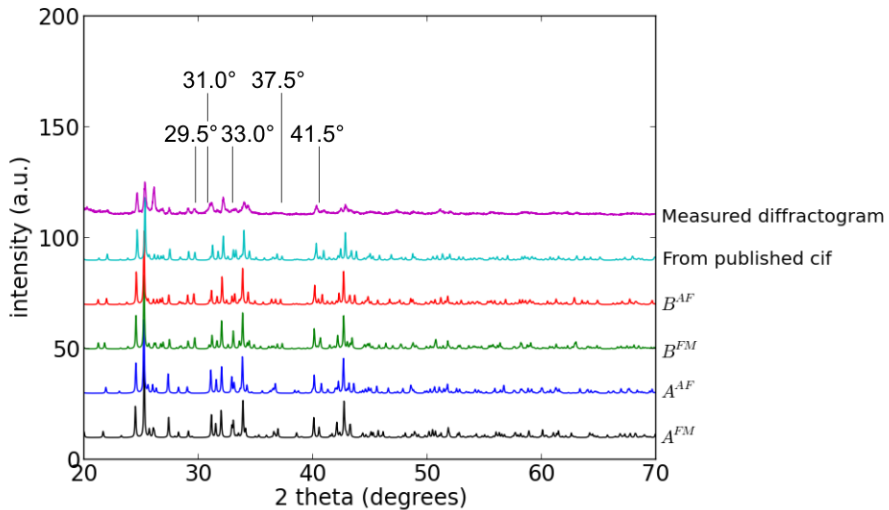


Figure 3.23. Example of a qualitative comparisons between a measured diffractogram and different models, the main differences are denoted.

Table 3.6. Quantitative comparison for different structures in different 2θ ranges.

	Full (3°-70°)	High angle (20°-70°)	Low angle (3°-20°)
A ^{FM}	48.27	44.25	30.26
A ^{AF}	45.63	52.81	16.58
B ^{FM}	38.31	39.30	21.00
B ^{AF}	43.28	44.77	16.87
published	41.45	45.25	16.11

At a low angle the calculated geometries for the FM structures provide a bad fit. This observation is not surprising since it has been reported several times that the PBE functional overestimates the unit cell parameters^[43, 44]. The error on the unit cell parameters will induce a shift in the diffraction positions. This will have more influence in the low angle region since this region is characterized by high but narrow peaks. In the high angle region the geometry has a larger influence than the unit cell parameters. In this area the peak intensity, that is a function of the geometry, is most important due to the diffraction peaks being sufficiently broad so that small shifts have little influence on the fit. The results from the quantitative procedure confirm the initial conclusions that the presence of displaced vanadium chains is a critical geometrical feature. Moreover, the subtle structural differences between the two electronic structures under investigation lead to significant differences in the fit, with the FM geometry being preferred even over the structure reported in literature^[45] (**Paper VI**).

Metal organic frameworks are very challenging systems for structure determination, both from a computational and experimental point of view. In this work various generated structures of MIL-47(V) were compared to experimental X-ray diffractograms. A distinction between geometrical differences that correspond to small energy differences in the computational model (about 50 meV) could be made both in a qualitative and quantitative manner. With fitting of calculated geometries to the experimental diffractogram via Rietveld's equation it could also be shown that minute structural difference that are a consequence of different electronic

structures chosen during the computational modeling could be compared. In the case of the MIL-47(V) structure this led to the FM geometry fitting the experiments better. When an accurate model of a crystal structure is required, for example when calculating mechanical properties, the technique shown here can be crucial to choose the best model for the material.

3.7 CONTRIBUTIONS TO OTHER PAPERS: COMPUTER ASSISTED INTERPRETATION OF SPECTROSCOPY

General

Spectroscopic techniques such as UV/Vis- and IR spectroscopy are indispensable for the characterization of novel materials. However, for the analysis of solids these methods often yield spectra that are difficult to analyze due to a multitude of broad peaks with significant noise. Therefore a simulation of the spectra can provide complementary insight in the fine structure of the materials. These simulations are only viable if a correct model for the material is used. In this section the interpretation of spectroscopic data for MOFs with the aid of computational models is presented.

The UV/Vis modelling of a gallium-bipyridine MOF (COMOC-4)

In **paper VII** and **paper VIII** the design and applications of a metal organic framework containing gallium nodes and 2,2'-bipyridine-5,5'-dicarboxylate linkers is explored. The goal of this material is to use the bipyridine moiety as a ligand for further tethering of metal centers. While the global structure of this MOF can be deduced from powder XRD, this only provides an average geometry. Therefore other techniques are vital for determining the fine structure of the material. In this case UV/Vis measurements in methanol suspension were used. The pristine material has two significant bands, one at 307 nm and a shoulder at 328 nm, as shown in Figure 3.24.

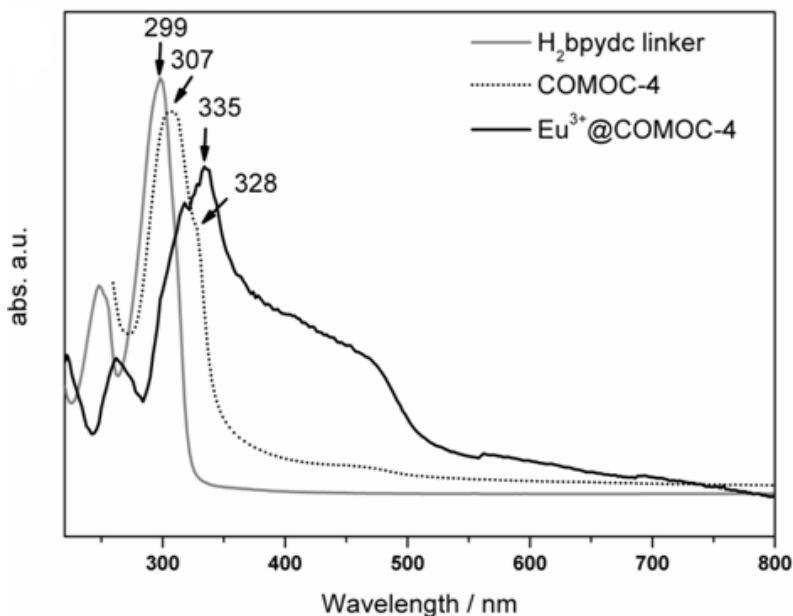


Figure 3.24. Measured UV/Vis spectra of COMOC-4 as a methanol suspension. Reprinted with permission from^[46]. Copyright 2015 American Chemical Society.

The measured spectrum was used to improve the understanding of the structure of the material and this in combination with molecular modeling tools. First, different models are investigated in order to explain the band and the shoulder in the observed spectrum. The computational methodology used here are TDDFT calculations with a B3LYP functional and a PCM implicit solvent model. From a benchmark with only the linker, presented in **paper VII**, B3LYP was found to provide the best correspondence with experimental data while a double and triple zeta basis set provided similar results. Two global models are proposed for the COMOC-4 structure, a small model with two gallium ions and linkers and a large model with three metal centers and four linkers (Figure 3.25). Both these models provide the same main band at 310 nm as observed experimentally but the shoulder at 328 nm is not found. This shows that the models provided here do not contain every detail of the structure since they fail to represent all bands of the UV/Vis spectrum. Therefore several modifications on the structure are proposed that could explain the observations. A common occurrence at MOF synthesis is the coordination of solvent molecules to the metal nodes, since COMOC-4 is

synthesized in DMF the effect of DMF coordination on the excitation energies was analyzed. Another alternative is the coordination of a $\text{Ga}(\text{NO}_3)_3$ on the bipyridine center. Both of these alternatives do not represent the measurements. The third alternative is a cationic defect, this can be the consequence of a missing linker or a bridging $-\text{OH}$ group in the gallium chain. In the small model the cationic defect is represented by a missing $-\text{OH}$ group since removing a linker does not represent enough of the crystal structure. The results for the cationic model are shown in Figure 3.26. The missing $-\text{OH}$ group induces a red-shift of the main excitation towards 326 nm for both models (Figure 3.26), while the missing linker leads to a main band at 321 nm. Both of these defects could explain the shoulder at 328 nm. These cationic species could exist in the bulk of the framework but they are most likely an effect of termination at the particle surface. They are generated due to solvation with the suspending methanol.

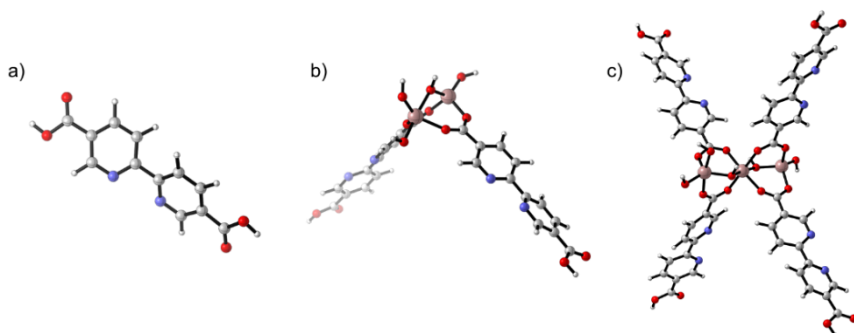


Figure 3.25. Models for COMOC-4, the linker reference (a), the small model where only two linkers are present and the metal chain consists of two Ga atoms (b), and the large model that consists of four linkers and three gallium atoms in the chain (c) Reprinted with permission from^[46]. Copyright 2015 American Chemical Society..

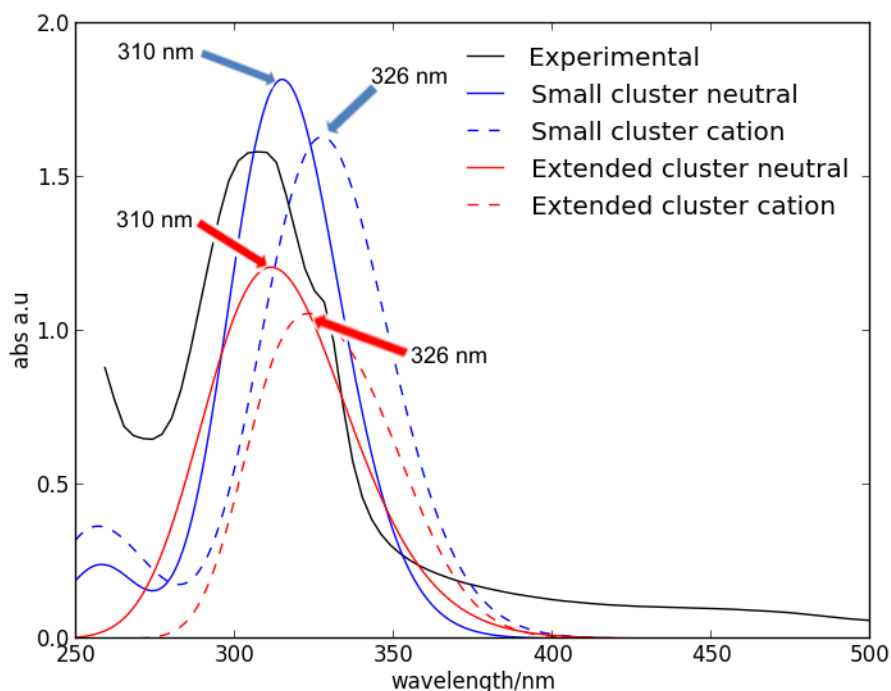


Figure 3.26. Overview of measured and calculated results for the neutral and cationic model. Reprinted with permission from^[46]. Copyright 2015 American Chemical Society.

From these results we can conclude the small model is sufficient to reproduce the measured UV/Vis spectra. By considering different models we are able to provide more detailed information on the fine structure of the material. The presence of cationic defects in the structures explains the observations in the UV/Vis spectrum.

Using COMOC-4 as a basis for a bimetallic MOF

The bipyridine moiety is an ideal chelating group to immobilize other metal centers that would be active for catalysis. The grafting of metal centers on the this moiety should not induce a change in the X-ray diffractogram. There can be some line broadening but the main reflections do not change, since not every site is modified and the modification is not periodic. When the aim is the design of a bimetallic MOF, UV/Vis data can be used as a characterization technique to identify the modification (**Paper VIII**). UV/Vis

measurements of the pristine linker and the linker coordinated with CuCl_2 in methanol solution shows a shift of the main absorption band to 317 nm and new bands at 334 nm and 420 nm. While similar changes are also observed in the spectrum of the modified MOF the band at 420 nm cannot be seen when measuring the material in methanol suspension. A solid state UV/Vis of the MOF does show a band at 460 nm. To verify whether these changes are indeed due to coordination of CuCl_2 on the bipyridine site, the UV/Vis spectrum was modeled to show if CuCl_2 coordination would indeed lead to the observed effects.

A static model is in many cases not sufficient for an accurate representation of the system, since the measured UV/Vis spectrum is dependent on conformational freedom of the molecule^[47, 48]. Therefore the complex was modeled with the aid of ab initio molecular dynamics techniques to capture the complete conformational freedom. From this simulation over time, 100 snapshots were taken and the excitation energies were calculated with TDDFT on the B3LYP/6-311+G(d) LOT. This allowed for the generation of a time-average spectrum (Figure 3.27). The results indeed showed the shift of the main band after coordination (315 nm) and the appearance of a shoulder at 338 nm which corresponds nicely to the experimental data. A band at 450 nm can also be attributed to the metal coordination. To verify whether these new absorption bands were indeed a consequence of the CuCl_2 coordination, the contribution of this moiety to the orbitals involved in the excitation were calculated (Figure 3.28). For the band at 338 nm and at 450 nm the orbitals contained a contribution of both the linker and the coordinated CuCl_2 , leading to the conclusion that these bands are indeed indicative for a successful incorporation.

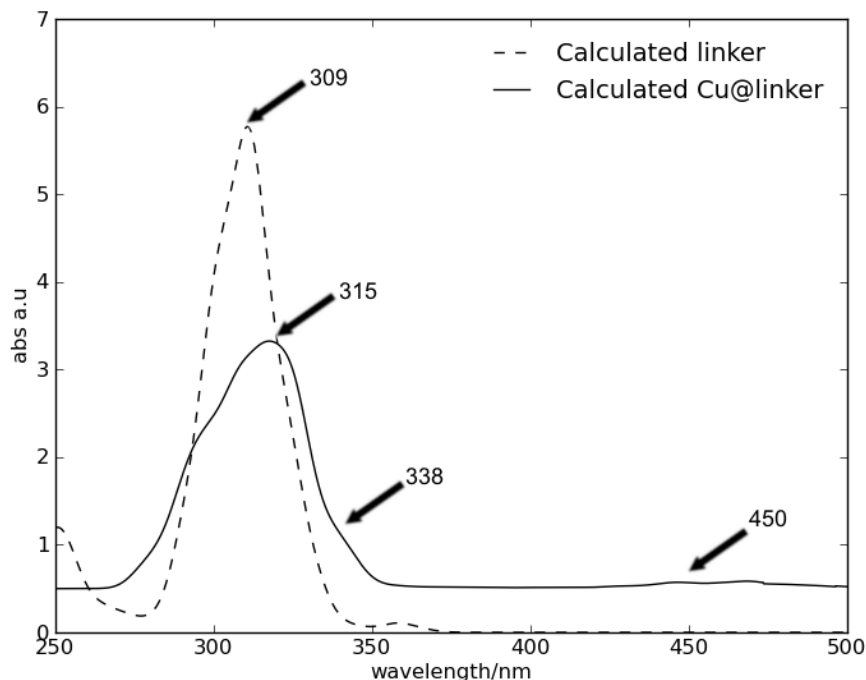


Figure 3.27. Calculated spectra of the linker and linker CuCl_2 chelated on the linker^[49]. Reprinted with permission from Wiley-VCH Verlag.

Immobilization of $\text{TiO}(\text{acac})_2$ on $\text{NH}_2\text{-MIL-47(V)}$, characterization via IR spectroscopy

In **paper IX** the modification of an $\text{NH}_2\text{-MIL-47(V)}$ MOF is reported in order to further improve its catalytic activity in the epoxidation of cyclohexene. Due to the complex IR spectrum, it is hard to characterize the material by this technique alone and additional methods are proposed such as MAS-NMR measurements. To assist in the interpretation of the spectra, a computational model was studied to verify the successful grafting. Since the modification only took place on the linker, a very limited model was proposed, considering amino-terephthalic acid as a representation for the pristine MOF and the grafted $\text{TiO}(\text{acac})_2$ complex as a modification. From a normal mode analysis the changes in the IR spectrum due to grafting can be deduced. The vibrations at 3494 and 3386 cm^{-1} , that are due to the NH_2 stretching vibrations, decrease. That decrease points towards the disappearance of this group and is an indication of a successful grafting

procedure. The presence of $\text{TiO}(\text{acac})_2$ is shown by the appearance of the C-C-H twisting at 735 cm^{-1} and C-CO-C wagging at 1026 cm^{-1} . These results indicate that even a relatively small model system can give valuable insights in the effect of modifications on the vibrational spectrum of the MOF. These case studies show that modeling may be used as an indispensable tool in the design of new catalytic materials.

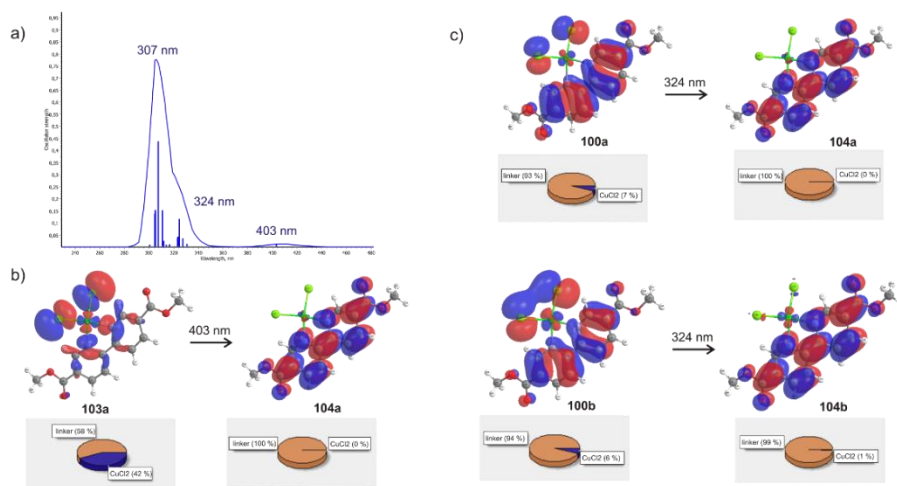


Figure 3.28. Contribution of grafted metal on the excitations calculated from a single snapshot that makes up the average spectrum^[49]. Reprinted with permission from Elsevier.

3.8 REFERENCES

- [1] Cavallo, L.; Jacobsen, H., Radical Intermediates in the Jacobsen – Katsuki Epoxidation. *Angewandte Chemie International Edition* **2000**, *39* (3), 589-592.
- [2] Linde, C.; Akermark, B.; Norrby, P. O.; Svensson, M., Timing is critical: Effect of spin changes on the diastereoselectivity in Mn(salen)-catalyzed epoxidation. *J. Am. Chem. Soc.* **1999**, *121* (21), 5083-5084.
- [3] Jacobsen, H.; Cavallo, L., Re-evaluation of the Mn(salen) mediated epoxidation of alkenes by means of the B3LYP* density functional. *Phys. Chem. Chem. Phys.* **2004**, *6* (13), 3747-3753.
- [4] Ivanic, J.; Collins, J. R.; Burt, S. K., Theoretical study of the low lying electronic states of oxoX(salen) (X = Mn, Mn-, Fe, and Cr-) complexes. *J. Phys. Chem. A* **2004**, *108* (12), 2314-2323.
- [5] Sears, J. S.; Sherrill, C. D., The electronic structure of oxo-Mn(salen): Single-reference and multireference approaches. *J. Chem. Phys.* **2006**, *124* (14), 144314.

- [6] Wouters, S.; Poelmans, W.; Ayers, P. W.; Van Neck, D., CheMPS2: A free open-source spin-adapted implementation of the density matrix renormalization group for ab initio quantum chemistry. *Computer Physics Communications* **2014**, *185* (6), 1501-1514.
- [7] Wouters, S.; Bogaerts, T.; Van der Voort, P.; Van Speybroeck, V.; Van Neck, D., DMRG-SCF study of the singlet, triplet, and quintet states of oxo-Mn(Salen). *J. Chem. Phys.* **2014**, *140* (24), 241103.
- [8] Handy, N. C.; Cohen, A. J., Left-right correlation energy. *Mol. Phys.* **2001**, *99* (5), 403-412.
- [9] Hoe, W.-M.; Cohen, A. J.; Handy, N. C., Assessment of a new local exchange functional OPTX. *Chemical Physics Letters* **2001**, *341* (3-4), 319-328.
- [10] Bogaerts, T.; Wouters, S.; Van Der Voort, P.; van Speybroeck, V., Mechanistic investigation on the oxygen transfer with the manganese-salen complex. *ChemCatChem* **2015**, *submitted*.
- [11] Fu, H.; Look, G. C.; Zhang, W.; Jacobsen, E. N.; Wong, C. H., Mechanistic study of a synthetically useful monooxygenase model using the hypersensitive probe trans-2-phenyl-1-vinylcyclopropane. *J. Org. Chem.* **1991**, *56* (23), 6497-6500.
- [12] Linde, C.; Arnold, M.; Norrby, P. O.; Akermark, B., Is there a radical intermediate in the (salen)Mn-catalyzed epoxidation of alkenes? *Angew. Chem.-Int. Edit. Engl.* **1997**, *36* (16), 1723-1725.
- [13] Linker, T., The Jacobsen-Katsuki epoxidation and its controversial mechanism. *Angew. Chem.-Int. Edit. Engl.* **1997**, *36* (19), 2060-2062.
- [14] Linde, C.; Koliai, N.; Norrby, P. O.; Akermark, B., Experimental evidence for multiple oxidation pathways in the (salen)Mn-catalyzed epoxidation of alkenes. *Chem.-Eur. J.* **2002**, *8* (11), 2568-2573.
- [15] Abashkin, Y. G.; Burt, S. K., (Salen)Mn-catalyzed epoxidation of alkenes: A two-zone process with different spin-state channels as suggested by DFT study. *Org. Lett.* **2004**, *6* (1), 59-62.
- [16] Jacobsen, H.; Cavallo, L., A Possible Mechanism for Enantioselectivity in the Chiral Epoxidation of Olefins with [Mn(salen)] Catalysts. *Chemistry – A European Journal* **2001**, *7* (4), 800-807.
- [17] Zhang, W.; Jacobsen, E. N., Asymmetric olefin epoxidation with sodium-hypochlorite catalyzed by easily prepared chiral Mn(III) salen complexes. *J. Org. Chem.* **1991**, *56* (7), 2296-2298.
- [18] Jacobsen, E. N.; Zhang, W.; Muci, A. R.; Ecker, J. R.; Deng, L., Highly enantioselective epoxidation catalysts derived from 1,2-diaminocyclohexane. *J. Am. Chem. Soc.* **1991**, *113* (18), 7063-7064.
- [19] Bogaerts, T.; Wouters, S.; Van Der Voort, P.; van Speybroeck, V., The enantioselectivity of the manganese-salen complex in the epoxidation of unfunctionalized olefins and the influence of grafting. *J. Mol. Catal. A: Chem* **2015**, *in Press*.
- [20] Angelino, M. D.; Laibinis, P. E., Polymer-supported salen complexes for heterogeneous asymmetric synthesis: Stability and selectivity. *Journal of Polymer Science Part A: Polymer Chemistry* **1999**, *37* (21), 3888-3898.
- [21] Canali, L.; Sherrington, D. C.; Deleuze, H., Synthesis of resins with pendently-bound chiral manganese-salen complexes and use as

- heterogeneous asymmetric alkene epoxidation catalysts. *React. Funct. Polym.* **1999**, *40* (2), 155-168.
- [22] Ji, R. N.; Yu, K.; Lou, L. L.; Gu, Z. C.; Liu, S. X., Mesoporous Silica Supported Unsymmetric Chiral Mn(III) Salen Complex: Synthesis, Characterization and Effect of Pore Size on Catalytic Performance. *J. Inorg. Organomet. Polym. Mater.* **2010**, *20* (4), 675-683.
- [23] Roy, T.; Kureshy, R. I.; Khan, N.; Abdi, S. H. R.; Sadhukhan, A.; Bajaj, H. C., Immobilized dimeric chiral Mn(III) salen complex on short channel ordered mesoporous silica as an effective catalyst for the epoxidation of non-functionalized alkenes. *Tetrahedron* **2012**, *68* (31), 6314-6322.
- [24] Wei, S. L.; Tang, Y. H.; Zhao, R. Q.; Xu, G. J.; Zheng, Y. S., Monodisperse crosslinked pHEMA particle-supported chiral Mn(III)salen catalyst for asymmetric epoxidation of olefin. *Appl. Organomet. Chem.* **2012**, *26* (3), 114-120.
- [25] Das, P.; Silva, A. R.; Carvalho, A. P.; Pires, J.; Freire, C., Enantioselective Epoxidation of Alkenes by Jacobsen Catalyst Anchored onto Aminopropyl-functionalised Laponite, MCM-41 and FSM-16. *Catal. Lett.* **2009**, *129* (3-4), 367-375.
- [26] Ferey, G.; Mellot-Draznieks, C.; Serre, C.; Millange, F.; Dutour, J.; Surble, S.; Margiolaki, I., A chromium terephthalate-based solid with unusually large pore volumes and surface area. *Science* **2005**, *309* (5743), 2040-2042.
- [27] Goesten, M. G.; Sai Sankar Gupta, K. B.; Ramos-Fernandez, E. V.; Khajavi, H.; Gascon, J.; Kapteijn, F., Chloromethylation as a functionalisation pathway for metal-organic frameworks. *CrystEngComm* **2012**, *14* (12), 4109-4111.
- [28] Angelino, M. D.; Laibinis, P. E., Synthesis and Characterization of a Polymer-Supported Salen Ligand for Enantioselective Epoxidation. *Macromolecules* **1998**, *31* (22), 7581-7587.
- [29] De Decker, J.; Bogaerts, T.; Muylaert, I.; Delahaye, S.; Lynen, F.; Van Speybroeck, V.; Verberckmoes, A.; Van der Voort, P., Covalent immobilization of the Jacobsen catalyst on mesoporous phenolic polymer: A highly enantioselective and stable asymmetric epoxidation catalyst. *Mater. Chem. Phys.* **2013**, *141* (2-3), 967-972.
- [30] El-Bahraoui, J.; Wiest, O.; Feichtinger, D.; Plattner, D. A., Rate Enhancement and Enantioselectivity of the Jacobsen-Katsuki Epoxidation: The Significance of the Sixth Coordination Site. *Angewandte Chemie International Edition* **2001**, *40* (11), 2073-2076.
- [31] Hartmann, M.; Fischer, M., Amino-functionalized basic catalysts with MIL-101 structure. *Microporous Mesoporous Mat.* **2012**, *164*, 38-43.
- [32] Bogaerts, T.; Van Yperen-De Deyne, A.; Liu, Y.-Y.; Lynen, F.; Van Speybroeck, V.; Van Der Voort, P., Mn-salen@MIL101(Al): a heterogeneous, enantioselective catalyst synthesized using a 'bottle around the ship' approach. *Chem. Commun.* **2013**, *49* (73), 8021-8023.
- [33] Rietveld, H., A profile refinement method for nuclear and magnetic structures. *Journal of Applied Crystallography* **1969**, *2* (2), 65-71.

- [34] Harris, K. D. M.; Tremayne, M., Crystal Structure Determination from Powder Diffraction Data. *Chemistry of Materials* **1996**, *8* (11), 2554-2570.
- [35] McCusker, L. B.; Von Dreele, R. B.; Cox, D. E.; Louer, D.; Scardi, P., Rietveld refinement guidelines. *Journal of Applied Crystallography* **1999**, *32* (1), 36-50.
- [36] David, W. I. F.; Shankland, K.; McCusker, L. B.; Bärlocher, C., *Structure Determination from Powder Diffraction Data*. OUP Oxford: 2006.
- [37] Kresse, G.; Joubert, D., From ultrasoft pseudopotentials to the projector augmented-wave method. *Phys. Rev. B* **1999**, *59* (3), 1758-1775.
- [38] Kresse, G.; Furthmüller, J., Efficient iterative schemes for ab initio total-energy calculations using a plane-wave basis set. *Phys. Rev. B* **1996**, *54* (16), 11169-11186.
- [39] Kresse, G.; Hafner, J., Ab initio molecular dynamics for liquid metals. *Phys. Rev. B* **1993**, *47* (1), 558-561.
- [40] Blöchl, P. E., Projector augmented-wave method. *Phys. Rev. B* **1994**, *50* (24), 17953-17979.
- [41] Perdew, J. P.; Burke, K.; Ernzerhof, M., Generalized gradient approximation made simple. *Phys. Rev. Lett.* **1996**, *77* (18), 3865-3868.
- [42] Vanpoucke, D. E. P.; Jaeken, J. W.; De Baerdemacker, S.; Lejaeghere, K.; Van Speybroeck, V., Quasi-1D physics in metal-organic frameworks: MIL-47(V) from first principles. *Beilstein Journal of Nanotechnology* **2014**, *5*, 1738-1748.
- [43] Solomon, E. I.; Scott, R. A.; King, R. B., *Computational Inorganic and Bioinorganic Chemistry*. Wiley: 2013.
- [44] He, L.; Liu, F.; Hautier, G.; Oliveira, M. J. T.; Marques, M. A. L.; Vila, F. D.; Rehr, J. J.; Rignanese, G. M.; Zhou, A., Accuracy of generalized gradient approximation functionals for density-functional perturbation theory calculations. *Phys. Rev. B* **2014**, *89* (6), 064305.
- [45] Barthelet, K.; Marrot, J.; Riou, D.; Férey, G., A Breathing Hybrid Organic–Inorganic Solid with Very Large Pores and High Magnetic Characteristics. *Angewandte Chemie International Edition* **2002**, *41* (2), 281-284.
- [46] Liu, Y.-Y.; Decadt, R.; Bogaerts, T.; Hemelsoet, K.; Kaczmarek, A. M.; Poelman, D.; Waroquier, M.; Van Speybroeck, V.; Van Deun, R.; Van Der Voort, P., Bipyridine-Based Nanosized Metal–Organic Framework with Tunable Luminescence by a Postmodification with Eu(III): An Experimental and Theoretical Study. *The Journal of Physical Chemistry C* **2013**, *117* (21), 11302-11310.
- [47] De Meyer, T.; Hemelsoet, K.; Van der Schueren, L.; Pauwels, E.; De Clerck, K.; Van Speybroeck, V., Investigating the Halochromic Properties of Azo Dyes in an Aqueous Environment by Using a Combined Experimental and Theoretical Approach. *Chemistry – A European Journal* **2012**, *18* (26), 8120-8129.
- [48] Barone, V.; Bloino, J.; Monti, S.; Pedone, A.; Prampolini, G., Theoretical multilevel approach for studying the photophysical properties of organic dyes in solution. *Phys. Chem. Chem. Phys.* **2010**, *12* (35), 10550-10561.

- [49] Liu, Y.-Y.; Leus, K.; Bogaerts, T.; Hemelsoet, K.; Bruneel, E.; Van Speybroeck, V.; Van Der Voort, P., Bimetallic–Organic Framework as a Zero-Leaching Catalyst in the Aerobic Oxidation of Cyclohexene. *ChemCatChem* **2013**, *5* (12), 3657-3664.

CHAPTER 4. CONCLUSIONS AND PERSPECTIVES

In the last decades computational chemistry has made a huge progress as a tool in the research on heterogeneous catalysis. In many cases molecular modeling is used to understand the behavior of existing catalysts by unraveling the reaction mechanism, temperature dependence, the selectivity etc. Understanding of the reaction mechanism at the nanoscale gives invaluable insight into the overall process and behavior of the catalyst. Ideally, molecular modeling can go one step further and might also assist in designing and optimizing new or existing materials. In this thesis, molecular modeling was used in the design process of new heterogeneous material for the enantioselective epoxidation of unfunctionalized olefins.

The reaction under investigation has attracted the attention of many researchers in the field of homogeneous catalysis. The chiral Mn-salen complex, and more specifically the Jacobsen variant of this complex, has been found to be very performant for the reaction under investigation. In this thesis, various procedures were exploited to find a heterogeneous equivalent of this catalyst. The most straight-forward approach for the design of a heterogeneous analogue for this catalyst is the immobilization of salen type complexes on solid supports. Metal organic frameworks were chosen as a carrier material. Since the selectivity is crucial for this type of reactions we must propose a heterogenation procedure that allows to maintain the selectivity of the original complex. In order to obtain the same high selectivity as the homogeneous catalyst, the underlying mechanism has to be thoroughly understood. As a first step the mechanism for oxygen transfer from the oxidant to the olefin has to be clarified. With that

knowledge the selectivity may be modelled and the influence of the immobilization procedure can be assessed. From earlier computational work on the salen catalyst it became clear that the obtained results were highly dependent on the used electronic structure method as the system can have various spin states and is very sensitive to the way electron correlation is accounted for.

As the final system to be studied is quite large, preference goes to computationally efficient methods such as density functional theory methods. Therefore we first assessed the viability of various DFT functionals to model the salen complex accurately. The results of this work were taken up in **Paper I** and **II**. Using DMRG-SCF calculations, an accurate description of the electronic structure of a salen-type complex can be provided. However, due to the large system size this high-level method cannot be applied for the modelling of the mechanism and selectivity. A good functional was selected by comparing the relative energies of the different spin states obtained from DMRG-SCF calculations with a variety of DFT based methods. From this theoretical benchmark study on the Mn-salen complex, OPBE could be identified as a good method to model the behavior of the catalyst. The study also showed that some of the commonly used, very popular functionals like B3LYP or M06-2X, gave inaccurate results for this specific system. Especially when studying transition metal complexes, great care has to be taken with the choosing of a proper electronic structure method. In cases where no good benchmark studies are available from literature, a thorough investigation of the various electronic structure methods should be conducted to validate their accuracy for the description of the system at hand.

The mechanism of olefin epoxidation with the salen complex has been a topic of much debate in the literature. While some studies pointed to the existence of a radical intermediate, experiments with ‘radical probes’ seemed to imply other mechanisms. In **Paper II** the mechanism of oxygen transfer was re-evaluated and some interesting conclusions could be drawn. From a test with ethene as a simplified model for the substrate, the existence of intermediates other than the radical was shown to be unlikely. At first sight, these results seem contradictory to the radical probe

experiments and therefore additional mechanistic calculations were performed taking into account the full catalyst and the full radical probe as substrate. These results showed that the existence of the radical intermediate could also explain the experimental observations. The barrier for the closing of the epoxide ring was similar to the barrier for ring opening of the radical probe. This was in contradiction with the intuitive hypothesis that the high ring strain in the probe would ‘capture’ all radical intermediates via ring opening. It can be concluded that a radical intermediate mechanism is the only possible candidate as a route for the epoxide formation.

Starting from the knowledge on the mechanism, further computational studies were performed to understand the nanoscale origin of the selectivity. To achieve that we focused on the formation of the first C-O bond, that is determining the selectivity. The aim of this study was the elucidation on how different immobilization procedures will influence the selectivity and which procedures may be followed to maintain the selective behavior of the original complex in homogeneous conditions. In **Paper III** and **Paper IV** the method to model the selectivity was proposed and the influence of immobilization was clarified. The computational study allowed to assess the importance of certain substituents on the salicylaldehyde wings of the ligand. Especially the bulky *tert*-butyl groups on C3/C3' positions were shown to be of paramount importance to control the selectivity of the catalyst. Immobilization procedures that change these substituents for less bulky ones lead to a smaller energy difference between the approaches for different enantiomers. It can thus be concluded that a heterogenation procedure with a minimal interaction between the host material and the active site is required to preserve the high selectivity of the original catalyst.

In **Paper III**, **Paper IV** and **Paper V** three immobilization methods for the salen catalyst were proposed. We compared a ‘classical’ immobilization method, where the active site is covalently grafted on a MIL-101(Cr) MOF to the immobilization by connecting the complex on via the sixth coordination site and a ship-in-a-bottle catalyst. The experiments confirm the insights obtained from the mechanistic modeling study. In the covalent

grafting procedure the bulky substituents on the salen complex were omitted in one side to include an anchoring point and this led to a decrease in the selectivity. However, the other grafting procedures maintained the selectivity, since the ligand was left unchanged. The activity of the catalyst was also found to vary with the applied grafting procedure. It was observed that the ship-in-a-bottle approach showed a minimal decrease in activity while maintaining the selectivity as it has the least interaction with its carrier material.

In a next step we showed that experimental diffractograms can also be used to verify the geometric and electronic structure obtained from *ab initio* calculations (**Paper VI**). Structure determination of complex flexible materials such as MOFs is often very challenging also from a computational point of view. In many cases various plausible geometries may be proposed which are close in energy. In this thesis a new approach was introduced which uses experimental XRD diffractograms to assess which structure obtained from theory would be most plausible. This can be done in several ways, a qualitative comparison is very easy and can already provide much information. In the case study of MIL-47(V) this approach allowed to distinguish between structures that possessed an energy difference of barely 50 meV. With a quantitative approach the distinction between geometries with subtle structural differences, induced by different electronic structures (ferromagnetic or antiferromagnetic), could be made.

While the first part of this work was focused on the complete design of a heterogeneous catalyst starting from computational results, the computer aided design of nanoporous materials can be done on a significantly smaller scale as well. In **Paper VII** and **Paper VIII** the use of computational models to assist in the interpretation of UV/VIS spectra has been proposed. While in **Paper IX** a similar exercise is done for infrared spectra. Especially the study of the electronic spectra has proven interesting to unravel the fine structure of MOFs. Bands that were not resulting from the pristine material could be attributed to cationic defects in the structure of a gallium-bipyridine MOF. Moreover the effects on the UV/Vis spectrum of CuCl_2 coordinated in the bipyridine moiety could also be calculated allowing to use this technique to identify a successful coordination.

Since computational speed increases continuously and more efficient computational algorithms have become available, larger and more complex systems can be modelled from a theoretical point of view. In this thesis, systems were modelled for which the electronic structure determination was very challenging. Very accurate wavefunction based methods such as CASSCF and fullCI can still not be applied to the full catalytic systems under investigation. However within the framework of this work very high level DMRG-SCF calculations were performed on quite large systems. It may be anticipated that in the future modeling of even larger systems and systems of higher complexity will become within reach.

There are two important points that have been omitted in this work. Firstly the full structure of the solid material was not consistently taken into account in the calculations. In cases where the host was included, it had to be simplified to a large extent or a very low level of theory had to be adopted. Secondly, experiments were conducted in the liquid phase but it was impossible to take this liquid into account from a computational point of view. For the work on the modelling of UV/Vis spectroscopy presented in this thesis a simplified PCM continuum solvent model was proposed to capture some of the molecular environment. However it should be kept in mind that this approach fails in modeling explicit interactions with solvent molecules. Nowadays more advanced models are available to model the solvent environment such as embedding the system in a solvent box and applying molecular dynamics techniques. However for the chiral salen complex, such methodologies were computationally too expensive. Despite these apparent shortcomings, the calculation of free energy profiles provide much insight that can be applied in the design of advanced heterogeneous catalysts.

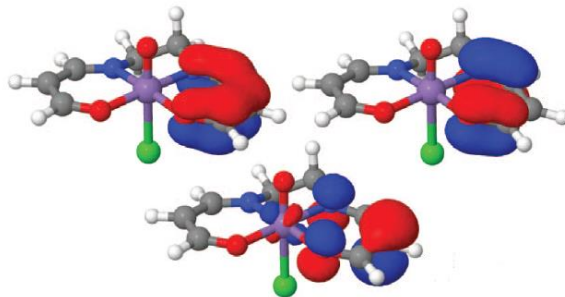
Furthermore, it was shown in this work that metal organic frameworks are an interesting choice for heterogenizing homogeneous catalysts. The high chemical versatility allows to use different approaches and choose the material that has the most optimal properties for the process at hand. For practical applications we must acknowledge that MOF materials are relatively expensive to produce but in high-tech applications where very specific properties are required that are provided by the material this is not

an issue. Some nice features of MOFs are highlighted in this work, especially their light and open structure which allows much freedom around the active site to preserve the activity and selectivity as much as possible.

In general we can conclude that a close interaction between theoretical research and experimental synthesis of novel materials can be extremely advantageous. A computational study may help tailor a strategy for the design of a heterogeneous catalyst. The mechanism of a reaction can be understood even before the material has been synthesized. This allows for a targeted design of a novel catalyst. The computations can also assist during the synthesis phase, in the characterization of the material. Indeed, various spectroscopic techniques are used in the synthesis and testing of materials, but the interpretation of the spectra at the molecular level is sometimes far from trivial. In this thesis we have also shown by means of selected examples that theory may also assist in helping the characterization of materials and interpretation of experimentally obtained spectra. Overall, in the design of novel catalytic materials, theory and experiment can strengthen each other to a large extent.

Part II: Published papers

PAPER I: COMMUNICATION: DMRG-SCF STUDY OF THE SINGLET, TRIPLET, AND QUINTET STATES OF OXO-MN(SALEN)



S. Wouters, T. Bogaerts, P. Van der Voort, V. Van Speybroeck, D. Van Neck, *Journal of Chemical Physics*, 140, 241103, **2014**.

T. Bogaerts assisted in the analysis of the results

Reprinted with permission from AIP Publishing LLC. © 2015, AIP Publishing LLC.

Communication: DMRG-SCF study of the singlet, triplet, and quintet states of oxo-Mn(Salen)

Sebastian Wouters,^{1,a)} Thomas Bogaerts,^{1,2} Pascal Van Der Voort,²
 Veronique Van Speybroeck,¹ and Dimitri Van Neck¹

¹Center for Molecular Modelling, Ghent University, Technologiepark 903, 9052 Zwijnaarde, Belgium

²Center for Ordered Materials, Organometallics and Catalysis, Ghent University, Krijgslaan 281 (S3), 9000 Gent, Belgium

(Received 26 May 2014; accepted 18 June 2014; published online 30 June 2014)

We use CHEMPS2, our free open-source spin-adapted implementation of the density matrix renormalization group (DMRG) [S. Wouters, W. Poelmans, P. W. Ayers, and D. Van Neck, *Comput. Phys. Commun.* **185**, 1501 (2014)], to study the lowest singlet, triplet, and quintet states of the oxo-Mn(Salen) complex. We describe how an initial approximate DMRG calculation in a large active space around the Fermi level can be used to obtain a good set of starting orbitals for subsequent complete-active-space or DMRG self-consistent field calculations. This procedure mitigates the need for a localization procedure, followed by a manual selection of the active space. Per multiplicity, the same active space of 28 electrons in 22 orbitals (28e, 22o) is obtained with the 6-31G*, cc-pVDZ, and ANO-RCC-VDZP basis sets (the latter with DKH2 scalar relativistic corrections). Our calculations provide new insight into the electronic structure of the quintet. © 2014 AIP Publishing LLC. [<http://dx.doi.org/10.1063/1.4885815>]

The manganese-salen complex is a high-yield catalyst for the enantioselective epoxidation of unfunctionalized olefins.^{1–4} Many density functional theory^{5–10} and *ab initio*^{11–13} studies have tried to gain insight into its electronic structure and the energy barriers for possible reaction paths. A longstanding question in these studies is the relative stability of the singlet, triplet, and quintet states of the oxo-Mn(Salen) intermediate. This question has recently been addressed in several *ab initio* multireference (MR) studies,^{14–16} using the model in Fig. 1. The singlet and triplet were found to be nearly degenerate, and about 40 kcal/mol more stable than the quintet. The latter is well described by a single determinant, while the former two have outspoken MR character.

Only the singlet geometry can be optimized at the complete active space self-consistent field (CASSCF) level.¹⁴ The triplet and quintet states are unstable with respect to dissociation into an oxygen atom (triplet) and the Mn(Salen) complex (quintet). This dissociation is spin-forbidden for the singlet. The CASSCF(10e, 10o)/6-31G* optimized singlet geometry from Ivanic *et al.*¹⁴ was therefore used here, as in the previous MR studies.

The relative stability of the singlet and triplet states is still under debate. Several MR studies have been performed in different active spaces, with various basis sets, and with or without the inclusion of dynamic correlation and relativistic effects.^{14–16} The importance of relativistic effects for the relative energies has been estimated both with an effective core potential¹⁴ and with the perturbational Cowan-Griffin operator,¹⁵ and was found to be smaller than 0.2 kcal/mol. The effect of dynamic correlation has been assessed by applying MR perturbation theory on top of the CASSCF

wavefunction.^{14,16} The corresponding variations in relative energy were about 5 kcal/mol, and can therefore not be neglected. The basis set choice shifted relative CASSCF energies by as much as 1.3 kcal/mol.¹⁵

In this work, we attempt to settle the debate on the active space selection for the geometry of Ref. 14 with C₁ symmetry (see Figs. 3 and 4). Three double zeta basis sets with polarization functions are used in this work. The 6-31G* basis,¹⁷ also used in previous MR studies,^{14,15} yields 273 (cartesian) orbitals. The cc-pVDZ basis¹⁸ has [6s5p3d1f] basis functions for Mn, and yields 293 (spherical) orbitals. And the ANO-RCC-VDZP basis¹⁹ with DKH2 scalar relativistic corrections²⁰ (ANODZ), also used in Ref. 16, yields 284 (spherical) orbitals. Restricted Hartree-Fock molecular orbitals were obtained with Ps14²¹ for the 6-31G* and cc-pVDZ basis sets and with MOLPRO²² for ANODZ.

We now briefly describe the level of theory used in this work. For a more thorough discussion, we refer the reader to Refs. 23 and 24. The exact wavefunction in an active space of L orbitals

$$|\Psi\rangle = \sum_{\{n_{\mu}\}} C^{n_1 n_2 \dots n_L} (\hat{a}_{1\uparrow}^\dagger)^{n_{1\uparrow}} (\hat{a}_{1\downarrow}^\dagger)^{n_{1\downarrow}} (\hat{a}_{2\uparrow}^\dagger)^{n_{2\uparrow}} \dots (\hat{a}_{L\downarrow}^\dagger)^{n_{L\downarrow}} |-\rangle, \quad (1)$$

grows exponentially fast (as 4^L). One way to make computations tractable is by means of the density matrix renormalization group (DMRG),^{23–25} This method approximates the C-tensor of Eq. (1) by a matrix product state (MPS):

$$C^{n_1 n_2 \dots n_L} = \sum_{\{\mu_i\}} A[1]_{\mu_1}^{n_1} A[2]_{\mu_2}^{n_2} A[3]_{\mu_3}^{n_3} \dots A[L]_{\mu_L}^{n_L}. \quad (2)$$

^{a)}Electronic mail: sebastianwouters@gmail.com

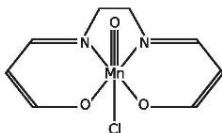


FIG. 1. Model for the oxo-Mn(Salen) complex.

The indices α_k are called the *bond* or *virtual* indices. They have to grow exponentially towards the middle of the MPS chain to represent a general C -tensor. The exponential complexity is removed when their rank is truncated to a fixed virtual dimension D : $\dim(\alpha_k) = \min(4^k, 4^{L-k}, D)$. By properly exploiting the gauge freedom of the MPS ansatz,²⁴ the simultaneous optimization of two neighbouring MPS site tensors can always be written as a numerically stable standard Hermitian eigenvalue problem. The DMRG algorithm sweeps back and forth through the chain, while locally optimizing the MPS site tensors, until energy and/or wavefunction convergence is reached.^{23,24}

The so-called discarded weight is a nonnegative measure which indicates the aptitude of a matrix product state to represent the exact solution.^{23,24} Both the variational energy and the discarded weight decrease with increasing virtual dimension. A linear extrapolation between both allows to estimate the exact ground state energy,^{23,24,34} see Fig. 2.

To reduce the computational cost, as well as to be able to tackle different symmetry sectors separately, symmetry-adapted MPSs are often used.^{24,32} CHEMPS2, our free open-source spin-adapted implementation of DMRG,^{24,35} exploits SU(2) spin symmetry, U(1) particle-number symmetry, and the abelian point groups with real-valued character tables.³⁶ We can therefore calculate the lowest singlet, triplet, and quintet states of the oxo-Mn(Salen) complex as three ground-state calculations in different symmetry sectors.

In methods which use a full-configuration-interaction (FCI) solver, this solver can be replaced by DMRG. DMRG

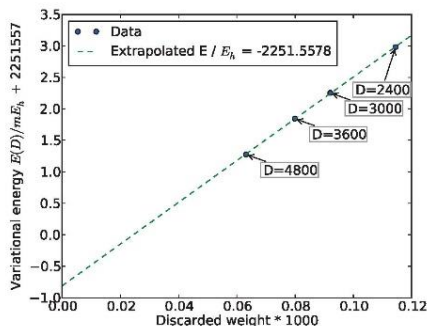


FIG. 2. Energy extrapolation for the converged (28e, 22o) active space of the triplet in the 6-31G* basis. D denotes the number of *reduced* virtual basis states.

allows for an efficient extraction of the reduced two-body density matrix (2-RDM).^{37,38} The 2-RDM of the active space is required in the CASSCF method to compute the gradient and the Hessian with respect to orbital rotations.³⁹ It is therefore natural to introduce a CASSCF variant with DMRG as active space solver, called DMRG-SCF,^{38,40,41} which allows to treat static correlation in large active spaces. In CHEMPS2, we have implemented the augmented Hessian Newton-Raphson DMRG-SCF method, with exact Hessian.^{24,39}

DMRG is an ideal candidate to study the electronic structure of transition metal systems, as they typically have large active spaces. Reiher and coworkers realized this capability of DMRG, and identified Cr_2 and $[\text{Cu}_2\text{O}_2]^{2+}$ as interesting cases.^{28,42,43} Yanai and coworkers were eventually able to fully resolve their potential energy surfaces.^{30,44,45} This has triggered many interesting DMRG studies of transition metal systems.^{32,46-50}

For CASSCF calculations, an initial active space is required. It is often constructed by localizing the occupied and virtual molecular orbitals separately, and by manually selecting an interesting subset.^{14,15} However, this subset can be biased, and might converge to a local minimum. Conversely, orbitals with occupation numbers far from empty of filled, lie close to the Fermi level.⁵¹ To bypass the localization procedure and the manual selection of the active space, we have performed approximate DMRG calculations for the singlet in a large window around the Fermi level (with $D_{\text{SU}(2)} = 2000$ the *reduced* virtual dimension). The window was chosen based on the shapes of the molecular orbitals: it should include at least (in rotated form) the active space of Ref. 16. For the basis sets 6-31G*, cc-pVDZ, and ANODZ, the active space window had the size (50e, 40o); (50e, 44o); and (56e, 45o), respectively. From the approximate DMRG calculation, the natural orbitals with occupation number (NOON) in the range 0.015–1.985 were kept, and used for the subsequent DMRG-SCF singlet calculations (with $D_{\text{SU}(2)} = 3000$). Remarkably, with the three basis sets the same (28e, 22o) active space was retrieved. When the 2-norm of the gradient was smaller than 10^{-4} , the DMRG-SCF calculations were branched to calculate the triplet and quintet as well. After convergence of the active spaces, a larger DMRG calculation with $D_{\text{SU}(2)} = 4800$ was performed to extrapolate the variational energies to the exact result, see Fig. 2. For the DMRG calculations, the natural orbitals were used, and they were ordered according to the NOON.⁵²

The converged (28e, 22o) singlet active space in the ANODZ basis is shown in Fig. 3. The same (28e, 22o) singlet active space is found with the 6-31G* and cc-pVDZ basis sets. The (18e, 17o) active space of Ref. 16 is augmented in Fig. 3 with two extra π -orbitals for the conjugated system, so that the active space now contains a π -orbital per participating atom. In addition, the nonbonding $3d_{x^2-y^2}$ orbital of Mn interacts with the in-plane π -orbitals of the oxygen and nitrogen atoms of the Salen ligand, further augmenting the active space with three extra orbitals. The NOON are listed in Table I. The triplet has the same natural orbitals as the singlet, and can roughly be interpreted as the electron excitation $3d_{x^2-y^2} \rightarrow \pi_1^*(O_{ax})$ from the singlet, as noted by Ref. 14. In the quintet, the $\pi_2(C)$, $\pi_4(C)$, and $\pi_6(C)$ orbitals are rotated

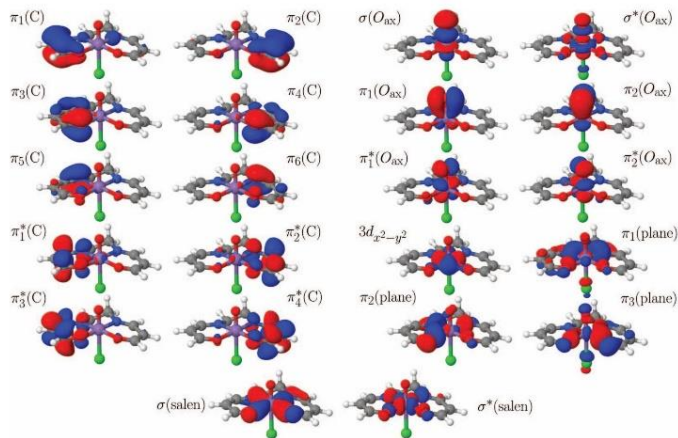


FIG. 3. Natural orbitals of the converged (28e, 22o) singlet active space in the ANODZ basis. The same natural orbitals were found with the 6-31G* and cc-pVDZ basis sets.

into new natural orbitals, which are shown in Fig. 4 together with their NOON. The same rotated quintet natural orbitals are found with the 6-31G* and cc-pVDZ basis sets. The quintet can hence be interpreted as the additional electron excitation $\pi(C) \rightarrow \pi_2^*(O_{ax})$ from the triplet. The electronic structure of the quintet differs from previous studies,^{14,15} where it was identified as the electron excitation $\pi_2(O_{ax}) \rightarrow \pi_2^*(O_{ax})$ from the triplet.

Our study found a different electronic structure for the quintet due to the larger active space for the conjugated system. References 14 and 15 only considered two bonding and two antibonding orbitals for the conjugated system, i.e., four π -orbitals instead of the ten π -orbitals in our study. (Reference 16 did not study the quintet.) In the quintet, the NOON of all five π -orbitals on the right wing of the structure

deviate significantly compared to the singlet and triplet, see Table I and Fig. 4. It is hence crucial for the description of the electronic structure of the quintet to incorporate these five π -orbitals in the active space. To have an equilibrated description, the corresponding orbitals on the left wing should also be included, requiring a total of ten π -orbitals. In hindsight, the inclusion of the three in-plane $\pi_{1,2,3}(\text{plane})$ orbitals was not necessary, given the NOON in Table I.

In the simplified single determinant picture based on Table I, in which the quintet ground state corresponds to,

$$[[\pi(C)]^\uparrow [\pi_2(O_{ax})]^\uparrow [3d_{x^2-y^2}]^\uparrow [\pi_1^*(O_{ax})]^\uparrow [\pi_2^*(O_{ax})]^\uparrow], \quad (3)$$

we can interpret the quintet from Refs. 14 and 15,

$$[[\pi(C)]^\uparrow [\pi_2(O_{ax})]^\uparrow [3d_{x^2-y^2}]^\uparrow [\pi_1^*(O_{ax})]^\uparrow [\pi_2^*(O_{ax})]^\uparrow], \quad (4)$$

as the single electron excitation $\pi_2(O_{ax}) \rightarrow \pi(C)$ from the quintet ground state determinant (3). The reason why Refs. 14 and 15 found a different quintet ground state

TABLE I. NOON of the converged (28e, 22o) singlet (1A), triplet (3A), and quintet (5A) active spaces in the ANODZ basis. The natural orbitals $\pi_2(C)$, $\pi_4(C)$, and $\pi_6(C)$ are rotated for the quintet; they are given in Fig. 4. The singlet-triplet and triplet-quintet transitions correspond to, respectively, the $3d_{x^2-y^2} \rightarrow \pi_1^*(O_{ax})$ and $\pi(C) \rightarrow \pi_2^*(O_{ax})$ electron excitations (NOON in boldface).

	1A	3A	5A		1A	3A	5A
$\pi_1(C)$	1.99	1.99	1.99	$\sigma(O_{ax})$	1.91	1.90	1.89
$\pi_2(C)$	1.99	1.99	...	$\sigma^*(O_{ax})$	0.11	0.11	0.12
$\pi_3(C)$	1.96	1.96	1.96	$\pi_1(O_{ax})$	1.86	1.77	1.94
$\pi_4(C)$	1.96	1.96	...	$\pi_2(O_{ax})$	1.85	1.95	1.94
$\pi_5(C)$	1.94	1.94	1.94	$\pi_1^*(O_{ax})$	0.17	1.04	1.05
$\pi_6(C)$	1.94	1.94	...	$\pi_2^*(O_{ax})$	0.17	0.24	1.04
$\pi_1^*(C)$	0.07	0.07	0.07	$3d_{x^2-y^2}$	1.97	1.00	1.00
$\pi_2^*(C)$	0.07	0.07	0.11	$\pi_1(\text{plane})$	1.99	1.99	1.99
$\pi_3^*(C)$	0.03	0.03	0.03	$\pi_2(\text{plane})$	1.98	1.98	1.99
$\pi_4^*(C)$	0.03	0.03	0.06	$\pi_3(\text{plane})$	1.98	1.98	1.99
$\sigma(\text{salen})$	1.95	1.93	1.98	$\sigma^*(\text{salen})$	0.08	0.10	0.07

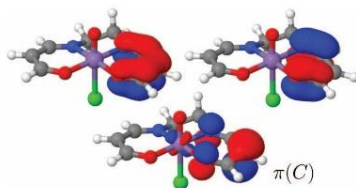


FIG. 4. The three natural orbitals of the converged (28e, 22o) quintet active space in the ANODZ basis, which are not present in Fig. 3. NOON(top left) = 1.93; NOON(top right) = 1.89; and **NOON**($\pi(C)$) = **1.01**. The same natural orbitals were found with the 6-31G* and cc-pVDZ basis sets. The triplet-quintet transition corresponds to the $\pi(C) \rightarrow \pi_2^*(O_{ax})$ electron excitation (NOON in boldface).

TABLE II. Absolute energies in Hartree and relative energies in kcal/mol; obtained by extrapolating the DMRG-SCF(28e, 22o) energies with discarded weight. In square brackets the CASSCF(12e, 11o)/6-31G* and GASSCF(18e, 17o)/ANODZ results from Refs. 15 and 16 are given for comparison.

	6-31G*	cc-pVDZ	ANODZ
E(¹ A)	-2251.5498	-2251.7509	-2261.0226
E(³ A)	-2251.5578	-2251.7593	-2261.0290
E(⁵ A)	-2251.5268	-2251.7316	-2260.9994
E(³ A) - E(¹ A)	-5.0 [0.3]	-5.3	-4.0 [-3.6]
E(⁵ A) - E(¹ A)	14.5 [42.9]	12.1	14.5

determinant can then be recast to: (a part of) the $\pi(C)$ orbital was explicitly kept doubly occupied.

The energies for the different multiplicities and basis sets are given in Table II. The energies are consistent for the three basis sets studied. The triplet has the lowest energy. The quintet lies only 12–14 kcal/mol above the singlet, much lower than what was observed in a smaller active space.^{14,15} Note that the addition of dynamic correlation can still shift the relative energies by ~ 5 kcal/mol.^{14,16}

In conclusion, we have studied the active spaces and the relative stability of the lowest singlet, triplet, and quintet states of the oxo-Mn(salen) complex. With an initial approximate DMRG calculation in a large window around the Fermi level, we have obtained a good set of starting orbitals for the DMRG-SCF calculations, *without* an explicit localization procedure and subsequent manual selection of the active space. Per multiplicity, the same active space was obtained with the basis sets 6-31G*, cc-pVDZ, and ANODZ. The electronic structure of the quintet differs from previous studies. It can be interpreted by the two-electron excitation $3d_{z^2-y^2} \rightarrow \pi_1^*(O_{ax})$ and $\pi(C) \rightarrow \pi_2^*(O_{ax})$ from the singlet. We found that the triplet is 5 kcal/mol more stable than the singlet, and that the quintet lies only 12–14 kcal/mol higher than the singlet. In the future, we would like to study the experimental structure,¹ use a triple zeta basis, and add dynamic correlation. The experimental structure has a larger π -conjugated system, in which the quintet electron excitation takes place. Dynamic correlation can be added with perturbation theory (DMRG-CASPT2),^{45,50} configuration interaction (DMRG-MRCI),^{50,53} or canonical transformations (DMRG-CT).⁴⁴ We would also like to study reactions with the Mn(Salen) catalyst.⁵⁴

S.W. acknowledges a Ph.D. fellowship from the Research Foundation Flanders. The research was financed by UGent GOA grant 01G00710, and by the European Research Council through the European Community's Seventh Framework Programme FP7(2007-2013), ERC grant 240483. The computational resources (Stevin Supercomputer Infrastructure) and services used in this work were provided by the VSC (Flemish Supercomputer Center), funded by Ghent University, the Hercules Foundation and the Flemish Government—department EWI.

¹W. Zhang, J. L. Loebach, S. R. Wilson, and E. N. Jacobsen, *J. Am. Chem. Soc.* **112**, 2801 (1990).

²R. Irie, K. Noda, Y. Ito, N. Matsumoto, and T. Katsuki, *Tetrahedron Lett.* **31**, 7345 (1990).

³E. N. Jacobsen, W. Zhang, A. R. Muci, J. R. Ecker, and L. Deng, *J. Am. Chem. Soc.* **113**, 7063 (1991).

⁴E. M. McGarrigle and D. G. Gilheany, *Chem. Rev.* **105**, 1563 (2005).

⁵C. Linde, B. Åkermarck, P.-O. Norrby, and M. Svensson, *J. Am. Chem. Soc.* **121**, 5083 (1999).

⁶T. Strassner and K. N. Houk, *Org. Lett.* **1**, 419 (1999).

⁷L. Cavallo and H. Jacobsen, *Angew. Chem. Int. Ed.* **39**, 589 (2000); *J. Org. Chem.* **68**, 6202 (2003); *J. Phys. Chem. A* **107**, 5466 (2003); *Eur. J. Inorg. Chem.* **2003**, 892; *Inorg. Chem.* **43**, 2175 (2004); H. Jacobsen and L. Cavallo, *Chem. Eur. J.* **7**, 800 (2001); *Phys. Chem. Chem. Phys.* **6**, 3747 (2004).

⁸I. V. Khavrutskii, D. G. Musaev, and K. Morokuma, *Inorg. Chem.* **42**, 2606 (2003); *J. Am. Chem. Soc.* **125**, 13879 (2003); *Proc. Natl. Acad. Sci. U.S.A.* **101**, 5743 (2004); *Inorg. Chem.* **44**, 306 (2005); I. V. Khavrutskii, R. R. Rahim, D. G. Musaev, and K. Morokuma, *J. Phys. Chem. B* **108**, 3845 (2004).

⁹Y. G. Abashkin and S. K. Burt, *Org. Lett.* **6**, 59 (2004).

¹⁰A. Scheurer, H. Mäid, F. Hampel, R. W. Saalfrank, L. Toupet, P. Mosset, R. Puchta, and N. J. R. van Eikema Hommes, *Eur. J. Org. Chem.* **2005**, 2566.

¹¹Y. G. Abashkin, J. R. Collins, and S. K. Burt, *Inorg. Chem.* **40**, 4040 (2001).

¹²J. S. Sears and C. D. Sherrill, *J. Phys. Chem. A* **112**, 3466 (2008).

¹³T. Takatani, J. S. Sears, and C. D. Sherrill, *J. Phys. Chem. A* **114**, 11714 (2010).

¹⁴J. Ivancic, J. R. Collins, and S. K. Burt, *J. Phys. Chem. A* **108**, 2314 (2004).

¹⁵J. S. Sears and C. D. Sherrill, *J. Chem. Phys.* **124**, 144314 (2006).

¹⁶D. Ma, G. Li Manni, and L. Gagliardi, *J. Chem. Phys.* **135**, 044128 (2011).

¹⁷P. C. Hariharan and J. A. Pople, *Theor. Chim. Acta* **28**, 213 (1973).

¹⁸T. H. Dunning, *J. Chem. Phys.* **90**, 1007 (1989).

¹⁹P.-O. Widmark, P.-A. Malmqvist, and B. O. Roos, *Theor. Chim. Acta* **77**, 291 (1990).

²⁰M. Reiher and A. Wolf, *J. Chem. Phys.* **121**, 2037 (2004).

²¹J. M. Turney, A. C. Simmonett, R. M. Parrish, E. G. Hohenstein, F. A. Evangelista, J. T. Fernann, B. J. Mintz, L. A. Burns, J. J. Wilke, M. L. Abrams, N. J. Russ, M. L. Leininger, C. L. Janssen, E. T. Seidl, W. D. Allen, H. F. Schaefer, R. A. King, E. F. Valeev, C. D. Sherrill, and T. D. Crawford, *WIREs Comput. Mol. Sci.* **2**, 556 (2012).

²²H.-J. Werner, P. J. Knowles, G. Knizia, F. R. Manby, and M. Schütz, *WIREs Comput. Mol. Sci.* **2**, 242 (2012).

²³G. K.-L. Chan and M. Head-Gordon, *J. Chem. Phys.* **116**, 4462 (2002).

²⁴S. Wouters, W. Poelmans, P. W. Ayers, and D. Van Neck, *Comput. Phys. Commun.* **185**, 1501 (2014).

²⁵S. R. White and R. L. Martin, *J. Chem. Phys.* **110**, 4127 (1999).

²⁶A. O. Mitrushenkov, G. Fano, F. Ortolani, R. Linguerri, and P. Palmieri, *J. Chem. Phys.* **115**, 6815 (2001).

²⁷O. Legeza, J. Röder, and B. A. Hess, *Phys. Rev. B* **67**, 125114 (2003).

²⁸G. Moritz, B. A. Hess, and M. Reiher, *J. Chem. Phys.* **122**, 024107 (2005).

²⁹D. Zgid and M. Nooijen, *J. Chem. Phys.* **128**, 014107 (2008).

³⁰Y. Kurashige and T. Yanai, *J. Chem. Phys.* **130**, 234114 (2009).

³¹H.-G. Luo, M.-P. Qin, and T. Xiang, *Phys. Rev. B* **81**, 235129 (2010).

³²S. Sharma and G. K.-L. Chan, *J. Chem. Phys.* **136**, 124211 (2012).

³³S. Wouters, P. A. Limacher, D. Van Neck, and P. W. Ayers, *J. Chem. Phys.* **136**, 134110 (2012).

³⁴O. Legeza and G. Fáth, *Phys. Rev. B* **53**, 14349 (1996).

³⁵S. Wouters, *CHEMPS2: a spin-adapted implementation of DMRG for ab initio quantum chemistry*, 2014, see <https://github.com/SebWouters/CHEMPS2>.

³⁶Each spin multiplet in a spin-adapted MPS is represented by only one reduced basis state. This is the *reduced* to which is referred in the caption of Fig. 2.

³⁷D. Zgid and M. Nooijen, *J. Chem. Phys.* **128**, 144115 (2008).

³⁸D. Ghosh, J. Hachmann, T. Yanai, and G. K.-L. Chan, *J. Chem. Phys.* **128**, 144117 (2008).

³⁹P. E. M. Siegbahn, J. Almöf, A. Heiberg, and B. O. Roos, *J. Chem. Phys.* **74**, 2384 (1981).

⁴⁰D. Zgid and M. Nooijen, *J. Chem. Phys.* **128**, 144116 (2008).

⁴¹T. Yanai, Y. Kurashige, D. Ghosh, and G. K.-L. Chan, *Int. J. Quant. Chem.* **109**, 2178 (2009).

⁴²G. Moritz and M. Reiher, *J. Chem. Phys.* **124**, 034103 (2006).

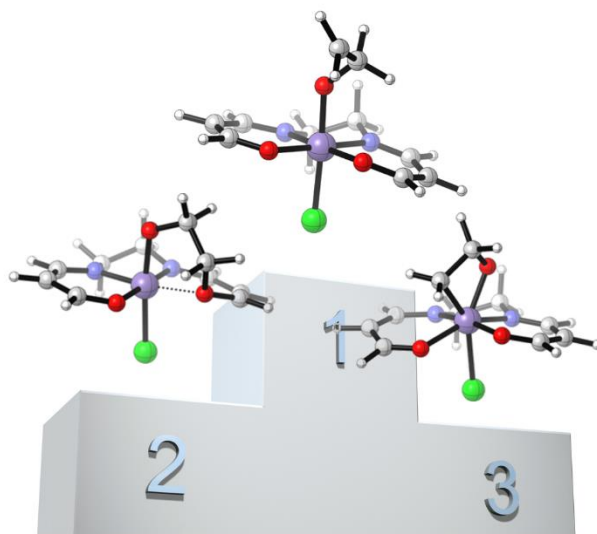
⁴³K. H. Marti, I. M. Ondk, G. Moritz, and M. Reiher, *J. Chem. Phys.* **128**, 014104 (2008).

⁴⁴T. Yanai, Y. Kurashige, E. Neuscammann, and G. K.-L. Chan, *J. Chem. Phys.* **132**, 024105 (2010).

⁴⁵Y. Kurashige and T. Yanai, *J. Chem. Phys.* **135**, 094104 (2011).

- ⁴⁶K. Boguslawski, K. H. Marti, Ö. Legeza, and M. Reiher, *J. Chem. Theory Comput.* **8**, 1970 (2012).
- ⁴⁷K. Boguslawski, P. Tecmer, O. Legeza, and M. Reiher, *J. Phys. Chem. Lett.* **3**, 3129 (2012).
- ⁴⁸Y. Kurashige, G. K.-L. Chan, and T. Yanai, *Nat. Chem.* **5**, 660 (2013).
- ⁴⁹T. V. Harris, Y. Kurashige, T. Yanai, and K. Morokuma, *J. Chem. Phys.* **140**, 054303 (2014).
- ⁵⁰Y. Kurashige, M. Saitow, J. Chalupsky, and T. Yanai, *Phys. Chem. Chem. Phys.* **16**, 11988 (2014).
- ⁵¹W. H. Dickhoff and D. Van Neck, *Many-body Theory Exposed!*, 2nd ed. (World Scientific, 2008).
- ⁵²Using natural orbitals, and ordering them according to the NOON, is not an optimal choice for DMRG. It is better to group corresponding bonding and antibonding orbitals. However, this procedure allows for an unmonitored optimization.
- ⁵³M. Saitow, Y. Kurashige, and T. Yanai, *J. Chem. Phys.* **139**, 044118 (2013).
- ⁵⁴T. Bogaerts, A. Van Yperen-De Deyne, Y.-Y. Liu, F. Lynen, V. Van Speybroeck, and P. Van Der Voort, *Chem. Commun.* **49**, 8021 (2013).

PAPER II: MECHANISTIC INVESTIGATION ON THE OXYGEN TRANSFER WITH THE MANGANESE-SALEN COMPLEX



T. Bogaerts, S. Wouters, P. Van der Voort, V. Van Speybroeck, ChemCatChem, Submitted, **2015**.

T. Bogaerts performed the research and prepared the manuscript.

Mechanistic investigation on the oxygen transfer with the manganese-salen complex

Thomas Bogaerts^[a,b], Sebastian Wouters^[a,c], Pascal Van Der Voort^{*[b]}, Veronique Van Speybroeck^{*[a]}

Abstract: The most well-known application of salen complexes is the use of a chiral ligand loaded with manganese to form the Jacobsen complex. This organometallic catalyst is used in the epoxidation of unfunctionalized olefins and can achieve very high selectivities. Although this application was proposed many years ago, the mechanism of oxygen transfer remains a question until now. In this paper, the epoxidation mechanism is investigated by an ab initio kinetic modeling study. First of all a proper DFT functional is selected which yields the correct ordering of the various spin states. Our results show that the epoxidation proceeds via a radical intermediate. Starting from the radical intermediate, these results can explain the experiments with radical probes. The subtle influences in the transition state using the full Jacobsen catalyst explain the experimentally observed product distribution.

loaded with various metals. Different functional groups on the salicylaldehyde moieties can influence the activity and selectivity of the resulting catalyst^[7]. When the backbone consists of a chiral diamine such as ethylenediamine, cyclohexanediamine or diphenylethylene-diamine, the complex can be used to catalyze various enantioselective reactions. The most well-known variant of this catalyst consists of a cyclohexanediamine backbone, two 3,5-*tert*-butylsalicylaldehyde 'wings' and is loaded with manganese. This is the so-called Jacobsen catalyst^[8].

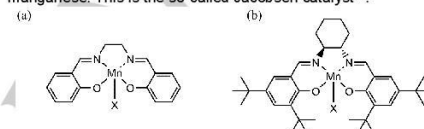


Figure 1. Motif of salen type complexes in general (a) and the arguably most well-known chiral variant, the Jacobsen complex.

Introduction

Since their discovery by Jacobsen and Katsuki,^[1] chiral manganese-salen complexes (Figure 1) have been an important tool for many organic chemists^[2]. These manganese complexes allow the epoxidation of unfunctionalized olefins with an unprecedented conversion and selectivity. Especially conjugated olefins can be quantitatively converted with this system^[3]. Other substrates such as thio-ethers and secondary alcohols have also been successfully oxidized with a high selectivity using salen-type complexes featuring different metals or modifications on the backbone^[4]. The compatibility of this catalyst with different oxidizing agents, both in a watery as well as in a water-free medium is another strong feature. The use of sodium-hypochlorite^[5] as a cheap oxidant and the possibility of producing chiral salen catalysts on a ton scale^[3a, 6] have made this catalytic system very interesting for the chemical industry.

Salen complexes in general consist of a diamine backbone connected with two salicylaldehyde moieties (Figure 1) and are

The mechanism of olefin epoxidation with these complexes has been a topic for debate for many years. An important breakthrough was the isolation of the Mn^{IV}-oxo intermediate with the use of mass spectroscopy^[9]. Starting from this intermediate a two-step mechanism seemed the most plausible (Scheme 1(B)), this was supported by the observation that *cis*-olefins lead to both *cis*- and *trans*-epoxides^[3c]. This isomerization suggests there is some sort of intermediate where a free rotation around the C-C bond is possible. In the two-step mechanism (Scheme 1(B)) the first carbon-oxygen bond is formed leading to a radical intermediate, in this intermediate a rotation around the olefin C-C bond is possible which would explain the experimental observations. In a next step the intermediate collapses with the formation of the second C-O bond.

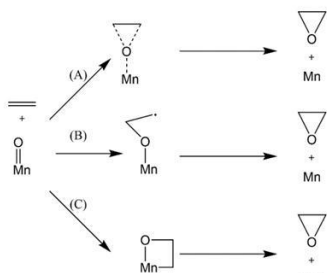
However, this straightforward explanation was quickly questioned by experimental results from Wong *et al.*^[10] They proposed to investigate the mechanism further using a radical probe, this is a molecule where a three-membered ring is placed vicinal to the double bond that is epoxidized. The hypothesis of the authors was that any radical intermediate that appeared would be 'captured' by the opening of this unstable ring. The approach was further optimized by Linde *et al.*^[11] The probes used in their study were improved with strategically placed phenyl rings to improve the radical stability (Figure 2). To ensure an unbiased result, a molecule was chosen that had phenyl groups to stabilize both radicals (ring-opened and intermediate) equally.

The results of this latter study were surprising; different substituents on the one side of the double bond yielded different distributions of ring-opening and epoxide products (Scheme 2 and Table 1). Those observations lead to the conclusion that two different mechanisms for the epoxidation would be operating

- [a] Prof Dr. V. Van Speybroeck, T. Bogaerts, Center for Molecular Modelling (CMM) Ghent university Technologiepark 903, 9052 Zwijnaarde, Belgium E-mail: Veronique.vanspeybroeck@ugent.be
- [b] Prof Dr. P. Van Der Voort Center for Ordered Materials, Organometallics and Catalysis (CO-MOC), Department of Inorganic and Physical Chemistry Ghent University Krijgslaan 281-S3, 9000 Ghent, Belgium
- [c] Dr S. Wouters, Department of Chemistry Princeton University Frick Laboratory 351, Princeton, NJ 08544, USA

Supporting information for this article is given via a link at the end of the document.

parallel to each other, the first featuring a radical intermediate, the second one via a different approach.



Scheme 1. Different mechanisms that have been proposed for the oxygen transfer from the manganese-salen complex: The concerted (A), radical (B) and manganese-oxetane (C) pathway.

The possible existence of a different mechanism has led to numerous *ab initio* studies to unravel the mechanism of the oxygen transfer. Initial results already showed that the spin state of the complex will play an important role in how exactly the transfer takes place^[12]. By using a B3LYP functional and reducing the salen-type complex to a cationic Manganese-acacen system as a model Linde *et al.*^[12a] found the existence of a concerted pathway (Scheme 1(A)) that was more stable on the spin two plane, while for the spin 1 plane a two-step mechanism with a radical intermediate was found the most favored. Abashkin *et al.*^[13] found that the addition of a counter ion on the manganese center radically shifted the results. A two-step mechanism was found for both the spin 1 and 2 states while a concerted mechanism was proposed for the spin zero state. Next to the use of a more realistic model featuring a counter ion, the BP86 functional was used since it agreed well with the high level CCSD(T) method. Using this functional, the group of Jacobsen further analyzed this interesting reaction^[14] while considering various alternative intermediates next to the radical variant. Using this analysis Cavallo *et al.*^[15] proposed a full catalytic cycle for the epoxidation with sodiumhypochloride as an oxidant. Next to the radical intermediate other intermediates (e.g Scheme 1(C)) were proposed in various modeling studies,^[12a, 16] however, no full pathway via these intermediates was reported.

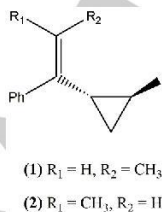
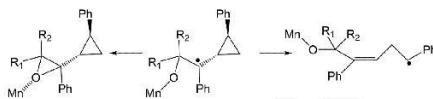


Figure 2. Two variants of the radical probe used by Linde *et al.*^[12b] to assess the existence of a radical intermediate.



Scheme 2. Competitive ring-opening and epoxidation pathways with the radical probe experiments.

Despite these many interesting results the question of the influence of the selected density functional remained. Due to the near-degenerate spin states, the electronic description of this complex is a challenge. For that reason, CASSCF calculations are often proposed to model the active species in the epoxidation with the salen complex^[17]. This method has shown that the Mn^V-oxo complex (Figure 3) has a high multireference character, thus static correlation should be adequately described. In an earlier study we reported that the DMRG-SCF method^[18] allows to model this multireference system with high accuracy^[19]. With that approach a very good estimation of the electronic structure and relative free energy of the different spin states for the Mn^V-oxo complex was achieved.

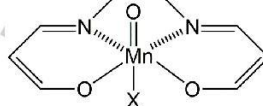


Figure 3. Mn^V-oxo structure on the Mn-acacen' complex.

On the other hand, we also have shown earlier that a proper description of the full catalyst (similar to Figure 1(b)) is necessary to obtain a proper description of the selectivity^[20]. It can be expected that the large model will be required here as well. This large model cannot be modeled with these high-level post-HF methods. In this paper we aim to unravel the epoxidation mechanism by the means of an advanced theoretical approach. Therefore we have first investigated whether a good density functional can be found that allows to reproduce the relative free energies of the different spin states of the Mn^V-oxo acacen' complex obtained by the DMRG-SCF method. Secondly the oxygen transfer mechanism will be assessed on the small complex, using ethene as a test substrate. Finally the oxygen transfer with the radical probe as a substrate will be considered to find the mechanistic explanation for the distribution between ring-opening and epoxidation products. In this case the full model for the catalyst will be used.

Table 1. Experimentally observed distribution percentage of epoxide formation.^[12b]

	NaOCl/ CH ₂ Cl ₂ (a)	Iodosylbenzene/ benzene (b)
R ₁ =H R ₂ =Me (1)	100%	83%
R ₁ =Me R ₂ =H (2)	56%	54%

Results and Discussion

Computational description of the salen complex

To model the full catalyst we aim to use density functional methods. Thus the selection of a proper functional has to be investigated first. Since the possible spin states during the reaction are energetically close to each other, an important feature of a good functional is its capability of finding the right energetic ordering of the various spin states. As a reference we will use the energies found by the DMRG-SCF approach with a 6-31G* basis set for the Mn^V-oxo acacen' complex¹⁸⁻¹⁹. Using this method it was possible to obtain a multireference result with a very large active space. The spin 1 state was found to be the most stable, followed by the spin 0 and spin 2 state (DMRGSCF in Figure 4). Herein, single point energy calculations were done on the same geometry with the same basis set and using a broad scale of functionals to assess the capability of the functional to describe the right spin ordering. The energy differences relative to the spin 0 state were compared to the reference DMRGSCF calculations (Figure 4).

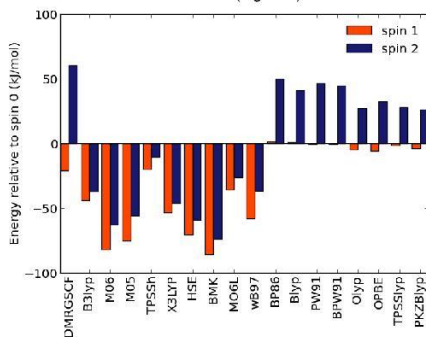


Figure 4. Energies of various spin states with a selected set of for the acacen' complex.

From this comparison some trends could be deduced, there is a whole range of functionals that overestimate the high spin states. Especially functionals containing Hartree-fock exchange exhibit this behavior. A few functionals, including the BP86 functional seem to overestimate the stability of the spin 0 state, however the results are closer to the multireference values. The next set of functionals (OLYP, OPBE,...) reproduce the correct ordering but not the numerical values. The best results seem to come from the functionals containing Handy's²¹ modification of the Becke exchange functional (OPTX). From this benchmark we have selected the OPBE functional as the preferred method. These results are also supported by the success of this functional in the modelling of systems with a challenging electronic configuration where different spin states are energetically close to each other²².

This level of theory will be used hereafter on three models to obtain mechanistic insight into the epoxidation reactions. First of

all, the manganese-acacen' complex (Figure 3) will be investigated in combination with ethylene as olefin. This is a very small model system, which allows to quickly analyze the various proposed mechanisms and possible intermediates.

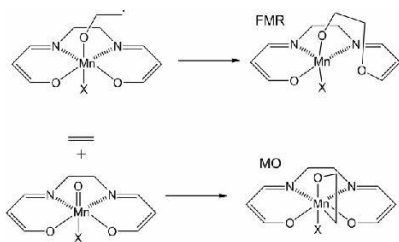
In a second step with the same manganese-acacen' representation of the organometallic complex the two variants of the radical probe were modeled as reactants (the substituted styrenes are shown in Figure 2). With this model we aim to describe the observed distribution between epoxidation and ring-opening products (Table 1). We will focus on the question whether an epoxidized olefin can be formed via a radical intermediate or if these radicals will always lead to ring opening products.

Our third model accounts for the full salen complex which was shown earlier to be important for a reliable description of the selectivity.^[20a] In this case, the steric influence of the complex is fully taken into account. For this model, important steps in the ring-opening and epoxidation of the substituted styrenes will be modeled. However, the size of this system does not allow the usage of the larger basis set in the optimization procedure. In this case the system was optimized using a 6-31+g(d) level of theory for H,C,N and oxygen. And on Mn and Cl, a 6-311++G(2df,2p) basis set was used. Free energies were calculated as mentioned in the computational details.

Mechanistic investigation on the manganese-acacen' complex with ethylene

Using ethylene as a test molecule, the free energy diagram for the oxygen transfer was calculated with the manganese-acacen' complex containing a Cl counter-ion. On the spin 1 and spin 2 planes the earlier proposed two step mechanism with a radical intermediate is found, on the spin 0 plane we could not find a pathway that led to oxygen transfer. The free energy diagrams are shown in Figure 5.

The barrier for the formation of the first carbon-oxygen bond is similar on the spin 1 and spin 2 plane, but since the complexes on the spin 1 plane are generally lower in energy than the ones on the spin 2 plane the first one will be preferred. The collapse of the radical into the epoxide seems to preferably take place on the spin 2 plane but the two states are energetically very close to each other. Since the Mn^{III}-salen complex seems to be most stable on the spin 2 plane it is likely that a spin-crossover occurs somewhere after the first transition state. A detailed energetic picture of this crossover would require more advanced calculations and is omitted here. It must be recognized that the energy differences after the formation of the first C-O bond is small and in the following discussion both the spin 1 and spin 2 state will be shown



Scheme 3. Possible alternative intermediates FMR-intermediate (top), manganeseoxetane intermediate (bottom).

Next to the two-step mechanism, different pathways for the oxygen transfer have been proposed in literature. The first possibility is a concerted oxygen transfer in which the epoxide is formed in a single step. However, we were unable to identify a concerted transition state. This observation is in agreement with earlier studies where the concerted step -if it could be isolated- had a significantly higher activation barrier^[23]. Other intermediates that have gained attention are the manganeseoxetane structure^[12a] (MO) and the five membered ring (FMR) intermediate^[24] (Scheme 3). In the first case a four membered ring is formed with the manganese, oxygen and the two carbon atoms of the olefin. In the second case a five membered ring is formed between the same atoms and one of the oxygen atoms from the complex. The different intermediates were optimized and their free energies are shown in Table 2.

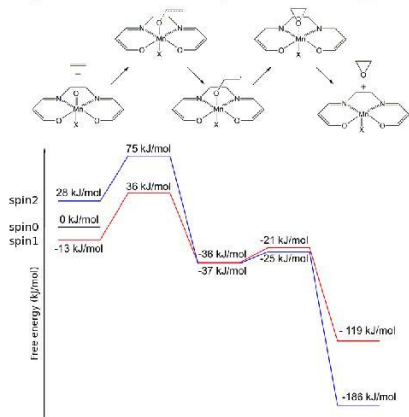


Figure 5. Free energy diagram for the oxygen transfer to ethene relative to the free energy of the reactants on the spin 0 plane (X=Cl).

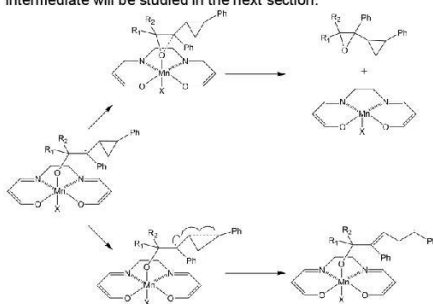
The first possibility, the manganeseoxetane structure, was only found on the spin 0 plane, it has a significantly higher free energy than other intermediates and will thus be of a limited

influence. The FMR-intermediate however seems to be more stable than the radical intermediate on the spin 1 plane and could thus provide a viable alternative pathway. A search for the transition state showed there was a plausible pathway (with a barrier of 41.5 kJ/mol) from the radical intermediate to the FMR-intermediate on the spin 1 plane, however we could not find a direct pathway to this intermediate. Moreover, a route from this intermediate to the epoxide could not be identified, making it implausible that this structure plays a significant role in the overall reaction.

Table 2. Free energies of different intermediates relative to the reactants on the spin 0 plain (X=Cl).

Structure	Spin state occurrence	Free energy
	Spin 0	119.0 kJ/mol
	Spin 0	-4.1 kJ/mol
	Spin 1	-71.3 kJ/mol
	Spin 1	-36.6 kJ/mol
	Spin 2	-37.5 kJ/mol

The study on the small manganese-acacen' complex with ethylene shows that the mechanism with the radical intermediate is the most plausible. Within this mechanism, the reaction would preferably occur on the spin 1 plane, however a spin-crossing could occur during the course of the reaction to allow formation of the most stable product. Given this observation, the radical trapping experiments of Linde et al. still needs to be explained. Therefore the competition between the ring opening reaction and the epoxidation reaction starting from the radical intermediate will be studied in the next section.



Scheme 4. Competitive pathways between epoxidation (top) and ring opening (bottom) with the radical probe starting from the radical intermediate.

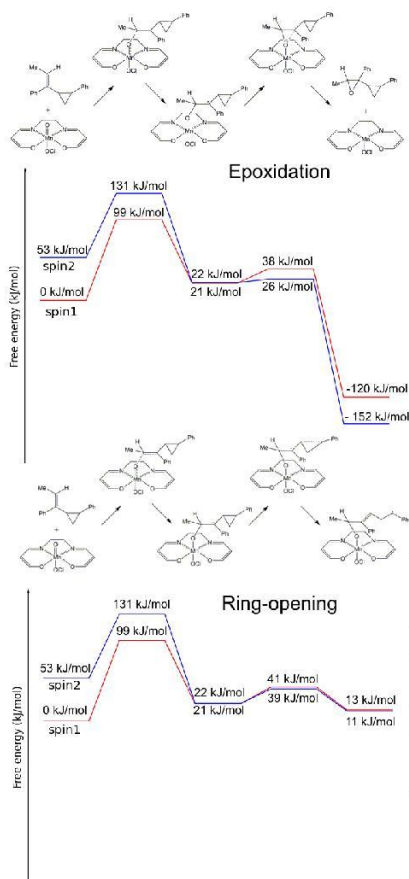


Figure 6. Epoxidation versus ring-opening pathway free energy diagram for probe (1) (nomenclature in Table 1) Free energies are relative to the reactants on spin 1.

Ring opening versus epoxidation on the manganese-acacen' complex

The experiments from Linde *et al.*^[11b] suggested that the existence of a radical intermediate should lead to a majority of ring-opening products when there is a three-membered ring adjacent to this radical (Scheme 4). In order to obtain more insight into these experimental observations, we investigated the behavior of these substrates on the Mn-acacen' model of complex. Experimental results^[11b] showed the amount of ring-

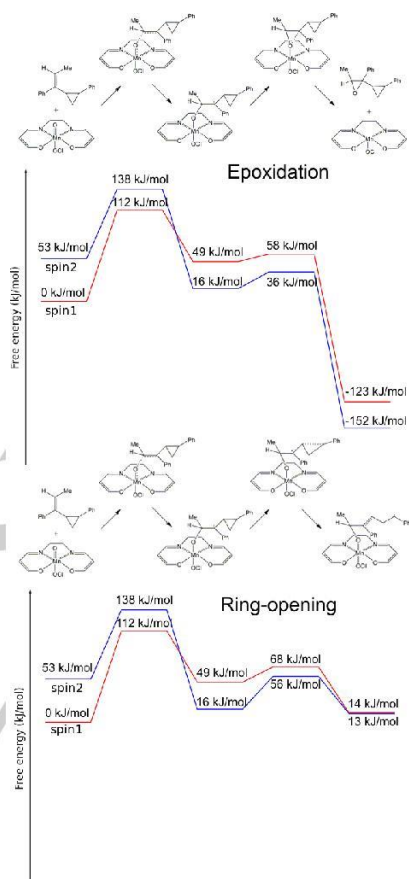


Figure 7. Epoxidation versus ring-opening pathway free energy diagram for probe (2) (nomenclature in Table 1) Free energies are relative to the reactants on spin 1.

opening products did not only vary with the exact substrate used, but also with the oxidant present (Table 1). In our models we considered two variants of the radical probe as shown in Figure 2. The dependence on the oxidant could be explained by the sixth coordination site on manganese. Jacobsen *et al.*^[15] showed that the counter-ion of the complex would be a hypochlorite anion when the epoxidation was conducted in a sodiumhypochlorite/CH₂Cl₂ system, thus we have used this as a counter-ion in our models.

We will study the competition between the epoxidation and ring opening reaction starting from the radical intermediate that was shown to be favored from our initial calculations. From the radical intermediate the reaction can occur via two ways: The intermediate can collapse, forming the epoxide product or the three-membered ring can open, forming a new, ring-opened intermediate. Experiments have shown that substrate (1) yields more epoxide product compared to substrate (2) (Table 1). Our theoretical results for both substrates on spin 1 and spin 2 and for both mechanisms are shown in Figure 6 and Figure 7.

For both substrates the epoxide product is thermodynamically more favored. This is not surprising since the ring-opening reaction leads to another radical that is only an intermediate for the observed ring-opening products. From the height of the barrier we can draw some conclusions on what product is kinetically most favored. For substrate (1) the barrier

for epoxidation is about 13 kJ/mol lower than the barrier for ring-opening (Figure 6) on the most stable spin plane. This shows the epoxide formation is kinetically more favored, and it is also the experimentally observed majority product. For substrate (2) the barrier is more than 20 kJ/mol lower in favor of the epoxide, which would mean the epoxide should also be the majority product here. However this system exhibits a fifty-fifty distribution experimentally. For the system with iodosylbenzene/benzene as oxidant/solvent combination, the results are in closer agreement with the experimental observations (Figure S1 and S2 of the supporting information). Here the epoxide product is also thermodynamically favored but with probe (2) the ring opening is kinetically favored which could correspond to the observed fifty-fifty distribution.

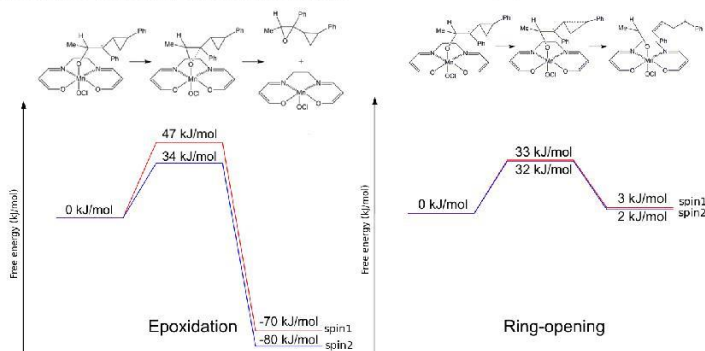


Figure 8. Free energy diagrams for the competitive ring-opening and epoxidation reaction for probe (1).

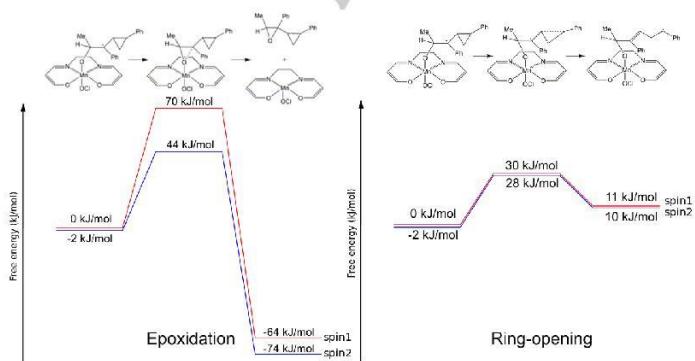


Figure 9. Free energy diagrams for the competitive ring-opening and epoxidation reaction for probe (2).

These results allow us to conclude that the radical intermediate is not necessarily 'trapped' by the ring-opening of the three-membered ring. The barrier for this opening is indeed very low, however the collapse of the radical intermediate to form the epoxide is also lowly activated, making both pathways competitive. Detailed structural parameters that explain the observations cannot easily be deduced from this relatively small model. To fully obtain mechanistic insight, the reaction with the hypochlorite anion on the sixth coordination site will be examined further using the full Jacobsen complex as a model.

Ring-opening versus epoxidation on the full Jacobsen complex

To fully account for the steric influences of the catalyst, the reaction on the full Jacobsen catalyst is modeled hereafter^[20b]. In this case the model becomes quite large and therefore the optimizations were performed using a lower basis set for part of the system, as explained in the computational details.

Furthermore, we will only consider the last step of the mechanism to unravel the competition between the epoxidation and ring-opening. The thermodynamic diagrams for both probes are shown in Figure 8 and Figure 9. These results give insight into the difference between the various radical probes. For probe (1) the ring-opening and epoxidation pathway have a similar barrier height (32.3 kJ/mol and 34.2 kJ/mol respectively on the spin 2 plane, see Figure 8). This leads to the thermodynamically most favored epoxidation product being formed quantitatively. Probe (2), that leads experimentally to a mixture of ring-opening and epoxidized products, has a significant difference in barrier height (Figure 9). The thermodynamically favored epoxide formation has a higher free energy barrier than the ring opening, thus it is not surprising that a mixture between the thermodynamically and kinetically favored product is formed.

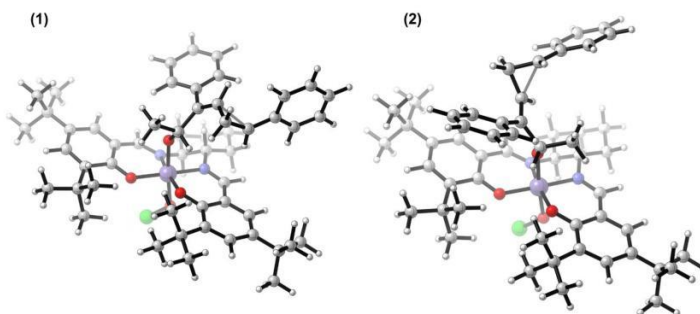


Figure 10. Geometries of the ring-opening transition states (spin 2 plane), an internal rotation in the probe occurs due to the interaction with the methyl group, but this has no influence on transition state energy.

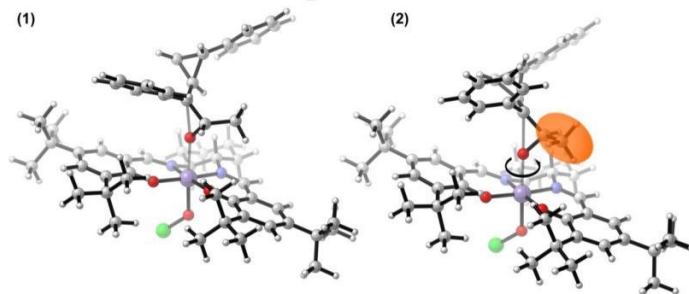


Figure 11. Geometries for the epoxidation transition states (spin 2 plane), the place of the substituents induces a steric interaction with the complex that changes the orientation between substrate and complex (rotation denoted with an arrow). This effect has an influence on the transition state.

The difference between the behavior of the two probes can also be deduced from the geometries of the transition states for the ring-opening and the epoxidation reaction. As can be seen from the transition state for both probes, shown in Figure 10, the ring-opening reaction is not hindered by the catalytic complex, allowing the probes to assume their most favored form.

For the epoxidation reaction the nature of R_1 and R_2 substituents do seem very important due to interactions with the catalyst (Figure 11). This is according to intuition, the ring-opening is not influenced by the transferred oxygen nor by the catalyst, while in the epoxidation this influence does exist, since the reaction takes place closer to the complex. With probe (1) there is no steric influence between the catalyst and the substrate during the epoxidation, this leads to a dihedral angle between the oxygen of the ligand, manganese, the transferred oxygen and the first carbon of the substrate of 7.5° . For probe (2) the methyl group (marked orange in Figure 11 (2)) would be hindered by the *tert*-butyl group of the complex, forcing the probe to twist during the transition state. This results in a dihedral angle of 133° on the spin 1 plane and 60° on the spin 2 plane, the twist appears to be energetically unfavorable resulting in a higher barrier. The main reason for the difference in product distribution between the probes is thus not the presence of different mechanisms but the steric influence of the complex on the transition state for the epoxidation reaction. It is logical that the epoxidation is affected more, since during the formation of the second C-O bond the substrate occurs closer to the complex compared to the ring-opening step.

Conclusions

The nature of the intermediate during the oxidation of unfunctionalized olefins with Mn-salen complexes has triggered many experimental and theoretical studies so far. In this study we have presented a full mechanistic study using contemporary methods to give more insight into the nature of the intermediate and its repercussions on the reactions starting from it.

As the manganese salen complex is an ambitious system to describe electronically, it was necessary to first determine an electronic level of theory that was able to describe the subtle energy differences between the various spin states, whereas also being computationally feasible. Indeed, as it was our intention to study the mechanism on the full Jacobsen catalyst, an accurate yet computationally efficient method had to be selected. A computational benchmark study was performed on the Mn-acacen' complex for which recently high level DMRG-SCF results became available on the stability of the various spin states. A variety of contemporary functionals were tested and hereof the OPBE functional gave an acceptable agreement with the DMRG-SCF results. In a next step we investigated all mechanistic proposals for the epoxidation reaction on the small Mn-acacen' complex with ethene as a test substrate. It was shown that the radical intermediate mechanism is the only likely candidate. At first sight, these results seem contradictory to the experimental observation using radical probes. Intuitively the

opening of the three-membered ring seems more facile than the epoxidation. However for the same model system we observed that there is a competition between the epoxidation and ring-opening reaction starting from the radical intermediate, which shows that the radical intermediate will in reality not necessarily be trapped by the radical probe. However to fully understand the observed product distribution in terms of varying substrates and varying oxidants, it was necessary to account for the full Jacobsen catalyst and to account for all steric effects. Indeed, steric interactions between the methyl group on the radical probe and the catalyst induce a free energy difference between the transition state for epoxidation and that for ring-opening, in agreement with the experimental observations. All of these results show the most probable mechanism of oxygen transfer via a manganese-salen complex is the one featuring a radical intermediate. Starting from this intermediate both epoxidation and ring-opening can occur with the radical probes. This pathway can explain much of the experimental results, not only the distribution between *cis* and *trans* epoxides starting from *cis* olefins, but these results also provide an explanation for the observed product distribution between epoxidation and ring-opening products when using radical probes. These conclusions are of fundamental importance for the optimizations of salen catalysts for enantioselective olefin epoxidations.

Computational methodology

As a first step a good density functional for the modelling has to be identified. Therefore a series of calculations were done with the Gaussian09 suite of programs^[25] using a variety of functionals. In the next steps all optimizations were done using a 6-311++G(2df,2p) basis set unless otherwise mentioned. For all results the stability of the wavefunction was checked. After optimization Grimme D3 corrections were applied to include van der Waals contributions^[26]. Free energies are calculated from frequency calculations, which are done on the same level of theory as the optimizations, using the in-house TAMkin package^[27]. More information on theoretical procedures to obtain kinetic data can be found in the review by Van Speybroeck *et al.*^[28] All transition state structures were verified by the presence of a single imaginary frequency.

Acknowledgements

The research was financed by UGent GOA grant 01G00710, the European Research Council for funding through the European Community's Seventh Framework Programme (FP7(2007-2013) ERC grant agreement no. 240483) and the Research Board of Ghent University (BOF). S.V. acknowledges Research Foundation Flanders for a predoctoral and the Belgian-American educational foundation for a postdoctoral fellowship. Computational resources and services were provided by Ghent University (Stevin Supercomputer Infrastructure).

Keywords: Ab initio calculations • Oxidation • Quantum chemistry • Manganese • Homogeneous catalysis

- [1] a) W. Zhang, J. L. Loebach, S. R. Wilson, E. N. Jacobsen, *J. Am. Chem. Soc.* **1990**, *112*, 2801-2803; b) R. Irie, K. Noda, Y. Ito, N. Matsumoto, T. Katsuki, *Tetrahedron Lett.* **1990**, *31*, 7345-7348.
- [2] T. Katsuki, *Coord. Chem. Rev.* **1995**, *140*, 189-214.
- [3] a) J. F. Larrow, E. N. Jacobsen, Y. Gao, Y. P. Hong, X. Y. Nie, C. M. Zepp, *J. Org. Chem.* **1994**, *59*, 1939-1942; b) M. Palucki, P. J. Pospisil, W. Zhang, E. N. Jacobsen, *J. Am. Chem. Soc.* **1994**, *116*, 9333-9334; c) N. H. Lee, E. N. Jacobsen, *Tetrahedron Lett.* **1991**, *32*, 6533-6536.
- [4] a) A. P. Gao, M. Wang, J. C. Shi, D. P. Wang, W. Tian, L. C. Sun, *Appl. Organomet. Chem.* **2006**, *20*, 830-834; b) H. Egami, T. Katsuki, *J. Am. Chem. Soc.* **2007**, *129*, 8940-8941; c) A. Y. Choi, G. S. Hwang, B. K. Senapati, D. H. Ryu, *Bull. Korean Chem. Soc.* **2008**, *29*, 1879-1880.
- [5] W. Zhang, E. N. Jacobsen, *J. Org. Chem.* **1991**, *56*, 2296-2298.
- [6] a) G. J. Kim, S. J. Kim, H. S. Lee, D. W. Park, J. W. Yun, Google Patents, **2001**; b) Y. Ishikawa, H. Eguchi, Google Patents, **2013**.
- [7] M. Palucki, G. J. McCormick, E. N. Jacobsen, *Tetrahedron Lett.* **1995**, *36*, 5457-5460.
- [8] E. N. Jacobsen, W. Zhang, A. R. Muci, J. R. Ecker, L. Deng, *J. Am. Chem. Soc.* **1991**, *113*, 7063-7064.
- [9] D. A. Plattner, D. Feichtinger, J. El-Bahraoui, O. Wiest, *Int. J. Mass Spectrom.* **2000**, *195*, 351-362.
- [10] H. Fu, G. C. Look, W. Zhang, E. N. Jacobsen, C. H. Wong, *J. Org. Chem.* **1991**, *56*, 6497-6500.
- [11] a) C. Linde, N. Kolai, P. O. Norrby, B. Akemark, *Chem.-Eur. J.* **2002**, *8*, 2568-2573; b) C. Linde, M. Arnold, P. O. Norrby, B. Akemark, *Angew. Chem.-Int. Edit. Engl.* **1997**, *36*, 1723-1725.
- [12] a) C. Linde, B. Akemark, P. O. Norrby, M. Svensson, *J. Am. Chem. Soc.* **1999**, *121*, 5083-5084; b) T. Strassner, K. N. Houk, *Org. Lett.* **1999**, *1*, 419-421.
- [13] Y. G. Abashkin, J. R. Collins, S. K. Burt, *Inorg. Chem.* **2001**, *40*, 4040-4048.
- [14] a) L. Cavallo, H. Jacobsen, *Eur. J. Inorg. Chem.* **2003**, 892-902; b) L. Cavallo, H. Jacobsen, *J. Phys. Chem. A* **2003**, *107*, 5466-5471; c) L. Cavallo, H. Jacobsen, *J. Org. Chem.* **2003**, *68*, 6202-6207.
- [15] L. Cavallo, H. Jacobsen, *Inorg. Chem.* **2004**, *43*, 2175-2182.
- [16] I. V. Khavrutskii, D. G. Musaev, K. Morokuma, *Proceedings of the National Academy of Sciences of the United States of America* **2004**, *101*, 5743-5748.
- [17] a) J. S. Sears, C. D. Sherrill, *J. Chem. Phys.* **2006**, *124*, 144314; b) J. Ivanic, J. R. Collins, S. K. Burt, *J. Phys. Chem. A* **2004**, *108*, 2314-2323; c) D. Ma, G. Li Manni, L. Gagliardi, *The Journal of Chemical Physics* **2011**, *135*, -.
- [18] S. Wouters, W. Poelmans, P. W. Ayers, D. Van Neck, *Computer Physics Communications* **2014**, *185*, 1501-1514.
- [19] S. Wouters, T. Bogaerts, P. Van der Voort, V. Van Speybroeck, D. Van Neck, *J. Chem. Phys.* **2014**, *140*, 241103.
- [20] a) T. Bogaerts, A. Van Yperen-De Deyne, Y.-Y. Liu, F. Lynen, V. Van Speybroeck, P. Van Der Voort, *Chem. Commun.* **2013**, *49*, 8021-8023; b) T. Bogaerts, S. Wouters, P. Van Der Voort, V. van Speybroeck, *J. Mol. Catal. A: Chem* **2015**, In Press.
- [21] a) N. C. Handy, A. J. Cohen, *Mol. Phys.* **2001**, *99*, 403-412; b) W.-M. Hoe, A. J. Cohen, N. C. Handy, *Chemical Physics Letters* **2001**, *341*, 319-328.
- [22] a) M. Swart, *Inorg. Chim. Acta* **2007**, *360*, 179-189; b) M. Swart, A. R. Groenhof, A. W. Ehlers, K. Lammertsma, *J. Phys. Chem. A* **2004**, *108*, 5479-5483.
- [23] a) L. Cavallo, H. Jacobsen, *Angewandte Chemie International Edition* **2000**, *39*, 589-592; b) H. Jacobsen, L. Cavallo, *Phys. Chem. Chem. Phys.* **2004**, *6*, 3747-3753.
- [24] Y. G. Abashkin, S. K. Burt, *Org. Lett.* **2004**, *6*, 59-62.
- [25] G. W. T. M. J. Frisch, H. B. Schlegel, G. E. Scuseria, M. A. Robb, J. R. Cheeseman, G. Scalmani, V. Barone, B. Mennucci, G. A. Petersson, H. Nakatsuji, M. Caricato, X. Li, H. P. Hratchian, A. F. Izmaylov, et al., *Revision D.01*, Gaussian, Inc., Wallingford CT ed., **2009**.
- [26] a) S. Grimme, J. Antony, S. Ehrlich, H. Krieg, *J. Chem. Phys.* **2010**, *132*; b) S. Grimme, *J. Comput. Chem.* **2004**, *25*, 1463-1473.
- [27] A. Ghysels, T. Verstraelen, K. Hemelsoet, M. Waroquier, V. Van Speybroeck, *J. Chem. Inf. Model.* **2010**, *50*, 1736-1750.
- [28] V. van Speybroeck, R. Gani, R. J. Meier, *Chem. Soc. Rev.* **2010**, *39*, 1764-1779.

Supporting information

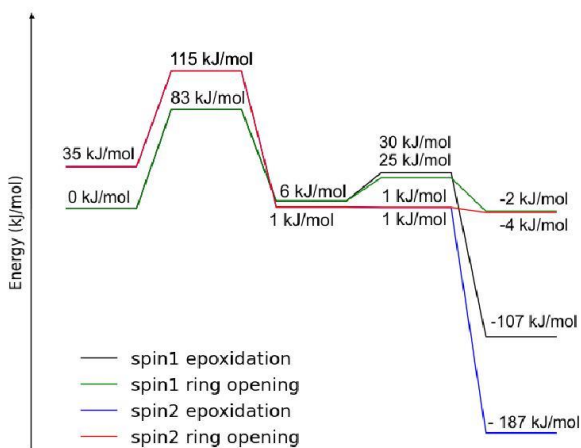


Figure S1. Epoxidation versus ring-opening pathway free energy diagram for probe (1) in the iodossylbenzene/benzene, free energies are relative to the reactants on spin 1.

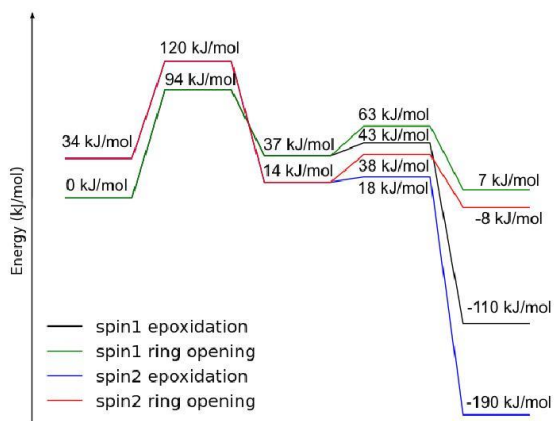
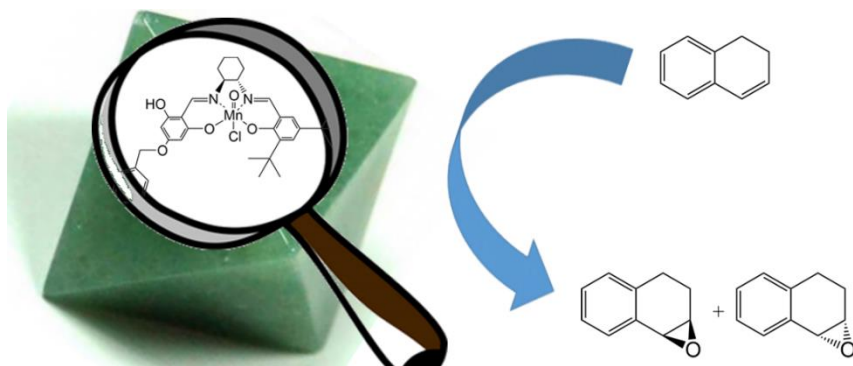


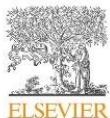
Figure S2. Epoxidation versus ring-opening pathway free energy diagram for probe (2) in the iodossylbenzene/benzene, free energies are relative to the reactants on spin 1.

PAPER III: THE ENANTIOSELECTIVITY OF THE MANGANESE-SALEN COMPLEX IN THE EPOXIDATION OF UNFUNCTIONALIZED OLEFINS AND THE INFLUENCE OF GRAFTING



T. Bogaerts, S. Wouters, P. Van der Voort, V. Van Speybroeck, *Catalysis A: Chemical*, in press, **2015**

T. Bogaerts performed the research and prepared the manuscript.



Editor's choice paper

The enantioselectivity of the manganese-salen complex in the epoxidation of unfunctionalized olefins and the influence of grafting



Thomas Bogaerts^{a,b}, Sebastian Wouters^a, Pascal Van Der Voort^{b,*},
Veronique Van Speybroeck^{a,*}

^a Center for Molecular Modelling (CMM), Ghent University, Technologiepark 903, 9052 Zwijnaarde, Belgium

^b Center for Ordered Materials, Organometallics and Catalysis (COMOC), Department of Inorganic and Physical Chemistry, Ghent University, Krijgslaan 281-S3, 9000 Ghent, Belgium

ARTICLE INFO

Article history:

Received 4 November 2014
Received in revised form 2 May 2015
Accepted 25 May 2015
Available online 29 May 2015

Keywords:

Ab initio modelling
Metal organic frameworks
Enantioselective catalysis
Heterogeneous catalysis

ABSTRACT

Jacobsen's complexes are famous for their usability for enantioselective epoxidations. However, the applicability of this catalytic system has been severely limited by several practical problems such as deactivation and separation after reaction. Grafting of Jacobsen-type complexes on solid supports is an attractive way to overcome these problems but led to a decrease in selectivity. A combined theoretical and experimental approach is presented to unravel the factors governing enantioselectivity. The importance of different substituents was determined by analyzing the transition state for the oxygen transfer using the full system as a model. An analysis of the asymmetric complex has shown an inherent tendency for a decreased selectivity due to the lack of specific bulky groups. Experimentally an immobilized Jacobsen catalyst on a metal organic framework (MIL-101) was synthesized which confirms the computational tendencies but the decrease in selectivity is limited, indicating that the MIL-101(Cr) is a suitable carrier for this complex.

© 2015 Elsevier B.V. All rights reserved.

1. Introduction

Reactive chiral products are of great value in the chemical industry [1–3]. Many commercial products contain some sort of chiral center and the production of these can be facilitated by readily accessible chiral intermediates. One compound that can serve as such an intermediate is a chiral epoxide. These compounds are very reactive due to the epoxide ring and the chirality can be transferred to further products.

Given the synthetic value of chiral epoxides many catalytic systems have been developed to produce these compounds with high selectivity, with the titanium tartrate catalyst [4–10] and the chiral metal-salen complex [11–16] as the most well-known. The latter complexes, originally designed by Jacobsen and Katsuki, are highly performant in the epoxidation of unfunctionalized olefins. With optimized conditions, olefins such as styrene [16] and chromene derivatives [14] could be epoxidized with high (>85% ee) selectivities. Different oxidizing agents can be applied with the catalytic system,

for example NaOCl in aqueous media or meta-chloroperoxybenzoic acid in organic solvents.

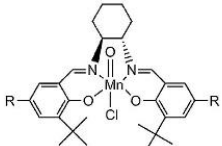
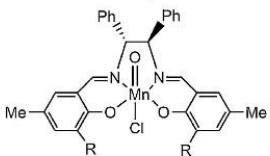
Despite their large applicability and commercial availability the mechanism that controls the enantioselectivity is not thoroughly understood. Several experiments have been conducted to probe the approach vectors [13,14,17] (Table 1). From a computational approach numerous ab initio studies on the mechanism of oxygen transfer using a smaller model for the Jacobsen catalyst [18–21] have been performed. Linde et al. [22,23] acknowledged early on that the choice of a different spin state (spin 0, 1 or 2) has a huge influence on the resulting reaction mechanism. They proposed the existence of different intermediates depending on the spin state of the complex. Cavallo et al. [24,25] further investigated this phenomenon and noticed the importance of the choice of the right DFT functional. Their research allowed for the proposition of a catalytic cycle for the epoxidation using sodium hypochlorite [20]. However next to these studies on the mechanism of oxygen transfer, the research on the selectivity has always been performed with molecular mechanics methods [19]. To obtain a full understanding of all interactions contributing to the overall selectivity it is recommended to model the complete catalyst at a higher level of theory. Such studies have now become feasible with current computational resources.

* Corresponding author. Tel.: +32 92646558.

** Corresponding author.

E-mail addresses: pascal.vandervoort@ugent.be (P.V.D. Voort), Veronique.vanspeybroeck@ugent.be (V.V. Speybroeck).

Table 1
Selectivity of salen-type catalysts bearing different substitutions in the epoxidation of methylstyrene [13,14].

Catalyst	Substituents	%ee
	R = Me R = <i>tert</i> -butyl	80% 92%
	R = H R = <i>tert</i> -butyl	0–3% 81%

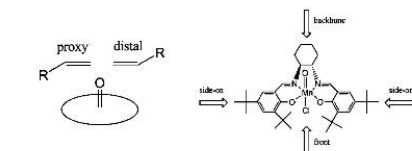


Fig. 1. Schematic representation of various approach vectors to the salen complex, adapted from Fristrup et al. [17] and Jacobsen et al. [19].

Experiments with styrene derivatives featuring different substituents [17] have led to the conclusion that the so called distal, side-on approach (schematically shown in Fig. 1), where the substrate approaches from the side and the most bulky group is pointed away from the complex is preferred, except for some tri-substituted variants. However, an experiment where different substituents were introduced on the salen ligand [14] seemed to point to an approach via the backbone (diamine). The molecular mechanics study allowed to identify different possibilities for the approach but, due to the use of classical force fields, no transition states could be considered. Therefore no conclusion on the influence of the transition state on the selectivity could be drawn. Regardless of these previous studies, the most important feature of a salen type complex with a diaminocyclohexane backbone appear to be the substituents on the 3/3' positions as schematically shown in Fig. 2. In the absence of bulky groups at these positions all selectivity is inhibited [13]. The substituents on the 5/5' positions [14] also have an influence on the resulting selectivity but the above mentioned studies could not provide a rationale for this observation

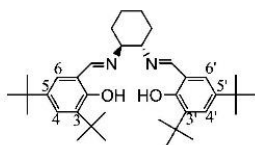


Fig. 2. Symmetrical salen ligand with a diamine backbone and the numbering of the substituents.

In this paper we provide an in depth study on the selectivity of the salen complex by localizing the transition states of various approach modes using a density functional theory (DFT) methodology in which the full catalyst complex is taken into account. This is, to our knowledge, the first time a DFT methodology is applied on the Jacobsen complex without simplification of the complex by omitting functional groups or larger parts of the complex. A report by Morokuma et al. [26] already showed the importance of including the salicylaldehyde parts in the model, but the inclusion of functional groups on these moieties will further improve the results. Both symmetrical and asymmetrical salen complexes will be investigated to get an in-depth view on the effect of substituents at various positions of the ligands on the selectivity. This is important when considering the effect of the covalent grafting of salen-type complexes, where an asymmetric substitution is often used to bind the complex to a support [27–29]. Such grafting procedures, or in general the immobilization of the homogeneous system into a heterogeneous system might be beneficial. Similar to many other homogeneous catalysts, the separation of the complex after reaction is a significant bottleneck for its applicability. Moreover, manganese-salen type complexes undergo deactivation via an irreversible stacking of the oxidized species, impeding their long-term use. The most effective way to optimize the catalyst is the immobilization of the homogeneous system on a solid support that impedes any stacking and facilitates the separation of the catalyst. On the other hand care needs to be taken in how far such procedure maintains the original high selectivity of the homogeneous system. In an earlier study [30] of the present authors a heterogeneous system was developed by the encapsulation of the Jacobsen complex in the pores of a metal organic framework. This immobilization omitting, all covalent bonds, resulted in a material that maintained the selectivity of the original catalyst. This could be explained by simulations of the epoxidation reaction where it was shown that the transition state governing the selectivity fitted perfectly in the cage of the host structure.

In this study we will assess the effect of a grafting procedure of the salen complex on its selectivity. The host material for the grafting procedure is the metal organic framework (MOF) MIL-101 [31,32]. This material has been chosen for the high stability in the various media that are used in the postmodification process. There have been various studies where the salen complex was immobilized on different supports [28,29,33–35]. This mostly led to a decrease in selectivity unless there was no covalent interaction between the complex and the host, allowing a high freedom of movement [30]. One possible approach to immobilizing the complex is building it up piece by piece on the solid support, as reported by Angelino et al. [28,29] In this paper a similar approach is used anchoring the catalyst on a chloromethylated MIL-101.

2. Computational and experimental methods

2.1. Reaction mechanism and models used for the catalyst

In an earlier study we have proven that by using the full salen complex as a model (Fig. 3(a)) the different approach vectors leading to the various enantiomers could be found. In addition, the difference in free energies between the various transition states were able to explain the observed selectivity of the catalyst [30]. In order to obtain a sufficient amount of detail, the full catalyst was used as a model, since any simplification would risk the loss of critical information on the steric influence. It was also shown that the calculations on the homogeneous system were able to rationalize also the observed selectivities for the same catalyst which was embedded in the NH₂-MIL-101(Al) system. In this paper we use the same model system for the computational study but both symmet-

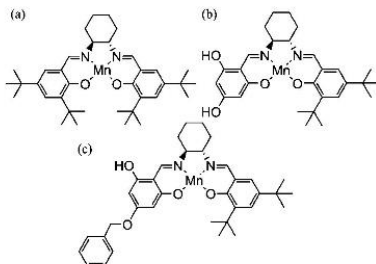


Fig. 3. Different models used in this study.

ric and asymmetric salen complexes have been considered to get insight into the effect of grafting on the selectivity. Indeed, a grafting procedure always disrupts the symmetry in the ligand system. All considered systems are shown in Fig. 3. Model (a) represents the symmetric salen complex which is taken as the reference system. Model (b) consists of a 2,4,6-trihydroxybenzaldehyde moiety at one side and 3,5-di-tert-butylbenzaldehyde at the other side. Model (c) has a methylbenzene substituted on one of the hydroxyl groups to mimic the grafting.

Early after the discovery of the salen ligands and their usefulness in selective epoxidation reactions the $Mn^V=O$ species was identified as a plausible intermediate [36,37]. Starting from the oxidized form of the complex the epoxide is formed in a two-step reaction, in the first step a single oxygen-carbon bond is formed leading to a radical intermediate, as shown in the mechanism in figure S3 of the supporting information. Afterwards this intermediate loses its radical character by forming the epoxide, this mechanism has been supported by the previous computational studies [20]. It has been proposed that this reaction can take place in different spin states, spin 0, 1 or 2 [38]. A detailed study of the spin states of oxidized complexes was reported before [39]. The step where the first carbon-oxygen bond is formed determines the resulting selectivity, this step is most favorable on the spin 1 plane, which will be used for the following calculations. The various transition states leading to the different enantiomers can be formed by considering all possible approach vectors. The model complex used has a (1*S*,2*S*)-diaminocyclohexane backbone, as a probe reactant to find these approach vectors dihydronaphthalene was used.

2.2. Localizing the transition states that control the selectivity

The transition states were optimized with the gaussian09 package [40], using the OPBE functional which consist of Handy's OPTX exchange [41] part and the well-known PBE [42] correlation part. This exchange-correlation combination has proven to be very performant for metal complexes with various spin states that are energetically close to each other [43,44]. These optimizations were done using a 6-311G Pople basis set. Starting from these initial guesses of the transition state, the distance of the forming C–O bond was fixed and a rotational scan was done around the Mn–O bond (Fig. 4). The rotational scan is necessary to determine whether the original structure is the only transition state possible.

The minimum from the rotational scan was isolated and reoptimized using the same functional with a 6-31+G(d) basis set on C,H,N and O and a 6-311++G(2df,2p) for Mn and Cl, van der Waals contributions were added afterwards via Grimme's D3 corrections [45].



Fig. 4. Rotational scans were done over the C–O⁺–Mn–O² dihedral angle of the transition state geometry as indicated.

For model (c) with the methylbenzene substituents, optimized geometries from the first step were modified directly without a prior rotational scan. Those structures were optimized directly on the high level. Frequency calculations were executed in order to calculate free energies at 295 K using the in-house software package, TAMkin [46]. A comparison of the free energies allows for the analysis of the enantioselectivity.

2.3. MOF synthesis

MIL-101(Cr) is synthesized according to a literature recipe [32] which differs from the original report by Férey et al. [31] only by the omission of the use of hydrogen fluoride. This results in a significant decrease in surface area but still yields a good crystalline and porous material. 4 mmol of $Cr(NO_3)_3 \cdot 9H_2O$ is mixed with 4 mmol of terphthalic acid and 20 ml of water in a teflon-lined steel autoclave. The autoclaves were heated to 210 °C over two hours and then kept at that temperature for eight hours. Afterwards the autoclaves were allowed to naturally cool to room temperature. The resulting precipitation was filtered off on a membrane filter. A green powder remained on the filter together with a significant amount of needle-like crystals that point to unreacted terphthalic acid. The MOF was washed two times on the filter with 20 ml of DMF to wash away the bulk of remaining terphthalic acid. The remaining solid was then stirred at 60 °C in DMF to wash out the last remaining acid. The solid was then again filtered off and dried under vacuum at 100 °C. The powder XRD pattern of the result was in agreement with the reported pattern of MIL-101 and a Langmuir surface area of 2541 m²/g was calculated from nitrogen sorption.

2.4. Chloromethylation

In order to introduce an anchor point for further postmodification a chloromethylation reaction as proposed earlier by Goesten et al. [47] was used. 1 g of MIL-101 (± 1.3 mmol) was suspended in 70 ml of nitromethane together with 7.8 mmol of $AlCl_3 \cdot 6H_2O$ and 3.6 mmol of methoxyacetyl chloride. The suspension was stirred for 5 h at 100 °C under reflux cooling. The chloromethylated material was filtered off and washed with water at 60 °C for 4 h and DMF at 60 °C for 4 h. Compared to the original MIL-101 structure the DRIFT spectrum (Fig. 9) shows a shoulder peak at 888 cm⁻¹ and a new peak at 919 cm⁻¹ the first can be attributed to trisubstituted benzene while the latter can be attributed to the H–C–H rocking vibration of the chloromethyl group. The powder showed a Langmuir surface area of 2479 m²/g, powder XRD showed no structural changes compared to the original material (Fig. 11). The amount of chlorine was determined by XRF to be about 30% of the present terphthalic groups. A schematic representation of the modifications is shown in Fig. 5.

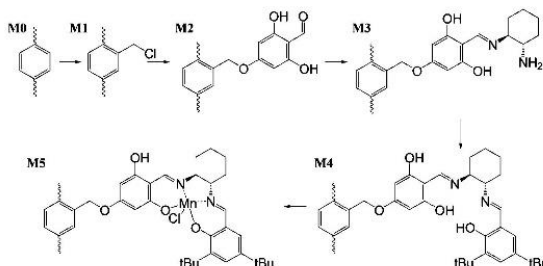


Fig. 5. Different steps in the build-up of the complex on a terephthalic linker of the MIL-101 metal organic framework.

2.5. Grafting 2,4,6-trihydroxybenzaldehyde

0.65 g of chloromethylated MIL-101 (± 0.962 mmol of chlorine) was brought in a schlenk flask together with 2.02 mmol of 2,4,6-trihydroxybenzaldehyde and 8.0 mmol of potassium hydroxide and 0.1 mmol of 18-crown-6. The contents of the flask were then dried under vacuum for a short time at room temperature before placing it under an argon atmosphere. 10 ml of anhydrous DMF was added via a septum. The mixture was stirred at 95 °C for 24 h. Afterwards the solid was filtered and washed overnight with DMF at 60 °C and two times with water at room temperature for three hours. The resulting powder showed a deep-red color instead of the original green color of the MIL-101(Cr). It was then dried under vacuum at 90 °C. For the further steps it is vital that any potassium hydroxide is removed from the system. The Langmuir surface area was determined to be 2312 m²/g and the XRD pattern showed no structural changes (Fig. 11). In the DRIFT spectrum (Fig. 9) a new vibration at 1686 cm⁻¹ appears that can be assigned to an aldehyde C=O vibration.

2.6. Grafting (1R,2R)-(-)-1,2-cyclohexanediamine

0.5 g of the carrier with the first benzaldehyde moiety grafted (± 0.75 mmol of benzaldehyde groups when assuming full conversion in the previous step) was suspended in 7.5 ml dioxane together with 5.6 mmol of (1R,2R)-(-)-1,2-cyclohexanediamine and 11.5 mmol of pyridine. The mixture was stirred under reflux conditions for 24 h after filtration the red powder was washed two times with DMF for 3 h at room temperature and 1 time in water at 60 °C overnight. It was then dried in vacuum at 90 °C. DRIFT analysis (Fig. 9) of the material showed two new peaks at 2852 cm⁻¹ and 2919 cm⁻¹. The peak at 1686 cm⁻¹ is still present but has diminished. The Langmuir surface area was 2016 m²/g while powder XRD (Fig. 11) showed the structure was preserved.

2.7. Grafting of 3,5-di-tert-salicylaldehyde

0.5 g of the material from the previous step was suspended in 7.5 ml of dioxane together with 1.14 mmol of 3,5-di-tert-butylbenzaldehyde and 11 mmol of pyridine. The suspension was stirred under reflux conditions for 24 h after which the material was filtered off. The resulting red powder was washed two times overnight in water at 60 °C and dried in vacuum at 80 °C. The surface area was 1805 m²/g and the structure was unchanged as analysed via powder XRD (Fig. 11). The DRIFT spectrum (Fig. 9) shows the same distinct peaks as the previous step: 1686 cm⁻¹, 2852 cm⁻¹ and 2919 cm⁻¹.

2.8. Chelating manganese

0.4 g of salen ligand@MIL-101(Cr) and 0.5 mmol of manganese(II) acetate tetrahydrate was mixed in 16 ml DMF and refluxed for 24 h. The filtered powder was stirred in 20 ml saturated aqueous NaCl solution. Afterwards the powder was washed in DMF at 60 °C and acetone at room temperature. The material was dried in vacuum at 80 °C. The manganese was quantified via XRF and shown to be 0.382 mmol/g. The Langmuir surface area was found to be 1418 m²/g and the structure remained virtually unchanged compared to the original MIL-101 system as shown by XRD analysis (Fig. 11).

2.9. Catalytic test

20 mg of heterogeneous salen catalyst (0.0076 mmol of active sites) was mixed in 5 ml of dichloromethane in a 10 ml vial. 0.154 mmol of dihydronaphthalene was added together with 0.768 mmol N-methylmorpholine-N-oxide (NMO) 1 mmol of toluene was added as internal standard and 0.2 mmol 3-chloroperbenzoic acid was added in 2 equal steps. The system was left to stir for 2 h at room temperature before the catalyst was filtered off. The product was analyzed with HPLC using a daicel AD-H column with a volumetric mixture of 98/2 hexane/isopropoxide with a flowrate of 0.9 ml/min as mobile phase. The detector was an UV-detector operating at 220 nm. The catalyst was washed with dichloromethane and dried for two hours at 80 °C and then reused for two more times with the same conditions. A blank reaction without any catalyst and with unmodified MIL-101 (using the same amount of chromium) was done under the same conditions.

3. Results and discussion

3.1. Theoretical rationalization for the selectivity

The salen variant with tert-butyl groups on both sides leads to two possible approaches of the substrate with respect to the active complex, as we have reported before [30]. Rotational scans show that these are indeed the most stable transition states (Figure S1 of the supporting information). One leads to the (1R,2S)-enantiomer, the other to the (1S,2R)-enantiomer (shown in Fig. 6). The specific bended shape of the salen complexes offers a clear cause for this selectivity. For the (1R,2S)-approach the substrate is sterically hindered by the wing of the salen complex facing upwards. The (1S,2R)-approach does not suffer from this unfavorable interaction and is thus found to be 10 kJ/mol more stable (Fig. 6). The calculated energy difference is small, and should of course be treated with care. However, small energy differences are expected for different

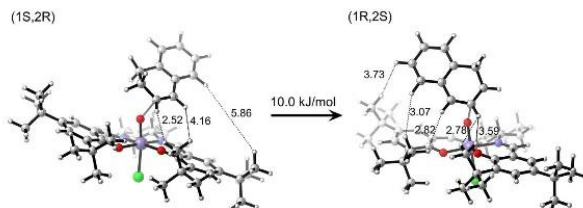


Fig. 6. Most stable transition state for the (1S,2R)-approach and the (1R,2S)-approach for model (a). The steric hindrance for the latter is significantly larger leading to it being 10 kJ/mol lower in free energy (distances in ångström).

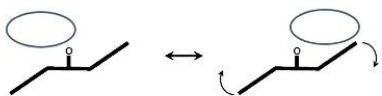


Fig. 7. Schematic representation of the change in the twist of the complex for the different approaches.

approaches in enantioselective reactions and thus this number is not surprising. Another difference between both approaches is the twist of the complex, an unfavorable approach pushes the wings down, inducing extra strain. This can be assessed by drawing a plane through the manganese and perpendicular to the manganese-oxygen bond. A measurement for the twist is the sum of the distance of the C5 and C5' carbon to this plane. For the favorable approach this distance is 3.69 Å, for the unfavorable (1R,2S)-approach this is 3.29 Å indicating the unfavorable approach pushes the wings of the complex open (Fig. 7), contributing to the energy difference.

When grafting a salen complex covalently on a substrate an anchor point has to be introduced, in order to achieve this, the bulky groups on the 5 and/or 3 positions are often omitted for more reactive groups which are not necessarily on the same position. In order to simulate this, —OH groups were placed on one side of the complex on the 4 and 6 position, which corresponds to the grafting method we used to bind the complex to the support (Fig. 5). When the substituents on the salen complex are asymmetrical, the number of possible approaches of the substrate to the catalyst increases. For both enantiomers two possibilities exist, the first one has the —OH groups closest to the substrate. The second one has the groups on the opposite side. This leads to four possibilities in total. For the symmetrical salen complex with bulky groups the wing facing upwards blocks the (1R,2S)-approach with the aid of those substituents. When those groups on the ring facing upwards are the —OH groups, this approach is no longer blocked, effectively decreasing the selectivity as seen in the energy differences between the transition states (Fig. 8). Most methods for constructing an asymmetric salen complex allow no control over which side of the ligand the non-bulky group are present on. Therefore the global selectivity will be lower as a combination of selective and less selective approaches will occur.

In order to further mimic the surroundings of the support a methylbenzene group was substituted on the hydroxyl group on the 4 position. This is only one of the possibilities how the complex can be grafted on the support, the substituent on the 6 position was not considered due to it being sterically less favorable. The results for this case are similar to the ones without the substitutions (Figure S4 of the supporting information), showing the methylbenzene groups are too far away to have any influence on the selectivity.

Looking at the structures in more detail (Fig. 6) one can see the importance of the tert-butyl groups for the induction of enan-

Table 2
Comparison of the complex shape to the selectivity.

	Vertical C5/C5' distance (Å)	Relative transition state free energy at 293 K (kJ/mol)
(1S,2R) _J	3.559	0
(1S,2R) _{Jl}	3.335	0.6
(1R,2S) _J	2.138	12.4
(1R,2S) _{Jl}	2.877	7.2

tioselectivity. Especially the substituents on the 3 and 3' positions seem crucial in blocking the (1R,2S)-approach. Once these groups are replaced by sterically less bulky —OH groups on the 4/6 positions the transition state for the less-favorable approach becomes unhindered. This is in agreement with the findings of Jacobsen et al. [13] who examined various substituents on the salen complex. The biggest part of the substrate, the aromatic ring in this case, interacts with the tert-butyl groups on the 3 position of the upward facing wing. The least-bulky part of the substrate also interacts with the complex via the tert-butyl group on the 3' position. However distances between the substrate and the upward facing wing are the smallest making this specific interaction the governing factor for enantioselectivity.

The substituents on the 5/5' positions are significantly less influential for the induction of selectivity which was also shown in experiments of Jacobsen et al. [14] The steric hindrance that blocks the (1R,2S)-approach is relatively small, with a distance of only 3.58 Å compared to less than 3 Å for the interaction with the tert-butyl group on the 3 position. This can imply there are two separate effects at work in inducing the selectivity. The transition state selectivity is the first effect, this is guided for the most by the 3 and 3' substituents. The transition state effect is crucial since the absence of these substituents leads to a non-selective catalyst. The second effect is probably the approach of the substrate toward the activated oxygen. The path followed by a reactant molecule to reach the active site and the orientation of this molecules is also managed by the ligand and the substituents present. Since the 5 and 5' groups have only a small influence on the transition state selectivity but experimental observations show they do have an effect on the resulting enantioselectivity they will probably manage the orientation of the approach.

Similar to the symmetrical salen complex the shape of the asymmetrical complex for the different transition states can be correlated to the stability of the approach (Table 2). This effect is also a consequence of the steric hindrance, if the complex is 'pushed' open the transition state is less stable. Table 2 shows the comparison between the C5/C5' out of plane displacement and the relative free energy of the transition states. When comparing the geometry of a transition state for different enantiomers both the substrate-ligand distance and the twist of the complex have to be taken into account to assess the possibilities of approach.

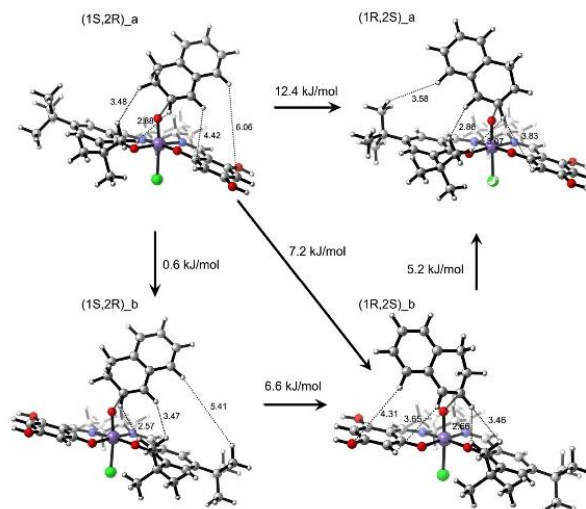


Fig. 8. Different transition states for the asymmetric salen complex with hydroxy-groups (model (b)). The two possible positions of the groups are denoted I and II, (1S,2R) J is the most stable (distances in ångström).

Until now we have focused on the influence of the steric effects on the enantioselectivity of the material, but the modification of substituents also has some electronic effects. To assess these effects different groups of similar size with different electron withdrawing and donating effects have to be compared. Although the asymmetric catalyst with methylbenzene substituents on the $-OH$ modification is more bulky than the variant without those substituents, we showed before that for dihydronaphthalene this group is too far away from the active site to have any steric effect. Thus the only effects at work here are electron donating effects. The

electron donating power of an ether is slightly lower as for an alcohol, which slightly decreases the selectivity. But this conclusion has to be drawn with care since the energy difference is barely 1 kJ/mol (figure S4 of the supporting information). This allows us to conclude the steric effects are significantly more important than the electronic effects. That conclusion is in agreement with an experimental study from Jacobsen et al. [48] where strongly electron donating groups on the C5/C5' positions yielded a slight improvement of the enantioselectivity. These electronic effects have shown to have a much more pronounced effect on the activity of the cat-

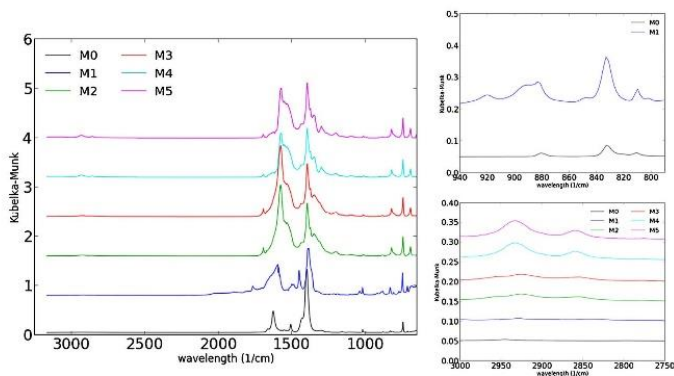


Fig. 9. Evolution of the IR pattern during the postmodification steps.

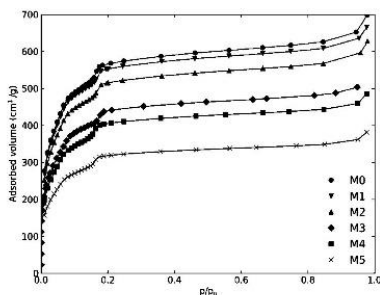


Fig. 10. Evolution of the nitrogen sorption for the different steps in the construction of the complex (M0–M5).

alyst as studied by Kochi et al. [36] but this is beyond the scope of our report.

3.2. Selectivity of asymmetric grafted complexes

To confirm the decrease in selectivity with asymmetrical complexes we have immobilized the salen complex via a reported procedure on an alternative substrate, the MIL-101(Cr) metal organic framework. The MIL-101(Cr) MOF is a very stable material, both thermally as in most common solvents. However its use as a carrier material for catalytically active sites is severely limited by the lack of any functional groups available for postmodification. The chloromethylation procedure proposed by Goesten et al. [47] is an excellent way to solve this. The procedure is relatively mild, and is applicable to structures which are far less stable than the proposed material. The primary chlorine moiety is a good leaving group for further modifications.

The Jacobsen salen complex was systematically built up as shown in Fig. 5 and followed by various characterization techniques. All reactions have been analyzed by DRIFT measurements (Fig. 9). The chloromethylation is characterized by some slightly visible absorption peaks around 900 cm^{-1} . The coupling of 2,4,6-trihydroxybenzaldehyde is observed by the presence of a C=O stretching vibration at 1686 cm^{-1} . The presence of this peak after thorough washing shows that the benzaldehyde is grafted on the structure. The next step, involving the formation of the first imine bond, coupling (1R,2S)-diaminocyclohexane is shown by two peaks at 2852 cm^{-1} and 2919 cm^{-1} corresponding to the hydrogen vibrations of the cyclohexane moiety. A broad peak around 1633 cm^{-1} could point to the formation of the C=N bond but it is only slightly visible. The further steps featuring the formation of a second imine bond grafting 3,5-di-tert-butylbenzaldehyde and the chelating of manganese does not lead to any new vibrations.

The successful chelating of manganese is determined by XRF analysis, after washing the final material several times the manganese was still present and could be quantified at 0.38 mmol/g . This is a relatively high loading, indicating there will probably be complexes both in the pores and on the outer surface of the MOF. When employing a postmodification procedure on a metal organic framework the structural integrity of the host should be assessed at every step. The way to confirm this is verifying the crystallinity of the sample. This is achieved by a powder XRD measurement after every step (Fig. 11). These show the original crystallinity remains during the grafting steps, thus the structural integrity of the host is maintained.

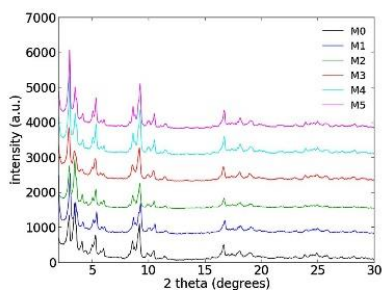


Fig. 11. Evolution of the XRD pattern during the postmodification steps (M0–M5).

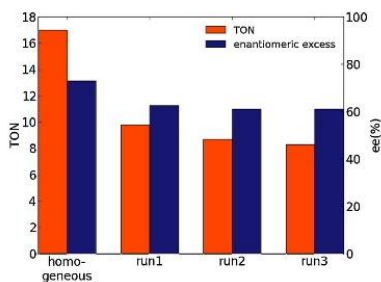


Fig. 12. Turn over numbers and selectivities for the various runs using the homogeneous, symmetrical complex and the grafted, asymmetrical complex.

The catalytic activity of the immobilized salen complex is assessed by a test reaction. For that we selected the epoxidation of dihydronaphthalene, which is a widely used benchmark reaction for the system [12,49–51]. The use of 3-chloroperbenzoic acid and 4-Methylmorpholine N-oxide has shown to be performed in combination with manganese salen complexes. In our hands the commercial salen catalyst gave a conversion of 85% and 70% enantiomeric excess. The proposed catalyst showed a conversion of 48% with a %ee of 62.5%. The conversion is significantly lower compared to the commercial Jacobsen complex in homogeneous conditions, which yielded a conversion of approximately 85%. The selectivity is also lower; which has been observed in similar grafting procedures on other carrier materials [28,29,33,52,53]. Some alternative immobilization procedures such as electrostatic grafting and encapsulation have shown to maintain the original selectivity as we have shown in earlier reports [30,35]. However we can still conclude this metal organic framework is a good carrier for the covalent grafting since the loss of selectivity is very limited.

To verify the reusability of the crafted catalyst two consecutive runs were executed using the same batch. During these runs the selectivity remained the same, while the conversion decreased significantly. However when comparing the turn over number (TON) for the different runs it remains virtually unchanged (Fig. 12). Meaning the decrease in activity is mostly due to the loss of material in the washing and drying steps between the runs. This shows the complex is firmly grafted to the MIL-101 host structure and there is minimal leaching of the active sites. The same is shown by the lack of any detectible amount of manganese present in the reaction

mixture. These results confirm the conclusions from the *ab initio* modelling, the grafting of the asymmetric complex decreases the selectivity compared to a reaction in the homogeneous phase with the symmetrical complex.

4. Conclusions

By using the full salen complex as a model and dihydronaphthalene as a probe substrate we were able to obtain insight in the selectivity of the manganese-salen complex in the epoxidation of unfunctionalized olefins. It can be shown that there is one optimal geometry for each enantioselective approach, rotational scans on the transition state show only one minimum for the (1*R*,2*S*) and (1*S*,2*R*) structure. The transition states provide a rationale for the experimental observed dependence of the selectivity with respect to the type and place of substituents on the ligand. The 3/3' positions are the most crucial and they induce the most significant interaction with the approaching substrate. Substituents on the 5/5' position are less crucial and will probably manage the orientation of the approach rather than the actual transition state. A second geometrical effect is the shape of the complex, an unfavorable approach pushes the complex in a more flattened geometry while the favorable approach allows the complex more freedom to form its folded orientation. These results allow us to propose a rationale for the best method of immobilizing salen-type complexes, since covalent grafting will always lead to some decrease in selectivity. Alternative approaches such as electrostatic immobilization and encapsulation are much more promising.

Many approaches for heterogenizing a salen complex require the use of an asymmetric complex on which the more bulky groups are replaced by a more reactive group that can couple to the carrier. The models of asymmetric complexes show the energy difference in the transition state for the (1*S*,2*R*)- and (1*R*,2*S*)-approach is significantly smaller than for the symmetric complex with *tert*-butyl substituents that were taken as a reference. Therefore the grafted asymmetric complexes are prone to be less selective than the homogeneous ones. As an example of covalent grafting we applied a well-established postmodification procedure on an alternative substrate, the MIL-101(Cr) metal organic framework. Compared to the homogeneous catalyst, this system still yields a very selective catalyst showing MIL-101(Cr) is a good carrier material for the salen complex.

In order to design a heterogeneous salen catalyst with a minimal loss of selectivity a less-invasive grafting procedure should be used. Possible approaches are electrostatic grafting where the support material is charged and acts as a counter ion on the axial position of the salen complex [35,53]. Another approach is the encapsulation of the complex in the cages of the support material confining it by sufficiently small window sizes, as shown earlier by these authors [30].

Acknowledgements

The research was financed by UGent GOA grant 01G00710, the European Research Council for funding through the European Community's Seventh Framework Programme (FP7(2007-2013) ERC grant agreement no. 240483) and the Research Board of Ghent University (BOF). S.W. acknowledges Research Foundation Flanders for a fellowship. Computational resources and services were provided by Ghent University (Stevin Supercomputer Infrastructure).

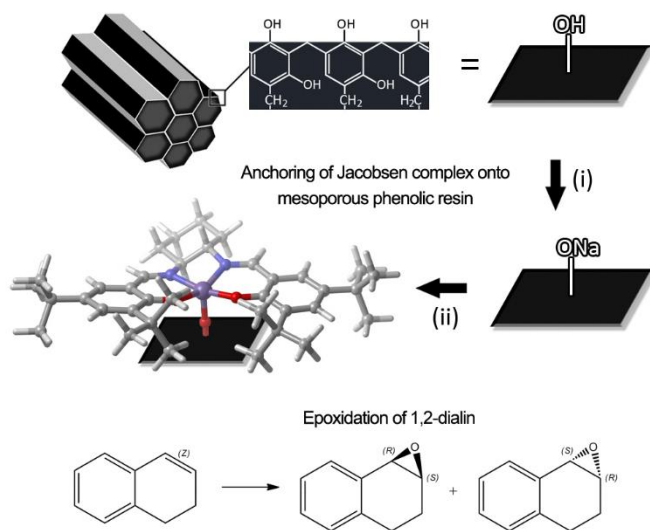
Appendix A. Supplementary data

Supplementary data associated with this article can be found, in the online version, at <http://dx.doi.org/10.1016/j.molcata.2015.05.020>

References

- [1] M. Breuer, K. Ditrach, T. Habicher, B. Hauer, M. Keßler, R. Stürmer, T. Zelinski, *Angew. Chem. Int. Ed.* 43 (2004) 788.
- [2] J.M. Hawkins, T.J.N. Watson, *Angew. Chem. Int. Ed.* 43 (2004) 3224.
- [3] H.U. Blaser, F. Spindler, M. Studer, *Appl. Catalysis, General* 221 (2001) 119.
- [4] Y. Gao, R.M. Hanson, J.M. Klunder, S.Y. Ko, H. Masamune, K.B. Sharpless, *J. Am. Chem. Soc.* 109 (1987) 5765.
- [5] P.R. Carlier, K.B. Sharpless, *J. Org. Chem.* 54 (1989) 4016.
- [6] D.V. Deubel, G. Frenking, P. Gisdakis, W.A. Herrmann, N. Rosch, J. Sundermeyer, *J. Acc. Chem. Res.* 37 (2004) 645.
- [7] K.A. Jørgensen, R.A. Wheeler, R. Hoffmann, *J. Am. Chem. Soc.* 109 (1987) 3240.
- [8] T. Katsuki, K.B. Sharpless, *J. Am. Chem. Soc.* 102 (1980) 5974.
- [9] K.B. Sharpless, S.S. Woodard, M.G. Finn, *Pure Appl. Chem.* 55 (1983) 1823.
- [10] S.S. Woodard, M.G. Finn, K.B. Sharpless, *J. Am. Chem. Soc.* 113 (1991) 106.
- [11] T. Katsuki, *J. Synth. Org. Chem. Jpn.* 53 (1995) 940.
- [12] R. Irie, K. Noda, Y. Ito, N. Matsumoto, T. Katsuki, *Tetrahedron Lett.* 31 (1990) 7345.
- [13] W. Zhang, E.N. Jacobsen, *J. Org. Chem.* 56 (1991) 2296.
- [14] E.N. Jacobsen, W. Zhang, A.R. Muci, J.R. Ecker, L. Deng, *J. Am. Chem. Soc.* 113 (1991) 7063.
- [15] N.H. Lee, A.R. Muci, E.N. Jacobsen, *Tetrahedron Lett.* 32 (1991) 5055.
- [16] M. Palucki, G.J. McCormick, E.N. Jacobsen, *Tetrahedron Lett.* 36 (1995) 5457.
- [17] F. Fréchet, B.B. Dideriksen, D. Tanner, P.O. Norrby, *J. Am. Chem. Soc.* 127 (2005) 13672.
- [18] L. Cavallo, H. Jacobsen, *Angew. Chem. Int. Ed.* 39 (2000) 589.
- [19] H. Jacobsen, L. Cavallo, *Chem. Eur. J.* 7 (2001) 800.
- [20] L. Cavallo, H. Jacobsen, *Inorg. Chem.* 43 (2004) 2175.
- [21] Y.G. Abashkin, S.K. Burt, *Org. Lett.* 6 (2004) 59.
- [22] C. Linde, M. Arnold, P.O. Norrby, B. Åkermark, *Angew. Chem. Int. Ed. Engl.* 36 (1997) 1721.
- [23] P.O. Norrby, C. Linde, B.J. Åkermark, *Am. Chem. Soc.* 117 (1995) 11035.
- [24] L. Cavallo, H. Jacobsen, *Eur. J. Inorg. Chem.* (2003) 892.
- [25] L. Cavallo, H. Jacobsen, *J. Org. Chem.* 68 (2003) 6202.
- [26] I.V. Khavrutskii, D.G. Musae, K. Morokuma, *Proc. Natl. Acad. Sci. U.S.A.* 101 (2004) 5743.
- [27] L. Canali, D.C. Sherrington, H. Deleuze, *React. Funct. Polym.* 40 (1999) 155.
- [28] M.D. Angelino, P.E. Laibinis, *Macromolecules* 31 (1998) 7581.
- [29] M.D. Angelino, P.E. Laibinis, *J. Polym. Sci. Part A: Polym. Chem.* 37 (1999) 3888.
- [30] T. Bogaerts, A. Van Puyen-De Deyne, Y.-Y. Liu, F. Lynen, V. Van Speybroeck, P. Van Der Voort, *Chem. Commun.* 49 (2013) 8021.
- [31] G. Ferey, C. Mellot-Draznieks, C. Serre, F. Millange, J. Dutour, S. Surble, I. Margiolaki, *Science* 309 (2005) 2040.
- [32] D. Jiang, A.D. Burrows, K.J. Edler, *CrystrEngComm* (2011).
- [33] P. Das, A.R. Silva, A.P. Carvalho, J. Pires, C. Freire, *Catal. Lett.* 129 (2009) 367.
- [34] R.N. Ji, K. Yu, L.L. Lou, Z.C. Gu, S.X. Liu, *J. Inorg. Organomet. Polym. Mater.* 20 (2010) 675.
- [35] J. De Decker, T. Bogaerts, I. Muylaert, S. Delahaye, F. Lynen, V. Van Speybroeck, A. Verberckmoes, P. Van der Voort, *Mater. Chem. Phys.* 141 (2013) 967.
- [36] K. Srinivasan, P. Michaud, J.K. Kochi, *J. Am. Chem. Soc.* 108 (1986) 2309.
- [37] D.A. Plattner, D. Feichtinger, J. El-Bahraoui, O. Wiest, *Int. J. Mass. Spectrom.* 195 (2000) 351.
- [38] Y.G. Abashkin, J.R. Collins, S.K. Burt, *Inorg. Chem.* 40 (2001) 4040.
- [39] S. Wouters, T. Bogaerts, P. Van der Voort, V. Van Speybroeck, D. Van Neck, *J. Chem. Phys.* 140 (2014) 241103.
- [40] M.J. Frisch, G.W.T., H.B. Schlegel, G.E. Scuseria, M.A. Robb, J.R. Cheeseman, G. Scalmani, V. Barone, B. Mennucci, G.A. Petersson, H. Nakatsuji, M. Caricato, X. Li, H.P. Hratchian, A.F. Izmaylov, et al. *Revision B.0.1*, Gaussian, Inc. Wallingford CT ed. 2008.
- [41] N.C. Handy, A.J. Cohen, *Mol. Phys.* 99 (2001) 403.
- [42] J.P. Perdew, K. Burke, M. Ernzerhof, *Phys. Rev. Lett.* 77 (1996) 3865.
- [43] M. Swart, *Inorg. Chim. Acta.* 360 (2007) 179.
- [44] M. Swart, A.R. Groenhof, A.W. Ehlers, K. Lammertsma, *J. Phys. Chem. A* 108 (2004) 5479.
- [45] S. Grimme, J. Antony, S. Ehrlich, H. Krieg, *J. Chem. Phys.* (2010) 132.
- [46] A. Ghyssels, T. Verstraeten, K. Hemelsoet, M. Waroquier, V. Van Speybroeck, *J. Chem. Inf. Model.* 50 (2010) 1736.
- [47] M.G. Goesten, K.B. Sai Sankar Gupta, E.V. Ramos-Fernandez, H. Khajavi, J. Gascon, F. Kapteijn, *CrystrEngComm* 14 (2012) 4109.
- [48] S. Chang, R.M. Heid, E.N. Jacobsen, *Tetrahedron Lett.* 35 (1994) 669.
- [49] W. Zhang, J.L. Loebach, S.R. Wilson, E.N. Jacobsen, *J. Am. Chem. Soc.* 112 (1990) 2801.
- [50] T. Yamada, K. Imagawa, T. Nagata, T. Mukaiyama, *Chem. Lett.* (1992) 2231.
- [51] R. Irie, K. Noda, Y. Ito, N. Matsumoto, T. Katsuki, *Tetrahedron Asymmetry* 2 (1991) 481.
- [52] I. Kuznetarska-Biernacka, C. Pereira, A.P. Carvalho, J. Pires, C. Freire, *Appl. Clay. Sci.* 53 (2011) 195.
- [53] F. Maia, N. Mahata, B. Jarras, A.R. Silva, M.F.R. Pereira, C. Freire, J.L. Figueiredo, *J. Mol. Catal. A-Chem.* 305 (2009) 135.

PAPER IV: COVALENT IMMOBILIZATION OF THE JACOBSEN CATALYST ON MESOPOROUS PHENOLIC POLYMER: A HIGHLY ENANTIOSELECTIVE AND STABLE ASYMMETRIC EPOXIDATION CATALYST



J. De Decker, T. Bogaerts, I. Muylaert, S. Delahaye, F. Lynen, V. Van Speybroeck, A. Verberckmoes, P. Van der Voort, *Materials Chemistry and Physics*, 141 (2013), 967-972, **2013**.

T. Bogaerts assisted in the catalytic tests presented here.

Reprinted with permission from Elsevier. © Elsevier 2015



Covalent immobilization of the Jacobsen catalyst on mesoporous phenolic polymer: A highly enantioselective and stable asymmetric epoxidation catalyst



Jeroen De Decker^a, Thomas Bogaerts^{a,b}, Ilke Muylaert^a, Sander Delahaye^c, Frederic Lynen^c, Veronique Van Speybroeck^b, An Verberckmoes^d, Pascal Van Der Voort^{a,*}

^a Department of Inorganic and Physical Chemistry, Center for Ordered Materials, Organometallics and Catalysis (COMOC), Ghent University, Krijgslaan 281-S3, 9000 Ghent, Belgium

^b Center for Molecular Modeling, Ghent University, Technologiepark 903, 9052 Zwijnaarde, Belgium

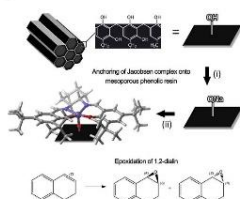
^c Department of Organic Chemistry, Separation Sciences, Ghent University, Krijgslaan 281-S4, 9000 Ghent, Belgium

^d Department of Applied Engineering Sciences, University College Ghent, Valentin Vaerwyckweg 1, 9000 Ghent, Belgium

HIGHLIGHTS

- Synthesis of mesoporous phenolic resin with high specific surface area and large pores.
- Covalent immobilization of a manganese-salen complex on mesoporous polymer.
- Enantioselective epoxidation of dialin with a heterogeneous catalyst.
- Demonstration of leaching resistance in organic solvent.

GRAPHICAL ABSTRACT



ARTICLE INFO

Article history:

Received 3 April 2013
Received in revised form
6 June 2013
Accepted 19 June 2013

Keywords:

Polymers
Microporous materials
Chemical synthesis
Fourier Transform Infrared Spectroscopy (FTIR)
Chemisorption
Oxidation

ABSTRACT

The Jacobsen catalyst, *N,N*-bis(3,5-di-*tert*-butylsalicylidene)-1,2-cyclohexanediaminomanganese (III) chloride is covalently immobilized on mesoporous phenolic resin through a direct and simple procedure. The immobilization is evident from nitrogen sorption and quantitative XRF measurements. A complex loading of 0.09 mmol g⁻¹ is obtained, corresponding to well dispersed Mn-complexes on the surface of the mesoporous phenolic resin. This novel catalytic system shows good catalytic activity and excellent enantioselectivity in the asymmetric epoxidation of 1,2-dialin. The heterogenized Jacobsen catalyst is demonstrated to be a re-usable and non-leaching catalytic system.

© 2013 Elsevier B.V. All rights reserved.

1. Introduction

Epoxides are versatile intermediates in organic chemistry. Their inherent polarity and the strain in the three-membered ring makes them interesting compounds for regioselective ring opening

* Corresponding author. Tel.: +32 9 242 42 44
E-mail address: pascal.vandervoort@ugent.be (P. Van Der Voort).

reactions, followed by the formation of 1,2-difunctional products [1–3]. In particular, optically pure epoxides with two vicinal chiral centers are often used as intermediate in the synthesis of biologically and pharmaceutically active compounds [4]. Today, the synthesis of chiral epoxides generally occurs by oxidation of olefins. In this field, the asymmetric epoxidation of unsubstituted alkenes is not facile since no substituents are present to control the orientation of the substrate. The Jacobsen catalyst, a manganese (III) *salen* complex, has proven to be a very efficient catalyst for asymmetric alkene epoxidation reactions [5]. As shown in Fig. 1 (Left), these *salen*-type complexes have two chiral sp^3 hybridized carbon atoms (*) in the vicinity of the metal center. The presence of these two stereogenic centers enables excellent stereochemical control in the epoxidation step. Furthermore, these complexes possess bulky *t*-butyl groups on the aromatic rings, acting as substrate directing agents (Fig. 1). The Jacobsen catalyst can react with a variety of terminal oxidants, such as hydrogen peroxide, sodium hypochlorite and iodanyl arenes, forming activated oxo-manganese (V) species that are able to epoxidize contacting alkene substrates [6].

Fig. 1 (Right) shows the activated Jacobsen catalyst. Due to steric hindrance of the bulky *t*-butyl groups, the olefin substrates are forced to approach the activated manganese center via the dissymmetric diimine bridge (pathways *a*, *b* and *b'*) [7,8].

The major drawback of these catalysts, however, is the deactivation process in homogeneous phase due to the formation of inactive dimeric μ -oxo-manganese (IV) species [9–11]. In recent years, heterogenization through immobilization of these homogeneous *salen*-type catalysts on mesoporous supports has become an object of intensive research. Due to local site isolation of the complexes on a solid matrix, dimerisation can be prevented. Furthermore, the possibility of simple recyclability after the catalytic run makes these expensive complexes more economically attractive. The majority of the reports on the heterogenization of Mn (III) *salen* catalysts have mostly been centered on encapsulation, adsorption or covalent attachment to porous inorganic supports, such as zeolites, MCM-41, Al-MCM-41, mesoporous silicagel, SBA-15 and clays [1,12–19]. These strategies have proven to be efficient, yet for covalent immobilization the original structure of the manganese complex is modified or multiple synthetic steps and structural changes to the parent catalyst structure and support are required. Intensive research on the heterogenization of *salen*-type and other metal complexes has been performed by De Vos et al., being particularly successful in the field of zeolite encapsulation and silica grafting [20–22]. Various *metallasalen* complexes and analogues have been anchored successfully on hybrid porous materials such as ordered mesoporous organosilicas (PMOs) and metal organic frameworks (MOFs) [23]. Various attempts to produce polymer-supported Jacobsen catalysts have been reported, e.g. through attachment via the aromatic rings, by binding pre-formed Mn-complexes to a pyridine-containing polystyrene-based resin or by physical entrapment of the complex within a suitable polymer

matrix [24–28]. Silva et al. published the immobilization of the Jacobsen catalyst through a direct axial coordination of the metal center onto the phenolate groups of a modified, commercial, activated carbon [29]. This immobilization procedure involves a direct and simple reflux procedure. The newly developed catalysts showed high activity in the asymmetric epoxidation of styrene and α -methylstyrene, using PhIO and *m*-CPBA as oxidants. However, the obtained ee values were rather moderate [30]. Also, prior to the immobilization of the manganese complex on activated carbon, the carbon surface has to be pre-treated by an oxidation step (mostly by H_2O_2 treatment or with an air flow) in order to generate sufficient surface phenolic hydroxyl functions as anchoring points [29]. When the procedure was applied on carbon xerogels, the surface pre-treatment was performed under 5% O_2 [31].

In this study, mesoporous phenolic resins are introduced as a novel support for the manganese (III) *salen* complex. These phenolic resins are an advanced class of mesoporous materials combining a high porosity with the organic properties of the corresponding polymer. Moreover, this new generation of mesoporous materials has shown to be highly stable, both thermally and mechanically [32,33]. The mesoporous phenolic resins contain an abundance of phenolic hydroxyl groups in their framework. Consequently, the pre-oxidation is not required for these materials, providing a time efficient synthesis pathway. This newly developed catalyst is evaluated for its catalytic performance in the asymmetric epoxidation of dialin (1,2-dihydronaphthalene). The results are compared to the catalytic activity of the homogeneous Jacobsen catalyst system. To evaluate the recyclability and the resistance to leaching, the heterogeneous catalyst was used in three consecutive epoxidation reactions.

2. Experimental

2.1. Chemicals

Resorcinol, Formalin (36%), Pluronic F127, Jacobsen catalyst (*N,N'*-bis(3,5-di-*tert*-butylsalicylidene)-1,2-cyclohexanediaminomanganese (III) chloride), 1,2-dihydronaphthalene and sodium hypochlorite solution (10%) were purchased from Sigma Aldrich. Suprapur Nitric acid 65% was purchased from Merck Chemicals. All chemicals were used as received.

2.2. Synthesis of mesoporous phenolic resin

In a typical synthesis, resorcinol (2.2 g) and Pluronic F127 (2.2 g) were dissolved in ethanol (9.0 mL) containing HNO_3 (3 M, 9 mL) during 15 min at room temperature. Subsequently, 2.6 g of aqueous formaldehyde solution (36 wt %) was added dropwise to the above solution, under continuous stirring. After an additional 15 min of stirring, the resulting clear solution was poured and dried on a dish during 6 h to evaporate the ethanol. The sample was then collected

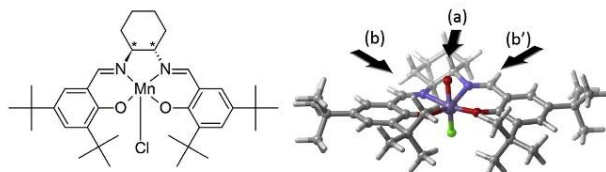


Fig. 1. (Left) Structure of the Jacobsen catalyst, *N,N'*-bis(3,5-di-*tert*-butylsalicylidene)-1,2-cyclohexanediaminomanganese (III) chloride. The chiral carbon atoms are denoted with an asterisk. (Right) Spatial structure of the activated Jacobsen catalyst. The arrows indicate the possible approaches of the olefin substrates to the active site of the catalyst.

and cured at 333 K for 11 h, resulting in a yellow-red colored resin. The template block copolymer was removed through calcination at 673 K for 6 h (heating rate: $1\text{ }^{\circ}\text{C min}^{-1}$), resulting in black colored resin.

2.3. Asymmetric epoxidation of dialin (1,2-dihydronaphthalene)

The performance of the novel heterogeneous catalyst was evaluated in the asymmetric epoxidation of 1,2-dialin, using sodium hypochlorite (NaOCl) as oxidant. In a typical reaction, 0.05 g of heterogeneous catalyst ($0.09\text{ mmol Mn g}^{-1}$) was added to a solution of dialin (0.077 mmol), NaOCl (0.077 mmol) and dichloromethane (5 mL, solvent). After stirring for 24 h at room temperature, the catalyst was filtrated from the reaction mixture and the conversion and enantiomeric excess were determined by HPLC, using toluene as internal standard. The formation of the epoxide is confirmed by $^1\text{H NMR}$. The heterogeneous catalyst was recovered and tested in a second and third run at the same conditions. The amount of homogeneous Jacobsen catalyst tested was 0.0113 g ($0.396\text{ mmol Mn g}^{-1}$) in order to have the same amount of Mn centers as are present in the heterogeneous catalyst ($0.0045\text{ mmol Mn per }0.05\text{ g}$).

2.4. Characterization

Nitrogen gas sorption experiments were conducted at 77 K with a Micromeritics Tristar 3000. Samples were vacuum dried at $120\text{ }^{\circ}\text{C}$ prior to analysis. The pore size distribution was calculated using the BJH method. Total pore volume was determined at $p/p^0 = 0.97\text{--}0.99$. The specific surface area was calculated using the BET method. DRIFT-spectra were measured on a Nicolet 6700 FTIR spectrometer from ThermoScientific. UV–vis measurements were performed on a Shimadzu Spectrophotometer UV-1800. X-ray fluorescence (XRF) spectroscopy measurements were performed on a Bruker system with molybdenum X-rays. XPS measurements were recorded on an X-ray photoelectron spectroscopy S-Probe XPS spectrometer with monochromated Al (1486 eV) exciting radiation from Surface Science Instruments (VG). A flood gun was used and set to 10 eV. A nickel grid was placed 3 mm above the samples in order to suppress charging of the samples.

Chiral HPLC analyses were performed on a Waters 2690 separation module, equipped with a UV detector (220 nm), using a

Daicel AD-H-type column with hexane/isopropanol (98/2 vol.%) as mobile phase at a flow rate of 0.900 mL min^{-1} .

The reaction products were identified by $^1\text{H NMR}$, 1,2-dihydronaphthalene oxide. $^1\text{H NMR}$ (300 MHz, CDCl_3): δ 7.4e7.2 (4H, m, Ar), 3.85 [1H, d, J 4.5 Hz, $\text{CH}(\text{O})\text{CHCH}_2$], 3.73 [1H, dd, J 4.3, 3.0 Hz, $\text{CH}(\text{O})\text{CHCH}_2$], 2.80 (1H, m), 2.55 (1H, dd, J 6.0, 15.5 Hz), 2.43 (1H, m), 1.78 (1H, m) [34].

3. Results and discussion

3.1. Covalent immobilization of manganese salen complex on mesoporous phenolic resin

Fig. 2 gives an overview of the synthesis strategy to immobilize the Jacobsen catalyst on the surface of mesoporous phenolic resin. In step (i), the hydroxyl surface was activated by refluxing with an aqueous solution of sodium hydroxide (0.03 M) for 1 h. A decrease in pH of the aqueous solution was observed, indicating the exchange of phenolic protons (p-OH) for sodium cations (p-ONa), which causes partial neutralization of the alkaline solution. The solid was then filtrated and deionized water was used to rinse the polymer, making it NaOH-free. This washing step was repeated until constant pH. Subsequently the material was vacuum dried at $120\text{ }^{\circ}\text{C}$. In step (ii), 0.5 g of the activated solid was refluxed for 6 h together with 0.05 g of commercial Jacobsen catalyst in 100 mL of absolute ethanol. Subsequently, in order to remove the excess of physisorbed complexes, Soxhlet extraction was performed. Ethanol was used in this extraction, being a good solvent to the Jacobsen complex. After 24 h of Soxhlet extraction the solid was filtrated and vacuum dried at $120\text{ }^{\circ}\text{C}$ for 15 h.

3.2. Characterization

The immobilization procedure of the Mn-salen complex on the phenolic resin was monitored by means of UV–vis spectroscopy of the solution of the homogeneous Jacobsen catalyst (0.05 g in 100 mL absolute ethanol) before and after 6 h reflux with 0.5 g of the activated phenolic resin. The peak at 492 nm of the d–d transition of Mn(III) was reduced with 45% after 6 h, indicating a successful loading (of about 0.072 mmol g^{-1}) of manganese salen complex onto the phenolic resin [35].

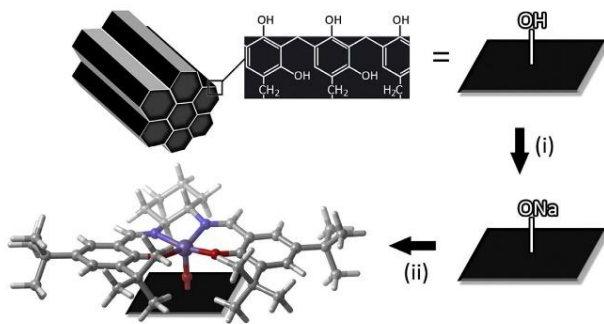


Fig. 2. Covalent immobilization of the Jacobsen catalysts through direct axial coordination on the surface phenol groups of a mesoporous phenolic resin. The resin contains a large abundance of surface phenolic hydroxyl groups. (i) Activation of surface hydroxyl groups by reflux in NaOH solution. (ii) Anchoring of the salen complex by exchanging the sodium cation with the manganese center of the complex. Color index: manganese (purple), nitrogen (blue), oxygen (red). (For interpretation of the references to colour in this figure legend, the reader is referred to the web version of this article.)

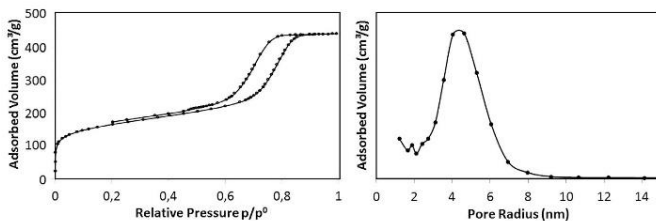


Fig. 3. Nitrogen sorption measurements and pore size distribution of mesoporous phenolic resin after covalent immobilization of the Jacobsen catalyst.

Table 1

Textural parameters of the phenolic resin support before and after complex loading.

	S_{BET}^a ($\text{m}^2 \text{g}^{-1}$)	Pore size ^b (nm)	V_p^c ($\text{cm}^3 \text{g}^{-1}$)
Original support	604	9.2	0.68
After immobilization	397	8.1	0.52

^a Specific surface area calculated using the BET theory.

^b Mean pore size determined by the BJH method.

^c Total pore volume determined at $p/p^0 = 0.97\text{--}0.99$.

The nitrogen sorption isotherm and the pore size distribution of the immobilized catalyst are shown in Fig. 3. The figure shows a type IV isotherm with an H_1 -type hysteresis loop, indicating the mesoporous structure of the support material. A clear capillary condensation step is observed between $p/p^0 = 0.7\text{--}0.9$. The corresponding pore parameters including the specific surface area, pore diameter and pore volume of the support before and after immobilization are summarized in Table 1.

After immobilization of the Mn-salen complex, the specific surface area, pore size and pore volume have decreased, also indicating a successful loading of the large complex inside the pores. It is suggested that the cylindrical open pores of the mesoporous phenolic resins are large enough to give easily access to both the bulky salen complexes ($17 \text{ \AA} \times 11 \text{ \AA}$) and the substrates after anchoring.

In the entire anchoring strategy, it is important to prove unambiguously that the chlorine atom is substituted and an axial manganese–oxygen support bond is formed, as shown in Fig. 2. This is not an easy task. The phenolic resin is a dark brown/black substrate that makes a lot of spectroscopic characterization techniques unreliable or impossible. Moreover, the intense aromatic and aliphatic vibrations complicate the infrared and Raman characterization. In this respect, the distinction of the vibrations of the salen-complex anchored on the phenolic resin support was impossible, as these vibrations were largely overshadowed by the support (see Fig. S1.1) [35–37].

Unfortunately, also XPS measurements have proven to be largely unreliable, probably due to a combination of the highly insulating character of the support, creating heavy surface charging and the fact that transition metals tend to reduce in high vacuum in the

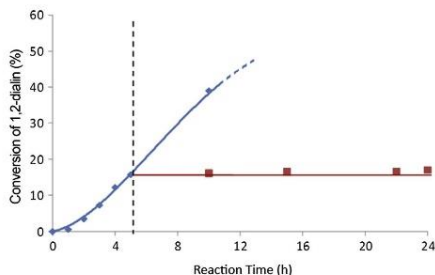


Fig. 5. Split test. After 5 h of reaction the filtrate was analyzed (square symbols).

presence of carbon or phenolic resins [38]. In any case, our XPS measurements resulted in an irreproducible mix of several oxidation types of Mn on the surface, even when the same batch of samples was measured several times. Similar problems with XPS measurements on VO_x loaded phenolic resins were observed by us previously [32].

We have therefore synthesized a mesoporous phenolic resin that is completely free from Cl-ions, by using high purity HNO_3 in the synthesis procedure, rather than the typical HCl, to create the required acidity in the synthesis mixture. After grafting the Mn-salen complex, the heterogeneous catalyst was analyzed for its manganese and chlorine content with XRF. In case of physisorption, the complex would be present in the resin as a chloride salt, while in the case of covalent attachment, the manganese centers would bond with the phenolic oxygens, releasing the chlorine ions into solution. Quantitative XRF measurements of this catalyst detected a chlorine content of only $0.005 \text{ mmol g}^{-1}$, compared to a manganese loading of 0.09 mmol g^{-1} . These results give a very good and direct proof of the covalent anchoring of the Jacobsen complex on our phenolic resin.

The Mn-content of 0.09 mmol Mn/g measured with XRF corresponds to $\sim 0.1 \text{ Mn-complexes/nm}^2$. This suggests that the Mn-

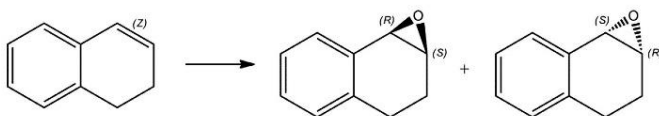


Fig. 4. Epoxidation of dialin (1,2-dihydronaphthalene) to 1,2-(R,S)-dihydronaphthalene oxide and 1,2-(S,R)-dihydronaphthalene oxide.

Table 2
Overview of the catalytic performance of the homogeneous and the immobilized Mn-salen catalysts in the asymmetric epoxidation of dialin.

	Manganese loading		First run			Second run			Third run		
	mmol Mn/g	#Mn/nm ²	Conv. ^a [%]	TON ^b	ee ^c [%]	Conv. ^a [%]	TON ^b	ee ^c [%]	Conv. ^a [%]	TON ^b	ee ^c [%]
Homog. catalyst	0.396	—	90	34.2	80	—	—	—	—	—	—
Heterog. catalyst	0.09	0.1	62	10.5	80	44	8.1	77	49	9.5	78

^a Conversions determined by chiral HPLC after 24 h, the masses of initial and recovered heterogeneous catalyst for each run are respectively 0.061, 0.052 and 0.048 g. The amount of homogeneous catalyst was adjusted to have the same amount of Mn centers as used in the heterogeneous system (about 0.0045 mmol Mn).

^b Turn over number (TON) determined as number of dialin converted per number of manganese centers after 24 h.

^c Enantiomeric excess determined by chiral HPLC.

complexes are well dispersed on the surface of the mesoporous phenolic resin, which will avoid the formation of μ -oxo-species through dimerization, and thus deactivation of the Jacobsen catalyst.

3.3. Catalytic performance of the immobilized Jacobsen catalyst in the epoxidation of dialin

The novel catalyst was evaluated for its catalytic performance in the epoxidation of dialin. As shown in Fig. 4, the epoxidation of this conjugated olefin yields two enantiomers: 1,2-(*R,S*)-dihydronaphthalene oxide and 1,2-(*S,R*)-dihydronaphthalene oxide.

The heterogeneous catalyst was used in three consecutive epoxidation runs of 24 h, and filtered off and washed with dichloromethane after each run. As a reference, the catalyst was compared to the Jacobsen catalyst in the homogeneous phase. The reaction mixtures were analyzed after 24 h reaction at room temperature. Table 2 shows an overview of the catalytic performance of the different catalysts in the epoxidation of 1,2-dialin. The homogeneous catalyst shows a high catalytic activity: after 24 h of reaction, 90% of the substrate is converted and a TON of 34 is calculated. For the Jacobsen catalyst immobilized on the mesoporous phenolic resin, a conversion of 62% is obtained, corresponding to a TON of 10.

The enantioselectivity of the catalysts was measured by means of chiral HPLC. The *ee* of the homogeneous Jacobsen catalyst was 80% (excess of 1,2-(*S,R*)-dihydronaphthalene oxide). The *ee* value of the Jacobsen catalyst immobilized on the mesoporous phenolic resin was 80% as well, which indicates that the immobilization of the complex did not alter the asymmetric induction character of the catalyst. In a second run the conversion of the immobilized catalyst decreased to 44%, although the *turn over number* indicates that the catalyst maintained its conversion efficiency. The *enantiomeric excess* in this run was 77%. In a third run the conversion was 49%, with a TON of 9.5 and an *ee* of 78%. These results show that the Jacobsen catalyst on the mesoporous phenolic resin can be reused and perfectly maintains its high enantioselectivity in the asymmetric epoxidation of dialin. There is a small reduction in conversion, but only from the first to the second run, after which the activity of the catalyst no longer decreases.

To assess possible manganese leaching from the support, the reaction mixtures were analyzed with XRF spectroscopy after each catalytic test. The manganese content of these filtrates was found to be below the detection limit of the XRF analyser (ppm range). Additionally, a split test was performed where the catalyst was filtrated from the reaction mixture after 5 h of reaction. The reaction mixture was further analyzed in time to verify if the conversion would increase. If catalytically active species (Jacobsen complex, Mn-species, radicals, ...) would have leached into the solution, the substrate conversion would continue in time. Fig. 5, however, shows that the conversion remains constant once the catalyst is removed. The XRF analyses and the split test indicate that the heterogeneous catalyst does not suffer from leaching.

The observed stability of this newly developed manganese *salen* catalyst can be understood by the highly stable phenolic support-oxygen-metal bond, as our group reported earlier [39]. Contrary to silica supports, the covalent C–O-metal bond does not hydrolyse easily, yielding leach-proof catalysts.

4. Conclusion

In this contribution, mesoporous phenolic resins are presented as novel support for the covalent immobilization of the Jacobsen catalyst. The catalyst anchoring consists of a simple and direct reflux procedure resulting in a direct axial coordination of the complex on the surface phenol groups. A manganese loading of 0.09 mmol g⁻¹ was obtained, corresponding to 0.1 Mn-complexes/nm². This loading suggests that the Mn-complexes are well dispersed on the surface of the mesoporous phenolic resin. The covalent bonding of the Mn center to the phenolic oxygen of the support has been proven by XRF of the immobilized Jacobsen catalyst on a chlorine-free mesoporous phenolic resin. The heterogeneous catalyst shows good catalytic activity in the asymmetric epoxidation of dialin, using sodium hypochlorite as oxidant. Conversions of 62% are obtained in the initial catalytic run where 1,2-(*S,R*)-dihydronaphthalene oxide is formed with an *ee* of 80%. The results of a second and third catalytic run indicate that the heterogeneous system can be recovered with maintained converting efficiency and enantioselectivity (~78%). A split test and reaction filtrate analysis with XRF proved that the Jacobsen catalyst bound on the mesoporous resin is a real heterogeneous catalyst that does not suffer from leaching.

Acknowledgments

The authors acknowledge the Special Research Fund Grants Nr. 05V00812 (AUGent) and 01J00107 (UGent), the Ghent University BOF Grant Nr. 01P02911T and the European Research Council (FP7(2007–2013) ERC Grant Nr. 240483). José Martins is acknowledged for the NMR measurements.

Appendix. A Supplementary data

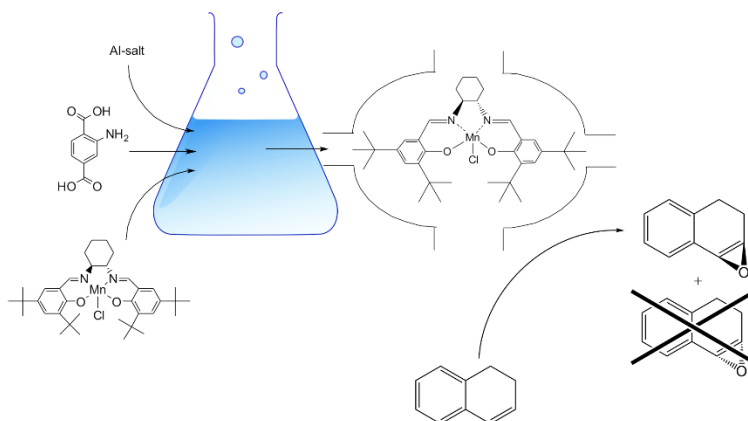
Supplementary data related to this article can be found at <http://dx.doi.org/10.1016/j.matchemphys.2013.06.035>.

References

- [1] R.C. Ewins, H.B. Henbest, M.A. Mckerverey, *Chem Commun.* (1967) 1085–1086.
- [2] J.G. Smith, *Synthesis-Stuttgart* (1984) 629–656.
- [3] P. Besse, H. Veschambre, *Tetrahedron* 50 (1994) 8885–8927.
- [4] M. Wu, C.X. Miao, S.F. Wang, X.X. Hu, C.G. Xia, F.E. Kuhn, W. Sun, *Adv. Synth. Catal.* 353 (2011) 3014–3022.
- [5] K. Srinivasan, P. Michaud, J.K. Kochi, *J. Am. Chem. Soc.* 108 (1986) 2309–2320.
- [6] T. Katsuki, in: I. Ojima (Ed.), *Catalytic Asymmetric Synthesis*, Wiley-VCH, US, 2000, pp. 287–326.
- [7] J.T. Groves, T.E. Nemo, *J. Am. Chem. Soc.* 105 (1983) 6243–6248.
- [8] P. Pietikainen, PhD thesis, University of Helsinki, FI, 2001.

- [9] B. Cardoso, J. Pires, A.P. Carvalho, I. Kuzniarska-Biernacka, A.R. Silva, B. de Castro, C. Freire, *Micropor. Mesopor. Mater.* 86 (2005) 295–302.
- [10] E.N. Jacobsen, M.H. Wu, in: E.N. Jacobsen, A. Pfaltz, H. Yamamoto (Eds.), *Comprehensive Asymmetric Catalysis*, Springer, 1999, pp. 649–677.
- [11] T. Katsuki, *Coord. Chem. Rev.* 140 (1995) 189–214.
- [12] R.N. Ji, K. Yu, L.L. Lou, Z.C. Gu, S.X. Liu, *J. Inorg. Organomet. P* 20 (2010) 675–683.
- [13] I. Kuzniarska-Biernacka, C. Pereira, A.P. Carvalho, J. Pires, C. Freire, *Appl. Clay Sci.* 53 (2011) 195–203.
- [14] I. Kuzniarska-Biernacka, A.R. Silva, A.P. Carvalho, J. Pires, C. Freire, *Catal. Lett.* 134 (2010) 63–71.
- [15] L.L. Lou, S. Jiang, K. Yu, Z.C. Gu, R.A. Ji, Y.L. Dong, S.X. Liu, *Micropor. Mesopor. Mater.* 142 (2011) 214–220.
- [16] T. Luts, W. Suprun, D. Hofmann, O. Klepel, H. Papp, *J. Mol. Catal. A-Chem.* 261 (2007) 16–23.
- [17] T.C.O. Mac Leod, M.V. Kirillova, A.J.L. Pombeiro, M.A. Schiavon, M.D. Assis, *Appl. Catal. A-Gen.* 372 (2010) 191–198.
- [18] D.P. Serrano, J. Aguado, C. Vargas, *Appl. Catal. A-Gen.* 335 (2008) 172–179.
- [19] X.C. Zou, X.K. Fu, Y.F. Luo, *Acta Chim. Sinica* 69 (2011) 431–437.
- [20] D.E. De Vos, M. Dams, B.F. Sels, P.A. Jacobs, *Chem. Rev.* 102 (2002) 3615–3640.
- [21] P.P. Knops-Gerrits, D.E. De Vos, P.A. Jacobs, *J. Mol. Catal. A-Chem.* 117 (1997) 57–70.
- [22] P.P. Knops-Gerrits, D.E. De Vos, F. Thibaultstarzyk, P.A. Jacobs, *Nature* 369 (1994) 543–546.
- [23] U. Diaz, M. Boronat, A. Corma, *P. Roy. Soc. A-Math. Phys.* 468 (2012) 1927–1954.
- [24] B. Clapham, T.S. Reger, K.D. Janda, *Tetrahedron* 57 (2001) 4637–4662.
- [25] B.M.L. Dijos, I.F.J. Vankelecom, P.A. Jacobs, *Adv. Synth. Catal.* 348 (2006) 1413–1446.
- [26] N.E. Leadbeater, M. Marco, *Chem. Rev.* 102 (2002) 3217–3273.
- [27] T.S. Reger, K.D. Janda, *J. Am. Chem. Soc.* 122 (2000) 6929–6934.
- [28] D.C. Sherrington, *Catal. Today* 57 (2000) 87–104.
- [29] A.R. Silva, C. Freire, B. de Castro, *Carbon* 42 (2004) 3027–3030.
- [30] P. Das, A.R. Silva, A.P. Carvalho, J. Pires, C. Freire, *Catal. Lett.* 129 (2009) 367–375.
- [31] F. Maia, N. Mahata, B. Jarrais, A.R. Silva, M.F.R. Pereira, C. Freire, J.L. Figueiredo, *J. Mol. Catal. A-Chem.* 305 (2009) 135–141.
- [32] I. Muylaert, M. Borgers, E. Bruneel, J. Schaubroeck, F. Verpoort, P. Van Der Voort, *Chem. Commun.* (2008) 4475–4477.
- [33] I. Muylaert, A. Verberckmoes, J. De Decker, P. Van der Voort, *Adv. Colloid Interfac.* 175 (2012) 39–51.
- [34] J.M. Vega-Perez, I. Perinan, M. Vega-Holm, C. Palo-Nieto, F. Iglesias-Guerra, *Tetrahedron* 67 (2011) 7057–7065.
- [35] M.P. Feth, C. Bolm, J.P. Hildebrand, M. Kohler, O. Beckmann, M. Bauer, R. Ramamonjisoa, H. Bertagnolli, *Chem-Eur. J.* 9 (2003) 1348–1359.
- [36] T. Ben Zid, I. Khedher, A. Ghorbel, *React. Kinet. Mech. Catal.* 100 (2010) 131–143.
- [37] J. Cubillos, I. Montilla, C.M. de Correa, *Appl Catal. A-Gen.* 366 (2009) 348–352.
- [38] B.M. Weckhuysen, D.E. Keller, *Catal. Today* 78 (2003) 25–46.
- [39] I. Muylaert, J. Musschoot, K. Leus, J. Dendooven, C. Detavernier, P. Van der Voort, *Eur. J. Inorg. Chem.* (2012) 251–260.

PAPER V: MN-SALEN@MIL101(AL) A HETEROGENEOUS, ENANTIOSELECTIVE CATALYST USING A 'BOTTLE AROUND THE SHIP' APPROACH



T. Bogaerts, A. Van Yperen-De Deyne, Y-Y Liu, F. Lynen, V. Van Speybroeck, P. Van der Voort , *Chemical Communications* , 2013 (49), 8021-8023 , **2013**.

T. Bogaerts performed the research and prepared the manuscript.

Reproduced with permission from The Royal Society of Chemistry. ©2015 The Royal Society of Chemistry.

Mn-salen@MIL101(Al): a heterogeneous, enantioselective catalyst synthesized using a 'bottle around the ship' approach†

Thomas Bogaerts,^{ab} Andy Van Yperen-De Deyne,^a Ying-Ya Liu,^b Frederic Lynen,^c Veronique Van Speybroeck^{*a} and Pascal Van Der Voort^{*b}

Cite this: *Chem. Commun.*, 2013, **49**, 8021

Received 14th June 2013,
Accepted 11th July 2013

DOI: 10.1039/c3cc44473b

www.rsc.org/chemcomm

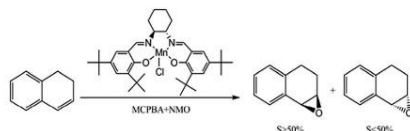
An enantioselective catalyst, consisting of a chiral Mn(II)salen complex entrapped in the MIL-101 metal organic framework, is reported. For the first time, we assemble a robust MOF-cage around a chiral complex. The heterogeneous catalyst shows the same selectivity as the homogeneous complex and is fully recyclable. Theoretical calculations provide insight into this retention of selectivity.

Chiral epoxides are valuable intermediates in the chemical industry. The high ring strain makes them very reactive and their enantioselectivity can be transferred to the products. Various methods have been proposed to enantioselectively synthesize these epoxides.¹ One of these methods is the use of the Jacobsen salen complex.² Such manganese complexes enable the epoxidation of unfunctionalized olefins (shown in Scheme 1) with selectivities one would expect from enzymes. In order for this system to be sustainable, an efficient recovery of this catalyst is required. Moreover deactivation of the manganese salen complex, that occurs readily *via* the formation of dimeric species,³ must be prevented. All these issues can be solved by immobilizing the complex on a solid material. Various processes for anchoring

chiral complexes to a support have already been proposed.⁴ We propose a simple immobilization procedure where the salen complex is encapsulated in a metal organic framework without any covalent bonds.

Metal organic frameworks (MOFs) are porous crystalline materials consisting of metal (oxide) building blocks connected with organic linkers. Using various metals, linkers and synthesis procedures, a wide array of structures are available. In this study NH₂-MIL101(Al) is used as the carrier material. This MOF was first reported by Kapteijn *et al.*⁵ The use of MOFs as catalyst supports has been investigated previously.⁶ MIL-101 type MOFs (MIL stands for Materials Institute Lavoisier) are known for the highly porous structure consisting of large cages (2.9–3.4 nm) connected by windows of 1.2 and 1.6 nm² diameter. The goal is to form the MOF around the complex, building a so-called 'bottle around the ship'. The dimensions of the Jacobsen salen complex (approximately 1.7 × 1.2 × 0.5 nm) allow it to reside in the cages without being able to pass through the windows, thus effectively immobilizing the complex. In contrast to using salen-type ligands as struts for the MOF⁶ the proposed method only makes use of easily available chemicals. "Ship in a bottle" methodologies for producing salen-type complexes have been proposed⁹ however they do not involve MOFs and require several reaction steps. In this communication we propose another approach, denoted as "bottle around a ship", in which the encapsulation procedure consists of a one-pot single-step synthesis. The linker and the commercially available salen complex were simultaneously dissolved in DMF after which AlCl₃ was added stepwise. While crystals are formed, the color of the solution changes from deep-red to a paler red-brownish color. This points to the decrease in concentration of the salen complex in the solution, meaning a fraction gets trapped in the pores.

Comparing the powder XRD pattern of pure NH₂-MIL101(Al) with the encapsulated catalyst shows minimal differences as shown in Fig. 1. This shows that the addition of the salen complex to the synthesis mixture has no effect on the formed structure. The Langmuir surface area, measured by N₂-sorption, was 2603 m² g⁻¹ and 2413 m² g⁻¹ for the empty and loaded structure respectively. The pore volume decreased from 0.984 cm³ g⁻¹ to 0.953 cm³ g⁻¹.



Scheme 1 The enantioselective epoxidation of dihydronaphthalene with the salen complex used in this study.

^a Center for Molecular Modelling (CMM), Ghent University, Technologiepark 903, 9052 Zwijnaarde, Belgium. E-mail: Veronique.vanspeybroeck@ugent.be

^b Center for Ordered Materials, Organometallics and Catalysis (COMOC), Department of Inorganic and Physical Chemistry, Ghent University, Krijgslaan 281-S3, 9000 Ghent, Belgium. E-mail: pascal.vandervoort@ugent.be

^c Separation Science group, Department of Organic Chemistry, Ghent University, Krijgslaan 281-S4bis, 9000 Ghent, Belgium

† Electronic supplementary information (ESI) available. See DOI: 10.1039/c3cc44473b

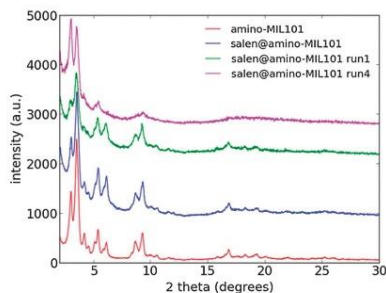


Fig. 1 Powder XRD patterns for the pure $\text{NH}_2\text{-MIL101(Al)}$, $\text{salen@NH}_2\text{-MIL101(Al)}$ and $\text{salen@NH}_2\text{-MIL101(Al)}$ after one and four catalytic runs. The encapsulation of the complex does not significantly change the crystal structure. The retained crystallinity after various catalytic runs shows the stability of the catalyst.

XRF analysis resulted in a loading of 0.02 mmol g^{-1} or one out of six cages containing a salen complex. This small loading is in good agreement with the limited decrease in internal volume. Given the high activity of the manganese–salen catalyst, a low loading is preferred to minimize pore blocking and diffusion limitations which lower the catalytic activity. To assess the behaviour of this encapsulated catalyst it was tested in a typical epoxidation of dihydronaphthalene with *meta*-chloroperoxybenzoic acid (MCPBA) and *N*-methylmorpholine *N*-oxide (NMO) as an axial ligand for the salen complex and adding toluene as an internal standard. This combination has been proven to be an effective oxidant to use in combination with the Mn(III) salen complex, both homogeneous as immobilized.^{10,11} The product distribution was analyzed by chiral HPLC. In a homogeneous medium the salen catalyst yielded a conversion of 82% with a %ee of 70. The heterogeneous catalyst showed a lower conversion of 69% when approximately the same amount of manganese was used (Table 1). However the enantioselectivity remained unchanged at a %ee of 70. This shows that the proposed encapsulation procedure has a minimal impact on the catalytic behaviour of the complex. After the catalytic run the solid catalyst is filtered off, and investigation of the crystallinity with XRD showed that the structure remained unchanged. The manganese content in the filtrate was analysed by XRF and was found to be below the detection limit of the device, showing none of the complex was leached out. This indicates that the catalyst is truly heterogeneous and stable in the reaction medium. To test the reusability of the catalyst, the powder was washed with dichloromethane and reused for another run, this was repeated three times. During the four runs the turn over number (TON) remained constant (see Fig. 2), proving this catalyst can be reused without significant loss in activity.

Table 1 Details on the amount of added catalyst in the experimental procedure

Catalyst	Weight(mg)	Mn (mmol)	Mn/substrate
Salen homogeneous	4	0.0062	1/22
Salen@NH ₂ -MIL101(Al)	330	0.0066	1/21

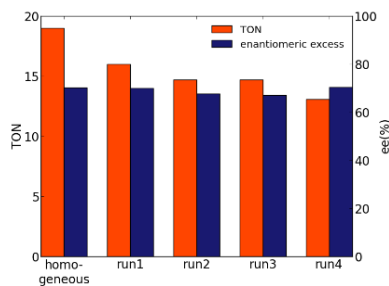


Fig. 2 TON and enantioselectivity for the $\text{salen@NH}_2\text{-MIL101(Al)}$ compared to homogeneous catalysis with the salen complex for the same conditions. It appears the encapsulation procedure has no effect on the selectivity of the catalyst.

Moreover the selectivity remains constant showing the catalyst is very stable and possesses excellent reusability. Blank reactions using the pristine MOF and the mixture without any catalyst yielded only marginal conversion after two hours. In order to obtain more insight into the bottle around the ship approach, *ab initio* calculations were performed. They allow us to make a realistic prediction of the dimensions of the Mn salen complex and its transition state, which can be compared with the cage size of a MIL101 structure. Here we will use a full DFT level of theory instead of using force fields in order to get a more detailed picture. The DFT method used is the OPBE functional, which has shown to yield accurate energies when comparing spin states of organometallic complexes,¹² which is important since the Mn–salen complex has a small energy separation between the different spin states.¹³ All optimizations were done with a 6-31+G(d) basis set for H,C,O,N and a 6-311+G(2df,2p) basis set for Cl and Mn. Computations were done using the gaussian09 suite of programs.¹⁴ Calculations were done on the (*S,S*)-variant of the salen complex, the axial ligand was omitted for computational feasibility. Starting from an oxidized manganese complex, which is an experimentally proven intermediate,³ the proposed methodology showed that a system with a spin multiplicity of three is most favourable and this will be used further. For the first transition state (Scheme S1 of the ESI†), two

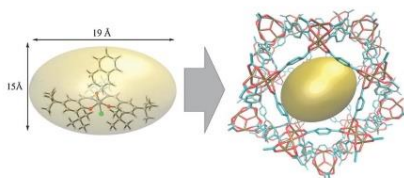


Fig. 3 Schematic representation of the transition state contained in the small (2.9 nm diameter) cage of MIL101. Hydrogens and amine-groups are omitted for clarity. The space needed for transition state to be contained in the cage is represented by an ellipsoid with radii of 19 and 15 Å. This fits readily in the MIL101 cage.

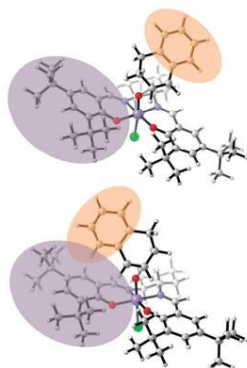


Fig. 4 Transition state for the two possible approaches of dihydronaphthalene leading to the (1*R*,2*S*)-enantiomer (left) and the (1*S*,2*R*)-enantiomer (right). The first approach suffers from more steric hindrance than the latter.

possible approaches leading to a different enantiomer were calculated. Both transition state dimensions were $1.7 \times 1.2 \times 1.0$ nm, taking NMO as an axial ligand into account this would increase to approximately $1.7 \times 1.5 \times 1.0$ nm. This means both transition states fit readily in the cages (Fig. 3).

Upon closely analyzing the mechanism of oxygen transfer, as presented in various theoretical contributions,¹⁵ it appears that the first transition state determines the resulting selectivity. Once the first C–O bond is formed the second one can only form on the same side. Since both transition states fit in the cages of the host without any interaction, the observed selectivity should be the same as the Jacobsen catalyst under homogeneous conditions, as can be observed from the experiments. Using the two approaches one can also rationalize reasons for the selectivity of the salen complex. The transition state leading to (1*R*,2*S*)-epoxydihydronaphthalene is clearly less favorable since the steric bulk of the substrate is directed towards the side of the complex facing upwards (Fig. 4). The (1*S*,2*R*)-approach does not suffer from this steric hindrance. This demonstrates that the folded structure of the salen complex is very important to induce selectivity of the substrate in the approaches. The free energy difference at 273 K between the transition states is 10 kJ mol^{-1} which can explain the preference for the formation of (1*S*,2*R*)-epoxydihydronaphthalene. To assess the influence of the cage we performed a single point calculation with a MIL-101 cage surrounding the transition states. The Jacobsen complex was modeled on the same level of theory as described before, the MOF cage was modeled with the universal force field (details in ESI[†]). The electronic energy difference between the transition states was 12 kJ mol^{-1} , which confirms the results described above.

In summary, we proposed a novel “bottle around the ship” encapsulation procedure for heterogenizing an enantioselective manganese complex in the pores of NH₂-MIL101(Al). The catalyst synthesis occurs in a single step using readily available chemicals which allows easy scale-up. The metal organic framework is used as a micro-reactor containing a single active complex, with limited influence of the walls. This results in a catalyst with good activity and a selectivity comparable to the homogeneous complex. The unchanged selectivity after heterogenization is due to the ‘soft’ encapsulation strategy. The trapping of the active complex without any covalent or coordinative bonds keeps the structure in the optimal shape needed for achieving the high selectivity. This catalyst was tested for up to four runs with a minimal decrease in activity and retention of the selectivity. This allows for the easy separation and the reuse of this catalyst without loss as was the case for the homogeneous variant. *Ab initio* calculations allow computing the dimensions of the important steps in the reaction, rationalizing the unchanged selectivity after encapsulation. The transition state which determines the selectivity fits the pores of the host unhindered, allowing the reaction to exhibit the same behaviour as with the homogeneous catalyst.

The research was financed by UGent GOA grant 01G00710, the European Research Council for funding through the European Community's Seventh Framework Programme (FP7(2007-2013) ERC grant agreement no. \240483) and the Research Board of Ghent University (BOF). Computational resources and services were provided by Ghent University (*Stevin Supercomputer Infrastructure*).

Notes and references

- Q. H. Xia, H. Q. Ge, C. P. Ye, Z. M. Liu and K. X. Su, *Chem. Rev.*, 2005, **105**, 1603–1662.
- W. Zhang, J. L. Loebach, S. R. Wilson and E. N. Jacobsen, *J. Am. Chem. Soc.*, 1990, **112**, 2801–2803.
- K. Srinivasan, P. Michaud and J. K. Kochi, *J. Am. Chem. Soc.*, 1986, **108**, 2309–2320.
- J. M. Fraile, J. I. Garcia, C. I. Herrerias, J. A. Mayoral and E. Pires, *Chem. Soc. Rev.*, 2009, **38**, 695–706.
- P. Serra-Crespo, E. V. Ramos-Fernandez, J. Gascon and F. Kapteijn, *Chem. Mater.*, 2011, **23**, 2565–2572.
- J. Canivet, S. Aguado, Y. Schuurman and D. Farrusseng, *J. Am. Chem. Soc.*, 2013, **135**, 4195–4198.
- G. Ferey, C. Mellot-Draznieks, C. Serre, F. Millange, J. Dutour, S. Surble and I. Margiolaki, *Science*, 2005, **309**, 2040–2042.
- S.-H. Cho, B. Ma, S. T. Nguyen, J. T. Hupp and T. E. Albrecht-Schmitt, *Chem. Commun.*, 2006, 2563–2565.
- B. Li, S. Y. Bai, P. Wang, H. Q. Yang, Q. H. Yang and C. Li, *Phys. Chem. Chem. Phys.*, 2011, **13**, 2504–2511.
- M. Palucki, G. J. McCormick and E. N. Jacobsen, *Tetrahedron Lett.*, 1995, **36**, 5457–5460.
- I. Canali, D. C. Sherrington and H. Deleuce, *React. Funct. Polym.*, 1999, **40**, 155–168.
- M. Swart, A. R. Groenhof, A. W. Ehlers and K. Lammertsma, *J. Phys. Chem. A*, 2004, **108**, 5479–5483.
- J. S. Scars and C. D. Sherrill, *J. Chem. Phys.*, 2006, **124**, 144314.
- M. J. Frisch, G. W. Trucks, H. B. Schlegel, G. E. Scuseria, M. A. Robb, J. R. Cheeseman, G. Scalmani, V. Barone, B. Mennucci, G. A. Petersson, H. Nakatsuji, M. Caricato, X. Li, H. P. Hratchian and A. F. Izmaylov, *et al.*, *Gaussian 09*, 2009.
- L. Cavallo and H. Jacobsen, *Inorg. Chem.*, 2004, **43**, 2175–2182.

Supporting information

Synthesis procedures

All chemicals were obtained from Sigma-Aldrich except for dimethyl-formamid (DMF) and dichloromethane which were obtained from Carl-Roth and were used without further purification.

(Salen@)NH₂-MIL101(Al)

270 mg of amino-terephthalic acid was dissolved in 60ml of DMF, when encapsulating the salen complex 50 mg of (R,R)-(-)-N,N'-Bis(3,5-di-tert-butylsalicylidene)-1,2-cyclohexanediamino-manganese(III) chloride (Jacobsen's salen complex) was added to this solution, which resulted in a deep-brown color. This solution was heated to 110°C and 730 AlCl₃·6H₂O was added in 6 equal portions, one each 15 minutes, solid material starts to form after about 30 minutes. After adding the last portion, the mixture was left stirring for three hours. In a last step the mixture was left under heating without stirring for 16 hours. The resulting solid was filtered off and washed several times with DMF after which a Soxhlet extraction with acetone was performed for 6 hours in order to remove any free linkers, AlCl₃ and salen complex.

Homogeneous catalytic test

4 mg of (R,R)-(-)-N,N'-Bis(3,5-di-tert-butylsalicylidene)-1,2-cyclohexanediamino-manganese(III) chloride was dissolved in 5 ml of dichloromethane. 20 µl of dihydronaphthalene and 90 mg N-Methylmorpholine N-oxide was added together with 62 µl toluene as internal standard. The mixture was left to stir at room temperature while 52 mg of meta-chloroperoxybenzoic acid was added in 3 equal portions spread over 10 minutes. After two hours the solution was analyzed with HPLC to determine the conversion and selectivity.

Heterogeneous catalytic test

330 mg of salen@NH₂-MIL101(Al) was added to 5 ml dichloromethane. 20 µl of dihydronaphthalene and 90 mg N-Methylmorpholine N-oxide was added together with 62 µl toluene as internal standard. The mixture was left to stir at room temperature while 52 mg of meta-chloroperoxybenzoic acid was added in 3 equal portions spread over 10 minutes. After two hours the catalyst was filtered off and the filtrate was analyzed with HPLC. The solid was washed 3 times with dichloromethane and reused for the next run with the same conditions.

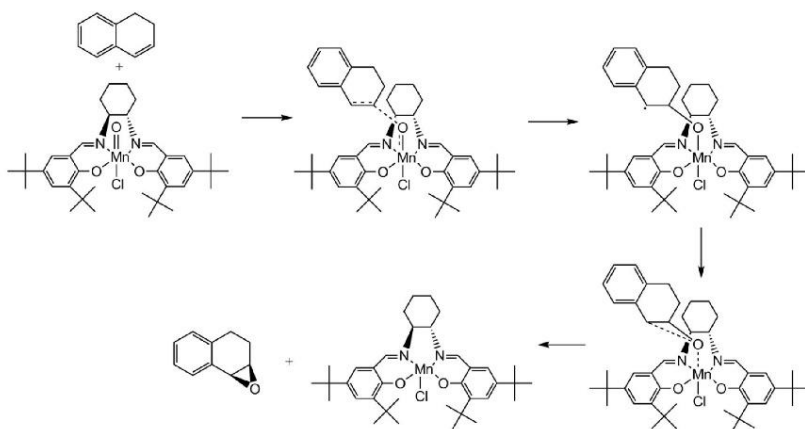
Blank test

For blank tests, the same mixture of 20 µl dihydronaphthalene, 90 mg N-Methylmorpholine N-oxide and 62 µl toluene in 5 ml dichloromethane was made. For the test with the empty NH₂-MIL101(Al) 330mg of MOF was added. The mixture was left to stir at room temperature while 52 mg of meta-chloroperoxybenzoic acid was added in 3 equal portions spread over 10 minutes. In the mixture without the MOF a slight precipitation was observed probably due to the reaction between N-Methylmorpholine N-oxide and meta-chloroperoxybenzoic acid. Both systems resulted in less than 5% conversion.

Characterization

Nitrogen sorption measurements were done with a Belsorp mini II gas analyzer at a temperature of -196°C . Powder XRD measurements were done with an ARL X'TRA X-ray diffractometer using $\text{K}\alpha$ radiation of copper with a wavelength of 0.15418 nm and a solid state detector. X-ray fluorescence (XRF) spectroscopy measurements were performed on Rigaku NexCG, Energy Dispersive X-ray Fluorescence (EDXRF) apparatus. DRIFT-spectra were measured on a Nicolet 6700 FT-IR spectrometer from ThermoScientific. HPLC analysis was done with a Waters 2690 separation module and a UV detector of 220 nm . The column was a Daicel AD-H type chiral column. The mobile phase was a 98/2 vol% mixture of hexane/isopropanol with a flowrate of 0.900 ml/min .

Mechanism



Scheme S1. Generally accepted two-step mechanism for the epoxidation of olefins. The selectivity of the reaction is determined in the first step since the side of the oxygen addition is fixed there.

N₂-sorption

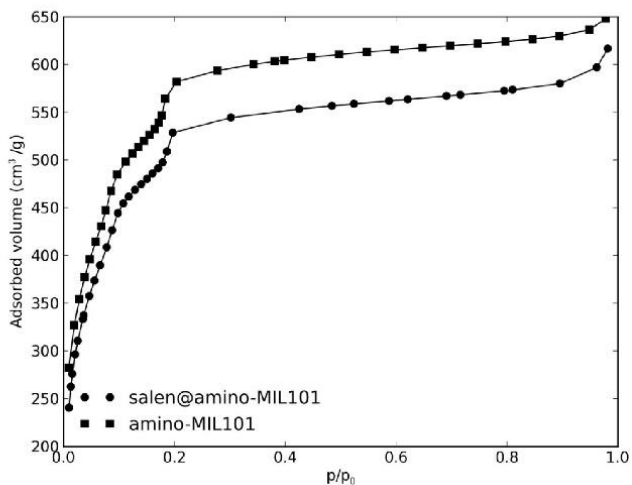


Figure S1. N₂-sorption experiment for both materials

Drifts measurement

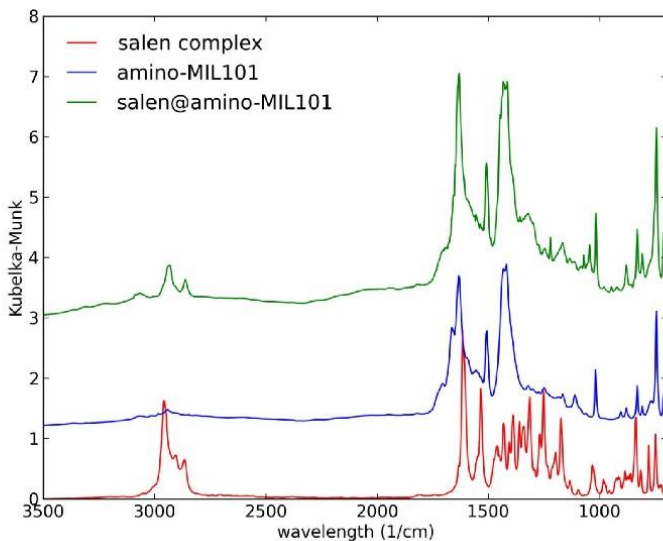


Figure S2. DRIFT spectra of the pure salen complex, NH₂-MIL101(AI) and salen@NH₂-MIL101(AI).

Influence of the MOF cage

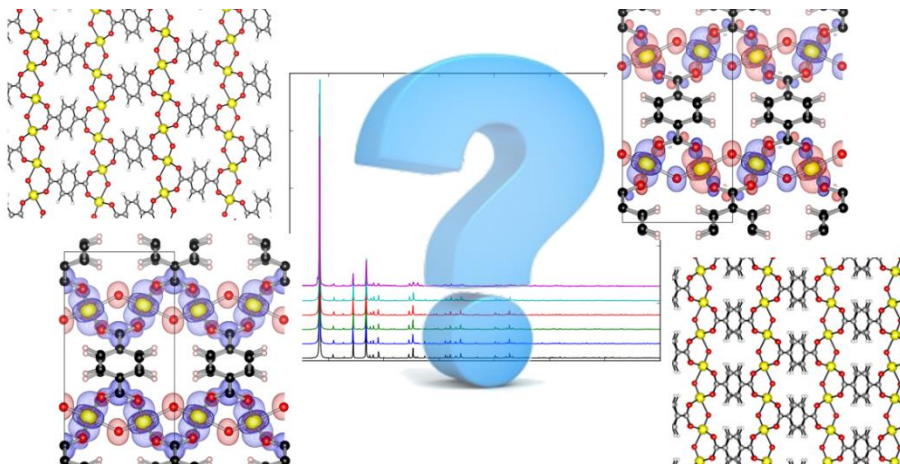
In order to assess the influence of the surroundings we isolated a cluster model for a single cage from the cif file of MIL101(Cr) and saturated the removed linkers with a formiate moiety. The amine moieties were omitted. In order to optimize this cage we replaced the Cr atoms with Co, we didn't use aluminium for this optimization since there are no parameters for hexagonal aluminium in the UFF-forcefield¹. The cage was optimized with UFF holding the saturating moieties and the metal atoms in place.

After optimization Co was replaced by aluminium again for the single point calculation, here we placed both transition states in the center of the cage with the same orientation. We applied an ONIOM-scheme using UFF for the MOF-cage and the OPBE DFT functional for the salen complex with the same LOT as we used for optimization. The electronic energy difference between the two transition states is 12,1 kJ/mol which is very similar to what we found without embedding, this further shows that the support has no influence on the selectivity behaviour

1. A. K. Rappe, C. J. Casewit, K. S. Colwell, W. A. Goddard and W. M. Skiff, *J. Am. Chem. Soc.*, 1992, **114**, 10024-10035.

PAPER VI: FINE-TUNING THE AB INITIO MODELED STRUCTURE OF MIL-47(V) WITH THE AID OF POWDER X-RAY DIFFRACTION

Thomas Bogaerts, Danny Vanpoucke, Pascal Van Der Voort, Veronique Van Speybroeck. *CrystEngComm*, submitted



T. Bogaerts performed the research and prepared the manuscript.

Fine-tuning the theoretically predicted structure of MIL-47(V) with the aid of powder X-ray diffraction

Received 00th January 20xx,
Accepted 00th January 20xx

DOI: 10.1039/x0xx00000x

www.rsc.org/

Thomas Bogaerts,^{a,b} Louis Vanduyfhuys,^a Danny E.P. Vanpoucke,^{a,b} Jelle Wieme,^a Michel Waroquier,^a Pascal Van Der Voort^b and Veronique Van Speybroeck^a

The structural characterization of complex crystalline materials such as metal organic frameworks can prove a very difficult challenge both for experimentalists as for theoreticians. From theory, the flat potential energy surface of these highly flexible structures often leads to different geometries that are energetically very close to each other. In this work a distinction between various computationally determined structures is made by comparing experimental and theoretically derived X-ray diffractograms which are produced from the materials geometry. The presented approach allows to choose the most appropriate geometry of a MIL-47(V) MOF and even distinguish between different electronic configurations that induce small structural changes. Moreover the techniques presented here are used to verify the applicability of a newly developed force field for this material. The discussed methodology is of significant importance for modelling studies where accurate geometries are crucial, such as mechanical properties and adsorption of guest molecules.

Introduction

Computational modelling is often used to assist in the structure determination from powder diffraction patterns. Very elusive structures such as the geometry of γ -alumina could be resolved by proposing the detailed geometry from computations and using this in further refinements¹. In the research on covalent organic frameworks, the use of initial geometries generated from molecular mechanics calculations has become indispensable for structure refinement^{2, 3}. This is mostly due to the fact that these materials cannot be synthesized as single crystals and structure determination has to be done with powder patterns, which is more prone to ambiguity. In the research on Metal-Organic frameworks (MOFs) this approach has also proven its merits, for example the well-known MIL-101 structure could only be refined with a structured database search combining metal nodes and linkers in different topologies⁴. Other MOF structures could be resolved via initial guesses of the structure provided by DFT simulations⁵. Again these techniques have to be applied since the materials are hard to obtain as single crystals. Flexible MOFs are characterized by very flat potential energy surfaces, making ab initio structure optimization and structure determination a highly non-trivial exercise⁶⁻⁸. Variations in the

atomic structure, often have a very strong influence on the calculated stability, electronic structure and physical properties. For example, in their construction of the CoRE database, Chung *et al.*⁹ investigated the methane adsorption in MIL-53(Al) for the different published, experimental MIL-53(Al) geometries. They found that the methane uptake varied about 48% in the set of structures, while the void fractions only varied about 10%. The authors discussed the influence that proximal framework atoms have in the presence of adsorption sites and concluded that the exact atomic structure plays a very important role. The same observation was made by Lawler *et al.*¹⁰ who showed the importance of an accurate crystal structure for gas sorption simulations.

In the computational research on metal organic frameworks the use of molecular mechanics methods has proven to be crucial for certain applications. For example, modelling diffusion phenomena or other physical effects that occur on longer length- or timescales cannot be done with quantum mechanical models. Due to the complexity of these materials, various force fields have been developed, each with their own strong features¹¹⁻¹⁵. For the development of these molecular mechanics methods a comparison between the obtained structures and experimental data on the crystal structure is very valuable to assess the ability of the force field to generate reliable geometries.

In this paper, computational models are not used for experimental structure validation, but a reverse procedure is adopted. We propose a methodology where results from an experimental powder XRD are used to aid in selecting between various ab initio models of MOF structures and to validate the structure obtained from a newly developed force field for MIL-47(V). In many cases theoretical calculations start from a model refined from a powder diffractogram. This is already a

^a Center for Molecular Modelling (CMM)
Ghent university
Technologiepark 903, 9052 Zwijnaarde, Belgium
E-mail: Veronique.vanspeybroeck@ugent.be

^b Center for Ordered Materials, Organometallics and Catalysis (COMOC),
Department of Inorganic and Physical Chemistry
Ghent University
Krijgslaan 281-S3, 9000 Ghent, Belgium
E-mail: pascal.vandervoort@ugent.be

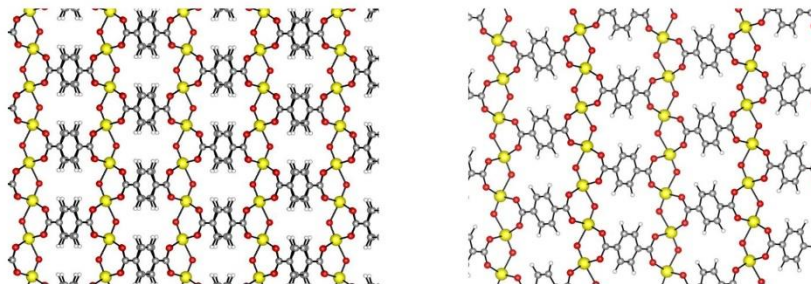


Figure 1. Projection of the geometry without (left) and with (right) displaced vanadium chains.

Table 1: energy differences of the different ab initio structures (meV per unit cell, (kJ/(mol.Vanadium))).

	Spin configuration			
	Ferromagnetic		Anti-ferromagnetic	
not displaced	A ^{FM}	0 (0)	A ^{AF}	-278 (-6.7)
displaced	B ^{FM}	-53 (-1.3)	B ^{AF}	-329 (-7.9)

generally accepted practice in the modelling of crystalline materials such as zeolites^{16–18} or MOFs^{19, 20} or other complex structures²¹. Currently it is not general practice to assess XRD patterns obtained from calculated geometries to experimental diffractograms. In this paper such a procedure is followed and applied to the well-known MIL-47(V) structure.

After the discovery of the MIL-47(V) structure, the Férey-group found a large pore structure belonging to the Pnma space group which contained displaced vanadium chains based on single crystal diffraction²². A slightly different structure with the Pnma space group, which didn't contain this displacement, was proposed by the Maurin-group as a result from molecular dynamics simulations²³. Furthermore, in a previous work, Vanpoucke *et al.* showed that the spin configuration of the MIL-47(V) system is strongly correlated with its mechanical properties and stability, indicating the importance of having an accurate representation of the electronic structure⁶. Discrimination between the various structures is very challenging. The direct experimental measurement of the spin configuration is in practice almost impossible. Moreover, different authors have proposed structures for this MOF with

small geometrical differences^{22, 23}. The current paper aims to unite well-defined X-ray diffractograms to resolve which modeled structure would be the most plausible. To that end, theoretical structures are determined from very accurate periodic structure calculations and also from a force field method derived from ab initio determined data. For the latter we have used a procedure proposed by some of the authors to quickly generate force fields for MOFs¹⁴. With the latter example we aim to verify how well the proposed force field can reproduce the ab initio calculations and how good it fits the experimental results.

Experimental details and computational methods

Experimental details

All chemicals were purchased from Sigma Aldrich and used without further purification. X-Ray powder diffraction (XRPD) patterns were collected on a ARL X'TRA X-ray diffractometer with Cu K α radiation of 0.15418 nm wavelength and a solid state detector, measurements were done over 48h to improve the resolution. Nitrogen adsorption experiments were carried out at -196 °C using a Belsorp-mini II gas analyzer.

MIL-47 was synthesized as reported by Férey *et al.*²² 1.37 g VCl₃ and 0.36 g terephthalic acid were mixed in 15.7 mL of deionized H₂O. The resulting mixture was transferred in a Teflon-lined autoclave and kept a 200°C for four days. After filtration the solid was washed with acetone and calcined at 300°C for 24h to obtain the final product. The Langmuir surface area was found to be 1150 m²/g

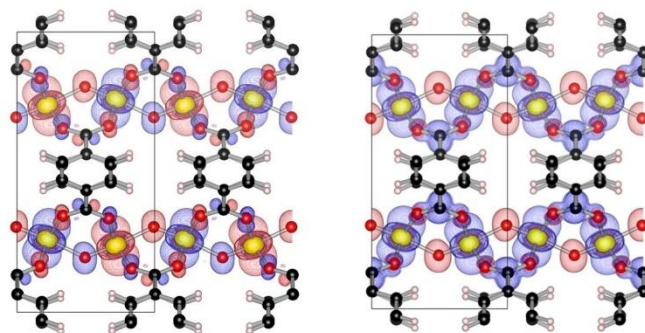


Figure 2. Visualization of the spin densities for the anti-ferromagnetic (left) and the ferromagnetic (right) structure. Red orbitals are spin up, blue spin down.

Computational details

Diffraction patterns were simulated from cif files with the aid of the mercury program²⁴. Rietveld analysis and profile-only fitting was done with Jana2006²⁵.

The ab initio structures used in this work are obtained from periodic Density Functional Theory (DFT) calculations, using the projector augmented wave (PAW) method and the generalized gradient approximation functional, as constructed by Perdew, Burke and Ernzerhof (PBE). Dispersion interactions are included through the damped DFT-D3 correction scheme.^{26, 27} Calculations were performed with the Vienna ab initio Simulation package (VASP)²⁸⁻³². The ab initio structures used are deposited with the Cambridge Crystallographic Data Center under the CCDC numbers: 1021380(A^{FM}), 1021384(A^{AF}), 1402266 (B^{FM}), 1402265 (B^{AF}). An overview of the computational methods is shown in Figure 4.

The calculated geometries were obtained using a Monkhorst-Pack special k-point grid of $2 \times 2 \times 6$ and the kinetic energy cutoff for the plane waves was set to 500 eV. Since the geometry of MIL-47(V) tends to collapse due to Pulay stresses,³³ the volume of the structures was optimized by fitting $E(V)$ data to the Rose-Vinet equation of state³⁴. This $E(V)$ data was obtained through constant volume optimization of the structure at volumes in a range of $\pm 4\%$ around the equilibrium volume. With this constant volume, simultaneous optimizations of atomic positions and cell shape were done. The electronic configuration (ferromagnetic or anti-ferromagnetic) was imposed before each optimization, and verified afterward. Using the equilibrium volume obtained from the equation of state fit, a final geometry optimization was performed, optimizing both atomic positions and cell shape. With this approach, four different structures for MIL-47(V) were isolated by varying two aspects of the structure.

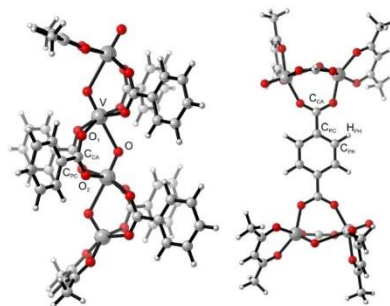


Figure 3. Clusters on which QuickFF was applied to derive a force field for MIL-47. The atom types that are relevant for the periodic structure are indicated on the figure as well.

Firstly, the spin configuration: we consider either ferromagnetic (FM) or anti-ferromagnetic (AF) V-O-V-chains (shown in Figure 2). In previous work, it was shown that the chains are nearly non-interacting, with the latter spin-configuration representing the ground state spin structure, being about 280 meV more stable than the FM structure⁶. Secondly, there is the relative positioning of the vanadium chains. Here the displaced chain structure is 50 meV more stable than the non-displaced structure. This displacement of the second chain is indicated in Figure 1. The resulting nomenclature used in this work is shown in Table 1. All the theoretical structures are compared with the published geometry of Férey *et al.*²² that is deduced from single crystal measurements and with a newly measured PXRD pattern.

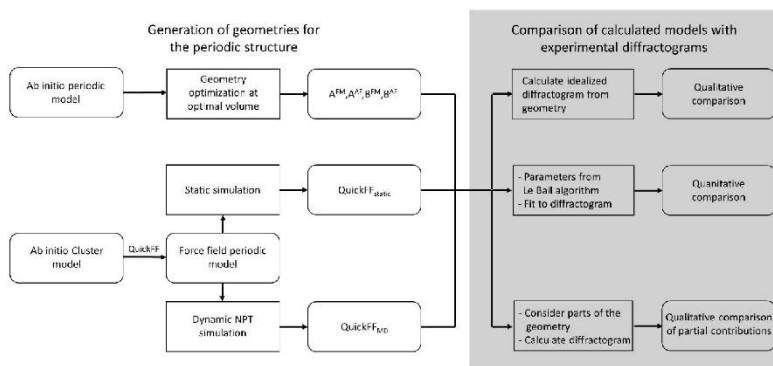


Figure 4. Flow scheme of the applied computational procedures to compare measured and calculated diffractograms.

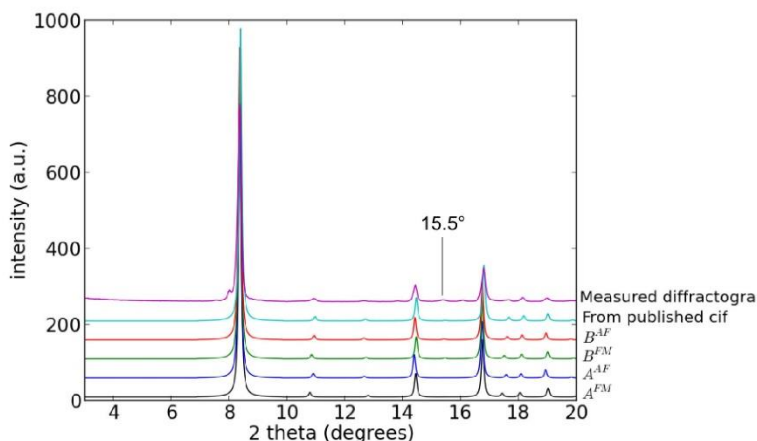


Figure 5. Measured and calculated diffractograms at low angle (Marked diffraction: (111)-plane).

To derive a fully flexible force field, QuickFF¹⁴ used the isolated clusters shown in Figure 3 as a training set. QuickFF is a software package to quickly derive force fields from ab initio training data. It was specifically designed for the derivation of force fields for metal-organic frameworks, but it can in principle be applied to a broader spectrum of materials including non-periodic molecular system. The required ab initio input data was generated using Gaussian09³⁵ by performing a geometry optimization followed by a frequency job to obtain the Hessian in equilibrium. Density Functional Theory was used with the B3LYP^{36–38} functional and a 6-311G(d,p)^{39, 40} basis set. The covalent contributions to the force field were estimated using the QuickFF procedure.

However, some ad hoc adaptations were implemented in order to better describe the asymmetry of the inorganic building unit. Two different atom types were used for the along the inorganic chain was described by means of sixth-order polynomial function with two distinct minima, corresponding to the large and small V-O bond length. Fixed atomic charges were derived a priori from the molecular electron density using the Minimal Basis Iterative Stockholder scheme implemented in Horton⁴¹. The van der Waals interactions were added to the force field a posteriori. They were taken from the MM3 force field of Lii *et al.*⁴², however, a uniform scaling of 0.7 was applied to the ϵ -parameters and a scaling of 1.1 was applied to the σ -parameters in order to

reproduce the experimental transition pressures from large pore to narrow pore and vice versa²³.

All force field calculations were done with Yaff⁴³, an in-house developed code for force field simulations. The non-bonded interactions were computed with a cutoff of 15 Å and the long-range electrostatics were computed using Ewald summation. Two sets of structures were generated. First we performed a regular optimization which gave a minimum on the potential energy surface. The resulting equilibrium was confirmed to be a true minimum by means of a normal mode analysis. This structure will be further referred to as QuickFF. In addition also an average structure at 300 K and 1 bar was calculated by means of a molecular dynamics run in the NPT ensemble for 800 ps with a timestep of 0.5 fs using the Nose-Hoover chain thermostat⁴⁴ and the Martyna-Tobias-Klein barostat⁴⁵.

For practical reasons all optimizations of the crystal structure were done without constraints on the symmetry⁷. Afterwards the real symmetry of the material was verified using the PLATON software package⁴⁶, the results are shown in Table 2.

Table 2. Space groups for different calculated geometries obtained with PLATON.

	Space Group
A ^{FM}	Ima2
A ^{AF}	Ima2
B ^{FM}	Pnma
B ^{AF}	Pnma
QuickFF ^{Static}	Pmc2 ₁
QuickFF ^{MD}	Pmc2 ₁

By examining the symmetry of the calculated structures it seems that the geometries featuring the displacement are in closest agreement with the published structure from Férey *et al.* The A^{AF} and A^{FM} geometries and the structures obtained by the force field exhibit another symmetry. This analysis already points out that the displaced structures should correspond the best to the previously published geometry derived from single crystal diffraction.

An overview of all models and techniques to compare them with experimental data is shown in Figure 4.

Results and discussion

Qualitative comparison between calculated and measured diffractograms

The simplest way to compare calculated geometries directly to the measured spectrum is a qualitative approach. The calculated geometry can be used to determine the peak positions and intensities in a diffractogram by applying simple gaussians as a model for the diffraction peaks. Thus, an idealized diffractogram is calculated that can be compared directly with the measurements. We can see that the system with displaced vanadium chains fits the diffractogram better. In the low angle area (Figure 5) the most important observation is the small peak at 15.5° that is only visible for the structures with displaced vanadium and corresponds with the experimental diffractogram. In the high angle region (Figure 6) the 29.5° reflection is the main difference between the structures with and without displaced chains. This reflection is also present in the measured spectrum. The same is valid for the reflection on 37.5°, but this peak is barely visible in the measured diffractogram. When only comparing the calculated diffractograms (from both DFT optimized and published geometry²²) the geometries with displaced vanadium chains (B^{FM}, B^{AF}) appear the most favorable as they are more similar to the published one (31°, 33°, 41.5°). From an analysis of the calculated and measured diffractogram we can already conclude the importance of the displaced vanadium chains for the correct geometry, despite the fact that the energy difference in the DFT models for these two structures is small (cf. Table 1). However, for further analysis of the different geometries we need to verify the correspondence between a calculated geometry and a measured diffractogram quantitatively.

When comparing the geometry generated by the QuickFF force field to the measured diffractogram (Figure 7) the differences are similar to the ab initio structure without the displaced vanadium chains, both in the static geometry as in the average geometry obtained by molecular dynamics (reflections at 15.5° and 29.5°). This is what has to be expected since the training set for the force field does not include any structural parameters to induce this displacement. Moreover there is a visual shift in the exact positions of the diffractions (for an overview see Figure S1 of the supporting information) indicating that the unit cell is not well reproduced by the force field. The deviation of the unit cell by the force field most probably results from the cluster training data that were used to generate the force field. Indeed, the bond lengths in the training data obtained from B3LYP clusters are systematically longer than the bonds from the periodic calculations (Table S1 in the supporting information). This shift is significantly lower at high angles in the geometry obtained via molecular dynamics, showing this approach better reproduces the geometry of MIL-47(V).

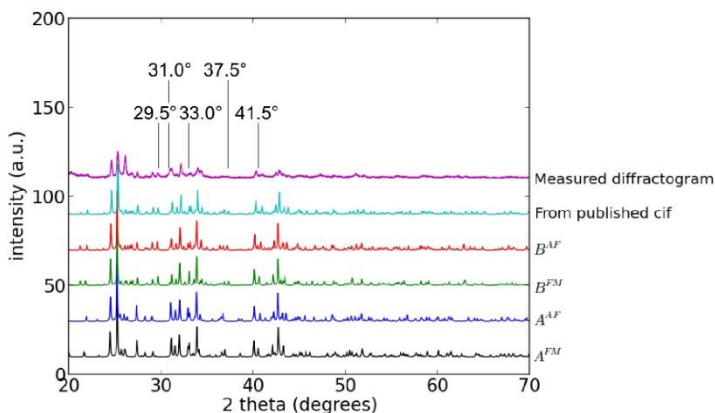


Figure 6. Measured and calculated diffractograms at high angle. The calculated structures with displaced vanadium chains correspond well with the reported structures. The diffraction at 29.5° is the main diffraction where only the displaced structures match with the measured pattern. (Marked diffractions from left to right: (2,1,2)-, (2,2,2)-, (2,1,3)-, (2,1,4)-, (1,1,6)-plane)

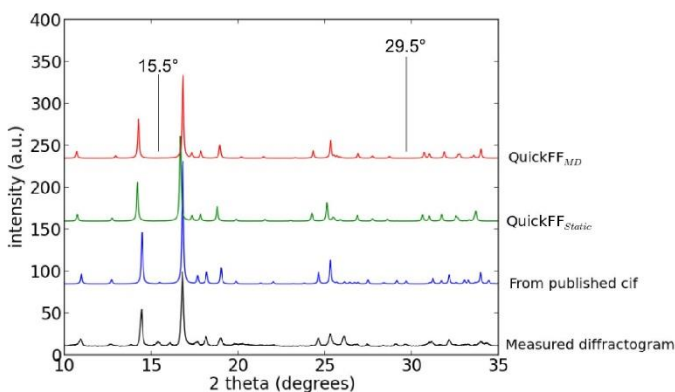


Figure 7. Comparison between the measured diffractogram and geometries generated by the force field. QuickFF refers to the data obtained from a regular optimization while QuickFF_{MD} is the structure obtained from an MD simulations at 300K as described in the methods section. The discrepancies are due to the shifted chains not being represented in the QuickFF model. (Marked diffractions from left to right: (1,1,1)-, (2,1,2)-plane)

Quantitative comparison between calculated geometries and measured diffractogram

One of the most important ways to analyze an XRD diffractogram is arguably the Rietveld method. Hugo Rietveld proposed an approach to fit a theoretical profile, dependent on the atomic coordinates, to a measured diffractogram using a least-squares algorithm⁴⁷⁻⁴⁹. With this procedure, the structure of a crystalline material can be found from powder diffraction measurements. In order to use this algorithm, a

good model for the diffractogram is required. For a single, fixed phase (denoted with subscript *j*) this can be presented schematically as:

$$I_i^{calc} = S_F \sum_{k=1}^{N_{peaks}} L_k |F_{k,j}|^2 S_j(2\theta_i - 2\theta_{k,j}) P_{k,j} A_j + bkg \quad (1)$$

with:

$$|F_{k,j}|^2 = m_k \left| \sum_{n=1}^N f_n e^{-B_n \frac{\sin^2 \theta_i}{\lambda^2}} \left(e^{2\pi i (hx_n + ky_n + lz_n)} \right) \right|^2 \quad (2)$$

This equation contains several parameters; i.e. a scale factor (S_f), peak shape (S_j), and the peak intensity depending of the atomic positions (F_{kj}). These parameters are in turn calculated via an (empirical) model that contains multiple parameters, which are all fitted by the Rietveld refinement. More information on the exact form of these empirical parameters can be found in numerous textbooks on the topic.⁵⁰ However, it is important to realize what the source of these parameters is; whether they are determined by the actual structure of the chemical substance under investigation, or the experimental setup. The only parameters in equation (1) and (2) that depend on the geometry are the peak positions (function of the unit cell parameters) and the peak intensity (F_{kj} function of the atomic positions). One can argue that other parameters, such as texture (P_{kj}) are also a function of the material. However, these parameters are not calculated in the *ab initio* model, therefore they will be treated as experimental parameters that will be refined during the analysis.

This equation allows the exact calculation of the diffractogram for a given geometry (contrary to the idealized model that was presented in the previous part) provided all experimental parameters are known. Therefore a procedure is required to fit the experimental parameters *a priori*. When doing this fit, care has to be taken to avoid biases where experimental parameters are correlated to the geometry under investigation. In order to do that, a profile-only fit, in this case the Le Bail algorithm^{51, 52}, was employed to determine these parameters *a priori*.

The calculated diffractogram can then be compared quantitatively to the measurement after defining a measure of fit. For this we will report the Rwp value defined as (with 0% being a perfect fit):

$$Rwp = \sqrt{\frac{\sum_{i=1}^N w_i (I_i^{exp} - I_i^{calc})^2}{\sum_{i=1}^N w_i (I_i^{exp})^2}} \cdot 100\% \quad (3)$$

This parameter will be assessed on different profiles. First of all it is applied on the full profile, measured for 2θ values from 3° to 70° . The second range that is considered is the so called low-angle (LA) from 3° to 20° and the third range are the high-angles (HA), going from 20° to 70° . At low angles the accuracy of the unit cell is very important. The error on the unit cell parameters will induce a shift in the diffraction positions. This will have more influence in the low angle region since this region is characterized by high but narrow peaks. In the high angle region, the geometry has a larger influence than the unit cell parameters. In this area the peak shift is larger in value, but due to the peak broadening at higher angles this shift has less influence on the fit compared to the exact geometry.

Table 3. Rwp values of the fit with a measured diffractogram with fixed unit cell during profile-only fit.

	Full (3° - 70°)	High angle (20° - 70°)	Low angle (3° - 20°)
A ^{FM}	48.27	44.25	30.26
A ^{AF}	45.63	52.81	16.58
B ^{FM}	38.31	39.30	21.00
B ^{AF}	43.28	44.77	16.87
QuickFF ^{Static}	51.98	57.86	30.86
QuickFF ^{MD}	61.78	47.11	57.32
Published cif	41.45	45.25	16.11

The fitting procedure is done in two steps as was discussed before: firstly a Le Bail fit is done where the unit cell parameters from the calculations are used. In this step the

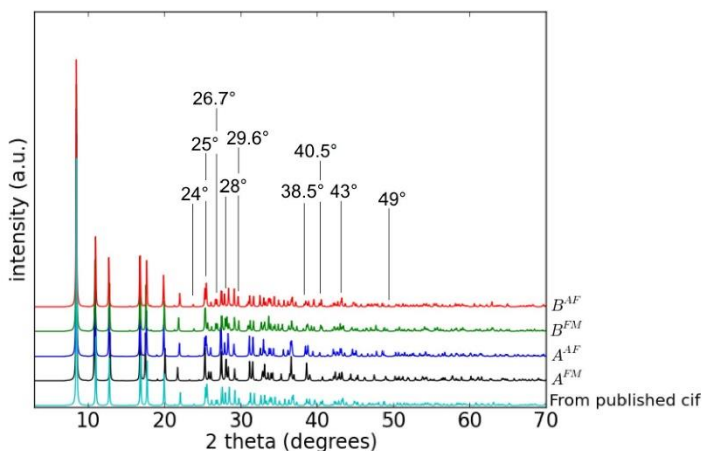


Figure 8. Comparisons when considering only the vanadium chains.

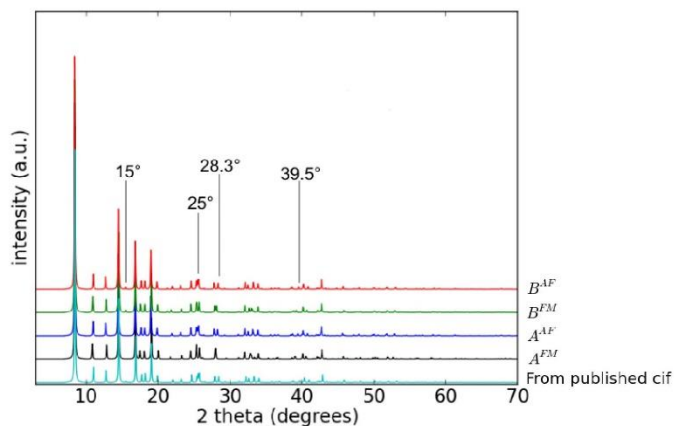


Figure 9. comparisons when considering only the linkers.

diffractions are modelled with a pseudo-Voigt model and a three-parameter asymmetry function. On top of that, the zero shift was optimized and as a background a 10-term Legendre polynomial was used. After the profile-only fit, the atomic coordinates are introduced and the measure of fit is calculated. As a comparison, the published structure of Férey *et al.*²² was investigated with the same algorithm. The latter structure was chosen as a literature reference since it contained the displaced vanadium chains that were shown to be crucial in the qualitative analysis.

When using the full diffractogram, the results from the first, qualitative analysis are confirmed. The structures with displaced vanadium chains provide a better fit (38.3% - 48.3% and 43.3% - 45.6%) (Table 3). Globally the B^{FM} structure seems to provide the best representation of the measured diffractogram, even better than the previously published geometry (38.3% - 41.45%). The difference is most clearly visible at high angles, where the atomic coordinates are the most important. At lower angles it becomes clear that the calculated unit cell parameters slightly deviate from the real structural parameters, especially for the ferromagnetic structures. This observation is not surprising since it has been reported several times that the PBE functional overestimates the unit cell parameters⁵³⁻⁵⁶. It can be concluded that the B^{FM} geometry would be the best representation of the MIL-47(V) structure, except for the unit cell parameters.

For the results from the force field the agreement with the visual comparison of the diffractograms is also apparent. While the overall fits are worse than the *ab initio* geometries, the molecular mechanics method adequately represents the experimental observations. The poorer fit at low angles indicates that the unit cell is not accurately represented by the force field calculation. At high angles the fit of the geometry is comparable to the *ab initio* calculations but still worse than

the best QM-geometry. The geometry found by averaging over a molecular dynamics run seems to have the best correspondence with the experimental result. This is probably due to the fact that the molecular dynamics approach naturally averages the structure. Since we show the potential energy plane of this MOF is relatively flat it is imaginable that different small variations on the geometry occur in a powder which leads to an average experimental XRD diffractogram.

Partial geometrical contributions to the diffractogram

To provide more insight in the differences between geometries, segments of the crystal structures are compared via their diffraction pattern. When isolating a part of a geometry, the idealized diffractogram of this structure can be calculated with the same techniques as shown in the first section. At first sight it appears easier to directly compare the coordinates of the different geometries but there is one important remark to be made. An X-ray diffractogram is actually a projection of the atomic coordinates on a (2 θ -Intensity)-graph, and like every projection to a lower dimension, some information is lost. By considering only parts of the structure one can deduce which geometrical features induce changes in the diffractogram. This partial diffractogram approach can give significant insight into the structure refinement. Of course, these patterns cannot be compared to an experimental diffractogram, thus as a reference the published geometry from single crystal measurements is used. In a first step only the vanadium atoms are considered, since the position of the heaviest atoms has the most influence on the diffractogram, it is a logical step to use this as a starting point. By considering parts of the model much more differences become visible and an even better distinction between various structures can be made compared to the diffractogram obtained by considering the full geometry. The

conclusions from the previous methods are clearly confirmed here, there is a large difference between the structure with and without displaced vanadium chains (Figure 8). The structure with displaced chains has the best agreement with the published geometry (i.e. the reflections at 24°, 26.7°/26.9° and 29.6°). There is also a visible difference between the FM and AF model with displaced vanadium chains. The latter variant corresponds better to the published structure (reflections at 25.5°, 28°, 38.5°, 40.5°, 43°, 49°). The same conclusions are valid when considering only the linkers (Figure 9) although fewer differences can be seen. Contrary to the results with the vanadium chains, the differences between the FM and AF structures are the most pronounced in the organic linkers, with the B^{AF} geometry fitting the published structure the best (reflections on 25°, 28.3°, 39.5°). The geometrical difference between the structure with and without displaced vanadium chains is very limited for the linkers and is only shown in the relatively small reflection at 15°. Generally, the linkers barely influence the calculated diffractogram, compared to the vanadium chains, even though their geometrical variations are much more pronounced, as can be seen by comparing the left and right panel of figure 1.

With this comparison it can be concluded that the B^{AF} structure is in close agreement with the published geometry, and the main differences between the structures are indeed a consequence of the geometry of the vanadium chains. The presented partial geometry approach allows to visualize the difference between geometries in more detail since only parts of the geometry are considered. It can again be seen that the displacement of vanadium chains is clearly visible while the different electronic structures induce only smaller geometrical differences.

The same exercise can be done for the force field geometries, as can be seen in figure S2 and S3 of the supporting information. The analysis shows that the main differences between the calculated and published geometries are to be found in the vanadium chains. The difference between the model derived from static calculations and the one from molecular dynamics can also be seen here, with the latter being in better agreement with the published geometry. This again shows the beneficial effect of the structure averaging by molecular dynamics calculations.

Conclusions

In this paper a methodology is presented to directly compare theoretically predicted geometries for crystalline materials to experimental X-ray diffractograms. The method has been applied on the well-studied case of the MIL-47(V) material. MOFs are particularly challenging for accurate structure determination due to their often flat potential energy surface. Herein we propose to directly compare theoretically determined diffractograms using a variety of input geometrical data with experimental X-ray diffractograms. Both a qualitative procedure where the diffractograms are compared visually

and a quantitative procedure based on Rietveld's model was proposed.

As a case study the MIL-47(V) material was chosen. High-level ab initio calculations on this material yielded several possible geometries with comparable energies. By comparing these results to a well-resolved X-ray diffractogram the geometry with displaced vanadium chains and a ferromagnetic electronic structure, B^{FM} , was identified as being the most plausible. Especially the displacement in the vanadium chains appears to be crucial, despite the displaced geometry being energetically very close to the non-displaced variant. Next to the ab initio calculations, a force field for this material was constructed using a generic tool, namely the QuickFF methodology. Herein a force field is constructed from ab initio cluster data. In order to validate this force field the same procedures were employed. It was found that the proposed force field was able to predict the geometry of the MOF very well up to the small displacement of the vanadyl chains which was not surprising as this shift was not incorporated in the two clusters of Figure 3, that are figuring as reference data for the force field construction. In addition, the concept of the use of the two clusters in the force-field determination also leads to a prediction of a too large unit cell for MIL-47(V) due to overestimation of bond lengths by the DFT reference calculations. However, overall the generated molecular dynamics geometry of the force field yields satisfactory agreement with the X-ray diffractograms.

The decomposition of the global structure into two partial structures with a separate derivation of the X-ray diffractogram learns that the position of the vanadium chains has a significant impact on the XRD pattern while the shape of the linkers has significantly less influence. This conclusion is valid for both the ab initio structure as for the molecular mechanics structure. This tool allows to determine the importance of certain parts of the geometry for the powder pattern, unbiased by visual structural differences. While the B^{FM} structure provided the best correspondence to the measured X-ray diffractogram it appears that the B^{AF} geometry is in closer agreement with the structure refined from single crystal data.

Generally it can be concluded that the tools presented here to compare theoretical structures are very versatile and easy to use, the procedure that should be followed is shown in the flow scheme (Figure 4). Powder patterns obtained by laboratory-scale diffractometers can be used to refine the fine structure of a very complex material by choosing the most well-suited geometry from ab initio calculations. This method is very useful when accurate geometries are necessary for applications such as adsorption, mechanical properties etc. Especially in the case where no single crystals are available it can prove crucial for structure resolution. Moreover, this method can assist in the design of new force field models for this crystalline materials by comparing the geometries obtained by it directly to experimental data.

Acknowledgements

The authors acknowledge financial the support from the European Research Council for funding through the European Community's Seventh Framework Programme (FP7(2007-2013) ERC Grant Agreement 240483). T.B. is grateful for the support from UGent GOA grant 01G00710. L.V. is an aspirant fellow at the FWO. D.E.P.V. is a postdoctoral researcher funded by the Foundation of Scientific Research-Flanders (FWO) (project no. 1253415N). The computational resources (Stevin Supercomputer Infrastructure) and services used in this work were provided by the VSC (Flemish Supercomputer Center), funded by Ghent University, the Hercules Foundation and the Flemish Government – department EWI.

Notes and references

- M. Y. Sun, A. E. Nelson and J. Adjaye, *J. Phys. Chem. B*, 2006, **110**, 2310-2317.
- P. Kuhn, M. Antonietti and A. Thomas, *Angew. Chem.-Int. Edit.*, 2008, **47**, 3450-3453.
- A. P. Cote, H. M. El-Kaderi, H. Furukawa, J. R. Hunt and O. M. Yaghi, *J. Am. Chem. Soc.*, 2007, **129**, 12914-+.
- G. Ferey, C. Mellot-Draznieks, C. Serre, F. Millange, J. Dutour, S. Surble and I. Margiolaki, *Science*, 2005, **309**, 2040-2042.
- M. E. Schweinfuss, S. Springer, I. A. Baburin, T. Hikov, K. Huber, S. Leoni and M. Wiebcke, *Dalton Trans.*, 2014, **43**, 3528-3536.
- D. E. P. Vanpoucke, J. W. Jaeken, S. De Baerdemacker, K. Lejaeghere and V. Van Speybroeck, *Beilstein Journal of Nanotechnology*, 2014, **5**, 1738-1748.
- D. Vanpoucke, K. Lejaeghere, M. Waroquier, V. Van Speybroeck and A. Ghysels, *Journal of Physical Chemistry C (submitted)*, 2015.
- S. Biswas, D. E. P. Vanpoucke, T. Verstraelen, M. Vandichel, S. Couck, K. Leus, Y.-Y. Liu, M. Waroquier, V. Van Speybroeck, J. F. M. Denayer and P. Van Der Voort, *The Journal of Physical Chemistry C*, 2013, **117**, 22784-22796.
- Y. G. Chung, J. Camp, M. Haranczyk, B. J. Sikora, W. Bury, V. Krungleviciute, T. Yildirim, O. K. Farha, D. S. Sholl and R. Q. Snurr, *Chemistry of Materials*, 2014, **26**, 6185-6192.
- K. V. Lawler, Z. Hulvey and P. M. Forster, *Phys. Chem. Chem. Phys.*, 2015, **17**, 18904-18907.
- J. K. Bristow, D. Tiana and A. Walsh, *J. Chem. Theory Comput.*, 2014, **10**, 4644-4652.
- M. A. Addicoat, N. Vankova, I. F. Akter and T. Heine, *J. Chem. Theory Comput.*, 2014, **10**, 880-891.
- S. Bureekaew, S. Amirjalayer, M. Tafipolsky, C. Spickermann, T. K. Roy and R. Schmid, *physica status solidi (b)*, 2013, **250**, 1128-1141.
- L. Vanduyfhuys, S. Vandenbrande, T. Verstraelen, R. Schmid, M. Waroquier and V. Van Speybroeck, *J. Comput. Chem.*, 2015, **36**, 1015-1027.
- L. Vanduyfhuys, T. Verstraelen, M. Vandichel, M. Waroquier and V. Van Speybroeck, *J. Chem. Theory Comput.*, 2012, **8**, 3217-3231.
- H. Fang, P. Kamakoti, P. I. Ravikovitch, M. Aronson, C. Paur and D. S. Sholl, *Phys. Chem. Chem. Phys.*, 2013, **15**, 12882-12894.
- S. L. C. Moors, K. De Wispelaere, J. Van der Mynsbrugge, M. Waroquier and V. Van Speybroeck, *ACS Catalysis*, 2013, **3**, 2556-2567.
- E. Verheyen, L. Joos, K. Van Havenbergh, E. Breynaert, N. Kasian, E. Gobechiya, K. Houthoofd, C. Martineau, M. Hinterstein, F. Taulelle, V. Van Speybroeck, M. Waroquier, S. Bals, G. Van Tendeloo, C. E. A. Kirschhock and J. A. Martens, *Nat. Mater.*, 2012, **11**, 1059-1064.
- B. K. Chang, N. C. Bristowe, P. D. Bristowe and A. K. Cheetham, *Phys. Chem. Chem. Phys.*, 2012, **14**, 7059-7064.
- M. Vandichel, J. Hajek, F. Vermoortele, M. Waroquier, D. E. De Vos and V. Van Speybroeck, *CrystEngComm*, 2015, **17**, 395-406.
- S. Henne, B. Bredenkotter, M. Alaghemandi, S. Bureekaew, R. Schmid and D. Volkmer, *ChemPhysChem*, 2014, **15**, 3855-3863.
- K. Barthelet, J. Marrot, D. Riou and G. Férey, *Angewandte Chemie International Edition*, 2002, **41**, 281-284.
- P. G. Yot, Q. Ma, J. Haines, Q. Yang, A. Ghoufi, T. Devic, C. Serre, V. Dmitriev, G. Ferey, C. Zhong and G. Maurin, *Chemical Science*, 2012, **3**, 1100-1104.
- C. F. Macrae, I. J. Bruno, J. A. Chisholm, P. R. Edgington, P. McCabe, E. Pidcock, L. Rodriguez-Monge, R. Taylor, J. van de Streek and P. A. Wood, *Journal of Applied Crystallography*, 2008, **41**, 466-470.
- V. Petricek, M. Dusek and L. Palatinus, *Z. Kristall.*, 2014, **229**, 345-352.
- S. Grimme, J. Antony, S. Ehrlich and H. Krieg, *J. Chem. Phys.*, 2010, **132**.
- S. Grimme, S. Ehrlich and L. Goerigk, *J. Comput. Chem.*, 2011, **32**, 1456-1465.
- P. E. Blöchl, *Phys. Rev. B*, 1994, **50**, 17953-17979.
- G. Kresse and J. Hafner, *Phys. Rev. B*, 1993, **47**, 558-561.
- G. Kresse and J. Furthmüller, *Phys. Rev. B*, 1996, **54**, 11169-11186.
- G. Kresse and D. Joubert, *Phys. Rev. B*, 1999, **59**, 1758-1775.
- J. P. Perdew, K. Burke and M. Ernzerhof, *Phys. Rev. Lett.*, 1996, **77**, 3865-3868.
- P. G. Dacosta, O. H. Nielsen and K. Kunc, *Journal of Physics C: Solid State Physics*, 1986, **19**, 3163.
- P. Vinet, J. R. Smith, J. Ferrante and J. H. Rose, *Phys. Rev. B*, 1987, **35**, 1945-1953.
- G. W. T. M. J. Frisch, H. B. Schlegel, G. E. Scuseria, M. A. Robb, J. R. Cheeseman, G. Scalmani, V. Barone, B. Mennucci, G. A. Petersson, H. Nakatsuji, M. Caricato, X. Li, H. P. Hratchian, A. F. Izmaylov, et al., *Journal*, 2009.
- A. D. Becke, *J. Chem. Phys.*, 1993, **98**, 5648-5652.
- C. T. Lee, W. T. Yang and R. G. Parr, *Phys. Rev. B*, 1988, **37**, 785-789.
- A. D. Becke, *Physical Review A*, 1988, **38**, 3098-3100.
- R. Krishnan, J. S. Binkley, R. Seeger and J. A. Pople, *The Journal of Chemical Physics*, 1980, **72**, 650-654.
- A. D. McLean and G. S. Chandler, *The Journal of Chemical Physics*, 1980, **72**, 5639-5648.
- T. Verstraelen, K. Boguslawski, P. Tecmer, F. Heidar-Zadeh, M. Chan, T. D. Kim, Y. Zhao, S. Vandenbrande, D. Yang, C. E. González-Espinoza, P. A. Limacher, D. Berruocal, A. Malek and P. W. Ayers, *HORTON 2.0.0*, <http://theochem.github.com/horton>, 2015.

42. N. L. Allinger, Y. H. Yuh and J. H. Lii, *J. Am. Chem. Soc.*, 1989, **111**, 8551-8566.
43. T. Verstraelen, L. Vanduyfhuys, S. Vandenbrande and S. M. J. Rogge, *Yaff, yet another forcefield*, Available at: <http://molmod.uqent.be/software/>.
44. S. Nose, *Mol. Phys.*, 1984, **52**, 255-268.
45. G. J. Martyna, D. J. Tobias and M. L. Klein, *The Journal of Chemical Physics*, 1994, **101**, 4177-4189.
46. A. Spek, *Acta Crystallographica Section D*, 2009, **65**, 148-155.
47. H. Rietveld, *Journal of Applied Crystallography*, 1969, **2**, 65-71.
48. K. D. M. Harris and M. Tremayne, *Chemistry of Materials*, 1996, **8**, 2554-2570.
49. L. B. McCusker, R. B. Von Dreele, D. E. Cox, D. Louer and P. Scardi, *Journal of Applied Crystallography*, 1999, **32**, 36-50.
50. W. I. F. David, K. Shankland, L. B. McCusker and C. Bärlocher, *Structure Determination from Powder Diffraction Data*, OUP Oxford, 2006.
51. A. Le Bail, *Powder Diffraction*, 2005, **20**, 316-326.
52. A. Le Bail, H. Duroy and J. L. Fourquet, *Mater. Res. Bull.*, 1988, **23**, 447-452.
53. E. I. Solomon, R. A. Scott and R. B. King, *Computational Inorganic and Bioinorganic Chemistry*, Wiley, 2013.
54. L. He, F. Liu, G. Hautier, M. J. T. Oliveira, M. A. L. Marques, F. D. Vila, J. J. Rehr, G. M. Rignanese and A. Zhou, *Phys. Rev. B*, 2014, **89**, 064305.
55. B. Schatschneider, S. Monaco, A. Tkatchenko and J.-J. Liang, *The Journal of Physical Chemistry A*, 2013, **117**, 8323-8331.
56. B. B. Averkiev, Z. A. Dreger and S. Chaudhuri, *The Journal of Physical Chemistry A*, 2014, **118**, 10002-10010.

Supporting information

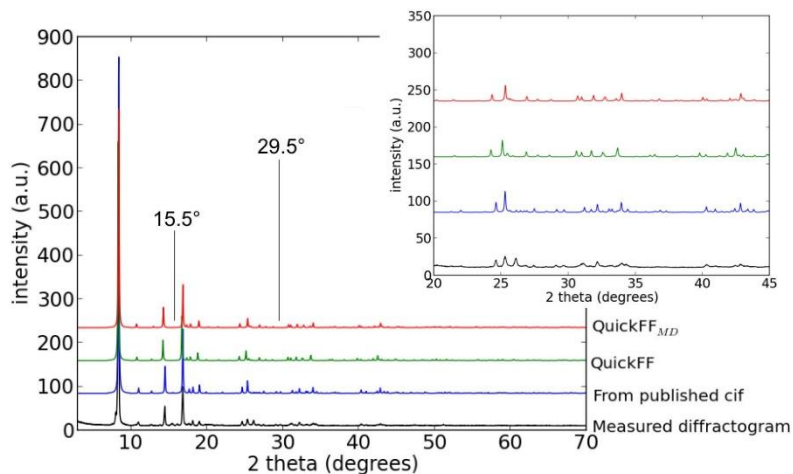


Figure S1. Overview of the comparison between the force field models, published structure and the experimental diffractogram.

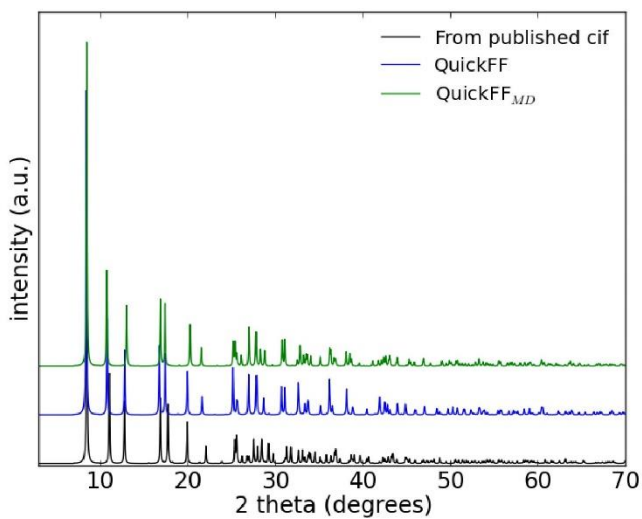


Figure S2. Comparison with the QuickFF geometry when only considering the vanadium chains.

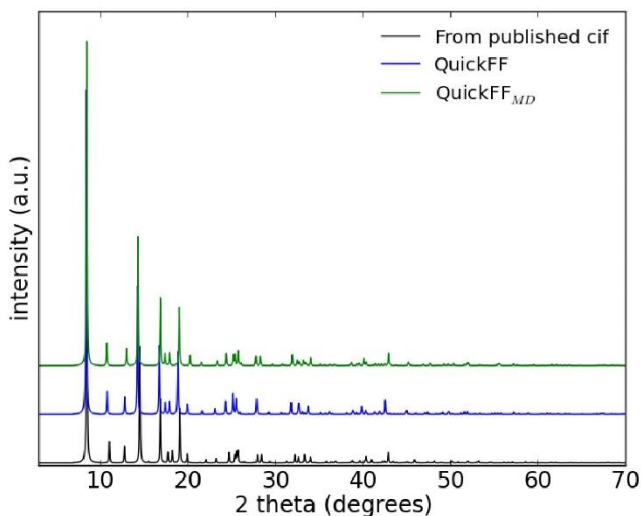


Figure S3. Comparison with the QuickFF geometry when only considering the linkers.

Table S1. Some key bond lengths and bending angles of the equilibrium structure of Mil-47 according to different sources. The symbol * indicates that these distances are taken from the linker cluster.

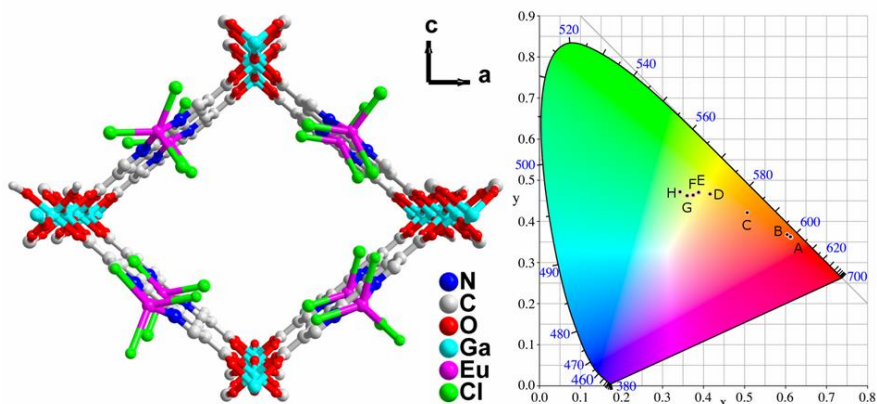
	Exp. periodic ¹	DFT (PBE) periodic ²	DFT (B3LYP) cluster	FF periodic
Bond lengths [Å]				
V - O (short)	1.672	1.654	1.588	1.593
V - O (long)	2.108	2.097	2.311	2.346
V - O ₁	1.970	1.990	1.977	1.980
V - O ₂	1.976	1.976	2.033	2.040
V - V	3.422	3.440	3.531	3.550
O ₁ - C _{ca}	1.277	1.281	1.275	1.273
O ₂ - C _{ca}	1.252	1.278	1.255	1.255
C _{ca} - C _{pc}	1.501	1.487	1.494*	1.496
C _{pc} - C _{ph}	1.372	1.404	1.399*	1.400
Bending angles [°]				
V - O - V	129.4	132.7	128.8	127.7
O ₁ - V - O ₁	91.5		91.3	90.3
O ₂ - V - O ₂	90.4		87.7	88.9
O ₁ - C _{ca} - O ₂	126.0	125.2	125.3	126.7

In Table S1, the force field values of some key bond lengths and bending angles in equilibrium are compared with several other sources, both ab initio and experimental. In first instance, the force field values (last column) need to be compared with the DFT cluster values (third column) that were used as input for the force field fitting. It is clear from the table that the force field reproduces these DFT cluster values very accurately, which illustrates the accuracy of the fitting methodology. However, when comparing the experimental values (first column) with the DFT cluster values (third

column) there is a clear discrepancy, especially in the vanadium oxygen bonds. These errors are mainly due to the lack of periodic constraints. Indeed, the periodic DFT computations (second column) do reproduce the experimental values well. As such, we can conclude that most of the errors that are found by using the force field are not due to the force field approximation itself. Instead, they can be traced back to the DFT cluster data and its inability to accurately represent the periodic constraints of the experimental structure.

1. K. Barthelet, J. Marrot, D. Riou and G. Férey, *Angewandte Chemie International Edition*, 2002, **41**, 281-284.
2. D. E. P. Vanpoucke, J. W. Jaeken, S. De Baerdemacker, K. Lejaeghere and V. Van Speybroeck, *Beilstein Journal of Nanotechnology*, 2014, **5**, 1738-1748.

PAPER VII: BIPYRIDINE-BASED NANOSIZED METAL-ORGANIC FRAMEWORK WITH TUNABLE LUMINESCENCE BY A POSTMODIFICATION WITH EU(III): AN EXPERIMENTAL AND THEORETICAL STUDY



Y-Y Liu, R. Decadt, T. Bogaerts, K. Hemelsoet, A.M. Kaczmarek, D. Poelman, M. Waroquier, V. Van Speybroeck, R. Van Deun, P. Van der Voort, *Journal of Physical Chemistry C*, 117 (21), 11302–11310, **2013**.

T. Bogaerts assisted in this paper by the calculation of UV/Vis spectra for the material characterization with these techniques.

Reprinted with permission from the American Chemical Society. Copyright 2015 American Chemical Society.

Bipyridine-Based Nanosized Metal–Organic Framework with Tunable Luminescence by a Postmodification with Eu(III): An Experimental and Theoretical Study

Ying-Ya Liu,[†] Roel Decadt,[‡] Thomas Bogaerts,^{†,§} Karen Hemelsoet,[§] Anna M. Kaczmarek,[‡] Dirk Poelman,^{||} Michel Waroquier,[§] Veronique Van Speybroeck,[§] Rik Van Deun,[‡] and Pascal Van Der Voort^{*,†}

[†]COMOC—Centre for Ordered Materials, Organometallics and Catalysis, Department of Inorganic and Physical Chemistry, Ghent University, Krijgslaan 281-S3, 9000 Ghent, Belgium

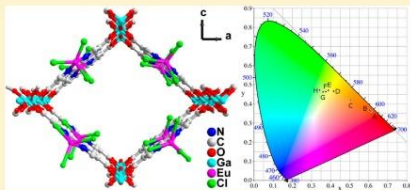
[‡]Element Coordination Chemistry Group, Department of Inorganic and Physical Chemistry, Ghent University, Krijgslaan 281-S3, 9000 Ghent, Belgium

[§]Center for Molecular Modeling, Ghent University, Technologiepark 903, 9052 Zwijnaarde, Belgium

^{||}LumiLab, Department of Solid State Sciences, Ghent University, Krijgslaan 281-S1, 9000 Ghent, Belgium

Supporting Information

ABSTRACT: A gallium 2,2'-bipyridine-5,5'-dicarboxylate metal–organic framework, Ga(OH)(bpydc), denoted as COMOC-4 (COMOC = Center for Ordered Materials, Organometallics and Catalysis, Ghent University) has been synthesized via solvothermal synthesis procedure. The structure has the topology of an aluminum 2,2'-bipyridine-5,5'-dicarboxylate – the so-called MOF-253. TEM and SEM micrographs show the COMOC-4 crystals are formed in nanoplates with uniform size of 30–50 nm. The UV–vis spectra of COMOC-4 in methanol solution show maximal electronic absorption at 307 nm. This results from linker to linker transitions as elucidated by time-dependent density functional theory simulations on the linker and COMOC-4 cluster models. When excited at 400 nm, COMOC-4 displays an emission band centered at 542 nm. Upon immersion in different solvents, the emission band for the framework is shifted in the range of 525–548 nm depending on the solvent. After incorporating Eu³⁺ cations, the emission band of the framework is shifted to even shorter wavelengths (505 nm). By varying the excitation wavelengths from 250 to 400 nm, we can fine-tune the emission from red to yellowish green in the CIE diagram. The luminescence behavior of Eu³⁺ cations is well preserved and the solid-state luminescence lifetimes of $\tau_1 = 45 \mu\text{s}$ (35.4%) and $\tau_2 = 162 \mu\text{s}$ (64.6%) are observed.



1. INTRODUCTION

Luminescent materials are of great interest and have numerous applications ranging from light emitting devices (LEDs) to materials for medical diagnostics and cell biology. Luminescent metal–organic frameworks (MOFs)^{1–4} combining a high, well-defined porosity and an intense fluorescence have gained a lot of attention in the past few years. A recent review article concluded that about 10% of all reported MOFs have interesting luminescence properties.⁵ The main advantage of a luminescent MOF is based on the unique inorganic–organic hybrid framework, in which the concentration of the emitting metal ions per unit cell can be systematically adjusted by simply varying the organic linkers. Second, the high surface area and pore volumes make these materials the ideal candidates for sensing.^{6,7}

To date, most of the research on synthesizing MOFs has been based on transition metal ions, which have certain coordination motifs, thus allowing a rational synthetic strategy to obtain the

desired structures. However, for lanthanide (Ln) MOFs, the research is less extensive, which is obviously due to the higher coordination numbers and the more variable nature of the Ln coordination sphere. This makes a rational design of Ln-based MOFs extremely difficult.^{8,9} Thus, to exploit their luminescence properties efficiently, alternative strategies have been explored such as the design or chemical modification of the organic linker to gain ligand emission or alternatively doping the porous MOF materials with a luminescent molecule.^{7,10} As Ln-doped materials¹¹ are widely employed as phosphors for photonic applications such as sensors, solid-state lighting, nonlinear optics, and biomedical analysis, it is obvious that Ln-doped MOFs can pave the way toward novel luminescent materials.

Received: March 2, 2013

Revised: April 24, 2013

Published: April 29, 2013



ACS Publications

© 2013 American Chemical Society

11302

dx.doi.org/10.1021/jp402154q.1. Phys. Chem. C 2013, 117, 11302–11310

Furthermore, for luminescence applications, control of the particle size is a powerful strategy to modulate the optical properties, especially for semiconductor nanoparticles.^{12–14} This also applies to MOFs and by controlling the synthesis procedure, the crystal size of the MOFs can be downsized to the nanometer scale. These so-called nano-MOFs can provide novel opportunities for catalysis, bioimaging, and sensing.^{15–18} For example, Chen et al. reported on Ln-MOFs with Lewis-basic pyridyl sites for sensing of metal ions.¹⁹ Recently, a mixed Ln-MOF has been developed as a luminescent thermometer.²⁰ However, very few examples of luminescent MOFs have been reported with collaborative functionalities of tunable luminescence and nanoscale processability.^{21,22}

To get more detailed information about the geometry and electronic structure of MOFs ab initio calculations can be used. Molecular modeling tools have proven useful in the investigation of electronic structure²³ and spectroscopic properties.^{24,25} A theoretical analysis allows us to provide more insight in the molecular structure of the MOF and more specifically the defects and impurities contained in the framework.²⁶

Here, we report a new luminescent active gallium-based nano-MOF Ga(OH)(bpydc) (bpydc²⁻ = 2,2'-bipyridine-5,5'-dicarboxylate), denoted as COMOC-4 (COMOC = Center for Ordered Materials, Organometallics and Catalysis, Ghent University). This MOF compound is isostructural to MOF-253, which was recently reported by Yaghi and co-workers.²⁷ It should be noted that this framework constitutes open 2,2'-bipyridine sites, which is a classical unit for chelating with transition metal or lanthanide ions to form complexes that show intense luminescence.^{28–30} By postsynthetic modification, 2,2'-bipyridine sites can bind luminescent Ln³⁺-ions resulting in luminescent MOFs.^{31,32}

2. EXPERIMENTAL AND COMPUTATIONAL SECTION

2.1. Syntheses. The H₂bpydc ligand was prepared according to a published procedure.³³ Methanol used for spectroscopic studies was spectroscopic grade. All other starting materials were commercially available reagents of analytical grade and were used without further purification.

COMOC-4 (Ga(OH)(bpydc) Synthesis. Ga(NO₃)₃·H₂O (0.06 g, 0.22 mmol), H₂bpydc (0.06 g, 0.25 mmol), and DMF (5 mL) were placed in a 15 mL Pyrex tube and heated at 150 °C for 48 h. This resulted in a green powdered phase in suspension. Upon contact with air, the solid color changed immediately from green to orange. The orange colored gel phase was filtered off, washed consecutively with DMF, methanol and acetone, and dried in vacuum. Afterward, the solid product was suspended in DMF solution (0.5 g per 50 mL DMF), heated at 80 °C for 4 h, filtered off, washed consecutively with DMF and acetone, and dried in vacuum. The yield was 33% based on gallium. IR spectrum (cm⁻¹, KBr pellet): 3379 (br), 1619 (s), 1595 (s), 1421 (s), 1394 (s), 1158 (w), 1050 (w), 847 (w), 775 (m), 705 (w), 600 (w), 479 (w). Calcd for Ga(OH)(C₁₂H₆N₂O₄)·2.7H₂O: C, 38.36; H, 3.27; N, 7.46; Found: C, 38.26; H, 3.12; N, 7.17.

To remove the organic species encapsulated within the pores of the open framework, the sample was activated by Soxhlet extraction in methanol for 24 h at 120 °C and then dried at 120 °C under vacuum overnight. Because of the presence of the -OH group on the gallium building unit, the 1D channels are highly hydrophilic. In ambient air, rehydration occurs. Thus, the activated sample was kept in an inert to prevent possible hydrolysis reactions.

Eu³⁺@COMOC-4 Preparation. Eu³⁺@COMOC-4 was prepared by stirring the mixture of 0.05 g of Ga(OH)(bpydc) and 0.033 g EuCl₃·6H₂O in 30 mL absolute ethanol at 50 °C for 24 h. The solid was then filtered off, and the yellowish powder was stirred in 15 mL pure ethanol for another 24 h followed by filtration. This procedure was repeated two times to guarantee that all excess EuCl₃ salt is removed. IR spectrum (cm⁻¹, KBr pellet): 3370 (br), 2925 (w), 2855 (w), 1616 (s), 1591 (s), 1412 (s), 1384 (s), 1164 (w), 1048 (w), 853 (w), 776 (m), 706 (w), 602 (w), 477 (w). Calcd for Ga(OH)(C₁₂H₆N₂O₄)·3H₂O·C₂H₆O·0.11EuCl₃: C, 36.76; H, 4.19; N, 6.12; Found: C, 36.82; H, 3.15; N, 5.90.

2.2. Characterization. X-ray Powder Diffraction Measurements and Thermal Gravimetric Analysis. X-ray powder diffraction (XRPD) patterns were recorded on a Thermo Scientific ARL X'Tra diffractometer, operated at 40 kV, 40 mA using Cu-K α radiation (λ = 1.5406 Å). The lattice parameters were determined using the DICVOL program³⁴ and refined using the STOE's WinXPow³⁵ software package. Thermal gravimetric analysis (TGA) data were obtained on a Netzsch STA 449 F3 Jupiter-Simultaneous TG-DSC analyzer with a heating rate of 10 °C min⁻¹ in air. N₂ sorption measurements were carried on Belsorp II, Bell Japan, inc. Each sample was activated under vacuum at 120 °C for 3h prior to measurement.

Spectroscopic Characterizations. Fourier transform infrared (FTIR) spectra were recorded in the region of 400–4000 cm⁻¹ on a Bruker EQUINOX 55 FTIR spectrometer. The UV–vis absorption spectra were recorded on a PerkinElmer Lambda 950 UV–vis spectrometer in the range of 260–1000 nm. The spectra were recorded using fine suspensions of powder samples (COMOC-4, Eu³⁺@COMOC-4) with methanol as dispersing solvent. In a typical measurement, 4 mg of powder sample was suspended in 3 mL of methanol in an ultrasonic bath for 5 min. The suspension was transferred to a 10 mm path length quartz cuvette to record the spectra. The diffuse UV–vis reflection spectra (DRS) experiments were carried out using a Varian Cary 500 UV–vis-NIR spectrophotometer with diffuse reflectance accessory (integrated sphere) for spectrophotometric measurements in the range of 200–800 nm. The spectra were converted using the Kubelka–Munk function.

Morphology Characterizations. The particle shape and size was determined using a JEOL JEM2200FS transmission electron microscope with an accelerating voltage of 200 kV. Images were obtained digitally on a Gatan CCD camera. The samples for TEM were prepared on copper grids (size 200 mesh) coated with a carbon support film. 0.01 g of the powder sample was dispersed in 2 mL of methanol and sonicated to prepare the suspension. A drop of the suspension was placed on a copper grid and left to dry in air. Scanning electron microscopy (SEM) images were taken on a FEI Quanta 200FEG microscope with 4 nm resolution operating at 30 kV.

Luminescence Measurements. The photoluminescence measurements were carried out on an Edinburgh Instruments FLSP920 UV–vis-NIR spectrofluorimeter, using a 450 W xenon lamp as the steady-state excitation source and a Hamamatsu R928P PMT detector, which has a response curve between 200 and 900 nm. For time-resolved measurements, the setup uses a 60W pulsed xenon lamp operating at a pulse frequency of 100 Hz.

COMOC-4 sample soaked with various solvents were prepared by immersing the desolvated COMOC-4 in different solvent solution, stirring at room temperature for 0.5 h, filtered, and collecting the solid sample for luminescence measurements.

Quantification of Eu Loadings by Means of XRF Analysis. The XRF measurements were performed on Rigaku NexCG, Energy Dispersive X-ray Fluorescence (EDXRF) apparatus. A standard addition method was used using $\text{VO}(\text{acac})_2$ as external standard.

2.3. Computational Methodology. All calculations were done with the Gaussian09³⁶ program. Geometries were optimized using the hybrid B3LYP functional,^{37,38} combined with a 6-31+G(d) Pople basis set. UV–vis absorption wavelengths were obtained using a static TD-DFT^{39–42} calculation on the optimized geometry using a 6-31+G(d) or a 6-311++G(2df,2p) basis set. Vertical transitions are known to provide good estimates of experimental electronic transitions.^{43,44} For the TD-DFT simulations, three DFT functionals have been employed. In order of increasing % HF exchange, we tested HCTH⁴⁵ (0% HF exchange), B3LYP^{37,38} (20% HF exchange), and CAM-B3LYP⁴⁶ (long-range corrected functional with varying amount of HF exchange, up to 63% at large distance). These functionals have already proven successful in the calculation of UV–vis spectra.^{24,47} Where applicable, a continuum PCM solvent model for methanol was applied.

For the optimization of the MOF models, clusters were extracted from the crystallographic file of DUT-5,⁴⁸ which is similar to COMOC-4; the model was then adapted to correspond with our MOF. In a first step, the carboxyl –OH and –O groups were allowed to relax keeping the rest of the structure fixed. In a second step, these groups were fixed while the rest of the structure was relaxed. This was repeated three times to allow the geometry to fully converge. This procedure is necessary since gallium is significantly bigger than aluminum (from the original crystallographic file) and the bond lengths must be allowed to relax. The fixation of the terminal atoms allows mimicking the rigidity of the crystal in the cluster model. Using this methodology, two clusters were isolated, a smaller one (2 linkers) and a larger one (4 linkers), as shown in Figure 3.

3. RESULTS AND DISCUSSION

The gallium-based nanosized MOF compound has been obtained by mixing gallium(III) nitrate and H_2bpydc (2,2'-bipyridine-5,5'-dicarboxylic acid) in dimethylformamide (DMF) to yield an orange crystalline powder "COMOC-4-as" (as: as-synthesized), $\text{Ga}(\text{OH})(\text{bpydc})\cdot 3\text{H}_2\text{O}$. Afterward, COMOC-4-as was activated by vacuum drying to yield COMOC-4 and this porous structure was postfunctionalized with a solution of europium(III) chloride in ethanol. Both COMOC-4 and Eu^{3+} @COMOC-4 were characterized by powder X-ray diffraction (XRD), thermogravimetric analysis, CHNS elemental analysis, scanning electron microscopy (SEM), transmission electron microscopy (TEM), FTIR spectroscopy, X-ray fluorescence spectroscopy (XRF), UV–vis absorbance, and diffuse reflectance spectroscopy (DRS), as well as steady state and time-resolved luminescence spectroscopy. In addition, the spectroscopic absorbance properties of COMOC-4 are compared with theoretical data using TD-DFT calculations on model clusters representative of the linker as well as of COMOC-4. Electronic transitions are computed using different theoretical methodologies and inspection of the involved molecular orbitals provide insight into the nature of the transitions.

3.1. Structural Characterization. The powder XRD pattern (Figure S1 of the Supporting Information) shows that COMOC-4 is isostructural with DUT-5 ($\text{Al}(\text{OH})(\text{bpd})$) (bpd^{2-} = biphenyl-4,4'-dicarboxylate).⁴⁸ Laboratory powder XRD data have been used to index the unit cell with

orthorhombic unit cell parameters of $a = 21.98(24)$ Å, $b = 7.302(8)$ Å, and $c = 17.470(24)$ Å. The COMOC-4 framework is based on infinite chains of octahedral $\text{GaO}_4(\text{OH})_2$ units, where each Ga^{3+} ion is bound to four bpydc^{2-} ligands and two μ_2 trans hydroxide anions. This is a common coordination motif that has already been encountered in a series of M^{3+} carboxylate frameworks ($M = \text{Al}, \text{Fe}, \text{V}, \text{Ga},$ and In).^{49,50} The $\text{GaO}_4(\text{OH})_2$ chains are aligned parallel to the crystallographic b axis, with the hydroxide and the carboxylate linker alternating on either side of the chains, further linked to each other to form a 3D open framework. After incorporating Eu^{3+} cations into the COMOC-4 framework, the material retained its crystallinity as evidenced by the powder XRD patterns (Figure S1 of the Supporting Information). TEM and SEM images have demonstrated that COMOC-4 crystalline compounds are in the nanosize range consisting of irregularly shaped, crystalline nanoplates with fairly uniform sizes of approximately 30–50 nm. The morphology and size of these nanoparticles does not change upon incorporation of EuCl_3 (Figure S2 of the Supporting Information). These crystalline nanoparticle sizes are consistent with the line broadening of the XRD peaks. The representative structure of EuCl_3 incorporated on the COMOC-4 framework is depicted in Figure 1. By immersing the COMOC-4 material in a europium-

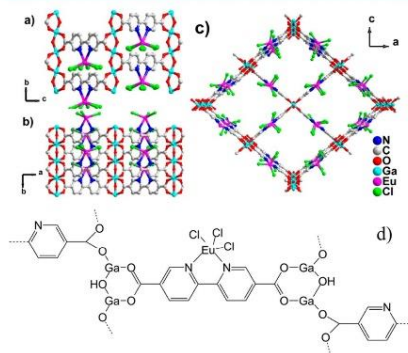


Figure 1. Representative structure of Eu^{3+} @COMOC-4. View perpendicular to (a,b) and along (c) the 1D pore system. The structure model was generated based on the crystal structure of DUT-5.⁴⁸ (d) Schematic representation of EuCl_3 tethered to the bipyridine site of the MOF by postsynthetic modification.

(III) chloride ethanol solution, $0.38 \text{ mmol g}^{-1} \text{Eu}^{3+}$ cations were successfully incorporated into the framework affording $\text{Ga}(\text{OH})(\text{bpydc})\cdot 0.11 \text{EuCl}_3$ (referred as Eu^{3+} @COMOC-4 hereafter). The number of europium(III) ions that had been incorporated in the COMOC-4 host has been determined by X-ray fluorescence (XRF) analysis. The XRF result clearly showing that the molar ratio of Eu/Cl is 1/2.993, which in perfect agreement with the incorporation of EuCl_3 .

The COMOC-4 nanoparticles maintain their permanent microporosity after guest removal, as demonstrated by a type I N_2 sorption isotherm (Figure S3 of the Supporting Information) showing a pore volume of $0.98 \text{ cm}^3/\text{g}$, together with BET and Langmuir surface areas of 747 and $918 \text{ m}^2/\text{g}$, respectively. After incorporating Eu^{3+} cations, the Eu^{3+} @COMOC-4 shows a

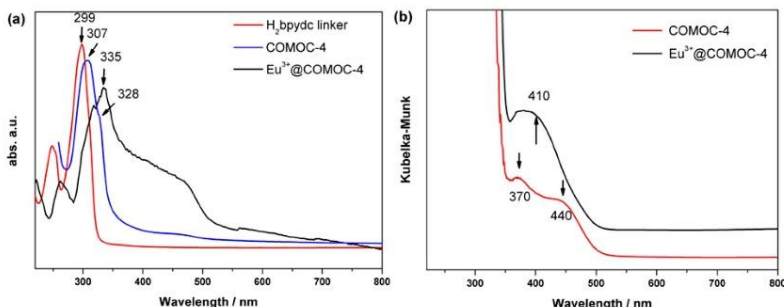


Figure 2. (a) UV-vis absorption spectra of suspended Eu^{3+} @COMOC-4, COMOC-4 in MeOH solution compared to the organic linker dissolved in MeOH solution; (b) solid-state UV-vis spectra calculated from diffuse reflection spectra.

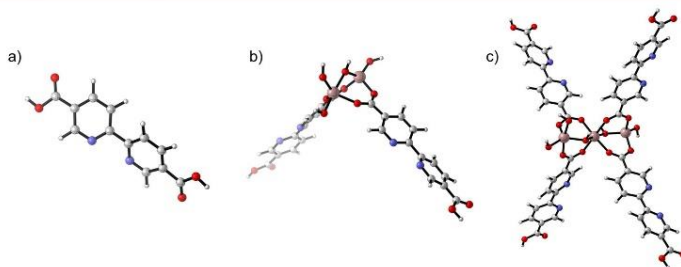


Figure 3. Model for the linker (a) and COMOC-4 (b,c). A small model with two linkers (b) and an extended model with four linkers (c) are investigated.

reduced BET and Langmuir surface area of 493 and 702 $\text{m}^2 \text{g}^{-1}$, respectively, and the pore volume reduced to 0.86 cm^3/g . The thermal behavior of COMOC-4 has been examined by means of thermogravimetric analysis (TGA) (Figure S4 of the Supporting Information). The first mass loss in the TGA profiles corresponds to the elimination of solvent in the pores (~ 8.5 wt %). The COMOC-4 material is thermally stable up to 300 $^\circ\text{C}$, above which a further weight loss of 62 wt % before 560 $^\circ\text{C}$ is indicative of the decomposition of the framework. The final residue (observed, 29.6 wt %; calculated 26.6 wt %) is Ga_2O_3 . As for Eu^{3+} @COMOC-4, the incorporation of Eu^{3+} cations does not influence the thermostability of the framework. The TGA curve shows a weight loss consist of 26 wt % of solvent release in the initial stage followed by 50.6 wt % of weight loss due to the framework decomposition. The residue of 24.6 wt % (calculated 24.8%) is Ga_2O_3 and Eu_2O_3 . Calculated values are based on the elemental analysis results.

In the FTIR spectra, the absorption bands of the C–O carboxyl bonds attached to the metal centers of the bpydc^{2-} ligand are visible at 1619 and 1595 cm^{-1} , respectively. No free carboxylate species, corresponding to the range 1730–1680 cm^{-1} , is observed (Figure S5 of the Supporting Information).

3.2. UV-vis Absorption Spectra. The UV-vis absorption spectra have been recorded using fine suspensions of powdered samples with methanol as dispersing solvent.

As shown in part a of Figure 2, the H_3bpydc ligand displays one strong absorption band in the UV spectral region centered at 299 nm arising from a $\pi\text{-}\pi^*$ transition in the aromatic rings. When coordinated to gallium ions, the absorption spectrum shows a significant red-shift by approximately 8 nm. This progressive red shift is due to the coordination process, which depopulates the electronic aromatic ring of the ligand increasing the HOMO energy and thus decreasing the HOMO–LUMO gap of the coordination compound with respect to the free ligand. Furthermore, the absorption band of COMOC-4 also shows a shoulder at 328 nm and a weak absorption at 440 nm. The Eu^{3+} @COMOC-4 shows only one broad band centered at 335 nm. DRS measurements have also been performed on powdered samples in order to get better resolution in the visible region. As shown in part b of Figure 2, COMOC-4 gives two distinguishable absorption bands at 370 and 440 nm, whereas after incorporation of Eu^{3+} cations these two bands have been replaced by a broader absorption band at around 410 nm.

Ab initio calculations have been used to aid the interpretation of the experimental UV-vis absorption spectra. The H_3bpydc linker is shown in part a of Figure 3. A scan was performed to investigate the geometrical stability of the isolated linker and its influence on the excitation energy. The central dihedral angle N–C–C–N (φ) was varied over 360 $^\circ$ during the scan. Results are displayed in Figure 4. It is shown that the isolated linker

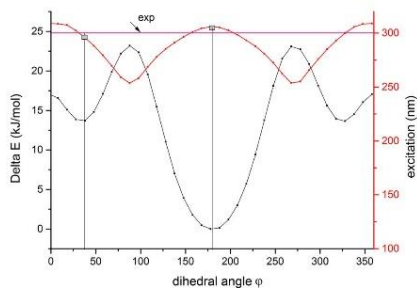


Figure 4. Potential energy in function of the dihedral angle φ ($=\text{N}-\text{C}-\text{C}-\text{N}$) relative to the absolute minimum at $\varphi = 180^\circ$ (both nitrogens facing away from each other) (black curve and left y axis). Also given is the vertical excitation energy at maximum absorbance (red curve and right y axis). The B3LYP/6-31+G(d) level of theory with a PCM solvent model for methanol was used. Experimental value of 299 nm is given for reference.

preferentially forms a planar structure with both nitrogen atoms facing away from each other ($\varphi = 180^\circ$). The corresponding vertical excitation wavelength with maximal absorbance (computed using B3LYP/6-31+G(d) TD-DFT) of this optimized geometry equals 305 nm without and 316 nm with PCM (polarizable continuum model), respectively. A second minimum (Figure 4) corresponds to a slightly twisted linker structure ($\varphi = 37^\circ$), which is only 14 kJ/mol higher in energy compared to the absolute minimum. The absorbance for this model is centered at 288 nm without and at 295 nm with the PCM model. The excitation energy fluctuates significantly in the whole range of the dihedral angle, but at the two minima of the potential energy the B3LYP predictions are quite close to the experimental value justifying the choice of the B3LYP functional. For the sake of completeness, we also performed vertical TD-DFT calculations using other levels of theory. The results are given in Table S1 of the Supporting Information. The main excitation always corresponds to a $\pi-\pi^*$ transition, predominantly a HOMO to LUMO transition. The other functionals or extended basis set do not perform better. An interesting feature in Figure 4 is that the experimental value of 299 nm is also fairly well reproduced at the local minimum when both nitrogen atoms are pointing toward each other. This position is ideal to allow interactions with metal ions, such as the Eu^{3+} ions as studied in this work.

For the interpretation of the COMOC-4 spectrum representative cluster models as shown in parts b and c of Figure 3 are used. Two clusters were isolated, containing 2 and 4 linkers, respectively.

Using the smaller cluster and including a PCM model for methanol, the main absorption is found at 310 nm, which is in excellent agreement with the band at 307 nm found experimentally for COMOC-4 in methanol suspension (part a of Figure 2). However, the shoulder at 328 nm is not present in the theoretical spectrum. To explain this second absorption band, different defects were introduced in the model (Figure S6 of the Supporting Information): a dimethyl formamide (DMF) molecule remaining in the pores, excess gallium nitrate on the bipyridine moiety or a cation due to a missing linker or bridging $-\text{OH}$ group. In the smaller model, the missing linker was represented by removing a saturating $-\text{OH}$ group instead of

removing a whole linker since this would make the structure less representative of the real crystal structure. This means that there is no distinction between the two cases. The first two options do not significantly change the position of the main absorption band (Figure S7 of the Supporting Information). The cationic model however, red shifts the main band to 326 nm (Figure 5), in

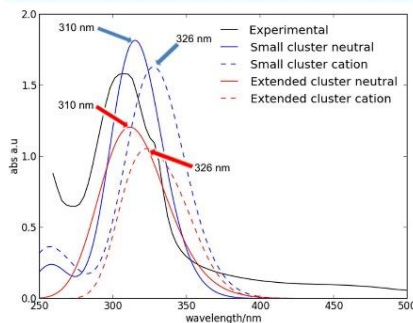


Figure 5. Comparison between the experimental (in black) and calculated (in blue and red) UV-vis spectra for the measurement in suspension using different models for COMOC-4. Results for the neutral models correspond to the full curves, whereas the cationic defect (due to a missing $-\text{OH}$ bridge) correspond to the dashed lines. TD-DFT computations were performed using B3LYP/6-31+G(d) including a methanol PCM solvent model.

agreement with experiment. This suggests that the COMOC-4 structure contains cationic defects. To further investigate the nature of this defect, a bigger model containing four linkers was also investigated. The results are also included in Figure 5 and Table S2 of the Supporting Information. With this extended cluster, removing a linker does not remove all features of the crystal structure, hence the different possibilities for a cationic defect could be considered separate. TD-DFT calculations on the extended cluster show an absorption band around 310 nm, which confirms the results of the smaller cluster. Introducing a missing linker defect causes a red-shift toward 321 nm. The missing $-\text{OH}$ bridge leads to a main absorption band at 326 nm. The shoulder in the experimental spectrum is thus probably due to the latter defect. These types of cations can occur anywhere in the structure but they are more likely to appear at the surface of a crystal.

The maximal absorption band corresponds with a HOMO-LUMO transition and consists primarily of $\pi-\pi^*$ excitations of the linker. This conclusion is manifested in the 3D representation of the HOMO and LUMO orbitals depicted in Figure 6. The coordination of the linker to the metal shifts the excitation to a higher wavelength. The same effect was reported for MOF-5 where the electronic excitations were attributed to the terephthalic acid linker.²⁵ These observations justify our choice for the B3LYP functional. It is known that CAM-B3LYP performs better when charge transfer is present,^{51,52} and this is apparently not the case for our systems.

3.3. Luminescence Properties. It is known that, due to the porous structure, some fluorescent MOF materials are sensitive to the presence or absence of guest solvent molecules and can be used as chemical sensors.^{53–58} The luminescence properties of

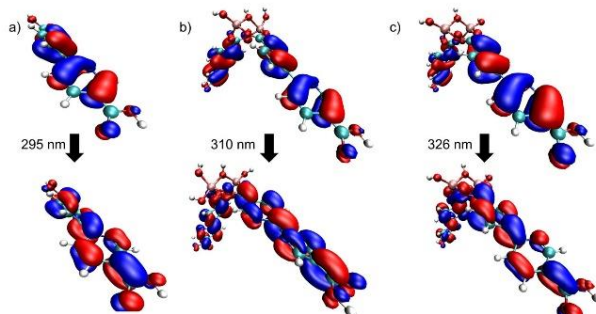


Figure 6. HOMO–LUMO orbitals of the linker (a) the neutral model (b) and the cationic model (c) involved in the π – π^* transitions exhibiting maximal absorbance.

COMOC-4 have been investigated in the solid state at room temperature. The data are summarized in Table 1 and the

Table 1. Luminescence Data of COMOC-4, Eu³⁺@COMOC-4, and H₂bpydc

compound	excitation maximum (nm)	emission maximum (nm)	$\tau_1/\mu\text{s}$	$\tau_2/\mu\text{s}$
COMOC-4 ^a	400	526		
Eu ³⁺ @COMOC-4 ^a	400	505, 579, 591, 612, 650, 699	45(35.4%)	162(64.6%)
		330		
H ₂ bpydc ^b	390	433, 485, 552		

^aSoaked with methanol guest molecules. ^bFrom literature data.⁵⁹

emission spectra are displayed in part a of Figure 7. A strong emission band at 526 nm emerges in COMOC-4 when excited at 400 nm. The influences of different solvents on the fluorescence properties of COMOC-4 have been investigated in the solid state at room temperature (Figure 8). With the excitation wavelength fixed at 400 nm, the fluorescence of hydrated COMOC-4 displays a strong emission band at 542 nm. Upon immersing in

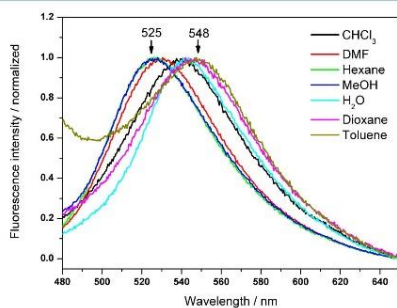


Figure 8. Room temperature solid-state emission spectra of COMOC-4 with different solvent molecules, $\lambda_{\text{exc}} = 400$ nm, $\lambda_{\text{em}} = 525$ –548 nm.

different solvents, the emission band for the framework is shifted in the range of 525–548 nm indicating a guest-responsive fluorescence property (Figure 8). Note that the free H₂bpydc ligand shows emission in the solid state with three bands centered at 433, 485, and 552 nm,⁵⁹ respectively. The blue shift in

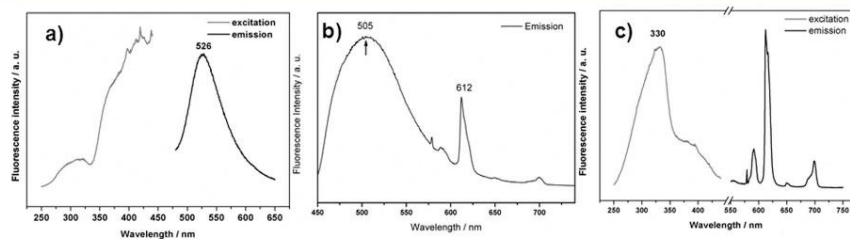


Figure 7. (a) Room temperature solid-state emission and excitation spectra of COMOC-4, $\lambda_{\text{exc}} = 400$ nm, $\lambda_{\text{em}} = 526$ nm; (b) room temperature solid-state emission spectra of Eu³⁺@COMOC-4, $\lambda_{\text{exc}} = 400$ nm; (c) luminescence spectra of Eu³⁺@COMOC-4 in the solid state at room temperature, $\lambda_{\text{exc}} = 330$ nm, $\lambda_{\text{em}} = 612$ nm.

of the emission band of COMOC-4 compound compared to the free organic ligand might be attributed to the ligand-to-metal Ga(III) center charge transfer (LMCT) process.

After incorporating Eu^{3+} cations, the emission band of the framework is shifted to shorter wavelength (505 nm), as shown in part b of Figure 7. In addition, the typical narrow-band emission of Eu^{3+} cations emerges (612 nm), indicating the presence of the Eu^{3+} cations inside the COMOC-4 framework. Part c of Figure 7 further illustrates the solid-state excitation and emission spectra of Eu^{3+} @COMOC-4 excited at 330 nm. When excited at that wavelength, the characteristic sharp emission bands corresponding to the encapsulated Eu^{3+} cations can be clearly observed. The emission spectrum shows peaks at 579, 591, 612, 650, and 699 nm corresponding to the ${}^3\text{D}_0 \rightarrow {}^7\text{F}_i$ ($i = 0-4$) transitions of the Eu^{3+} ion. The fact that the emission band at 612 nm, which corresponds to the hypersensitive ${}^5\text{D}_0 \rightarrow {}^7\text{F}_2$ transition, has a high intensity, indicates that the Eu^{3+} ions are not in an inversion center, but are most likely at a site with low symmetry. This is confirmed by the presence of the ${}^3\text{D}_0 \rightarrow {}^7\text{F}_0$ transition, located at 579 nm (Figure S8 of the Supporting Information) as this peak should only occur when the Eu^{3+} site symmetry is low. In addition, it appears that only one unique crystallographic Eu^{3+} site is present in the material, because of the fact that the ${}^3\text{D}_0 \rightarrow {}^7\text{F}_0$ transition only shows one peak in the emission spectrum (Figure S8 of the Supporting Information). As this is a transition between two nondegenerate states, only one peak can occur. If more than one peak would be seen, this would point to at least two different Eu^{3+} crystal sites. The luminescence decay profile shows a biexponential behavior yielding lifetime values of $\tau_1 = 45 \mu\text{s}$ and $\tau_2 = 162 \mu\text{s}$ (Figure S9 of the Supporting Information).

As both the parent structure and the incorporated Eu^{3+} ions contribute to the compound's luminescence properties, a fine-tuning of the emitted color emission can be easily achieved by adjusting the excitation wavelength. As depicted in Figure 9, by varying the excitation wavelengths from 250 to 400 nm, the CIE (Commission Internationale de l'Éclairage) diagram shows a tunable chromaticity of visible emission from red to yellowish green.

4. CONCLUSIONS

In summary, a gallium 2,2'-bipyridine-5,5'-dicarboxylate nano-MOF (COMOC-4) has been synthesized and fully characterized. Crystalline nanoplates are obtained with fairly uniform sizes of approximately 30–50 nm. The UV-vis spectra of COMOC-4 in methanol solution show maximal electronic absorption at 307 nm due to linker to linker transitions as elucidated by time-dependent DFT simulations on the linker and COMOC-4 cluster models. TD-DFT simulations on models containing a cationic defect due to a missing -OH group cause absorption at 328 nm. The porous framework displays luminescence mainly due to ligand emission but also shows a clear guest-responsive fluorescence property. Moreover, when COMOC-4 framework is further functionalized with Eu^{3+} cations, excitation of the Eu^{3+} @COMOC-4 at 330 nm results in bright red luminescence originating from the Eu^{3+} cations and thus enhanced the overall luminescence of the resulting material. As both the parent structure and the incorporated Eu^{3+} ions contribute to the luminescence properties, a fine-tuning of the emission color can be easily achieved by adjusting the excitation wavelength. The present work provides a convenient and effective route for tuning luminescent properties via a postsynthetic functionalization process.

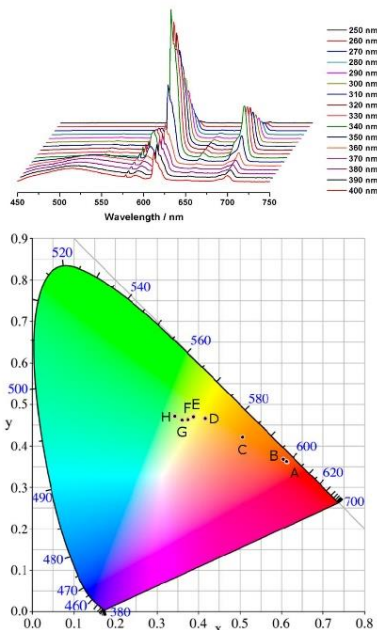


Figure 9. Steady-state emission spectra of Eu^{3+} @COMOC-4 at different excitation wavelengths (top). Emission spectra of Eu^{3+} @COMOC-4 plotted on a CIE diagram with excitation wavelengths varying from 250 nm (A) and from 340 to 400 nm (B ~ H, step size 10 nm) showing tunable chromaticity of visual emission image (bottom).

■ ASSOCIATED CONTENT

Supporting Information

Powder XRD, TEM, and SEM micrographs, N_2 sorption/desorption isotherms, TGA, FTIR spectrum, and additional information concerning theoretical calculations. This material is available free of charge via the Internet at <http://pubs.acs.org>.

■ AUTHOR INFORMATION

Corresponding Author

*Tel: +32-9-264.44.42, e-mail: pascal.vandervoort@ugent.be.

Notes

The authors declare no competing financial interest.

■ ACKNOWLEDGMENTS

The authors acknowledge the financial support from the Ghent University BOF Grant (Nr. 01P02911T, 01N01010) and GOA Grant (01G00710); the Hercules Foundation (project AUGE/09/024 "Advanced Luminescence Setup"); the Research Foundation-Flanders (FWO-Vlaanderen, project G.0081.10N); BELSPO in the frame of IAP 6/27 and the European Research Council (FP7(2007-2013) ERC Grant (Nr. 240483). Computa-

tional resources and services provided by Ghent University are greatly acknowledged.

REFERENCES

- (1) Park, Y. K.; Choi, S. B.; Kim, H.; Kim, K.; Won, B.-H.; Choi, K.; Choi, J.-S.; Ahn, W.-S.; Won, N.; Kim, S.; et al. Crystal Structure and Guest Uptake of a Mesoporous Metal–Organic Framework Containing Cages of 3.9 and 4.7 nm in Diameter. *Angew. Chem., Int. Ed.* **2007**, *46*, 8230–8233.
- (2) Cui, Y.; Xu, H.; Yue, Y.; Guo, Z.; Yu, J.; Chen, Z.; Gao, J.; Yang, Y.; Qian, G.; Chen, B. A Luminescent Mixed-Lanthanide Metal–Organic Framework Thermometer. *J. Am. Chem. Soc.* **2012**, *134*, 3979–3982.
- (3) Xiao, Y.; Cui, Y.; Zheng, Q.; Xiang, S.; Qian, G.; Chen, B. A Microporous Luminescent Metal–Organic Framework for Highly Selective and Sensitive Sensing of Cu(2+) in Aqueous Solution. *Chem. Commun.* **2010**, *46*, 5503–5505.
- (4) Takashima, Y.; Martinez Martinez, V.; Furukawa, S.; Kondo, M.; Shimomura, S.; Uehara, H.; Nakahama, M.; Sugimoto, K.; Kitagawa, S. Molecular Decoding Using Luminescence from an Entangled Porous Framework. *Nat. Commun.* **2011**, *2*.
- (5) Cui, Y.; Yue, Y.; Qian, G.; Chen, B. Luminescent Functional Metal–Organic Frameworks. *Chem. Rev.* **2012**, *112*, 1116–1162.
- (6) Rieter, W. J.; Taylor, K. M. L.; Lin, W. B. Surface Modification and Functionalization of Nanoscale Metal–Organic Frameworks for Controlled Release and Luminescence Sensing. *J. Am. Chem. Soc.* **2007**, *129*, 9852–9853.
- (7) Buso, D.; Jasieniak, J.; Lay, M. D. H.; Schiavuta, P.; Scopece, P.; Laird, J.; Amenitsch, H.; Hill, A. J.; Falcaro, P. Highly Luminescent Metal–Organic Frameworks through Quantum Dot Doping. *Small* **2012**, *8*, 80–88.
- (8) Decadt, R.; Van Hecke, K.; Depla, D.; Leus, K.; Weinberger, D.; Van Driessche, L.; Van Der Voort, P.; Van Deun, R. Synthesis, Crystal Structures, and Luminescence Properties of Carboxylate Based Rare-Earth Coordination Polymers. *Inorg. Chem.* **2012**, *51*, 11623–11634.
- (9) Ji, M.; Lan, X.; Han, Z. P.; Hao, C.; Qiu, J. S. Luminescent Properties of Metal–Organic Framework Mof-5: Relativistic Time-Dependent Density Functional Theory Investigations. *Inorg. Chem.* **2012**, *51*, 12389–12394.
- (10) An, J.; Shade, C. M.; Chengelis-Czegán, D. A.; Petoud, S.; Rosi, N. L. Zinc-Adeninate Metal–Organic Framework for Aqueous Encapsulation and Sensitization of Near-Infrared and Visible Emitting Lanthanide Cations. *J. Am. Chem. Soc.* **2011**, *133*, 1220–1223.
- (11) Wang, G. F.; Peng, Q.; Li, Y. D. Lanthanide-Doped Nanocrystals: Synthesis, Optical-Magnetic Properties, and Applications. *Acc. Chem. Res.* **2011**, *44*, 322–332.
- (12) Lee, J.; Govorov, A. O.; Dulka, J.; Kotov, N. A. Bioconjugates of CdTe Nanowires and Au Nanoparticles: Plasmon-Exciton Interactions, Luminescence Enhancement, and Collective Effects. *Nano Lett.* **2004**, *4*, 2323–2330.
- (13) Zheng, J.; Ding, Y.; Tian, B. Z.; Wang, Z. L.; Zhuang, X. W. Luminescent and Raman Active Silver Nanoparticles with Polycrystalline Structure. *J. Am. Chem. Soc.* **2008**, *130*, 10472–+.
- (14) Maldiney, T.; Sraiki, G.; Viana, B.; Gourier, D.; Richard, C.; Schermer, D.; Bessodes, M.; Van den Eckhout, K.; Poelman, D.; Smet, P. F. In Vivo Optical Imaging with Rare Earth Doped Ca₂Si₂N₈ Persistent Luminescence Nanoparticles. *Opt. Mater. Express* **2012**, *2*, 261–268.
- (15) Horcajada, P.; Chalati, T.; Serre, C.; Gillet, B.; Sebrie, C.; Baati, F.; Eubank, J. F.; Heurtaux, D.; Clayette, P.; Kreuz, C.; et al. Porous Metal–Organic Framework Nanoscale Carriers as a Potential Platform for Drug Delivery and Imaging. *Nat. Mater.* **2010**, *9*, 172–178.
- (16) Lin, W. B.; Rieter, W. J.; Taylor, K. M. L. Modular Synthesis of Functional Nanoscale Coordination Polymers. *Angew. Chem., Int. Ed.* **2009**, *48*, 650–658.
- (17) Wee, L. H.; Lohe, M. R.; Janssens, N.; Kaskel, S.; Martens, J. A. Fine Tuning of the Metal–Organic Framework Cu₃(BTC)₂ HKUST-1 Crystal Size in the 100 Nm to 5 Micron Range. *J. Mater. Chem.* **2012**, *22*, 13742–13746.
- (18) Aguado, S.; Canivet, J.; Faryusseng, D. Engineering Structured MOF at Nano and Macroscales for Catalysis and Separation. *J. Mater. Chem.* **2011**, *21*, 7582–7588.
- (19) Chen, B. L.; Wang, L. B.; Xiao, Y. Q.; Fronczek, F. R.; Xue, M.; Cui, Y. J.; Qian, G. D. A Luminescent Metal–Organic Framework with Lewis Basic Pyridyl Sites for the Sensing of Metal Ions. *Angew. Chem., Int. Ed.* **2009**, *48*, 500–503.
- (20) Cui, Y. J.; Xu, H.; Yue, Y. F.; Guo, Z. Y.; Yu, J. C.; Chen, Z. X.; Gao, J. K.; Yang, Y.; Qian, G. D.; Chen, B. L. A Luminescent Mixed-Lanthanide Metal–Organic Framework Thermometer. *J. Am. Chem. Soc.* **2012**, *134*, 3979–3982.
- (21) Liu, K.; You, H. P.; Zheng, Y. H.; Jia, G.; Song, Y. H.; Huang, Y. J.; Yang, M.; Jia, J. J.; Guo, N.; Zhang, H. J. Facile and Rapid Fabrication of Metal–Organic Framework Nanobelt and Color-Tunable Photo-Luminescence Properties. *J. Mater. Chem.* **2010**, *20*, 3272–3279.
- (22) Xu, H.; Rao, X. T.; Gao, J. K.; Yu, J. C.; Wang, Z. Q.; Dou, Z. S.; Cui, Y. J.; Yang, Y.; Chen, B. L.; Qian, G. D. A Luminescent Nanoscale Metal–Organic Framework with Controllable Morphologies for Spore Detection. *Chem. Commun.* **2012**, *48*, 7377–7379.
- (23) Fuentes-Cabrera, M.; Nicholson, D. M.; Sumpter, B. G.; Widom, M. Electronic Structure and Properties of Isoreticular Metal–Organic Frameworks: The Case of M-IRMOF1 (M = Zn, Cd, Be, Mg, and Ca). *J. Chem. Phys.* **2005**, *123*, 124713–124715.
- (24) Huang, Y.; Liu, T.; Lin, J.; Lue, J.; Lin, Z.; Cao, R. Homochiral Nickel Coordination Polymers Based on Salen(Ni) Metalloligands: Synthesis, Structure, and Catalytic Alkene Epoxidation. *Inorg. Chem.* **2011**, *50*, 2191–2198.
- (25) Ji, M.; Lan, X.; Han, Z.; Hao, C.; Qiu, J. Luminescent Properties of Metal–Organic Framework MOF-5: Relativistic Time-Dependent Density Functional Theory Investigations. *Inorg. Chem.* **2012**, *51*, 12389–12394.
- (26) Vermoortele, F.; Vandichel, M.; Van de Voorde, B.; Ameloot, R.; Waroquier, M.; Van Speybroeck, V.; De Vos, D. E. Electronic Effects of Linker Substitution on Lewis Acid Catalysis with Metal–Organic Frameworks. *Angew. Chem., Int. Ed.* **2012**, *51*, 4887–4890.
- (27) Bloch, E. D.; Britt, D.; Lee, C.; Doonan, C. J.; Uribe-Romo, F. J.; Furukawa, H.; Long, J. R.; Yaghi, O. M. Metal Insertion in a Microporous Metal–Organic Framework Lined with 2,2′-Bipyridine. *J. Am. Chem. Soc.* **2010**, *132*, 14382–14384.
- (28) Ziessel, R.; Maestri, M.; Prodi, L.; Balzani, V.; Vanderselaer, A. Dinuclear Eu³⁺, Tb³⁺, and Gd³⁺ Complexes of a Branched Hexaazacyclooctadecane Ligand Containing 6,2′-Bipyridine Pendant Units. *Inorg. Chem.* **1993**, *32*, 1237–1241.
- (29) Puntius, L. N.; Lyssenko, K. A.; Pekareva, I. S.; Bunzli, J. C. G. Intermolecular Interactions as Actors in Energy-Transfer Processes in Lanthanide Complexes with 2,2′-Bipyridine. *J. Phys. Chem. B* **2009**, *113*, 9265–9277.
- (30) Bhasikuttan, A. C.; Suzuki, M.; Nakashima, S.; Okada, T. Ultrafast Fluorescence Detection in Tris(2,2′-Bipyridine)Ruthenium(II) Complex in Solution: Relaxation Dynamics Involving Higher Excited States. *J. Am. Chem. Soc.* **2002**, *124*, 8398–8405.
- (31) Prodi, L.; Maestri, M.; Ziessel, R.; Balzani, V. Luminescent Eu³⁺, Tb³⁺, and Gd³⁺ Complexes of a Branched Triazaacyclononane Ligand Containing 3,2,2′-Bipyridine Units. *Inorg. Chem.* **1991**, *30*, 3798–3802.
- (32) Bekiarj, V.; Pistolis, G.; Lianos, P. Intensely Luminescent Materials Obtained by Combining Lanthanide Ions, 2,2′-Bipyridine, and Poly(Ethylene Glycol) in Various Fluid or Solid Environments. *Chem. Mater.* **1999**, *11*, 3189–3195.
- (33) Szeto, K. C.; Kongshaug, K. O.; Jakobsen, S.; Tilsted, M.; Lillerud, K. P. Design, Synthesis and Characterization of a Pt–Gd Metal–Organic Framework Containing Potentially Catalytically Active Sites. *Dalton Trans.* **2008**, 2054–2060.
- (34) Boulif, A.; Louer, D. Indexing of Powder Diffraction Patterns for Low-Symmetry Lattices by the Successive Dichotomy Method. *J. Appl. Crystallogr.* **1991**, *24*, 987–993.
- (35) STOE WinXPOW version 2.1.1, Stoe & Cie GmbH, Darmstadt, Germany, 2005.
- (36) Frisch, M. J.; G. W. T.; Schlegel, H. B.; Scuseria, G. E.; Robb, M. A.; Cheeseman, J. R.; Scalmani, G.; Barone, V.; Mennucci, B.; Petersson,

G. A., et al. *Gaussian 09*, Revision A.02; Gaussian, Inc.: Wallingford CT; 2009.

(37) Becke, A. D. Density-Functional Thermochemistry. 3. The Role of Exact Exchange. *J. Chem. Phys.* **1993**, *98*, 5648–5652.

(38) Lee, C. T.; Yang, W. T.; Parr, R. G. Development of the Colle-Salvetti Correlation-Energy Formula into a Functional of the Electron-Density. *Phys. Rev. B* **1988**, *37*, 785–789.

(39) Bauernschmitt, R.; Ahlrichs, R. Treatment of Electronic Excitations within the Adiabatic Approximation of Time Dependent Density Functional Theory. *Chem. Phys. Lett.* **1996**, *256*, 454–464.

(40) Runge, E.; Gross, E. K. U. Density-Functional Theory for Time-Dependent Systems. *Phys. Rev. Lett.* **1984**, *52*, 997–1000.

(41) Stratmann, R. E.; Scuseria, G. E.; Frisch, M. J. An Efficient Implementation of Time-Dependent Density-Functional Theory for the Calculation of Excitation Energies of Large Molecules. *J. Chem. Phys.* **1998**, *109*, 8218–8224.

(42) Dreuw, A.; Head-Gordon, M. Single-Reference Ab Initio Methods for the Calculation of Excited States of Large Molecules. *Chem. Rev.* **2005**, *105*, 4009–4037.

(43) Gonzalez, L.; Escudero, D.; Serrano-Andres, L. Progress and Challenges in the Calculation of Electronic Excited States. *Chem-PhysChem* **2012**, *13*, 28–51.

(44) Adamo, C.; Jacquemin, D. The Calculations of Excited-State Properties with Time-Dependent Density Functional Theory. *Chem. Soc. Rev.* **2013**, *42*, 845–856.

(45) Boese, A. D.; Handy, N. C. A New Parametrization of Exchange-Correlation Generalized Gradient Approximation Functionals. *J. Chem. Phys.* **2001**, *114*, 5497–5503.

(46) Yanai, T.; Tew, D. P.; Handy, N. C. A New Hybrid Exchange-Correlation Functional Using the Coulomb-Attenuating Method (CAM-B3LYP). *Chem. Phys. Lett.* **2004**, *393*, 51–57.

(47) De Meyer, T.; Hemelsoet, K.; Van der Schueren, L.; Pauwels, E.; De Clerck, K.; Van Speybroeck, V. Investigating the Halochromic Properties of Azo Dyes in an Aqueous Environment by Using a Combined Experimental and Theoretical Approach. *Chem.—Eur. J.* **2012**, *18*, 8120–8129.

(48) Senkovska, I.; Hoffmann, F.; Froba, M.; Getzschmann, J.; Bohlmann, W.; Kaskel, S. New Highly Porous Aluminium Based Metal-Organic Frameworks: Al(OH)(ndc) (ndc = 2,6-Naphthalene Dicarboxylate) and Al(OH)(bpdc) (bpdc = 4,4'-Biphenyl Dicarboxylate). *Microporous Mesoporous Mater.* **2009**, *122*, 93–98.

(49) Loiseau, T.; Serre, C.; Huguenard, C.; Fink, G.; Taulelle, F.; Henry, M.; Bataille, T.; Ferey, G. A Rationale for the Large Breathing of the Porous Aluminum Terephthalate (MIL-53) Upon Hydration. *Chem.—Eur. J.* **2004**, *10*, 1373–1382.

(50) Jacobson, A. J.; Vougo-Zanda, M.; Huang, J.; Anokhina, E.; Wang, X. Q. Tossing and Turning: Guests in the Flexible Frameworks of Metal(III) Dicarboxylates. *Inorg. Chem.* **2008**, *47*, 11535–11542.

(51) Jacquemin, D.; Planchat, A.; Adamo, C.; Mennucci, B. TD-DFT Assessment of Functionals for Optical 0–0 Transitions in Solvated Dyes. *J. Chem. Theory Comput.* **2012**, *8*, 2359–2372.

(52) Peach, M. J. G.; Tozer, D. J. Overcoming Low Orbital Overlap and Triplet Instability Problems in TDDFT. *J. Phys. Chem. A* **2012**, *116*, 9783–9789.

(53) Chen, B.; Yang, Y.; Zapata, F.; Lin, G.; Qian, G.; Lobkovsky, E. B. Luminescent Open Metal Sites within a Metal-Organic Framework for Sensing Small Molecules. *Adv. Mater.* **2007**, *19*, 1693–4.

(54) Wang, F.; Yu, R.; Zhang, Q.-S.; Zhao, Z.-G.; Wu, X.-Y.; Xie, Y.-M.; Qin, L.; Chen, S.-C.; Lu, C.-Z. Solvent-Dependent Luminescent Cu(I) Framework Based on 5-(4-Pyridyl)Tetrazole. *J. Solid State Chem.* **2009**, *182*, 2555–2559.

(55) Wang, C.; Lin, W. B. Diffusion-Controlled Luminescence Quenching in Metal-Organic Frameworks. *J. Am. Chem. Soc.* **2011**, *133*, 4232–4235.

(56) Bauer, C. A.; Timofeeva, T. V.; Settersten, T. B.; Patterson, B. D.; Liu, V. H.; Simmons, B. A.; Allendorf, M. D. Influence of Connectivity and Porosity on Ligand-Based Luminescence in Zinc Metal-Organic Frameworks. *J. Am. Chem. Soc.* **2007**, *129*, 7136–7144.

(57) Feng, P. L.; Leong, K.; Allendorf, M. D. Charge-Transfer Guest Interactions in Luminescent MOFs: Implications for Solid-State Temperature and Environmental Sensing. *Dalton Trans.* **2012**, *41*, 8869–8877.

(58) Stylianou, K. C.; Heck, R.; Chong, S. Y.; Bacsaj, J.; Jones, J. T. A.; Khimyak, Y. Z.; Bradshaw, D.; Rosseinsky, M. J. A Guest-Responsive Fluorescent 3d Microporous Metal-Organic Framework Derived from a Long-Lifetime Pyrene Core. *J. Am. Chem. Soc.* **2010**, *132*, 4119–4130.

(59) Zhao, J. W.; Shi, D. Y.; Cheng, H. L.; Chen, L. J.; Ma, P. T.; Niu, J. Y. One-Pot Syntheses, Structures and Properties of Two Novel 1-D Copper Complexes: [Cu₂(II)(hbpdc)₂Cl₂]·2H₂O and Cu–1(H₂bpdc)Cl (H₂bpdc = 2,2'-Bipyridyl-5,5'-Dicarboxylic Acid). *Inorg. Chem. Commun.* **2010**, *13*, 822–827.

Supporting information for

Bipyridine Based Nanosized Metal-Organic Framework with Tunable Luminescence by a Postmodification with Eu(III): An Experimental and Theoretical Study

Ying-Ya Liu,[†] Roel Decadt,[‡] Thomas Bogaerts,^{‡,§} Karen Hemelsoet,[§] Anna M. Kaczmarek,[‡] Dirk Poelman,^{||} Michel Waroquier,[§] Veronique Van Speybroeck,[§] Rik Van Deun,[‡] and Pascal Van Der Voort^{,‡}*

[†] COMOC - Centre for Ordered Materials, Organometallics and Catalysis,
Department of Inorganic and Physical Chemistry, Ghent University, Krijgslaan
281-S3, 9000 Ghent, Belgium

[‡] f-Element Coordination Chemistry Group, Department of Inorganic and Physical
Chemistry, Krijgslaan 281-S3, 9000 Ghent; Belgium

[§]Center for Molecular Modeling, Ghent University, Technologiepark 903, 9052
Zwijnaarde, Belgium

^{||}LumiLab, Department of Solid State Sciences, Ghent University, Krijgslaan 281-S1,
9000 Ghent; Belgium

E-mail: pascal.vandervoort@ugent.be

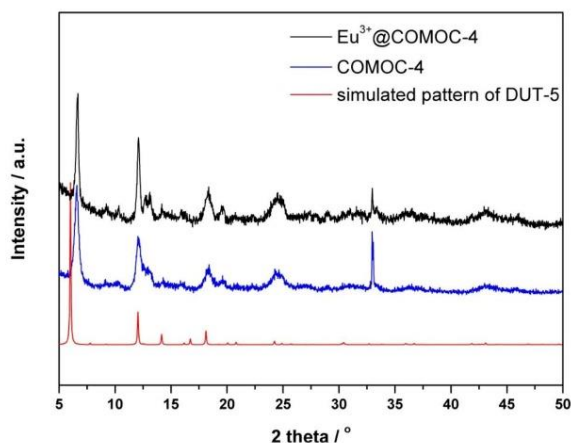


Figure S1. Powder XRD patterns of COMOC-4, EuCl_3 @COMOC-4 compared with simulated pattern of $\text{Al}(\text{OH})(\text{BPDC})$ (DUT-5, $\text{BPDC}^{2-} = 2,2'$ -biphenyl-5,5'-dicarboxylate) (The peak at 32.9° is due to the background of the silicon sample holder). Note that the low qualities of the PXRD patterns are partially due to the size of the nanocrystals (Figure S2).

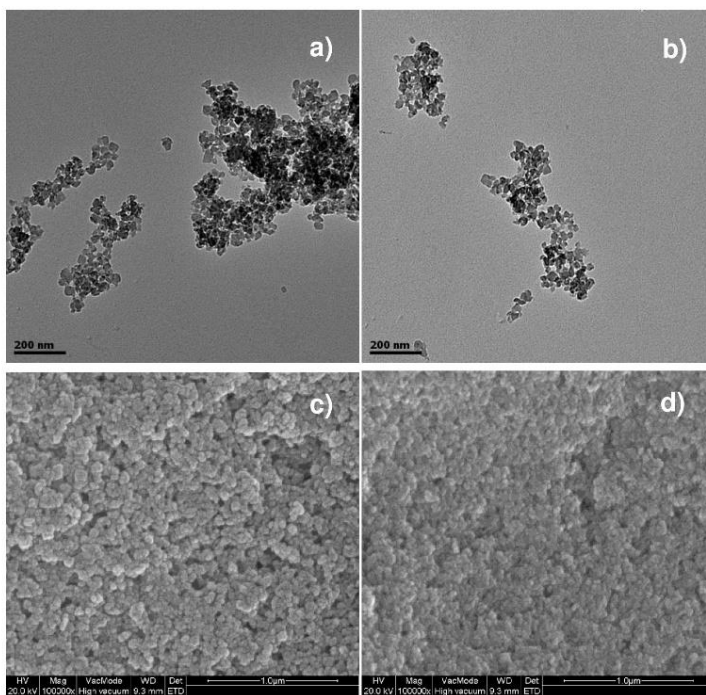


Figure S2. TEM and SEM micrographs of COMOC-4 nanocrystals (a, c) and Eu^{3+} @COMOC-4 nanocrystals (b, d).

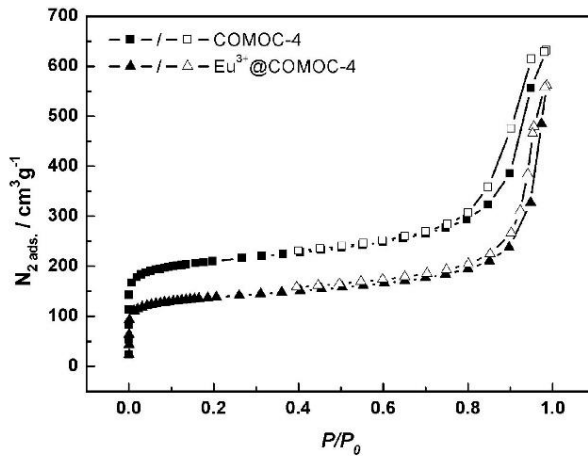


Figure S3. N₂ adsorption (solid symbols) and desorption (open symbols) isotherms of COMOC-4 and Eu³⁺@COMOC-4 at 77 K.

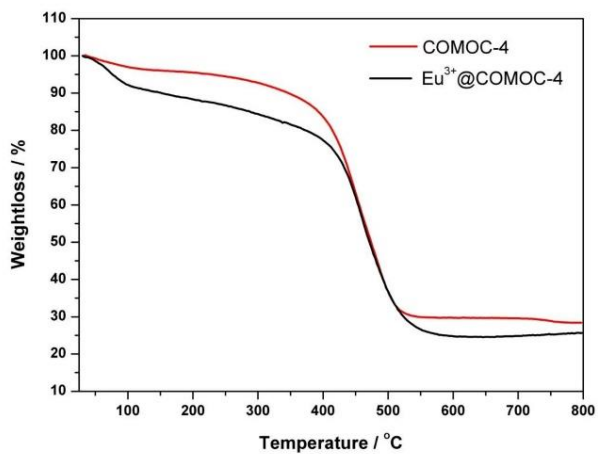


Figure S4. Thermal gravimetric analysis of COMOC-4 and Eu³⁺@COMOC-4.

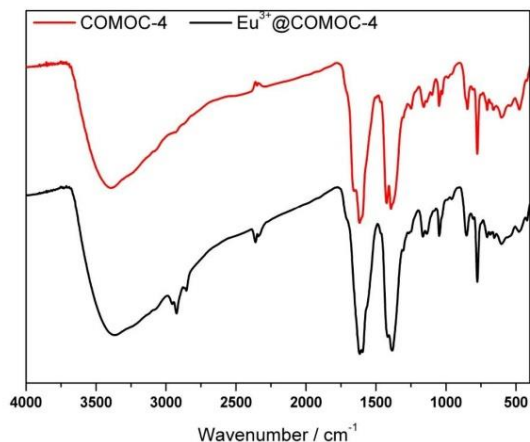


Figure S5. FT-IR spectra of COMOC-4 and Eu^{3+} @COMOC-4. In the Eu^{3+} @COMOC-4 FT-IR spectrum, the bands with maximum at $\sim 2923 \text{ cm}^{-1}$ and at $\sim 2853 \text{ cm}^{-1}$ are assigned to the stretching vibrations of n-alkyl chain from ethanol solvent: $\nu_{\text{as}}(\text{CH}_2)$ and $\nu_{\text{sym}}(\text{CH}_2)$ respectively. The absence of NO_3^- stretching band at 1385 and 825 cm^{-1} in MOFs indicates that no Ga^{3+} ions were absorbed in the pores of framework and/or coordinated with the bipyridine moiety.

Table S1. Computed excitation energies (in nm) with maximal absorbance for the isolated H_2bydc linker using different theoretical methodologies for the TD-DFT simulation. Optimized B3LYP/6-31+G(d) geometries are used.

	B3LYP/6-31+G(d)		6-311++G(2df,2p)	
	Without PCM	With PCM	Without PCM	With PCM
HCTH	316	324	317	327
B3LYP	288	295	290	297
CAM-B3LYP	264	271	267	273

Comparison of the computed maximal absorption with the experimental value of 299 nm (see Figure 2a) shows that B3LYP is the most favorable functional for this case. The results illustrate the well-known trend for singlet excitations^[1a, 1b]; the

HCTH GGA functional underestimates the excitation energies (and hence overestimates the wavelengths), while increasing the amount of exact exchange beneficially decreases the simulated wavelengths. The influence of the PCM solvent model on the excitation energy is almost uniform and translates into a red shift of about 7-11 nm. Summarizing, the B3LYP/6-31+G(d) level of theory with PCM solvation is found most appropriate to describe the excitation energies of the systems investigated in this study.

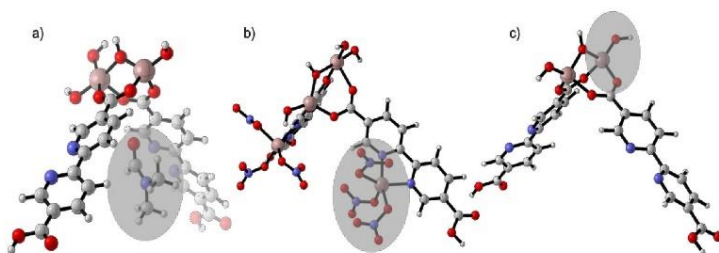


Figure S6. Possibilities considered for the extra observed shoulder, a) DMF in the structure (main band at 311 nm), b) galliumnitrate coordinated on the linker (main band at 313 nm), c) cationic defect (main band at 326 nm).

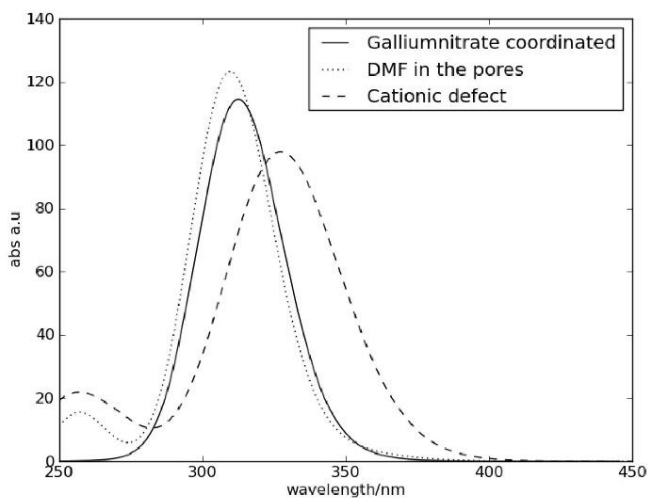


Figure S7. Calculated UV-VIS spectra for the different defects displayed in Figure S6.

Table S2. Computed excitation energies with maximal absorbance (in nm) for the different clusters.

	B3LYP/6-31+G(d)		6-311++G(2df,2p)	
	Without PCM	With PCM	Without PCM	With PCM
Small model, neutral	312	310	307	315
Small model, cation	362	326	360	327
Extended model, neutral	306	310	-	-
Extended model, linker defect	337	320	-	-
Extended model, -OH defect	388	326	-	-

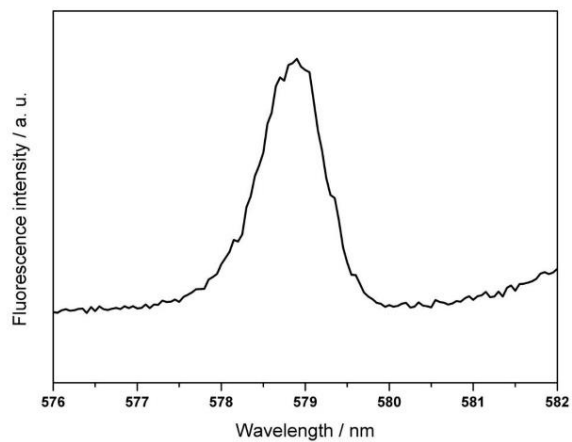


Figure S8. Luminescence spectra of Eu^{3+} @COMOC-4 at ${}^5\text{D}_0 \rightarrow {}^7\text{F}_0$ transition in the solid state at room temperature, $\lambda_{\text{exc}}=330$ nm.

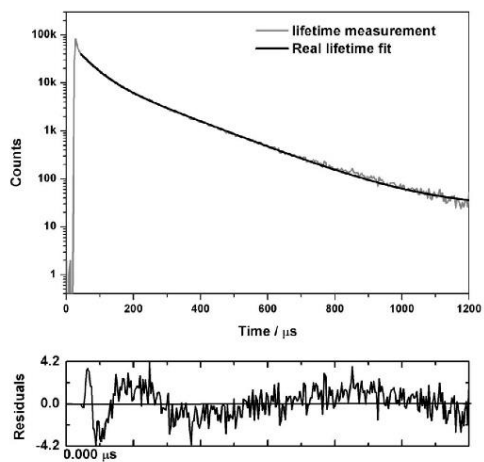
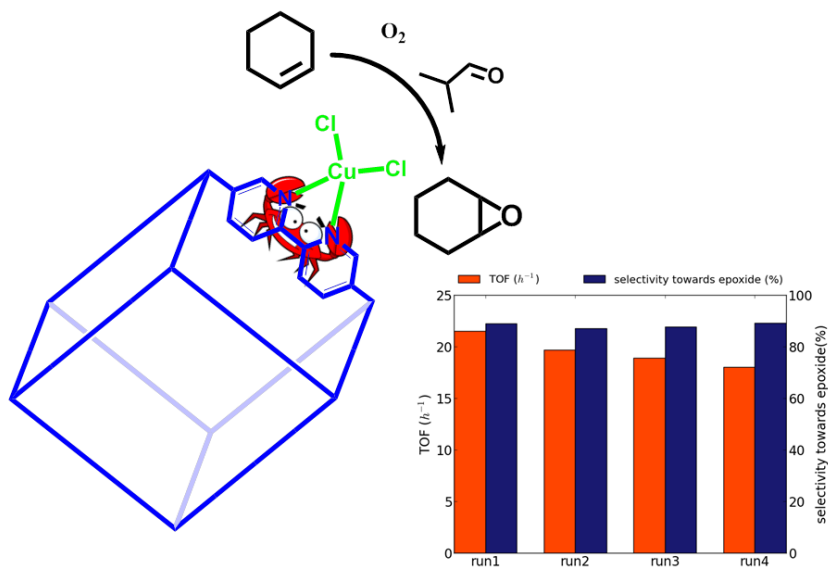


Figure S9. Lifetime measurements of Eu^{3+} @COMOC-4.

References

- [1] a) Peach, M. J. G.; Williamson, M. J.; Tozer, D. J., *J. Chem. Theory Comput.* **2011**, *7* (11), 3578-3585; b) Peach, M. J. G.; Tozer, D. J., *J. Phys. Chem. A* **2012**, *116* (39), 9783-9789

PAPER VIII: BIMETALLIC-ORGANIC FRAMEWORK AS A ZERO-LEACHING CATALYST IN THE AEROBIC OXIDATION OF CYCLOHEXENE



Y-Y Liu, K. Leus, T. Bogaerts, K. Hemelsoet, E. Bruneel, V. Van Speybroeck, P. Van der Voort, *ChemCatChem*, 5 (12), 3657–3664, **2013**.

T. Bogaerts assisted in this paper by the calculation of UV/Vis spectra for the material characterization with these techniques.

©2014 Wiley-VCH Verlag GmbH & Co Reprinted with permission from Wiley-VCH Verlag.

DOI: 10.1002/cctc.201300529

Bimetallic–Organic Framework as a Zero-Leaching Catalyst in the Aerobic Oxidation of Cyclohexene

Ying-Ya Liu,^[a] Karen Leus,^[a] Thomas Bogaerts,^[a, b] Karen Hemelsoet,^[b] Els Bruneel,^[c] Veronique Van Speybroeck,^[b] and Pascal Van Der Voort^{*[a]}

A gallium 2,2'-bipyridine-5,5'-dicarboxylate metal–organic framework (MOF), denoted as COMOC-4, has been synthesized by solvothermal synthesis. This MOF exhibits the same topology as MOF-253. CuCl₂ was incorporated into COMOC-4 by a post-synthetic modification (PSM). The spectroscopic absorption properties of the MOF framework before and after PSM were compared with theoretical data obtained by employing molecular dynamics combined with time-dependent DFT calculations on both the as-synthesized and functionalized linker. The catalytic behavior of the resulting Cu²⁺@COMOC-4 materi-

al was evaluated in the aerobic oxidation of cyclohexene with isobutyraldehyde as a co-oxidant. In addition, the catalytic performance of Cu²⁺@COMOC-4 was compared with that of the commercially available Cu-BTC (BTC = benzene-1,3,5-tricarboxylate) MOF. Cu²⁺@COMOC-4 exhibits a good cyclohexene conversion and an excellent selectivity towards cyclohexene oxide in comparison to the Cu-based reference catalyst. Furthermore, no leaching of the active Cu sites was observed during at least four consecutive runs.

Introduction

Catalyzed liquid-phase oxidation reactions are widely employed in industrial processes and are becoming increasingly important for the synthesis of fine chemicals.^[1] Among the different oxidation reactions, the epoxidation of olefins plays a prominent role as epoxides are highly reactive and versatile intermediates. Although homogeneous catalysts are still often utilized in industrial processes, there is an increasing interest in the employment of heterogeneous catalysts as they have a big advantage in terms of reuse and waste minimization. Metal–organic frameworks (MOFs) can be considered as potential candidates for use in catalysis.^[2] MOFs are 3D crystalline porous materials that consist of metal nodes connected by multifunctional organic linkers. Almost every transition metal ion and many different organic linkers can be used to obtain a MOF structure, which makes the plausible metal–ligand combinations endless.^[3] However, only a minor amount of MOFs are practi-

cally usable in catalysis as many of them show limited stability in typically employed catalytic reaction conditions.^[4] By pre-/post-synthetic modification of the organic linker, complementary catalytic active sites can be introduced.^[5] Very recently we reported on the post-synthetic modification of V-NH₂-MIL-47 with TiO(acac)₂ (acac = acetylacetonate). The resulting NH₂-MIL-47[Ti] material exhibited a significantly higher stability and activity in the oxidation of cyclohexene compared to nonfunctionalized NH₂-MIL-47.^[5c]

In this study we looked for another MOF support that is more rigid in comparison to NH₂-MIL-47. Within this context, the bipyridine-based MOF-253, synthesized by Yaghi and co-workers,^[6] is an excellent candidate to serve as a MOF support. The beauty of this Al(OH)(bpydc) (bpydc²⁻ = 2,2'-bipyridine-5,5'-dicarboxylate) framework lies in the fact that the organic linkers offer free 2,2'-bipyridine sites, which are often employed as chelating ligands in coordination chemistry. More specifically, it can form metal complexes in which the metal is bound to the two N atoms to make it a bidentate-secured stable complex. Several attempts have been made to graft secondary metal sites on the bipyridine site by a post-synthetic modification approach. For example, Pd²⁺ and Cu²⁺ ions have been incorporated into the MOF-253 framework and were subsequently evaluated for their CO₂ uptake.^[6] Zou and co-workers have incorporated RuCl₃ into MOF-253, and the product was examined as a catalyst for the selective oxidation of primary and secondary alcohols.^[5b] In a very recent report of Li et al., Cu⁺ ions were incorporated into MOF-253 to catalyze the cross-coupling of phenols and alcohols with aryl halides.^[7]

In this contribution, we report on the catalytic performance of a member of the M(OH)(bpydc) series with M = Ga, denoted as COMOC-4 (COMOC = Center for Ordered Materials, Organo-

[a] Dr. Y.-Y. Liu, Dr. K. Leus, T. Bogaerts, Prof. Dr. P. Van Der Voort
COMOC – Center for Ordered Materials, Organometallics and Catalysis
Department of Inorganic and Physical Chemistry
Ghent University
Krijgslaan 281-S3, 9000 Ghent (Belgium)
Fax: (+32)9-264-49-83
E-mail: pascal.vandervoort@ugent.be

[b] T. Bogaerts, Prof. Dr. K. Hemelsoet, Prof. Dr. V. Van Speybroeck
Center for Molecular Modeling
Ghent University
Technologiepark 903, 9052 Zwijnaarde (Belgium)

[c] Dr. E. Bruneel
SCRIPTS, Department of Inorganic and Physical Chemistry
Ghent University
Krijgslaan 281-S3, 9000 Ghent (Belgium)

Supporting information for this article is available on the WWW under <http://dx.doi.org/10.1002/cctc.201300529>.

metallics and Catalysis, Ghent University), which we published recently.⁹⁸ The MOF structure features an analogous structure to MOF-253 and is stable in air and water (50 °C for 24 h). CuCl_2 , which shows a good binding affinity towards the bipyridine sites, was grafted on the COMOC-4 framework by post-synthetic modification (PSM). The spectroscopic properties of the MOF before and after PSM were elucidated by using *ab initio* simulations. In particular, molecular dynamics (MD) computations were performed on a model linker with and without Cu coordination to simulate the flexibility of the structures. Subsequently, time-dependent density functional theory (TD-DFT) was applied on snapshots extracted from the MD runs to compute an average UV/Vis spectrum. This methodology has been shown to be successful previously.⁹⁹ The newly synthesized Cu^{2+} @COMOC-4 was extensively evaluated as a bimetallic catalyst in the aerobic epoxidation of cyclohexene with an aldehyde as co-oxidant.¹⁰⁰ Additionally, regenerability and stability tests were performed. Finally, the catalytic performance of Cu^{2+} @COMOC-4 was compared with another Cu-based reference MOF, namely, Cu-BTC (BTC = benzene-1,3,5-tricarboxylate).

Results and Discussion

The powder XRD pattern of COMOC-4 (Figure S1, Supporting Information) reveals that this framework is isostructural with DUT-5¹¹¹ ($\text{Al}(\text{OH})(\text{bpd})$, bpd^{2-} = biphenyl-4,4'-dicarboxylate) as well as with MOF-253.⁶¹ The structure is indexed with orthorhombic unit cell parameters of $a = 21.98(24)$, $b = 7.302(8)$, and $c = 17.470(24)$ Å. The COMOC-4 framework is constructed of infinite chains of octahedral $\text{GaO}_4(\text{OH})_2$ units, in which each Ga^{3+} ion is bound to four bpydc^{2-} ligands and two μ_2 -*trans* hydroxide anions (Figure 1). This is a common coordination motif that has already been observed in a series of M^{3+} carboxylate frameworks ($\text{M} = \text{Al}$, Fe , V , Ga , and In).¹¹² The $\text{GaO}_4(\text{OH})_2$ chains are aligned parallel to the crystallographic b axis, and the hydroxide and carboxylate moieties alternate on either side of the chains, which are further linked to each other to form a 3D open framework (Figure S2). After the incorporation of CuCl_2

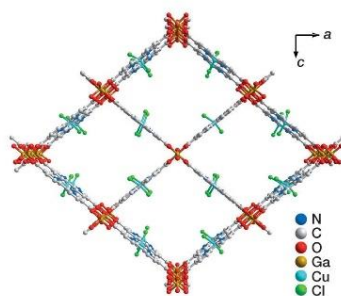


Figure 1. Representative structure of Cu^{2+} @COMOC-4. View along the 1D pore system. The structure model was generated based on the crystal structure of DUT-5 with 100% CuCl_2 occupancy.¹¹¹

into the COMOC-4 framework, the Bragg diffraction angles in COMOC-4 and Cu^{2+} @COMOC-4 are essentially identical, which confirm that the COMOC-4 crystalline structure is preserved. After Cu incorporation, the intensity of the reflections decreased. The main difference is seen in the diffraction peak at 6.5° , which is related to the (101) planes that are parallel to the linkers (both directions are equivalent because of symmetry). The incorporation of CuCl_2 will induce slight changes in the shape and angle of the linkers. This results in several new Bragg reflections close to the original ones that are then merged together into one broader peak of lower intensity as observed in the XRD pattern.

The UV/Vis absorption spectra of the synthesized materials are presented in Figure 2 (top). The H_2bpydc ligand displays one absorption band centered at 299 nm, which arises from a π - π^* transition in the aromatic rings. If the carboxylate linker is coordinated to Ga ions to form the COMOC-4 framework, the absorption spectrum exhibits a redshift of ≈ 8 nm. In addition, the absorption band reveals a shoulder at 330 nm. For comparison, $\text{Cu}(\text{Me}_2\text{bpydc})\text{Cl}_2$ was synthesized. As observed from the absorption spectra, the band that corresponds to the organic ligand is redshifted to 317 nm, whereas a shoulder peak appears at 334 nm and a broad band at 420 nm is observed, which indicates the metal-to-ligand coordination. Cu^{2+}

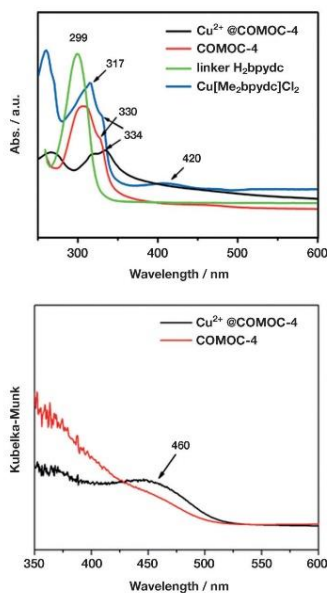


Figure 2. UV/Vis absorption spectra of suspended Cu^{2+} @COMOC-4 and COMOC-4 in MeOH solution compared to $\text{Cu}(\text{Me}_2\text{bpydc})\text{Cl}_2$ and Me_2bpydc dissolved in MeOH (top); Solid-state UV/Vis spectra calculated from diffuse reflection spectra (bottom).

@COMOC-4 exhibits two bands at 317 and 334 nm, which are in agreement with the absorption bands of $\text{Cu}(\text{Me}_6\text{bpydc})\text{Cl}_2$. However, the absorption band that corresponds to the blue color is not visible because of the rather high background signal of the spectra recorded from the suspension. Diffuse reflection spectra (DRS) have also been measured from powder samples to get better resolution in the visible region. COMOC-4 has a broad, weak absorption band in the range of 430–500 nm, whereas after incorporation of Cu^{2+} cations, a well-distinguished absorption band centered at 460 nm was observed (Figure 2 bottom).

The model used for the empty linker is shown in Figure 3. This is the most stable conformation.^[6] To allow CuCl_2 to coordinate to this ligand, both N atoms should be twisted to the same side as shown in Figure 3. Both models were optimized

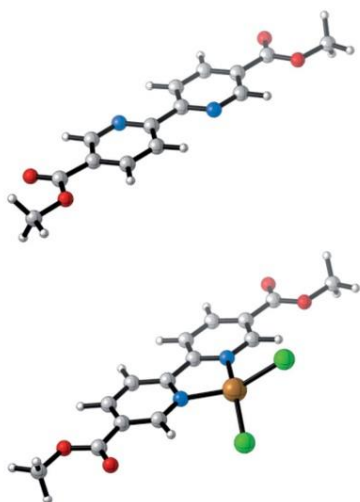


Figure 3. Optimized structure of the protected linker Me_6bpydc and with coordinated CuCl_2 .

by using the B3LYP/6-311+g(d) methodology to find their most stable conformations. UV/Vis spectra were calculated by using the computational method described below, which accounts for the flexibility of the structure. The main features from the experimental spectra are represented in the calculated dynamic spectra of Cu^{2+} coordinated to the bipyridine moiety compared with the as-synthesized linker. There is a slight shift to higher wavelengths, from 309 to 315 nm, but the shift is smaller in comparison to the experimental spectrum (299–317 nm; Figure 4a). The main absorption band for the empty linker (309 nm) is consistent with that shown before with static calculations.^[6] The shoulder at 338 nm (experimen-

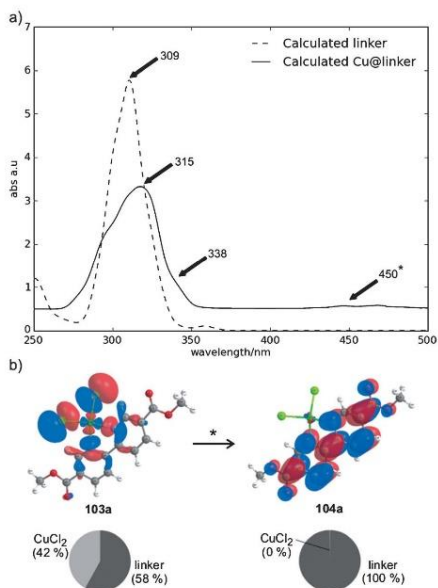


Figure 4. a) Comparison between the calculated UV/Vis spectra of the protected Me_6bpydc linker and with Cu coordinated to the linker. The most important features of the experimental spectrum are indicated. b) Visualization of the orbitals involved in the metal-to-ligand electron transfer that corresponds to the visible excitation in the Cu-modified linker. The corresponding participation of the linker (in dark grey) and CuCl_2 (in light grey) fragments are also given.

tal: 334 nm) is also present and is a consequence of Cu^{2+} encapsulation. The broad peak around 450 nm is also visible in the ab initio spectrum, though this is shifted to higher wavelength as compared to the measured result. To confirm that these changes are actually a result of metal coordination, one can take a closer look at the molecular orbitals involved in these excitations. The dominant orbitals involved in the excitation around 450 nm are displayed in Figure 4b and full details can be found in Figure S3. The orbitals and corresponding participation of the different fragments (Figure 4b) indicate that the coordinated metal contributes to the electronic transition. We can thus conclude that the observed changes in the UV/Vis spectrum are a result of the coordination of the CuCl_2 complex. The two bands at 338 and 450 nm can be employed to reveal the successful incorporation of CuCl_2 in the MOF framework, which was clearly observed in the absorption spectra (334 nm) and UV/Vis DRS spectra (460 nm) of Cu^{2+} @COMOC-4 UV/Vis (Figure 2 bottom).

COMOC-4 maintains a permanent microporosity after the removal of the guest molecules, as demonstrated by a type I N_2 sorption isotherm (Figure 5), and exhibits a Langmuir surface

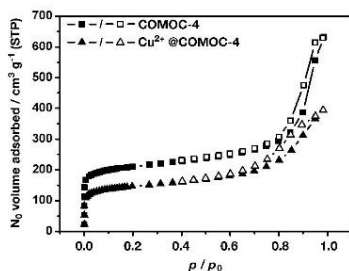


Figure 5. N_2 adsorption (solid symbols) and desorption (open symbols) isotherms of COMOC-4 and $Cu^{2+}@COMOC-4$ at 77 K.

area of $920 \text{ m}^2 \text{ g}^{-1}$. After the incorporation of $CuCl_2$, with a Cu/Ga ratio of 0.4:1, $0.4Cu^{2+}@COMOC-4$ reveals a reduced Langmuir surface area of $630 \text{ m}^2 \text{ g}^{-1}$. The thermal stability of COMOC-4 and $0.4Cu^{2+}@COMOC-4$ has been examined by thermogravimetric analysis (TGA; Figure 6). For COMOC-4, the first

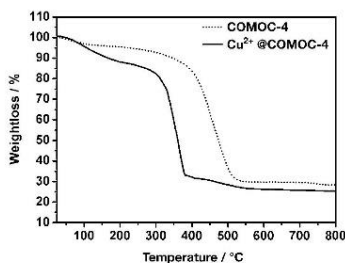


Figure 6. TGA curves of COMOC-4 and $Cu^{2+}@COMOC-4$ measured in an air flow.

mass loss in the TGA profile corresponds to the elimination of water from the pores ($\approx 6.5 \text{ wt}\%$). COMOC-4 is thermally stable up to $300 \text{ }^\circ\text{C}$, above which a further weight loss of $62 \text{ wt}\%$ before $560 \text{ }^\circ\text{C}$ is indicative of the decomposition of the framework. The final residue (observed: $29.6 \text{ wt}\%$, calculated $26.6 \text{ wt}\%$) is Ga_2O_3 . The incorporation of Cu^{2+} decreases the thermal stability of the MOF framework; a similar behavior was observed in $Ru@MOF-253$.^[56] The TGA profile of $Cu^{2+}@COMOC-4$ depicts the as-synthesized sample, the TGA curve shows a consistent weight loss of $11.5 \text{ wt}\%$ of solvent (water, methanol) release in the initial stage, and the delayed release (up to $200 \text{ }^\circ\text{C}$) can be assigned to weakly bound methanol molecules, which are presumably held by weak forces (hydrogen bonds and van der Waals interactions) within the channels of the main framework as well as water molecules that are more firmly bound to the $CuCl_2$. A second major weight loss ($62.5 \text{ wt}\%$) occurs at $230 \text{ }^\circ\text{C}$, which is attributed to the frame-

work decomposition. The residue of $26.1 \text{ wt}\%$ (calculated: $27.6 \text{ wt}\%$) is Ga_2O_3 and CuO . Calculated values are based on the results of elemental analysis.

The aerobic epoxidation of cyclohexene in the presence of an aldehyde as co-oxidant was used in this study. Such liquid-phase oxidation of cycloalkenes (or cycloalkanes) has been intensively studied by using MOF-based materials as catalysts. With variable active sites on MOF catalysts, and the use of different oxidants, this reaction can lead to different product distributions.^[13] Kholdeeva and co-workers^[13f] reported Cr- and Fe-MIL-101 materials as catalysts for the solvent-free selective oxidation of cyclohexane with O_2 and/or *tert*-butylhydroperoxide (TBHP) as oxidant. The substrate conversion was in the range of 9–36% within 8 h, the major product formed can be cyclohexyl hydroperoxide or cyclohexanone. This strongly depends on the nature of the active metal. Kleist and co-workers^[13a] investigated the aerobic epoxidation of olefins (*E*-stilbene and styrene) in a basic solvent (dimethylformamide, DMF), catalyzed by a Co-based MOF (STA-12(Co)). Different selectivities were obtained that depended on the substrates. The selectivity in styrene epoxidation was low because of substrate oligomerization. However, *E*-stilbene was epoxidized with high selectivities between 80–90%. Garcia and co-workers^[13b] have reported the aerobic oxidation of cycloalkenes catalyzed by an Fe-based MOF in the presence of *N*-hydroxyphthalimide, and the cycloalkenes were mainly converted to allylic oxidation products. More recently, Xamena, Corma, and co-workers^[13c] have reported that MOFs with Cu^{2+} centers linked to four N atoms from azaheterocyclic compounds are active catalysts for the aerobic oxidation of activated alkanes. Furthermore, a tandem reaction was designed that used a Cu-MOF combined with silylated Ti-MCM-41 as a solid catalyst, in which the Cu-MOF first catalyzed cumene oxidation to form cumene hydroperoxide as the major product, and the intermediate hydroperoxide together with silylated Ti-MCM-41 further catalyzed 1-octene to obtain 1-octene oxide. However, at high temperatures ($90 \text{ }^\circ\text{C}$) the presence of Cu-MOF will catalyze the 1-octene at the allylic position. Therefore, to increase the selectivity to the epoxide product, 1-octene and the Cu-MOF were kept in separate reactors. In the present work, we further explore the catalytic activity of Cu-MOFs in the epoxidation of alkenes by the Mukaiyama system.^[14]

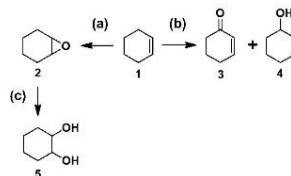
All our catalytic tests on the Cu-based MOFs were performed under identical reaction conditions to allow a fair comparison (see Table 1). Cu-BTC, a copper trimesate $Cu_3(BTC)_2(H_2O)_3$, known as HKUST-1, and commercially available as Basolite C300, was applied as a reference catalyst. This material forms face-centered cubic crystals that contain an intersecting 3D system of large square-shaped pores ($9 \times 9 \text{ \AA}$).

The TON and TOF values of the two Cu-based MOFs are depicted as a function of the reaction time in Figure 7. $Cu^{2+}@COMOC-4$ and Cu-BTC show a good catalytic performance as evidenced by the linear increase in the TON. Nevertheless, $Cu^{2+}@COMOC-4$ has a much higher TON value than Cu-BTC. After 7 h of catalysis, the TON value of Cu-BTC is 75, whereas $Cu^{2+}@COMOC-4$ exhibits a TON value of almost 138. Moreover, it can be seen that both catalysts reach a plateau in their TOF

Table 1. Results of the epoxidation of cyclohexene catalyzed by Cu-based compounds.

Catalyst	Conv. [%]	Sel. [%]	TOF [h ⁻¹]	Leaching [%]	Byproduct selectivity [%]			
					3 ⁶¹	4 ⁶¹	5 ⁶¹	
Cu ²⁺ @COMOC-4 ⁶¹	1 st run	49.0	89.0	21.5	0	4.3	2.6	3.9
	2 nd run	46.2	87.0	19.7	0	5.3	3.1	4.5
	3 rd run	41.5	87.8	18.9	0	5.6	3.1	3.4
	4 th run	41.6	89.2	18.0	0	5.1	2.7	2.9
Cu-BTC	41.7	77.5	11.1	13.2	6.9	8.5	7.0	
COMOC-4 ⁶¹	11.4	52.5	2.7	0	–	–	–	

[a] Reaction conditions: Cu²⁺@COMOC-4 (0.19 g in the first run, 0.2 mmol Cu sites), chloroform (40 mL), substrate (7 mL), isobutyraldehyde (11.4 mL), O₂ (7.7 mL min⁻¹), T = 313 K, τ = 7 h. [b] Based on Cu²⁺@COMOC-4, an equal amount of Ga sites (0.65 mmol) was used, and the TOF was calculated based on the number of moles of Cu sites. [c] Refer to Scheme 1 for product distributions.



Scheme 1. Oxidation of cyclohexene (1) towards the main reaction products: a) epoxidation to cyclohexene oxide (2), b) allylic oxidation to 2-cyclohexen-1-one (3) and 2-cyclohexen-1-ol (4), c) consecutive ring opening to cyclohexane-1,2-diol (5).

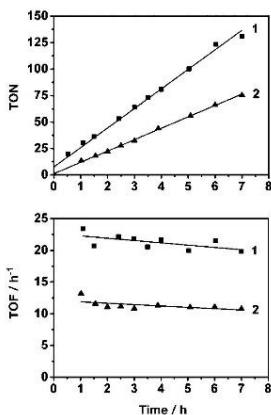


Figure 7. Catalytic activity expressed as TON (top) and TOF (bottom) for Cu²⁺@COMOC-4 (1) and Cu-BTC (2). Reaction conditions: 0.2 mmol Cu sites, 50 mmol cyclohexene, 100 mmol isobutyraldehyde, 40 mL chloroform, T = 40 °C, O₂ flow: 7.7 mL min⁻¹.

value after nearly 1 h of catalysis (Figure 7 bottom). The TOF value of Cu-BTC is approximately 12 h⁻¹, whereas for Cu²⁺@COMOC-4, a significantly higher TOF value of nearly 22 h⁻¹ is noted, which demonstrates that Cu²⁺@COMOC-4 converts cyclohexene much faster in comparison to the reference catalyst.

As presented in Table 1, both Cu-based catalysts gave cyclohexene oxide as the predominant product (Scheme 1, pathway a). Cu²⁺@COMOC-4 shows a remarkable catalytic activity to afford 49% of cyclohexene conversion after 7 h of catalysis with a selectivity of 89% towards the epoxide in the first run (Figure S4). No leaching of Cu and Ga sites was detected during the first run, which indicates that the catalysis occurs truly heterogeneously. In contrast to Cu²⁺@COMOC-4, for Cu-BTC, although the XRD pattern indicates no obvious changes in crystallinity after catalysis (Figure S5), a rather high Cu leach-

ing of 13.2% was detected after catalysis, which clearly demonstrates that the catalytic activity of Cu-BTC is mainly a result of homogeneous catalysis.

Additionally, the recyclability and stability of Cu²⁺@COMOC-4 was evaluated. In total, four successive runs were performed on Cu²⁺@COMOC-4. The results of the consecutive runs are presented in Table 1 and Figure S6. Although there is a slight reduction in the cyclohexene conversion during the additional runs, the TOF value remains fairly constant. This observation demonstrates the good recyclability of Cu²⁺@COMOC-4. The slight decrease in the observed cyclohexene conversion is probably because of a small loss of catalyst after each run. Moreover, the selectivity towards the epoxide stays fairly constant in the additional runs. Besides cyclohexane-1,2-diol, which is the result of epoxide opening owing to the presence of trace amounts of water adsorbed on the hydrophilic MOFs, 2-cyclohexen-1-ol and 2-cyclohexen-1-one are the observed byproducts during each catalytic test. The formation of these byproducts is a result of the allylic oxidation of cyclohexene.^[10c,15] No leaching of Cu and Ga species was observed during these successive runs, which demonstrates the stability and regenerability of the catalyst. The powder XRD patterns of the Cu²⁺@COMOC-4 catalyst before and after each consecutive run are presented in Figure 8. It can be seen that the structural integrity of the framework is well preserved during these four following runs.

The Cu-BTC catalyst, which also contains unsaturated Cu sites, exhibits a similar product distribution and cyclohexene conversion (41.7% for Cu-BTC and 49% for Cu²⁺@COMOC-4), however, a difference in selectivity was detected between the catalysts. In contrast to Cu²⁺@COMOC-4, which has an average selectivity of 89% towards the epoxide, Cu-BTC exhibits a lower selectivity of 77.5% towards cyclohexene oxide, which results from the formation of a larger amount of byproducts (2-cyclohexen-1-one (3), 2-cyclohexen-1-ol (4), and cyclohexane-1,2-diol (5)). This could be because of the different structure of the Cu-MOF in comparison to Cu²⁺@COMOC-4. The Cu paddlewheel units in Cu-BTC contain unsaturated Cu sites that favor the binding of water. The presence of this adsorbed water can play a prominent role in the ring opening of the epoxide.^[16] Moreover, the paddlewheel structure has been shown to have a catalytic influence on epoxide ring-opening reactions.^[16d]

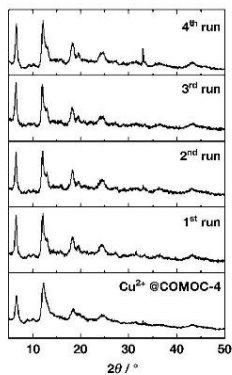
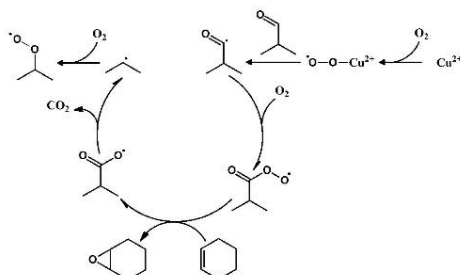


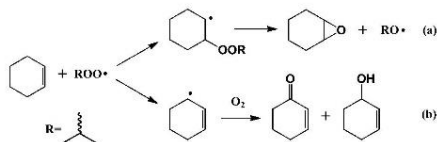
Figure 8. XRD patterns of Cu^{2+} @COMOC-4 before and after each catalytic run. (The peak at 32.9° is because of the background of the silicon sample holder)

The reaction mechanism for the transition-metal-catalyzed aerobic oxidation of alkenes in the presence of an aldehyde as a co-reagent is widely known in the literature as the Mukaiyama–Yamada epoxidation reaction (Scheme 2).^[14] In this study,



Scheme 2. Main mechanism to catalyze cyclohexene epoxidation in the presence of O_2 and isobutyraldehyde.

the autoxidation of the aldehyde plays a critical role in the catalytic process. Without the aldehyde, the Cu^{2+} -catalyzed alkene reaction is more in favor of the allylic reaction pathway.^[13a,17] The co-reactant isobutyraldehyde is transformed in situ into an acylperoxy radical, which is the predominant oxidizing species and facilitates the oxygen transfer to the olefin. Cyclohexene is a good substrate to investigate whether the oxidizing species prefers allylic oxidation or epoxidation.^[15] The acylperoxy radicals preferentially react with the double bond of the alkenes to yield the epoxide (Scheme 3). The latter pathway is the major reaction pathway observed during our catalytic tests, which indicates that the Cu^{2+} active sites mainly sta-



Scheme 3. The alkylperoxy radicals generated in the main catalytic cycle lead to the formation of byproducts (pathway b) in addition to cyclohexene oxide (pathway a). Adapted from Ref. [15a].

bilize the acylperoxy radical. Afterwards, the unstable carboxyl radical decomposes to form an alkyl radical, which can in turn be oxidized to an alkylperoxy radical. This species is less selective towards the formation of epoxides and leads to the formation of byproducts through the allylic oxidation pathway (Scheme 3, pathway b).

Conclusions

A Ga-based metal–organic framework (MOF), denoted as COMOC-4, has been successfully synthesized and characterized. In a second step CuCl_2 was incorporated into COMOC-4 by a post-synthetic modification approach. The successful incorporation was verified with the aid of ab initio techniques. The catalytic performance of the resulting Cu^{2+} @COMOC-4 material was investigated for the aerobic oxidation of cyclohexene in the presence of the co-oxidant isobutyraldehyde. In comparison to Cu-BTC (BTC = benzene-1,3,5-tricarboxylate), Cu^{2+} @COMOC-4 shows the best catalytic performance in terms of selectivity towards cyclohexene oxide. Furthermore, no leaching of either Ga or Cu species was detected over four successive runs, which indicates the good stability and reusability of the catalyst.

Experimental Section

General

The 2,2'-bipyridine-5,5'-dicarboxylic acid (H_2bpydc) ligand was prepared according to a procedure published elsewhere.^[18] Commercially available spectroscopic grade methanol was applied for the spectroscopic studies. All the other starting materials (analytical grade) were bought and used without further purification. Cu-BTC (Basolite™ C300, Sigma–Aldrich) as well as the as-synthesized porous compounds were activated at 120°C under vacuum for 3 h prior to use.

Synthesis

Synthesis of the Cu complex: $[\text{Cu}(\text{Me}_2\text{bpydc})\text{Cl}_2(\text{H}_2\text{O})_{1.5}]$

The dimethyl-(2,2'-bipyridine)-5,5'-dicarboxylate (Me_2bpydc) ligand was synthesized according to the procedure described by Gunyar et al.^[19] In a second step, Me_2bpydc (0.03 g) and $\text{CuCl}_2 \cdot 2\text{H}_2\text{O}$ (0.019 g) were mixed in a Pyrex tube with methanol (5 mL). The Pyrex tube was subsequently heated to 120°C and kept at this temperature overnight. The blue powder was collected by filtra-

tion, washed with acetone, and dried under vacuum. Elemental analysis calcd (%) for $\text{CuCl}_2 \cdot (\text{CH}_2)_2(\text{C}_6\text{H}_4)_2 \cdot 1.5\text{H}_2\text{O}$ (433.73): C 41.49, H 2.70, N 6.24; found: C 41.24, H 2.90, N 6.77.

Synthesis of COMOC-4 ($\text{Ga}(\text{OH})(\text{bpydc})$)

The synthesis of COMOC-4 was optimized at the gram scale based on our earlier reported synthesis procedure.³⁶ $\text{Ga}(\text{NO}_3)_3 \cdot \text{H}_2\text{O}$ (1.2 g, 4.4 mmol) and H_2bpydc (1.2 g, 5 mmol) were added to DMF (120 mL) in a 250 mL Schlenk flask equipped with a magnetic stirrer. In the first instance, the mixture was heated to 110 °C and kept at this temperature for 0.5 h. Afterwards the mixture was further heated to 150 °C and held at this temperature for 48 h with gentle stirring. An orange powder was collected over a membrane filter and washed thoroughly with DMF, methanol, and acetone. For the removal of unreacted linker from the pores, the solid product was suspended in DMF (0.5 g per 50 mL DMF), heated at 80 °C for 2 h, collected by filtration, washed with DMF and acetone, and dried under vacuum. To ensure the complete exclusion of the organic species encapsulated within the pores of the open framework, a Soxhlet extraction in methanol was performed over 48 h at 120 °C. Afterwards the COMOC-4 material was dried under vacuum overnight at RT. As a result of the presence of the –OH moiety on the Ga building unit, the 1D channels are highly hydrophilic. For this reason, the activated sample was stored under an inert atmosphere. The yield was 33% based on the Ga source. IR (KBr pellet): $\bar{\nu} = 3379$ (br), 1619 (s), 1595 (s), 1421 (s), 1394 (s), 1158 (w), 1050 (w), 847 (w), 775 (m), 705 (w), 600 (w), 479 cm^{-1} (w); elemental analysis calcd (%) for $\text{Ga}(\text{OH})(\text{C}_{12}\text{H}_8\text{N}_2\text{O}_4) \cdot 2.7\text{H}_2\text{O}$ (377.56): C 38.36, H 3.27, N 7.46; found: C 38.26, H 3.12, N 7.17.

Grafting the CuCl_2 complex onto the COMOC-4 framework

Cu^{2+} @COMOC-4 was prepared by stirring $\text{Ga}(\text{OH})(\text{bpydc})$ (0.5 g) and $\text{CuCl}_2 \cdot 2\text{H}_2\text{O}$ (0.1 g) in absolute methanol (30 mL) at 50 °C for 6 h. The green MOF powder was collected by filtration and was stirred in pure methanol (20 mL) for 6 h followed by filtration. This procedure was repeated twice to guarantee the complete removal of physisorbed CuCl_2 salts.

Characterization

Powder XRD and TGA

Powder XRD patterns were recorded by using a Thermo Scientific ARL X'Tra diffractometer, operated at 40 kV, 40 mA using CuK_α radiation ($\lambda = 1.5406 \text{ \AA}$). TGA data were obtained by using a Netzsch STA 449 F3 Jupiter-Simultaneous TG-DSC analyzer with a heating rate of $10^\circ\text{C min}^{-1}$ in air. N_2 sorption measurements were performed by using a Belsorp II, Bell Japan, Inc. All the samples were activated under vacuum at 120 °C for 3 h prior to analysis.

Spectroscopic characterization

FTIR spectra were recorded in the region of 400–4000 cm^{-1} by using a Bruker EQUINOX 55 FTIR spectrometer. UV/Vis absorption spectra were collected by using a Perkin-Elmer Lambda 950 UV/Vis spectrometer in the range of 260–900 nm. The spectra were recorded by using fine suspensions of powder samples (COMOC-4 and Cu^{2+} @COMOC-4) in methanol. In a typical measurement, 4 mg of powder sample was suspended in 3 mL of methanol in an ultrasonic bath for 5 min. The suspension was transferred to a 10 mm

path length quartz cuvette to record the spectrum. The UV/Vis DRS experiments were performed by using a Hitachi U-3000 UV/Vis Spectrophotometer with a diffuse reflectance accessory (integrated sphere) for spectrophotometric measurements in the range of 350–800 nm. The spectra were converted by using the Kubelka–Munk function. X-ray fluorescence spectrometry (XRF) measurements were performed by using a Rigaku NexCG, Energy Dispersive X-ray Fluorescence (EDXRF) instrument.

Computational methodology

MD simulations were performed on the linker with and without Cu coordination in a vacuum box of $20 \times 20 \times 20 \text{ \AA}$ by using the CP2K package.¹²⁰ All DFT calculations were performed by using the Gaussian plane waves (GPW) method,¹²¹ with a DZVP basis set, GTH pseudopotentials,¹²² and the BLYP functional. MD runs were conducted by using the canonical (NVT) ensemble at 300 K with a time step of 1 fs. A chain of five Nosé–Hoover thermostats was used to control the temperature. The system was first allowed to equilibrate after which a simulation of 20 ps was used for analysis. The dynamic UV/Vis spectra were obtained by taking 100 snapshots from the simulation on which vertical TD-DFT calculations were performed. This methodology has previously proven valuable for the simulation of absorption spectra.^{19,23} An average optical spectrum was then obtained. The influence of the methanol solvent was included with a polarizable continuum model (PCM). All TD-DFT calculations were performed by using the Gaussian 09²⁴ program using the B3LYP²⁵ functional and a 6-311+G(g) Pople basis set. We previously demonstrated that the B3LYP functional is very efficient for these types of systems.¹⁹ The effect of relativistic contributions was found to be small, and full details are given in the Supporting Information.

Catalysis

The oxidation of cyclohexene was performed in a 100 mL glass reactor equipped with a reflux condenser with recirculating cooling at -4°C . In a typical catalytic test, the reactor was loaded with Cu^{2+} @COMOC-4 (0.19 g, 0.2 mmol Cu active sites), cyclohexene (7 mL, 5 mmol), isobutyraldehyde (11.4 mL), chloroform (40 mL), and 1,2,4-trichlorobenzene (9 mL) employed as an internal standard. The molar ratio of cyclohexene/co-oxidant (isobutyraldehyde) was 1:2. The O_2 flow rate was set to 7.7 mL min^{-1} by using a mass flow controller. All the catalytic tests were performed at 40 °C. Blank reactions at this temperature showed no formation of oxidation products. During the catalytic tests, aliquots were gradually taken out of the mixture, diluted with ethyl acetate (500 μL), and subsequently analyzed by GC with flame ionization detection (FID). The reaction products were identified by using a TRACE GC \times GC (Thermo, Interscience) coupled to a TEMPUS TOF-MS detector (Thermo, Interscience). The first column consists of a dimethyl polysiloxane packing and has a length of 50 m with an internal diameter of 0.25 mm, and the second column has a length of 2 m with an internal diameter of 0.15 mm. The packing of the latter is a 50% phenyl polysilphenylene siloxane. He was used as the carrier gas with a constant flow (1.8 mL min^{-1}).

All the fresh catalysts were activated under vacuum at 120 °C for 3 h prior to catalysis. After each catalytic run, the catalyst was recovered by filtration, washed with acetone, and dried at RT overnight under vacuum to reuse it in another run. To investigate the recyclability of the Cu^{2+} @COMOC-4 catalyst, four consecutive runs were performed. Moreover, to examine the heterogeneity of the

catalyst, the filtrate, after the removal of the catalyst, was analyzed by XRF to quantify the possibly leached Cu and Ga species.

Acknowledgements

The authors acknowledge the financial support from the Ghent University BOF Grant (Nr. 01P02911T), GOA Grant (01G00710) and the Long Term Structural Methusalem grant nr. 01M00409 Funding by the Flemish Government. Furthermore, this research is co-funded by BELSPO in the frame of IAP 7/05 and the European Research Council (FP7(2007-2013) ERC Grant (Nr. 240483). Computational resources and services were provided by Ghent University.

Keywords: ab initio calculations · copper · epoxidation · heterogeneous catalysis · metal–organic framework

- [1] a) A. Corma, *J. Catal.* **2003**, *216*, 298–312; b) J. H. Clark, D. J. Macquarrie, *Org. Process Res. Dev.* **1997**, *1*, 149–162.
- [2] a) J. R. Long, O. M. Yaghi, *Chem. Soc. Rev.* **2009**, *38*, 1213–1214; b) K. K. Tanabe, S. M. Cohen, *Chem. Soc. Rev.* **2011**, *40*, 498–519; c) J. L. C. Rowse, O. M. Yaghi, *Microporous Mesoporous Mater.* **2004**, *73*, 3–14.
- [3] a) M. Eddaoudi, D. B. Moler, H. L. Li, B. L. Chen, T. M. Reineke, M. O'Keefe, O. M. Yaghi, *Acc. Chem. Res.* **2001**, *34*, 319–330; b) O. M. Yaghi, H. L. Li, C. Davis, D. Richardson, T. L. Groy, *Acc. Chem. Res.* **1998**, *31*, 474–484.
- [4] a) A. Dhakshinamoorthy, M. Alvaro, H. Garcia, *Catal. Sci. Technol.* **2011**, *1*, 856–867; b) V. Van Speybroeck, K. Leus, I. Muylaert, M. Vandichel, G. B. Marin, M. Waroquier, P. Van der Voort, *Chem. Commun.* **2010**, *46*, 5085–5087; c) A. Corma, H. Garcia, F. X. Llabres i Xamena, *Chem. Rev.* **2010**, *110*, 4606–4655.
- [5] a) L. Ma, J. M. Falkowski, C. Abney, W. Lin, *Nat. Chem.* **2010**, *2*, 838–846; b) F. Carson, S. Agrawal, M. Gustafsson, A. Bartoszewicz, F. Moraga, X. Zou, B. Martin-Matute, *Chem. Eur. J.* **2012**, *18*, 15337–15344; c) K. Leus, G. Vanhaelewyn, T. Bogaerts, Y.-Y. Liu, D. Esquivel, F. Callens, G. B. Marin, V. Van Speybroeck, H. Vrielinck, P. Van Der Voort, *Catal. Today*, **2013**, *208*, 97–105.
- [6] E. D. Bloch, D. Britt, C. Lee, C. J. Doonan, F. J. Uribe-Romo, H. Furukawa, J. R. Long, O. M. Yaghi, *J. Am. Chem. Soc.* **2010**, *132*, 14382–14384.
- [7] M. Wang, B. Yuan, T. Ma, H. Jiang, Y. Li, *RSC Adv.* **2012**, *2*, 5528–5530.
- [8] Y.-Y. Liu, R. Decadt, T. Bogaerts, K. Hemelsoet, A. M. Kaczmarek, D. Poelman, M. Waroquier, V. Van Speybroeck, R. Van Deun, P. Van Der Voort, *J. Phys. Chem. C* **2013**, *117*, 11302–11310.
- [9] a) T. De Meyer, K. Hemelsoet, L. Van der Schueren, E. Pauwels, K. De Clerck, V. Van Speybroeck, *Chem. Eur. J.* **2012**, *18*, 8120–8129; b) V. Barone, J. Bloino, S. Monti, A. Pedone, G. Prampolini, *Phys. Chem. Chem. Phys.* **2010**, *12*, 10550–10561; c) K. Hemelsoet, Q. Qian, T. De Meyer, K. De Wispelaere, B. De Sterck, B. M. Weckhuysen, M. Waroquier, V. Van Speybroeck, *Chem. Eur. J.* **2013**, doi: 10.1002/chem.201301965.
- [10] a) B. Monteiro, S. Gago, S. S. Balula, A. A. Valente, I. S. Gonçalves, M. Pilling, *J. Mol. Catal. A* **2009**, *312*, 23–30; b) M. Nandi, P. Roy, H. Uyama, A. Bhaumik, *Dalton Trans.* **2011**, *40*, 12510–12518; c) N. Komiya, T. Naota, Y. Oda, S.-I. Murahashi, *J. Mol. Catal. A* **1997**, *117*, 21–37.
- [11] I. Senkovska, F. Hoffmann, M. Froba, J. Getzschmann, W. Bohlmann, S. Kaskel, *Microporous Mesoporous Mater.* **2009**, *122*, 93–98.
- [12] a) T. Loiseau, C. Serre, C. Huguenard, G. Fink, F. Taulelle, M. Henry, T. Baille, G. Perey, *Chem. Eur. J.* **2004**, *10*, 1373–1382; b) A. J. Jacobson, M. Vougo-Zanda, J. Huang, E. Anokhina, X. Q. Wang, *Inorg. Chem.* **2008**, *47*, 11535–11542.
- [13] a) M. J. Beier, W. Kleist, M. T. Wharmby, R. Kissner, B. Kimmerle, P. A. Wright, J.-D. Grunwaldt, A. Baiker, *Chem. Eur. J.* **2012**, *18*, 887–898; b) A. Dhakshinamoorthy, M. Alvaro, H. Garcia, *J. Catal.* **2012**, *289*, 259–265; c) N. V. Maksimchuk, K. A. Kovalenko, V. P. Fedin, O. A. Kholdeeva, *Chem. Commun.* **2012**, *48*, 6812–6814; d) A. M. Balu, C. S. K. Lin, H. Liu, Y. Li, C. Vargas, R. Luque, *Appl. Catal. A* **2013**, *455*, 261–266; e) L. Luz, A. Leon, M. Boronat, F. X. Llabres i Xamena, A. Corma, *Catal. Sci. Technol.* **2013**, *3*, 371–379; f) I. Y. Skobelev, A. B. Sorokin, K. A. Kovalenko, V. P. Fedin, O. A. Kholdeeva, *J. Catal.* **2013**, *298*, 61–69.
- [14] T. Takai, T. Yamada, T. Mukaiyama, *Chem. Lett.* **1991**, *9*, 1499–1502.
- [15] a) B. B. Wentzel, P. L. Alsters, M. C. Feiters, R. J. M. Nolte, *J. Org. Chem.* **2004**, *69*, 3453–3464; b) W. W. Nam, H. J. Kim, S. H. Kim, R. Y. N. Ho, J. S. Valentine, *Inorg. Chem.* **1996**, *35*, 1045–1049.
- [16] a) H. L. Bao, J. Zhou, Z. Wang, Y. L. Guo, T. P. You, K. L. Ding, *J. Am. Chem. Soc.* **2008**, *130*, 10116–10127; b) K. Tanaka, K. Otani, T. Murase, S. Nishihote, Z. Urbanczyk-Lipkowska, *Bull. Chem. Soc. Jpn.* **2012**, *85*, 709–714; c) I. Vilotjevic, T. F. Jamison, *Science* **2007**, *317*, 1189–1192.
- [17] Y. Fu, D. Sun, M. Qin, R. Huang, Z. Li, *RSC Adv.* **2012**, *2*, 3309–3314.
- [18] K. C. Szeto, K. O. Kongshaug, S. Jakobsen, M. Tilset, K. P. Lillerud, *Dalton Trans.* **2008**, 2054–2060.
- [19] A. Gunyar, D. Betz, M. Drees, E. Herdtweck, F. E. Kuhn, *J. Mol. Catal. A* **2010**, *331*, 117–124.
- [20] <http://cp2k.berlios.de/>.
- [21] G. Lippert, J. Hutter, M. Parrinello, *Mol. Phys.* **1997**, *92*, 477–487.
- [22] a) S. Goedecker, M. Teter, J. Hutter, *Phys. Rev. B* **1996**, *54*, 1703–1710; b) C. Hartwigsen, S. Goedecker, J. Hutter, *Phys. Rev. B* **1998**, *58*, 3641–3662.
- [23] C. Adamo, D. Jacquemin, *Chem. Soc. Rev.* **2013**, *42*, 845–856.
- [24] Gaussian 09, Revision B.01, M. J. Frisch, G. W. Trucks, H. B. Schlegel, G. E. Scuseria, M. A. Robb, J. R. Cheeseman, G. Scalmani, V. Barone, B. Menucci, G. A. Petersson, H. Nakatsuji, M. Caricato, X. Li, H. P. Hratchian, A. F. Izmaylov, J. Bloino, G. Zheng, J. L. Sonnenberg, M. Hada, M. Ehara, K. Toyota, R. Fukuda, J. Hasegawa, M. Ishida, T. Nakajima, Y. Honda, O. Kitao, H. Nakai, T. Vreven, J. A. Montgomery, Jr., J. E. Peralta, F. Ogliaro, M. Bearpark, J. J. Heyd, E. Brothers, K. N. Kudin, V. N. Staroverov, R. Kobayashi, J. Normand, K. Raghavachari, A. Rendell, J. C. Burant, S. S. Iyengar, J. Tomasi, M. Cossi, N. Rega, J. M. Millam, M. Klene, J. E. Knox, J. B. Cross, V. Bakken, C. Adamo, J. Jaramillo, R. Gomperts, R. E. Stratmann, O. Yazyev, A. J. Austin, R. Cammi, C. Pomelli, J. W. Ochterski, R. L. Martin, K. Morokuma, V. G. Zakrzewski, G. A. Voth, P. Salvador, J. J. Dannenberg, S. Dapprich, A. D. Daniels, Ö. Farkas, J. B. Foresman, J. V. Ortiz, J. Cioslowski, D. J. Fox, Gaussian, Inc., Wallingford CT, **2009**.
- [25] a) A. D. Becke, *J. Chem. Phys.* **1993**, *98*, 5648–5652; b) C. T. Lee, W. T. Yang, R. G. Parr, *Phys. Rev. B* **1988**, *37*, 785–789.

Received: July 3, 2013

Revised: September 10, 2013

Published online on October 17, 2013

Heterogeneous & Homogeneous & Bio-

CHEMCATCHEM

CATALYSIS

Supporting Information

© Copyright Wiley-VCH Verlag GmbH & Co. KGaA, 69451 Weinheim, 2013

Bimetallic–Organic Framework as a Zero-Leaching Catalyst in the Aerobic Oxidation of Cyclohexene

Ying-Ya Liu,^[a] Karen Leus,^[a] Thomas Bogaerts,^[a, b] Karen Hemelsoet,^[b] Els Bruneel,^[c]
Veronique Van Speybroeck,^[b] and Pascal Van Der Voort^{*[a]}

cctc_201300529_sm_miscellaneous_information.pdf

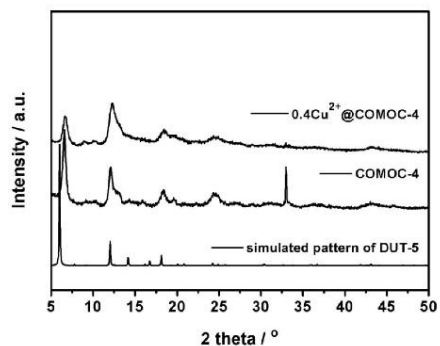


Figure S1 Powder XRD patterns of COMOC-4, Cu^{2+} @COMOC-4 compared with simulated pattern of $\text{Al}(\text{OH})(\text{BPDC})$ (DUT-5, $\text{BPDC}^{2-} = 2,2'$ -biphenyl-5,5'-dicarboxylate) (The peak at 32.9° is due to the background of the silicon sample holder).

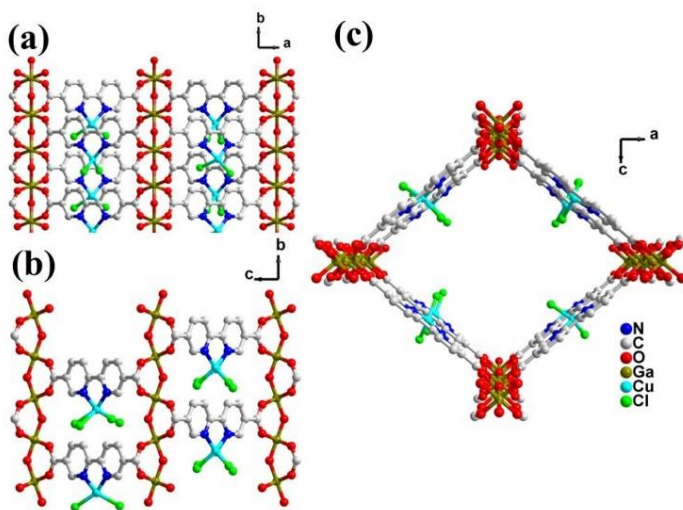


Figure S2 Representative structure of Cu^{2+} @COMOC-4. View perpendicular to (a,b) and along (c) the one dimensional pore system. The structure model was generated based on the crystal structure of DUT-5. ^[1]

Influence of metal coordination on the computed spectra – Metal-to-ligand character

In order to determine if the changes in the calculated UV/Vis spectrum are a consequence of the metal coordination, the molecular orbitals corresponding to the extra bands in the absorption spectrum were visualized. Figure S3(a) displays the theoretical UV/Vis spectrum of a the copper-modified linker. The spectrum was calculated for the optimized geometry using TD-DFT, in particular B3LYP/6-311+G(d).

Three peaks can be distinguished, with maxima around 403, 324 and 307 nm. These values deviate from the values of the averaged MD spectrum (see Figure 4 in the main manuscript) since it corresponds with one particular geometry, however the overall shape of the spectrum is maintained. This behavior is explained in more detail in refs.^[2a, 2b]

We focus on the absorption at 403 and 324 nm, which are due to the metal coordination. Investigation of the underlying transitions reveals that a variety of orbitals is involved. However, the feature at 403 nm mainly results from a HOMO to LUMO transition (in particular orbitals 103a and 104a are involved, see Figure S3(b)). The peak at 324 nm is mainly due to a transition from orbital 100a to 104a as well as from 100b to 104b (Figure S3(c)). The involved orbitals are depicted and the participation of the CuCl₂ and linker fragments in the orbitals are also given. From this information, it is clear that the observed peaks involve a metal-to-ligand transition.

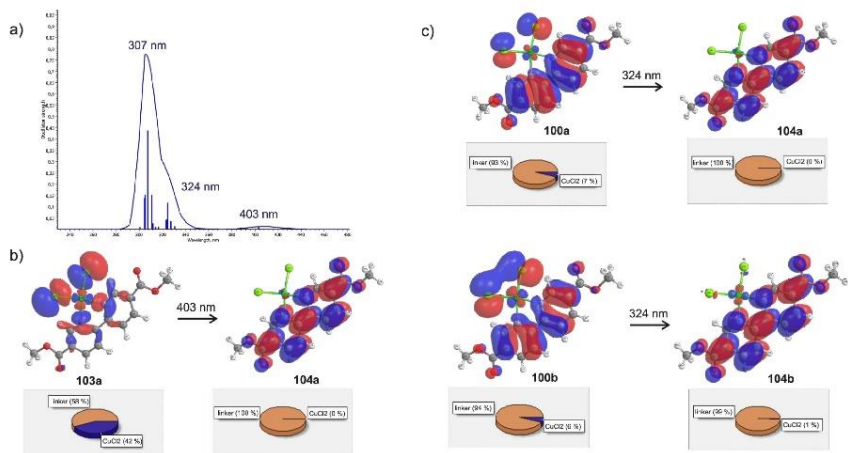


Figure S3 (a) Theoretical UV/Vis spectrum of the Cu-modified linker, calculated for a snapshot extracted from the MD simulation. (b) Iso-surfaces of dominant orbitals involved in the excitation at 403 nm. (c) Iso-surfaces of the dominant orbitals involved in the excitation at 324 nm. The participation of the separate fragments is also depicted; in particular in orange for the linker and in blue for the CuCl₂.

Influence of relativistic effects on the theoretical simulations of the Cu-modified linker

All TD-DFT simulations are done using the B3LYP/6-311+G(d) level of theory. We believe this method is adequate to model the systems under investigation, since we are aiming at describing the difference between the parent and modified linker. In this light, we refer to a study of Ghost et al.,^[3] who report on the successful use of B3LYP with a standard basis set on copper complexes for TDDFT calculations. However, relativistic contributions are necessary when results of high quantitative accuracy are targeted. To assess the influence of relativistic contributions on our results, additional simulations were performed using the Orca program. Relativistic effects were explicitly taken into account using the ZORA option. This methodology is similar to the one used by Ji et al.^[4] for the simulation of luminescent properties of MOF-5.

Table S1 lists the important absorption peaks of the Cu-modified linker. In addition to testing the influence of relativistic effects, also the performance of two basis sets (in particular SVP and TZVPP) and the BLYP and B3LYP functionals were assessed. This is necessary, since a straightforward comparison with the original results is not straightforward due to the use of different software packages and implementations. We note that in the computed spectra a large number of excitations, with small oscillator strengths, is observed. The results in Table S1 correspond to the excitations with maximal oscillator strength in the region of interest (between 400–480 nm). We indeed observe a substantial shift between the values computed using the Gaussian (403nm; Figure S3) and Orca (close to 450 nm; Table S1) programs. The values of Table S1 are in closer agreement with the averaged MD result (see Figure 4 of the main manuscript); a full analysis is however outside the scope of this paper.

Table S1. Computed excitation energies [in nm] for the Cu-modified bipyridine linker.

	Cu-bipyridine			
	BLYP		B3LYP ^[a]	
	Without ZORA	With ZORA	Without ZORA	With ZORA
SVP	454	457	460	453
TZVPP ^[a]	453	452	-	-

^[a] The B3LYP/TZVPP simulations are computationally too demanding for the Cu-modified linker

Importantly, the additional simulations support the observation that relativistic effects do not substantially change the qualitative behavior of the optical spectrum of the Cu-modified linker, a maximal shift of 7 nm is obtained between the results with and without ZORA effects. This conclusion suggests that the original methodology (i.e. TD-DFT simulations using the B3LYP/6-311+G(d) level of theory) succeeds at describing the systems under investigation.

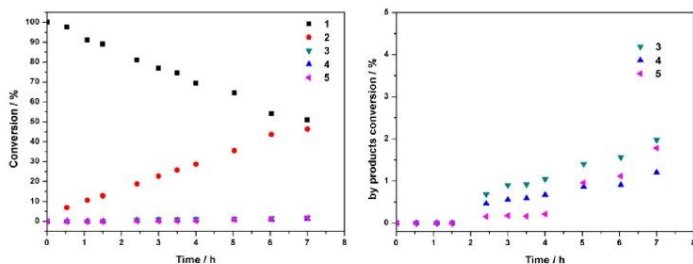


Figure S4 Left: Time conversion of cyclohexene (1) and time evolution of product distribution (cyclohexene oxide (2), 2-cyclohexene-1-one (3), 2-cyclohexen-1-ol (4) and cyclohexane-1,2-diol (5)) over Cu^{2+} @COMOC-4 during the 1st run. Right: detailed time evolution of by-product distribution over Cu^{2+} @COMOC-4 during the 1st run.

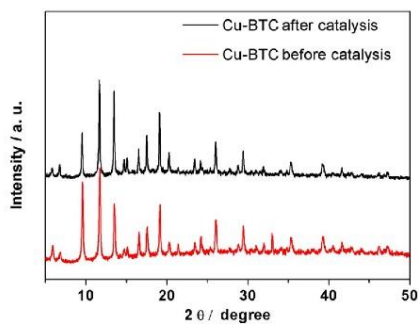


Figure S5 XRD comparison of Cu-BTC before and after catalysis.

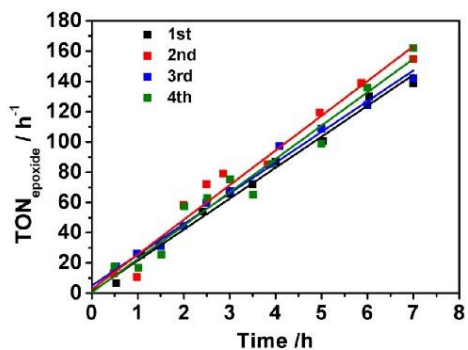
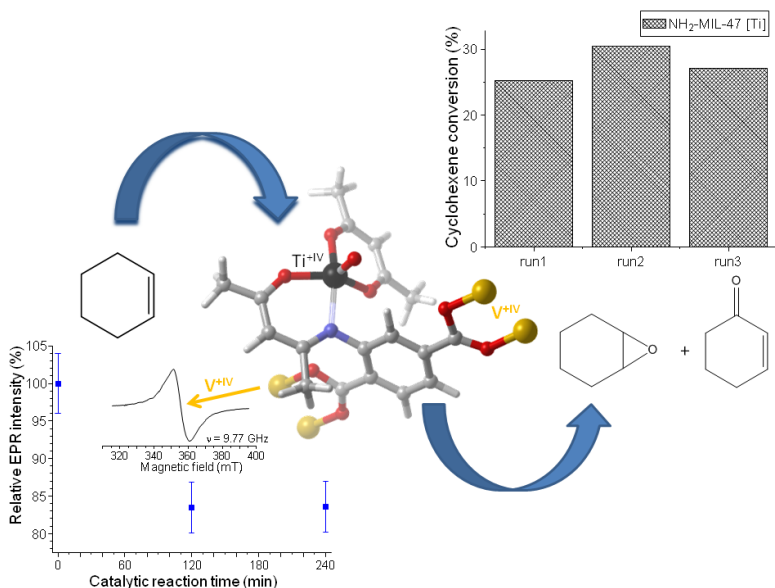


Figure S6 The catalytic activity expressed as TON for Cu^{2+} @COMOC-4 for 4 runs.

References

- [1] Senkovska, I.; Hoffmann, F.; Froba, M.; Getzschmann, J.; Bohlmann, W.; Kaskel, S., *Microporous Mesoporous Mater.* **2009**, 122 (1-3), 93-98
- [2] a) De Meyer, T.; Hemelsoet, K.; Van der Schueren, L.; Pauwels, E.; De Clerck, K.; Van Speybroeck, V., *Chem. - A Eur. J.* **2012**, 18 (26), 8120-8129; b) K. Hemelsoet, Q. Qian, T. De Meyer, K. De Wispelaere, B. De Sterck, B. M. Weckhuysen, M. Waroquier, V. Van Speybroeck, *Chem. - A Eur. J.* 2013, doi: 10.1002/chem.201301965
- [3] Alemayehu, A.; Conradie, J.; Ghosh, A., *Eur. J. Inorg. Chem.* **2011**, 2011 (12), 1857-1864
- [4] Ji, M.; Lan, X.; Han, Z.; Hao, C.; Qiu, J., *Inorg. Chem.* **2012**, 51 (22), 12389-12394

PAPER IX: TI-FUNCTIONALIZED NH₂-MIL-47: AN EFFECTIVE AND STABLE EPOXIDATION CATALYST



K. Leus, G. Vanhaelewyn, T. Bogaerts, Y-Y Liu, F. Esquivel, F. Callens, G.B. Marin, V. Van Speybroeck, H. Vrielinck, P. Van der Voort, *Catalysis Today*, 208, 97-105, **2013**.

T. Bogaerts assisted in this paper by the characterization with IR spectroscopy and with the catalytic reactions.

Copyright 2015, with permission from Elsevier



Ti-functionalized NH₂-MIL-47: An effective and stable epoxidation catalyst

Karen Leus^a, Gauthier Vanhaelewyn^b, Thomas Bogaerts^{a,c}, Ying-Ya Liu^a, Dolores Esquivel^a, Freddy Callens^b, Guy B. Marin^d, Veronique Van Speybroeck^c, Henk Vrielinck^{b,*}, Pascal Van Der Voort^{a,**}

^a Department of Inorganic and Physical Chemistry, Center for Ordered Materials, Organometallics and Catalysis (COMOC), Ghent University, Krijgslaan 281-S3, 9000 Ghent, Belgium

^b Department of Solid State Sciences, Ghent University, Electron Magnetic Resonance (EMR) Research Group, Krijgslaan 281-S1, 9000 Ghent, Belgium

^c Center for Molecular Modeling, Ghent University, Technologiepark 903, 9052 Zwijnaarde, Belgium

^d Laboratory for Chemical Technology, Ghent University, Krijgslaan 281-S5, 9000 Ghent, Belgium

ARTICLE INFO

Article history:

Received 13 July 2012

Received in revised form

14 September 2012

Accepted 18 September 2012

Available online 27 December 2012

Keywords:

Metal-organic frameworks

Vanadium

Titanium

Oxidation catalysis

ABSTRACT

In this paper, we describe the post-functionalization of a V-containing Metal-organic framework with TiO(acac)₃ to create a bimetallic oxidation catalyst. The catalytic performance of this V/Ti-MOF was examined for the oxidation of cyclohexene using molecular oxygen as oxidant in combination with cyclohexanecarboxaldehyde as co-oxidant. A significantly higher cyclohexene conversion was observed for the bimetallic catalyst compared to the non-functionalized material. Moreover, the catalyst could be recycled at least 3 times without loss of activity and stability. No detectable leaching of V or Ti was noted. Electron paramagnetic resonance measurements were performed to monitor the fraction of V-ions in the catalyst in the +IV valence state. A reduction of this fraction by ~17% after oxidation catalysis is observed, in agreement with the generally accepted mechanism for this type of reaction.

© 2012 Elsevier B.V. All rights reserved.

1. Introduction

Metal-organic frameworks (MOFs) are a highly versatile class of ordered porous materials constructed of metal nodes or metal clusters linked together by organic ligands. This recent class of crystalline materials has been extensively studied for their potential use in various applications, e.g. in gas storage and separations [1–3], catalysis [4–8] and luminescence [9,10]. MOFs possess many intriguing features including very high surface areas, well defined pore properties (pore size, shape and volume) and have easily tailorable structures and chemical functionalities. Several reports have appeared on the introduction of an additional functionality in the linker, by pre-functionalization with, e.g., –NH₂, –OH, –CH₃ and –NO₂ groups [11–15]. In the field of catalysis, it has been shown that the introduction of these additional functional groups can generate a significant alteration in the catalytic performance compared to the parent framework. In a recent report of Vermoortele et al., a UiO-66-X (X = H, NH₂, CH₃, OCH₃, F, Cl, Br, NO₂) series with different functional groups was tested for the citronellal cyclization [16]. This study demonstrated that the presence of –NO₂ groups enhanced

the catalytic activity in comparison with the parent framework. Alternatively, the catalytic activity can be influenced by the introduction of additional framework active sites [17]. Maksimchuk et al. reported the encapsulation of polyoxometalates into the nanocages of the MIL-101 framework [18]. The resulting material demonstrated a good catalytic activity for the epoxidation of various alkenes. Alkordi et al. encapsulated metalloporphyrins into zeolite-like MOFs which enhanced the catalytic activity for cyclohexane oxidation [19]. A third approach is to bring new catalytically active sites into the framework by a post-modification of the embedded functional groups [20]. Ingleson et al. reported the two steps modification of IRMOF-3 to an imine grafted VO(acac)₂ complex [21]. However, the resulting catalyst showed a rather low catalytic activity and stability for the oxidation of cyclohexene. The group of Battacharjee reported a more straightforward one step functionalization of the IRMOF-3 with Mn(acac)₂ [22]. Although a good catalytic and stability performance was obtained, the yield of the grafted complex was rather low (8%).

In our previous studies, we demonstrated that vanadium based MOFs (MIL-47 and COMOC-3), with saturated vanadium sites have a remarkable catalytic activity in the liquid phase epoxidation of cyclohexene with tert-Butyl hydroperoxide (TBHP) as oxidant [23–25]. However, both the experimental results and theoretical calculations showed that the catalytic cycle starts with the breaking of at least one V-carboxylate bond to coordinate the peroxide. The structural defects created during this process

* Corresponding author. Tel.: +32 9 264 43 56; fax: +32 9 264 49 96.

** Corresponding author. Tel.: +32 9 264 44 42; fax: +32 9 264 49 83.

E-mail addresses: Henk.Vrielinck@ugent.be (H. Vrielinck),

Pascal.Vandervoort@ugent.be (P. Van Der Voort).

contribute to the catalytic performance. Hence, a small amount of leaching was observed in the start of the catalysis. Our objective is to prevent leaching while maintaining or enhancing the catalytic performance. Therefore, we opted for a milder system using O_2 as oxidant in combination with cyclohexanecarboxaldehyde as a co-oxidant. To the best of our knowledge, a Ti grafted V-MOF has not been reported so far. Nevertheless, bimetallic Ti–V catalysts are reported to have a synergistic effect in oxidation catalysis [26].

In this contribution, we report a bimetallic V/Ti-MOF via post-functionalization of the V-MOF, NH₂-MIL-47 with a Titanylacetylacetonate complex (denoted as NH₂-MIL-47 [Ti] hereafter) (see Fig. 1). The obtained NH₂-MIL-47 [Ti] was examined in the oxidation of cyclohexene and was compared with the non-functionalized V-MOF as well as with the homogeneous TiO(acac)₂ catalyst. Additionally regeneration and stability tests were carried out. In our previous study of the catalytic activity of MIL-47 in the oxidation of cyclohexene with TBHP as oxidant, we used X-band (9.8 GHz) Electron Paramagnetic Resonance (EPR) measurements at room temperature (RT) to monitor the evolution in the fraction of V-ions in the paramagnetic +IV valence state [24]. We observed a reduction of the V^{IV} concentration by about 20% in the first few hours of reaction, as a result of V^{IV} → V^V oxidation, confirming a radical parallel reaction pathway suggested by density functional theory (DFT) calculations. Similar EPR experiments are performed in this study in order to gain insight in the catalytic reaction mechanisms. In view of the absence of hyperfine (HF) structure in the spectra, the X-band measurements are complemented with Q-band experiments (34 GHz) and spectral simulations (Easyspin [27] library in Matlab®) in order to corroborate the assignment of the spectrum to V^{IV}.

2. Materials and methods

2.1. General procedures

All chemicals were bought from Sigma–Aldrich and used without further purification. X-Ray Fluorescence (XRF) measurements were performed on a NEX CG from Rigaku using a Mo X-ray source. X-ray powder diffraction (XRPD) patterns were collected on a ARL X'TRA X-ray diffractometer with Cu-K α radiation of 0.15418 nm wavelength and a solid state detector. The Cross Polarization Magic Angle Spinning Nuclear Magnetic Resonance (¹³C CP/MAS NMR) spectra were recorded at 100.6 MHz on a Bruker AVANCE-400 WB spectrometer at RT. The samples were spun at 13 kHz. An overall 10,000 free induction decays were accumulated with 4 s of recycle time. Chemical shifts were measured relative to a tetramethylsilane standard. The ¹H NMR spectrum was recorded on a Bruker AVANCE DRX500 NMR spectrometer (500 MHz). Diffuse Reflectance Infrared Fourier Transform Spectroscopy (DRIFTS) measurements were recorded on a Thermo Nicolet 6700 FT-IR spectrometer equipped with a N₂ cooled MCT-A (mercury–cadmium–tellurium) detector. Nitrogen adsorption experiments were measured at –196 °C using a Belsorp mini II gas analyzer. The reaction products were identified with a TRACE GC × GC (Thermo, Interscience), coupled to a TEMPUS TOF-MS detector (Thermo, Interscience). The first column consists of a dimethyl polysiloxane package and has a length of 50 m, with an internal diameter of 0.25 mm, whereas the second column has a length of 2 m with an internal diameter of 0.15 mm. The package of the latter is a 50% phenyl polysilphenylene-siloxane. Helium was used as carrier gas with a constant flow (1.8 mL/min). An ultra-fast gas chromatograph (GC) equipped with a flame ionization detector (FID) and a 5% diphenyl/95% poly-dimethylsiloxane column with 10 m length and 0.10 mm internal diameter was used to follow the conversions of the products during the catalytic tests.

Helium was used as carrier gas, and the flow rate was programmed as 0.8 mL/min.

2.2. Synthesis of NH₂-MIL-47 [Ti]

In a first step NH₂-MIL-47 was prepared via a microwave synthesis route. Typically 1.7 mmol VCl₃ was mixed with 1.7 mmol 2-aminoterephthalic acid in 3.02 mL H₂O. The reaction was carried out at 150 °C for 20 min. Afterwards, an extraction in dimethylformamide (DMF) was performed at 125 °C for 90 min to remove unreacted linker.

In a second step TiO(acac)₂ was grafted onto the V-MOF. Different temperatures and reaction times have been applied as shown in Table S. 1 of the Supporting Information. In each experiment 0.0785 g TiO(acac)₂ was dissolved in 30 mL of dry toluene. After stirring the solution for 4 h at 55 °C, 0.15 g NH₂-MIL-47 was added to the solution. Subsequently this mixture was stirred at a certain temperature (55 °C, 70 °C and 90 °C) for 20 or 40 h under an inert argon atmosphere. Hereafter, the MOF was filtered on a combined nylon-membrane filter and washed several times with acetone to remove unreacted TiO(acac)₂. Afterwards the solid was dried overnight under vacuum.

2.3. Catalytic setup

In a typical catalytic test, a schlenk flask was loaded with 40.0 mL of acetonitrile as solvent, 7.0 mL cyclohexene (substrate) and 8.4 mL 1,2,4-trichlorobenzene used as internal standard. Oxygen (99.9% pure) was applied as the oxidant in combination with the co-oxidant cyclohexanecarboxaldehyde (7.6 mL). A constant oxygen flow of 7 mL/min was bubbled through the solution by means of a mass flow controller. Blank reactions were carried out in the absence of catalyst which showed no conversion of cyclohexene. All the catalytic tests were carried out at a temperature of 40 °C in a schlenk flask equipped with a liquid condenser coupled with recirculating cooling liquid at –4 °C to prevent evaporation of the reaction mixture. Aliquots were gradually taken out of the mixture, diluted with 500 μ l ethylacetate, and subsequently analyzed by GC-FID.

2.4. EPR measurements

For quantitative EPR analysis, spectra of dry powders, contained in quartz tubes with an outer diameter of 4 mm, filled to a height of approximately 6 mm (30–35 mg), were recorded at RT using a Bruker ESP300E X-band spectrometer (ER 4102-ST rectangular cavity). In the bottom part of the EPR cavity an open quartz tube was fixed, on which the sample tubes rested, in order to ensure reproducible positioning. The microwave frequency was measured using a HP 5350 B microwave frequency counter. The magnetic field was modulated at 100 kHz with a peak-to-peak amplitude of 0.1 mT and the microwave power was set to 2 mW, avoiding saturation. A broad magnetic field range was swept (350 mT) around the free electron *g*-value (2.0023). All spectra were normalized to a microwave frequency of 9.77 GHz for comparison and corrected for the background spectrum of the empty cavity. For comparison of intensities, the spectra were divided by the sample mass. In order to resolve the anisotropy, selected powders were also measured in Q-band (\approx 34 GHz) at RT on a Bruker Elexsys E500 spectrometer equipped with a Pendulum CNT-90XL frequency counter (spectra normalized to 33.98 GHz). These measurements were performed on powders contained in 2 mm outer diameter quartz tubes filled to a height of about 2 mm.

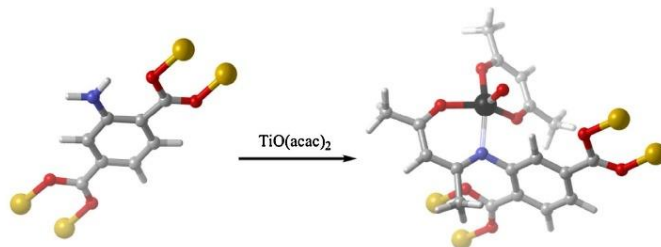


Fig. 1. Schematic representation of the post-functionalization of $\text{NH}_2\text{-MIL-47}$ with a Titanylacetylacetonate complex (the carbon atoms are shown in gray, the oxygen atoms are depicted in red and the N, Ti and V atoms are shown in blue, black and yellow, respectively). (For interpretation of the references to color in the artwork, the reader is referred to the web version of the article.)

2.5. Computational details

Ab initio calculations are performed with the gaussian09 program [28]. All models were optimized with a B3LYP [29,30] functional using a 6-31 + G(d) Pople basis set. Vibrational frequency calculations were done at the same level of theory. To compare the calculated frequencies with the experimental DRIFTS spectrum a scale factor of 0.9648 was imposed, as proposed by Merrick et al. [31].

3. Experimental results and discussion

3.1. Characterization of the functionalized materials

3.1.1. XRPD analysis and determination of the Ti loading

By means of XRF the Ti loading was determined of the functionalized MOF materials (see Table S. 1). Approximately the same loading was obtained in each experiment, with an average of

1.25 mmol Ti/g, which indicates that almost 30% of the $-\text{NH}_2$ groups on the organic linker are modified. It should be noted that this loading is much higher compared to the earlier reported one step functionalization of $\text{Mn}(\text{acac})_2$ on IRMOF-3, which was approximately 0.23 mmol Mn/g [22]. Furthermore, the crystallinity of all the obtained Ti-grafted materials was verified by XRPD measurements (see Fig. S.1 Supporting Information). As can be seen from this figure, the XRPD pattern of each functionalized material presents the pure phase of the non-functionalized $\text{NH}_2\text{-MIL-47}$. This explicitly shows that the framework integrity of the parent MOF was well preserved during the post-functionalization.

3.1.2. DRIFTS, ^{13}C CP/MAS NMR and ^1H NMR measurements

DRIFTS, ^{13}C CP/MAS and ^1H NMR measurements were carried out to verify if the $\text{TiO}(\text{acac})_2$ complex was actually grafted onto the V-MOF. We selected the sample $\text{NH}_2\text{-MIL-47}[\text{Ti}]$, 70 °C, 20 h, for a detailed characterization and subsequent catalytic studies. In Fig. 2 the ^{13}C CP/MAS NMR spectra of $\text{NH}_2\text{-MIL-47}$ and

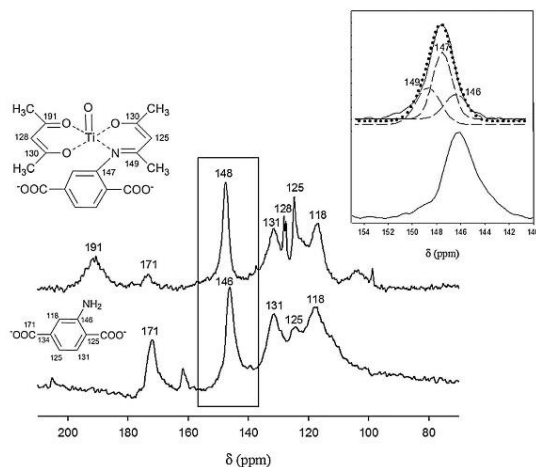


Fig. 2. ^{13}C CP/MAS NMR spectra of $\text{NH}_2\text{-MIL-47}$ and $\text{NH}_2\text{-MIL-47}[\text{Ti}]$. (INSET): detailed NMR spectrum of the signal at 148 ppm and its deconvolution.

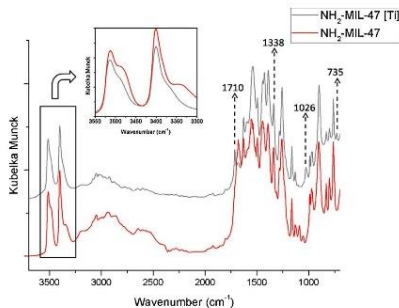


Fig. 3. DRIFTS spectra of $\text{NH}_2\text{-MIL-47}$ (shown in red) and $\text{NH}_2\text{-MIL-47 [Ti]}$, 70 °C, 20 h (shown in black) INSET: detailed DRIFTS spectra of both materials in the region 3550–3300 cm^{-1} . The spectra were normalized to the vibration at 800 cm^{-1} which corresponds to the aromatic C–H out of plane bend mode. (For interpretation of the references to color in the artwork, the reader is referred to the web version of the article.)

$\text{NH}_2\text{-MIL-47 [Ti]}$ are presented. The ^{13}C CP/MAS NMR spectrum of $\text{NH}_2\text{-MIL-47}$ gave several signals at 118, 125, 131 and 146 ppm associated with different sp^2 carbons of the organic linker and one peak at 171 ppm assigned to the carbonyl groups of the amino terephthalate linker [32]. In the non-functionalized $\text{NH}_2\text{-MIL-47}$ an additional signal at 162 ppm confirmed the incomplete removal of solvent (DMF) used in the synthesis of the material. After functionalization, $\text{NH}_2\text{-MIL-47 [Ti]}$ showed new bands which corroborate the presence of the grafted $\text{TiO}(\text{acac})_2$ complex on $\text{NH}_2\text{-MIL-47}$. An intense signal appeared at ca. 148 ppm. As can be seen from Fig. 2 (inset), this signal could be deconvoluted into 3 peaks: the signal at 146 ppm corresponds to the C–N bond (non-functionalized material), whereas the signal at 147 and 149 ppm can be associated to the C–N and C=N groups of the bimetallic MOF, respectively [32]. This proves the success of the post-functionalization. Moreover, the $\text{NH}_2\text{-MIL-47 [Ti]}$ showed several peaks in the aromatic region (120–130 ppm) and a new peak at ca. 191 ppm, which correspond to the C=C and C=O groups of the titaniumacetylacetonate complex, respectively [32]. The ^1H NMR spectrum (see Fig. S4) of the digested $\text{NH}_2\text{-MIL-47 [Ti]}$ shows peaks at 2.06, 1.94 and 1.85 ppm due to the $-\text{CH}_3$ groups further confirming the presence of acac and imine-functionalized acac ligands grafted onto $\text{NH}_2\text{-MIL-47}$.

The DRIFTS spectra of the $\text{NH}_2\text{-MIL-47}$ and $\text{NH}_2\text{-MIL-47 [Ti]}$, 70 °C, 20 h are shown in Fig. 3 (the DRIFTS spectra of the other materials are presented in Fig. S.2). It is clear that the characteristic vibrations of the parent MOF are still present. However, after the post-functionalization a decrease in intensity of some vibrations is observed, pointing toward a decrease in concentration of the $-\text{NH}_2$ groups. The typical vibrations of the benzene linker at 1510–1450 cm^{-1} (aromatic ring stretch), 1225–950 cm^{-1} (aromatic C–H in plane bend) and 900–670 cm^{-1} (aromatic C–H out of plane bend) [33] remain unchanged. Furthermore, the symmetric and asymmetric $-\text{CO}_2$ stretching vibrations in the region 1463–1415 cm^{-1} and 1616–1597 cm^{-1} are still present after grafting [34].

The principal changes in the spectrum before and after post-functionalization can be connected to the amine moiety. To obtain more insight in these changes, molecular modeling calculations were applied. The model of the catalyst was built by isolating the aromatic part of the linker with a $\text{TiO}(\text{acac})_2$ substituent, as shown in Fig. 4. For comparison, the $\text{NH}_2\text{-MIL-47}$ was modeled as aniline. Only the relevant parts of the structure have been taken



Fig. 4. Model used in the calculation of the IR vibrations after post-functionalization with the $\text{TiO}(\text{acac})_2$ moiety (the C atoms are shown in gray, N atoms in blue, and the O and Ti atoms are depicted in red and black, respectively). (For interpretation of the references to color in the artwork, the reader is referred to the web version of the article.)

into account to calculate the spectra. Therefore, in both models the carboxylic acid group and its coordination with vanadium was not included since it would not contribute any relevant information to the calculated spectrum. The absorbance due to the vibrations at 1338 cm^{-1} (C–N stretch) and the doublet at 3494 cm^{-1} and 3386 cm^{-1} (NH_2 asymmetric and symmetric stretch) decrease in comparison to the non-functionalized V-MOF [35,36]. Also the skeletal vibration bands that contain NH_2 rocking at 1050 cm^{-1} and 1100 cm^{-1} become less intense due to a partial modification of the amine groups. The presence of the $\text{TiO}(\text{acac})_2$ modification can be seen by the vibrations at 735 cm^{-1} (C–C–H twisting) and 1026 cm^{-1} (C–CO–C wagging). The C=N vibration cannot be seen since it overlaps with the vibrations from the parent MOF between 1600 cm^{-1} and 1700 cm^{-1} . The new peak that appears at 1710 cm^{-1} could not be assigned with this model. This vibration could be due to free C=O vibrations, which are the consequence of some $\text{TiO}(\text{acac})_2$ complexes that break during the post-functionalization. This would result in a ketone substituent which is not coordinated with titanium on the MOF.

3.1.3. Nitrogen sorption measurement

In Fig. 5 the nitrogen adsorption isotherms of $\text{NH}_2\text{-MIL-47}$ and $\text{NH}_2\text{-MIL-47 [Ti]}$, 70 °C, 20 h are compared. The Langmuir surface area of the non-functionalized and post-functionalized material is 650 m^2/g and 190 m^2/g respectively. Despite the high loading of Ti (approximately 30%), the post-functionalized MOF retains a partial

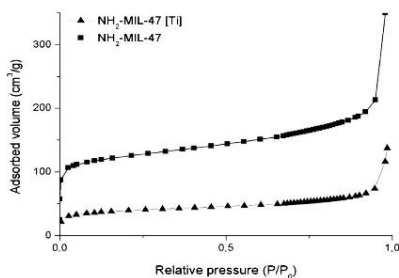


Fig. 5. Nitrogen adsorption isotherms of $\text{NH}_2\text{-MIL-47}$ and $\text{NH}_2\text{-MIL-47 [Ti]}$.

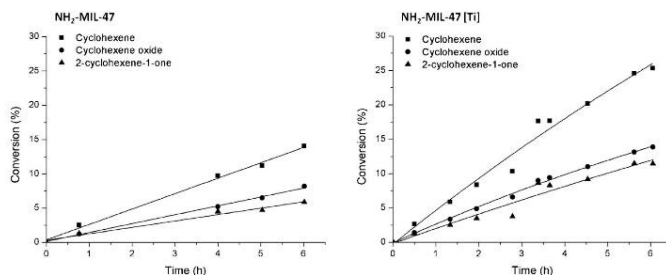


Fig. 6. Cyclohexene conversion (■) and the yield of cyclohexene oxide (●) and 2-cyclohexene-1-one (▲) for NH₂-MIL-47 and NH₂-MIL-47 [Ti] using acetonitrile as solvent and oxygen as oxidant in combination with the co-oxidant cyclohexanecarboxaldehyde at a temperature of 40 °C. In both experiments a V loading of 0.42 mmol was applied.

porosity. In addition, the calculated pore volume of the parent and post-modified MOF is 0.30 mL/g and 0.10 mL/g, respectively.

3.2. Evaluation of the catalytic performance in the oxidation of cyclohexene

The catalytic performance of NH₂-MIL-47 and NH₂-MIL-47 [Ti], 70 °C, 20 h was evaluated in the oxidation of cyclohexene. To make a fair comparison of both materials, the catalyst loading was chosen such that the number of V-sites was equal in the two experiments. Fig. 6 depicts the cyclohexene conversion and the detailed product distribution of both catalysts in the first run. Several features can be deduced from this figure. (1) A cyclohexene conversion of approximately 14.1% and 25% is observed respectively for the non-functionalized and bimetallic material after 6 h of reaction. This clearly shows that the bimetallic MOF exhibits a significantly higher catalytic performance than the (monometallic) V-MOF due to the presence of the extra active sites. (2) Moreover, faster conversion is observed for the bimetallic MOF. After 2 h of reaction, 10% of cyclohexene is already converted, whereas NH₂-MIL-47 shows only 6% of conversion. (3) Finally, it can be noted that both materials show only 2 products: cyclohexene oxide and the radical product 2-cyclohexene-1-one, which are produced in almost equal amounts. In Section 3.5 reaction mechanisms are proposed that explain this product distribution.

Additionally, the homogeneous catalyst TiO(acac)₂ has been tested using the same experimental conditions as for the MOF materials. The same amount of Ti has been used as in the post-functionalized material. The conversion pattern of this homogeneous catalyst is depicted in Fig. 7. After 6 h of reaction a cyclohexene conversion of 25% is reached, which is practically the same as for the Ti/V-MOF. It is interesting to note that the product distribution observed for the homogeneous catalyst is very similar as for the NH₂-MIL-47 and NH₂-MIL-47 [Ti]: almost equal percentages of the cyclohexene oxide and the ketone are observed.

3.3. Stability and regenerability of the catalysts

To test the regenerability of the V-MOFs, two additional runs have been executed on both materials. In Fig. 8, the cyclohexene conversion is shown after each run for the two catalysts, whereas in Table 1 the TON, TOF and leaching percentage are presented after each run for both materials. As can be seen from Fig. 8, the cyclohexene conversion for the post-functionalized material is slightly enhanced after the first run which is due to the generation of the extra catalytic V^{IV} sites (see Section 3.4). However, for the non-functionalized V-MOF a significantly higher cyclohexene

conversion is observed for the 2nd and the 3rd run (30% and 24%). This is due to the V leaching in each run as can be noted from Table 1. In each run a small amount of V-leaching is observed (1.8%, 2.5% and 3.5%) which gives rise to additional defects in the framework structure. Extra defects present in the structure can significantly influence the catalytic performance in the additional

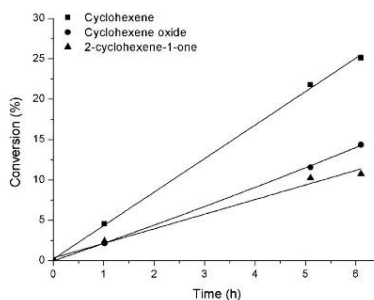


Fig. 7. Cyclohexene conversion (■) and the yield of cyclohexene oxide (●) and 2-cyclohexene-1-one (▲) for TiO(acac)₂ using acetonitrile as solvent and oxygen as oxidant in combination with the co-oxidant cyclohexanecarboxaldehyde at a temperature of 40 °C. The same Ti loading was applied as for the NH₂-MIL-47 [Ti] (0.22 mmol Ti).

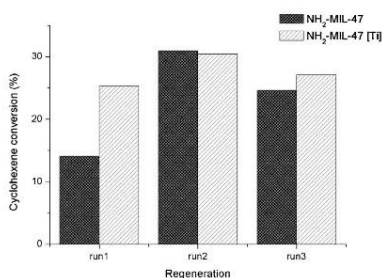


Fig. 8. Cyclohexene conversion for the executed additional runs on NH₂-MIL-47 and NH₂-MIL-47 [Ti].

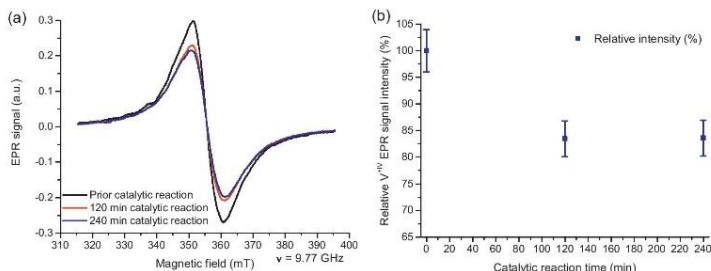


Fig. 9. (a) X-band EPR spectra at RT of the $\text{NH}_2\text{-MIL-47 [Ti]}$ samples before and after catalysis; (b) Relative V^{IV} EPR signal intensity with respect to the signal of $\text{NH}_2\text{-MIL-47 [Ti]}$ prior to catalysis. The error (σ) is estimated at 4% (see text). (For interpretation of the references to color in the artwork, the reader is referred to the web version of the article.)

runs [24]. The $\text{NH}_2\text{-MIL-47 [Ti]}$ did not show any detectable Ti or V leaching, which clearly demonstrates that the original MOF after post-functionalization becomes more stable. The exact reason for the enhanced leaching stability is currently unclear. Both shielding effects and electronic effects may influence the leaching behavior and would require advanced modeling techniques [37]. This falls beyond the scope of this current paper.

Comparison of the XRPD pattern of $\text{NH}_2\text{-MIL-47 [Ti]}$ before catalysis and after each run (see Fig. S.3) clearly shows that the framework integrity of the MOF is well preserved.

3.4. EPR measurements

The aim of the EPR measurements is gaining insight in the reaction mechanisms by monitoring the fraction of paramagnetic V^{IV} ions in the catalyst. Fig. 9 shows the RT X-band spectra of $\text{NH}_2\text{-MIL-47 [Ti]}$ dry powder samples before and after 2 and 4 h of catalysis. The spectra of the samples prior to and after catalysis appear as single broad lines exhibiting widths of about 9.2 mT before and 10.4 mT after catalysis. No ^{51}V hyperfine (HF) structure is resolved in the spectra. The line position in the X-band spectra is practically the same for all samples and already suggests a signal assignment to V^{IV} ($g = 1.96 < g_e = 2.0023$) [38]. Furthermore, spectra were recorded at higher microwave frequency (Q-band), which partially resolves the anisotropy of the ($\text{V}^{\text{IV}} = \text{O}$) O_4 complexes. In Fig. 10 the RT Q-band EPR spectrum of $\text{NH}_2\text{-MIL-47 [Ti]}$ is compared with that of $\text{NH}_2\text{-MIL-47}$ and MIL-47. Spectrum simulations show that in all three samples the paramagnetic species have (approximately) axial symmetry. The g_{\parallel} (along the $\text{V}=\text{O}$ bond direction) and g_{\perp} values obtained through fitting of the spectra are listed in Table 2. These values are typical for V^{IV} species [38] and are in very good agreement with earlier EPR reports on V-MOFs [39]. It is worth noting that both in the work of Meilikhov et al. [39] and in our own previous investigations of V-MOFs [24,25], no HF structure

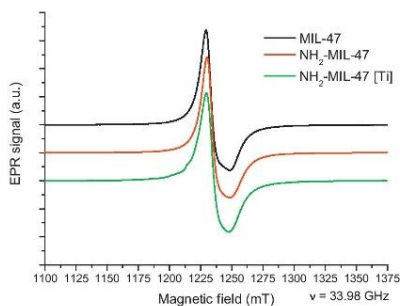


Fig. 10. Q-band (33.98 GHz) EPR spectrum of $\text{NH}_2\text{-MIL-47 [Ti]}$ compared with the spectra of non-functionalized $\text{NH}_2\text{-MIL-47}$ and MIL-47 at RT. (For interpretation of the references to color in the artwork, the reader is referred to the web version of the article.)

was resolved in the spectra, most probably as a result of interactions between spins in these paramagnetically concentrated samples. The number of paramagnetic centers in the samples was estimated by comparing the signal intensity with that of a $\text{VO}(\text{acac})_2$ grafted silica sample with known V^{IV} loading. It was found to be comparable to the number of V-sites in the catalyst, indicating that at RT EPR provides information on the majority of the metal V-sites, and not only on a minority fraction, e.g. corresponding to defects.

The intensity of the RT X-band spectra was evaluated by double integration of the EPR spectra over a range of 80.0 mT centered on the broad EPR line, in order to avoid errors due to non-perfect background correction in the broader range recorded. The data points in Fig. 9b represent the relative intensity with respect to the signal of $\text{NH}_2\text{-MIL-47 [Ti]}$ prior to catalytic reaction. The error (one standard deviation) is estimated at 4%, combining the effects of variations in consecutive measurements (sample positioning) and day-by-day changes in the spectrometer sensitivity. One observes that within

Table 1
TON, TOF and leaching percentage after each run for both V-based catalysts.

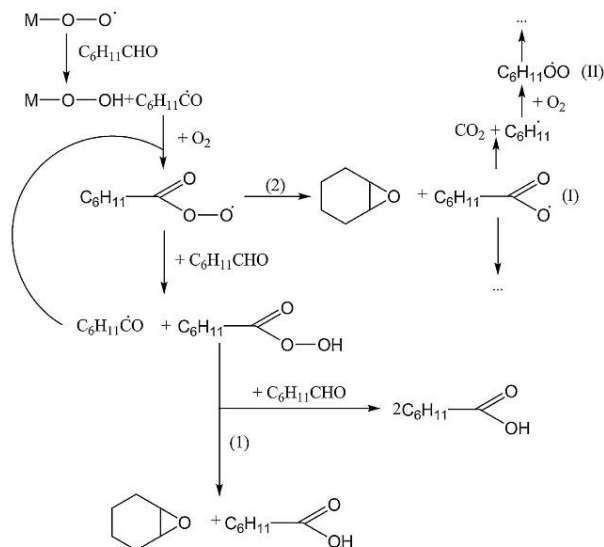
Sample	TON ^a	TOF ^b (h ⁻¹)	Leaching (%)
$\text{NH}_2\text{-MIL-47}$			
Run 1	17.7	6.0	1.8
Run 2	44.6	14.1	2.5
Run 3	63.9	10.4	3.5
$\text{NH}_2\text{-MIL-47 [Ti]}$			
Run 1	39.5	7.5	0
Run 2	44.8	12.1	0
Run 3	49.5	1.1	0

^a TON was calculated after 6 h of reaction.

^b TOF was calculated after 30 min of reaction.

Table 2
Best fit principal g values for the V^{IV} centers in MIL-47, $\text{NH}_2\text{-MIL-47}$ and $\text{NH}_2\text{-MIL-47 [Ti]}$ at RT (see Fig. 10).

T	Sample	g_{\parallel}	g_{\perp}
RT	MIL-47	1.972	1.941
	$\text{NH}_2\text{-MIL-47}$	1.970	1.940
	$\text{NH}_2\text{-MIL-47 [Ti]}$	1.970	1.940



Scheme 1. General mechanism of the epoxidation with O_2 and aldehydes, most termination steps where omitted for clarity.

the first 2 h of catalysis, the spectrum intensity decreases about 17%. Thereafter it remains stable or decreases more slowly. A very similar behavior was observed for MIL-47 in the oxidation of cyclohexene with TBHP/decane as oxidant [24]. Hence, we propose a similar interpretation: in the first few hours of catalysis a fraction of the V^{IV} centers is oxidized to diamagnetic V^{IV} centers. Mechanistic considerations in Section 3.5 suggest a radical parallel pathway, involving a partial oxidation of the V -metal sites.

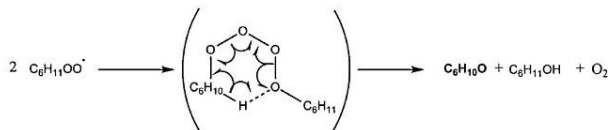
3.5. Reaction mechanisms

Based on the above described EPR and catalytic results a plausible reaction mechanism is proposed. The mechanism of oxidation using molecular oxygen and a sacrificial co-oxidant has been the subject of many studies. A radical mechanism involving a peracid radical as primary oxidizing species has been generally accepted (Scheme 1) [40]. The role of the catalyst is considered to be the activation of molecular oxygen by the generation of radicals. However, a metal-oxygen moiety can be present as alternative, direct oxidizing species in the metal-catalyzed system. This oxidation pathway is generally accepted for late transition metals [41,42]. Nevertheless, for metals like titanium and vanadium, this pathway is less likely as described in Sheldon et al. [43]. The

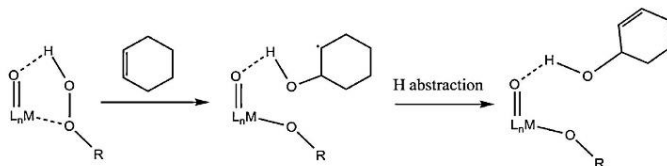
presence of metal-oxo species could explain the decrease of the V^{IV} signal intensity in the EPR measurements since the generation of vanadium-oxo species is accompanied by an oxidation to V^{IV} , which corresponds to what was already reported for the V -MIL-47 in the cyclohexene oxidation using TBHP as oxidant [24].

Another argument in favor of the mechanism shown in Scheme 1 is the presence of cyclohexanone in the product mixture. This is due to the formation of the peroxide radical ((II) in Scheme 1), followed by the formation of peroxide by a hydrogen abstraction. Afterwards, the obtained peroxide can react with another peroxide to form the cyclohexanone and oxygen (see Scheme 2).

This type of reaction generally exhibits a high (>80%) selectivity toward the epoxide when it is catalyzed by complexes where the metal can only have a low oxidation state (maximum II or III) [44]. A MOF containing the same metals as those mostly used as homogeneous catalysts (Ni, Cu, Co) for this reaction gave similar results [41]. In the present system however, the selectivity toward the epoxide is significantly lower. It is known that the presence of carboxylic acid radicals and peroxy radicals ((I) and (II) in Scheme 1) can lead to oxidation in the allylic position [40,41]. It is likely that these intermediates are stabilized by titanium and vanadium in the catalyst, leading to a decreased selectivity. Furthermore, the presence of $M=O$ species and peroxide moieties can lead to the formation



Scheme 2. formation of cyclohexanone, which was observed in the product mixture.



Scheme 3. Pathway to cyclohexenol formation.

of cyclohexenol as shown in Scheme 3. Cyclohexenol can then be oxidized further to 2-cyclohexene-1-one, this conversion was also shown by Murahashi et al. [44].

4. Conclusions

We succeeded in the post-functionalization of NH₂-MIL-47 with TiO(acac)₂. ¹³C CP/MAS NMR, ¹H NMR and DRIFTS measurements clearly established the effectiveness of the grafting procedure, whereas XRPD measurements proved the stability of the bimetallic MOF during the grafting process. The obtained NH₂-MIL-47 [Ti] exhibits a significantly higher cyclohexene conversion compared to the non-functionalized material, probably mainly due to the extra active sites. Furthermore, no leaching of V or Ti was detected. Regenerability tests have shown that only a slight increase in cyclohexene conversion is observed during the first 3 runs. EPR measurements indicate that about 17% of the V^{IV} sites are oxidized to V^V in the first two hours of catalysis. In agreement with the latter, the general mechanism of the epoxidation with O₂ and aldehydes shows the generation of vanadium-oxo species which is accompanied by a partial oxidation of the V centers toward V^V.

Acknowledgments

K.L. is grateful to the Long Term Structural Methusalem Grant No. 01M00409 funding by the Flemish Government. Furthermore, this research is co-funded by Ghent University, GOA Grant No. 01G00710, the Research Foundation Flanders (FWO-Vlaanderen) through Grant No. G.0700.08, BELSPO in the frame of IAP 6/27 and the European Research Council (FP7(2007–2013) ERC Grant No. 240483). Computational resources (Stevin Supercomputer Infrastructure) and services were provided by Ghent University. The authors would like to thank the research group FQM-346 and the SCAI from the University of Córdoba (Spain) for the ¹³C CP/MAS NMR measurements. The NMRSTR research group of Ghent University is acknowledged for performing the ¹H NMR measurements.

Appendix A. Supplementary data

Supplementary data associated with this article can be found, in the online version, at <http://dx.doi.org/10.1016/j.cattod.2012.09.037>.

References

- [1] J.R. Li, J. Sculley, H.C. Zhou, *Chemical Reviews* 112 (2012) 869–932.
- [2] J. Sculley, D.Q. Yuan, H.C. Zhou, *Energy and Environmental Science* 4 (2011) 2721–2735.
- [3] J.R. Li, Y.G. Ma, M.C. McCarthy, J. Sculley, J.M. Yu, H.K. Jeong, P.B. Balbuena, H.C. Zhou, *Coordination Chemistry Reviews* 255 (2011) 1791–1823.
- [4] D. Farrusseng, S. Aguado, C. Pinel, *Angewandte Chemie International Edition* 48 (2009) 7502–7513.
- [5] J. Lee, O.K. Farha, J. Roberts, K.A. Scheidt, S.T. Nguyen, J.T. Hupp, *Chemical Society Reviews* 38 (2009) 1450–1459.
- [6] Y. Liu, W.M. Xuan, Y. Cui, *Advanced Materials* 22 (2010) 4112–4135.
- [7] A. Corma, H. Garcia, F.X.L. Xamena, *Chemical Reviews* 110 (2010) 4606–4655.

- [8] M.G. Goesten, J. Juan-Alcaniz, E.V. Ramos-Fernandez, K.B.S.S. Gupta, E. Stavitski, H. van Bekkum, J. Gascon, F. Kapteijn, *Journal of Catalysis* 281 (2011) 177–187.
- [9] W.Q. Kan, B. Liu, J. Yang, Y.Y. Liu, J.F. Ma, *Crystal Growth and Design* 12 (2012) 2288–2298.
- [10] J. Rocha, L.D. Carlos, F.A.A. Paz, D. Ananias, *Chemical Society Reviews* 40 (2011) 926–940.
- [11] H. Liu, Y.G. Zhao, Z.J. Zhang, N. Nijem, Y.J. Chabal, H.P. Zeng, J. Li, *Advanced Functional Materials* 21 (2011) 4754–4762.
- [12] Y.G. Zhao, H.H. Wu, T.J. Emge, Q.H. Gong, N. Nijem, Y.J. Chabal, L.Z. Kong, D.C. Langreth, H. Liu, H.P. Zeng, J. Li, *Chemistry – A European Journal* 17 (2011) 5101–5109.
- [13] T.K. Prasad, D.H. Hong, M.P. Suh, *Chemistry – A European Journal* 16 (2010) 14043–14050.
- [14] J.P.S. Mowat, S.R. Miller, J.M. Griffin, V.R. Seymour, S.E. Ashbrook, S.P. Thompson, D. Fairen-Jimenez, A.M. Banu, T. Duren, P.A. Wright, *Inorganic Chemistry* 50 (2011) 10844–10858.
- [15] C. Zlotea, D. Phanom, M. Mazaj, D. Heurtaux, V. Guillemin, C. Serre, P. Horcajada, T. Devic, E. Magnier, F. Cuevas, G. Férey, P.L. Llewellyn, M. Latroche, *Dalton Transactions* 40 (2011) 4879–4881.
- [16] F. Vermoortele, M. Vandichel, B. Van de Voorde, R. Ameloot, M. Waroquier, V. Van Speybroeck, D. De Vos, *Angewandte Chemie International Edition* 51 (2012) 4887–4890.
- [17] S.M. Cohen, *Chemical Reviews* 112 (2012) 970–1000.
- [18] N.V. Maksimchuk, K.A. Kovalenko, S.S. Arzumanyan, Y.A. Chesalov, M.S. Melgunov, A.G. Stepanov, V.P. Fedin, O.A. Kholdeeva, *Inorganic Chemistry* 49 (2010) 2920–2930.
- [19] M.H. Alkordi, Y.L. Liu, R.W. Larsen, J.F. Eubank, M. Eddaoudi, *Journal of the American Chemical Society* 130 (2008) 12639–12641.
- [20] O.V. Zalomaeva, K.A. Kovalenko, Y.A. Chesalov, M.S. Mel'gunov, V.I. Zaikovskii, V.Y. Kaichev, A.B. Sorokin, O.A. Kholdeeva, V.P. Fedin, *Dalton Transactions* 40 (2011) 1441–1444.
- [21] M.J. Ingleson, J.P. Barrio, J.B. Guilhaud, Y.Z. Khimyak, M.J. Rosseinsky, *Chemical Communications* (23) (2008) 2680–2682.
- [22] S. Bhattacharjee, D.A. Yang, W.S. Ahn, *Chemical Communications* 47 (2011) 3637–3639.
- [23] K. Leus, I. Muylaert, M. Vandichel, G.B. Marin, M. Waroquier, P. Van der Voort, *Chemical Communications* 46 (2010) 5085–5087.
- [24] K. Leus, M. Vandichel, Y.Y. Liu, I. Muylaert, J. Musschoot, S. Pyl, H. Vrielandck, F. Callens, G.B. Marin, C. Detavernier, P.V. Wipier, Y.Z. Khimyak, M. Waroquier, V. Van Speybroeck, P. Van der Voort, *Journal of Catalysis* 285 (2012) 196–207.
- [25] Y.Y. Liu, K. Leus, M. Grzywa, D. Weinberger, K. Strubbe, H. Vrielandck, R. Van Deun, D. Volkmer, V. Van Speybroeck, P. Van der Voort, *European Journal of Inorganic Chemistry* 16 (2012) 2819–2827.
- [26] I. Muylaert, J. Musschoot, K. Leus, J. Dendooven, C. Detavernier, P. Van der Voort, *European Journal of Inorganic Chemistry* 12 (2012) 251–260.
- [27] S. Stoll, A. Schweiger, *Journal of Magnetic Resonance* 178 (2006) 42–55.
- [28] M.J.T. Frisch, G.W. Schlegel, H.B. Scuseria, G.E. Robb, M.A. Cheeseman, J.R. Scalmani, G. Barone, V. Mennucci, B. Petersson, G.A. Nakatsuji, H. Caricato, M. Li, X. Hratchian, H.P. Izmaylov, A.F. Bloino, J. Zheng, G. Sonnenberg, J.L. Hada, M. Ehara, M. Toyota, K. Fukuda, R. Hasegawa, J. Ishida, M. Nakajima, T. Honda, Y. Kitao, O. Nakai, H. Vreven, T. Montgomery Jr., J.A. Peralta, J.E. Ogliaro, F. Bearpark, M. Heyd, J.J. Brothers, E. Kudin, K.N. Staroverov, V.N. Kobayashi, R. Normand, J. Raghavachari, K. Rendell, A. Burant, J.C. Iyengar, S.S. Tomasi, J. Cossi, M. Rega, N. Millam, N.J. Klene, M. Knox, J.E. Cross, J.B. Bakken, V. Adamo, C. Jaramillo, J. Gomperts, R. Stratmann, R.E. Zayzev, O. Austin, A.J. Cammi, R. Pomelli, C. Ochterski, J.W. Martin, R.L. Morokuma, K. Zakrzewski, V.G. Voth, G.A. Salvador, P. Dannenberg, J.J. Dapprich, S. Daniels, A.D. Farkas, O. Foresman, J.B. Ortiz, J.V. Cioslowski, J. Fox, D.J. Gaussian 09, (Revision A), 02, Gaussian, Inc., Wallingford CT, 2009.
- [29] A.D. Becke, *Journal of Chemical Physics* 98 (1993) 5648–5652.
- [30] C.T. Lee, W.T. Yang, R.G. Parr, *Physical Review B* 37 (1988) 785–789.
- [31] J.P. Merrick, D. Moran, L. Radom, *Journal of Physical Chemistry A* 111 (2007) 11683–11700.
- [32] E. Pertsch, P. Bühlmann, C. Affolter, A. Herrera, R. Martínez, Determinación estructural de compuestos orgánicos, Elsevier Masson (2001).
- [33] J. Coates (Ed.), Interpretation of Infrared Spectra, A Practical Approach, 2000.
- [34] T. Loubeau, G. Serec, C. Huguenard, C. Fink, F. Taulerle, M. Henry, T. Bataille, G. Férey, *Chemistry – A European Journal* 10 (2004) 1373–1382.
- [35] J. Gascon, U. Aktyay, M.D. Hernandez-Alonso, G.P.M. van Klínk, F. Kapteijn, *Journal of Catalysis* 261 (2009) 75–87.

- [36] M. Kandiah, M.H. Nilsen, S. Usseglio, S. Jakobsen, U. Olsbye, M. Tilset, C. Larabi, E.A. Quadrelli, F. Bonino, K.P. Lillerud, *Chemistry of Materials* 22 (2010) 6632–6640.
- [37] J.M. Ho, C.J. Easton, M.L. Coote, *Journal of the American Chemical Society* 132 (2010) 5515–5521.
- [38] R. Pilbrow (Ed.), *Transition Ion Electron Paramagnetic Resonance*, Clarendon Press, Oxford, 1990.
- [39] M. Meilikhov, K. Yusenko, A. Torrisi, B. Jee, C. Mellot-Drazniak, A. Pöpl, R.A. Fischer, *Angewandte Chemie International Edition* 49 (2010) 6212–6215.
- [40] B.B. Wentzel, P.L. Alsters, M.C. Feiters, R.J.M. Nolte, *Journal of Organic Chemistry* 69 (2004) 3453–3464.
- [41] E. Angelescu, O.D. Pavel, R. Ionescu, R. Birjega, M. Badea, R. Zavoianu, *Journal of Molecular Catalysis A Chemical* 352 (2012) 21–30.
- [42] P. Mastroianni, C.F. Nobile, G.P. Suranna, L. Lopez, *Tetrahedron* 51 (1995) 7943–7950.
- [43] G.J. ten Brink, I.W.C.E. Arends, R.A. Sheldon, *Chemical Reviews* 104 (2004) 4105–4123.
- [44] N. Komiya, T. Naota, Y. Oda, S.I. Murahashi, *Journal of Molecular Catalysis A Chemical* 117 (1997) 21–37.

Supporting information

General experimental details

The sample for ^1H NMR was made following a procedure reported in literature from Burrows et al. ¹. Prior to the NMR measurements, the $\text{NH}_2\text{-MIL-47 [Ti]}$ was dried under vacuum at 100°C . Afterwards the sample was digested in 0.4 cm^3 DMSO- d_6 and 0.2 cm^3 stock DCl solution (0.1 cm^3 35% DCl/ D_2O , in 1.5 cm^3 DMSO- d_6)

Table S. 1 Applied temperatures and reaction times during the grafting of $\text{TiO}(\text{acac})_2$ onto $\text{NH}_2\text{-MIL-47}$ and the obtained Ti loading (mmol/g).

Sample	Temperature ($^\circ\text{C}$)	Reaction time (h)	Ti (mmol/g)
$\text{NH}_2\text{-MIL-47 [Ti]}$, 55°C , 20h	55	20	1.21
$\text{NH}_2\text{-MIL-47 [Ti]}$, 55°C , 40h	55	40	1.25
$\text{NH}_2\text{-MIL-47 [Ti]}$, 70°C , 20h	70	20	1.26
$\text{NH}_2\text{-MIL-47 [Ti]}$, 70°C , 40h	70	40	1.21
$\text{NH}_2\text{-MIL-47 [Ti]}$, 90°C , 20h	90	20	1.38
$\text{NH}_2\text{-MIL-47 [Ti]}$, 90°C , 40h	90	40	1.31

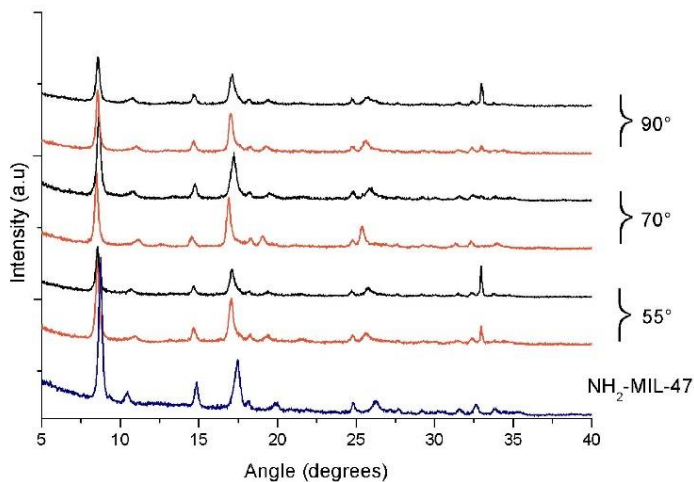


Fig. S.1 XRPD pattern of $\text{NH}_2\text{-MIL-47}$ (blue) and the post-functionalized $\text{NH}_2\text{-MIL-47 [Ti]}$ materials, the $\text{NH}_2\text{-MIL-47 [Ti]}$ stirred for 20 hours are shown in red and the samples stirred for 40 hours are depicted in black.

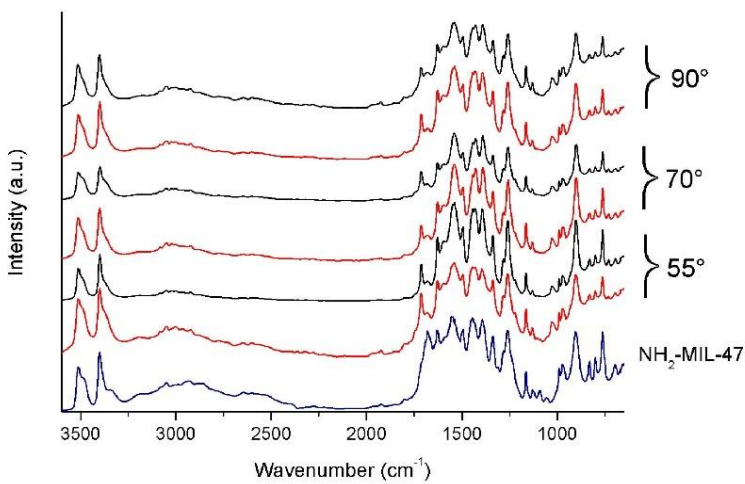


Fig. S.2 DRIFT patterns of NH₂-MIL-47 (blue) and the post-functionalized NH₂-MIL-47 [Ti] materials, the NH₂-MIL-47 [Ti] stirred for 20 hours are shown in red and the samples stirred for 40 hours are depicted in black.

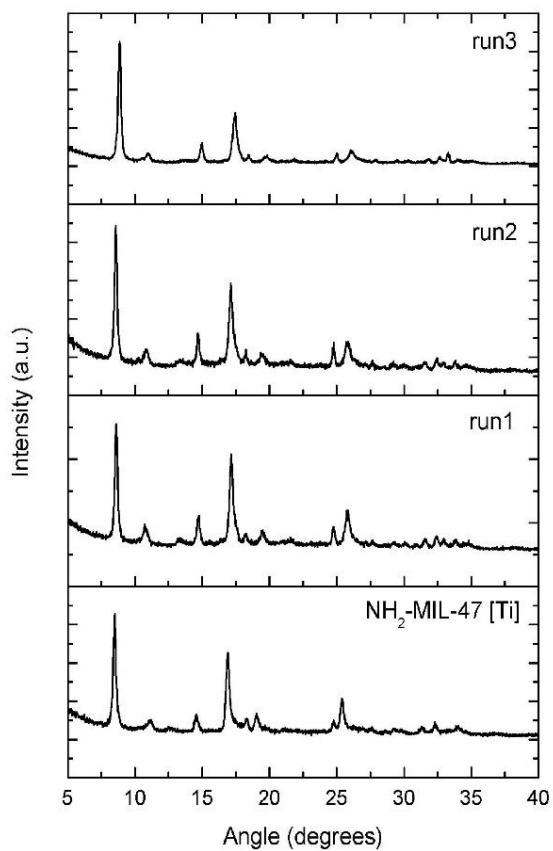


Fig. S3 XRPD pattern of the original NH₂-MIL-47 [Ti] before catalysis and the XRPD pattern of NH₂-MIL-47[Ti] after the first, second and third catalytic run.

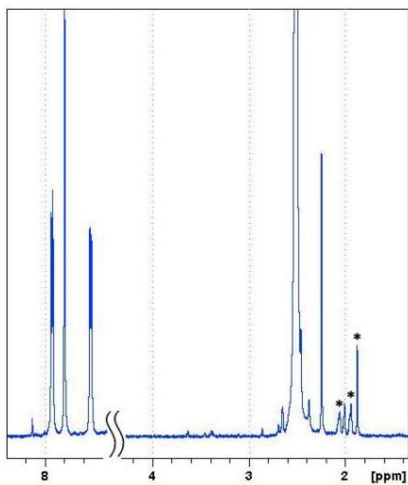


Fig.S4 ^1H spectrum of $\text{NH}_2\text{-MIL-47 [Ti]}$, the signals at 2.06, 1.94 and 1.85 ppm are indicated with an *.

1. A. D. Burrows and L. L. Keenan, *Crystengcomm*, 2012, **14**, 4112-4114.

APPENDIX A. PUBLICATION LIST

PUBLICATIONS IN INTERNATIONAL PEER-REVIEWED JOURNALS

Fine-tuning the theoretically predicted structure of MIL-47(V) with the aid of powder X-ray diffraction, T. Bogaerts, L. Vanduyfhuys, D.E.P. Vanpoucke, J. Wieme, M. Waroquier, P. Van der Voort, V. Van Speybroeck, *CrystEngComm*, accepted, **2015**, IF:4.034

T. Bogaerts, S. Wouters, P. Van der Voort, V. Van Speybroeck, *Mechanistic investigation on the oxygen transfer with the manganese-salen complex*, *ChemCatChem*, **7**, 2711–2719, 2015, IF:5.044

T. Bogaerts, S. Wouters, P. Van der Voort, V. Van Speybroeck, *The enantioselectivity of the manganese-salen complex in the epoxidation of unfunctionalized olefins and the influence of grafting*, *Journal of Molecular Catalysis A: Chemical*, **406**, 106-113, 2015, IF: 3.356

S. Wouters, T. Bogaerts, P. Van der Voort, V. Van Speybroeck, D. Van Neck, *Communication: DMRG-SCF study of the singlet, triplet, and quintet states of oxo-Mn(Salen)*, *Journal of Chemical Physics*, **140**, 241103, 2014, IF: 3.122

T. Bogaerts, A. Van Yperen-De Deyne, Y-Y Liu, F. Lynen, V. Van Speybroeck, P. Van der Voort, *Mn-salen@MIL101(Al) a heterogeneous, enantioselective catalyst using a ‘bottle around the ship’ approach*, *Chemical Communications*, **2013 (49)**, 8021-8023, 2013, IF: 6.718

Y-Y Liu, K. Leus, T. Bogaerts, K. Hemelsoet, E. Bruneel, V. Van Speybroeck, P. Van der Voort, *Bimetallic–Organic Framework as a Zero-Leaching Catalyst in the Aerobic Oxidation of Cyclohexene*, *ChemCatChem*, 5 (12), 3657–3664, 2013, IF: 5.044

K. Leus, G. Vanhaelewyn, T. Bogaerts, Y-Y Liu, F. Esquivel, F. Callens, G.B. Marin, V. Van Speybroeck, H. Vrielinck, P. Van der Voort, *Ti-functionalized NH₂-MIL-47: an effective and stable epoxidation catalyst*, *Catalysis Today*, 208, 97-105, 2013, IF: 3.309

J. De Decker, T. Bogaerts, I. Muylaert, S. Delahaye, F. Lynen, V. Van Speybroeck, A. Verberckmoes, P. Van der Voort, *Covalent immobilization of the Jacobsen catalyst on mesoporous phenolic polymer: a highly enantioselective and stable asymmetric epoxidation catalyst*, *Materials Chemistry and Physics*, 141 (2013), 967-972, 2013, IF: 2.129

Y-Y Liu, R. Decadt, T. Bogaerts, K. Hemelsoet, A.M. Kaczmarek, D. Poelman, M. Waroquier, V. Van Speybroeck, R. Van Deun, P. Van der Voort, *Bipyridine-Based Nanosized Metal–Organic Framework with Tunable Luminescence by a Postmodification with Eu(III): An Experimental and Theoretical Study*, *Journal of Physical Chemistry C*, 117 (21), 11302–11310, 2013, IF: 4.835

M. Ide, M. El-Roz, E. De Canck, A. Vicente, T. Planckaert, T. Bogaerts, I. Van Driessche, F. Lynen, V. Van Speybroeck, F. Thibault-Starzyk, P. Van der Voort, *Quantification of silanol sites for the most common mesoporous ordered silicas and organosilicas: total versus accessible silanols*, *Physical Chemistry Chemical Physics (PCCP)*, 15, 642-650, 2013, IF: 4.198

ORAL PRESENTATIONS ON INTERNATIONAL CONFERENCES

T. Bogaerts, V. Van Speybroeck, P. Van der Voort, *Immobilization of a chiral salen catalyst, a grafting versus an encapsulation approach*, *The meeting of the Dutch Zeolite Association*, Ghent Belgium, 07/10/2014

T. Bogaerts, A. Van Yperen-De Deyne, S. Wouters, D. Van Neck, P. Van der Voort, V. Van Speybroeck, *A mechanistic investigation of the manganese-salen epoxidation*, 15th International Conference on Theoretical Aspects of Catalysis (ICTAC15), London, United Kingdom, 30/06/2014 - 04/07/2014

T. Bogaerts, A. Van Yperen-De Deyne, S. Wouters, D. Van Neck, P. Van der Voort, V. Van Speybroeck, *Unraveling the mechanism of the manganese-salen epoxidation*, XVth Netherlands' Catalysis and Chemistry Conference (NCCC XV), Noordwijkerhout, The Netherlands, 10/03/2014 - 12/03/2014

T. Bogaerts, M. Vandichel, Y-Y Liu, M. Waroquier, V. Van Speybroeck, P. Van der Voort, *Design of enantioselective catalysts in MOF architectures: a combined computational and experimental approach*, Congress on Catalysis Applied to Fine Chemicals, Turku Finland, 16/06/2013 - 19/06/2013

POSTER PRESENTATIONS ON INTERNATIONAL CONFERENCES

T. Bogaerts, P. Van der Voort, V. Van Speybroeck, *The influence of immobilization on the selectivity of Jacobsen-salen complexes*, IAP meeting 2014, Louvain la Neuve Belgium, 19/09/2014

T. Bogaerts, V. Van Speybroeck, P. Van der Voort, *Immobilization of a chiral salen catalyst, a grafting versus an encapsulation approach*, FEZA2014, Leipzig, Germany, 08/09/2014 - 11/09/2014

S. Wouters, T. Bogaerts, P. Van der Voort, V. Van Speybroeck, D. Van Neck, *DMRG-SCF study of the singlet, triplet, and quintet states of oxo-Mn(Salen)*, Low-scaling and Unconventional Electronic Structure Techniques Conference, Telluride, CO, USA, 01/06/2014 - 05/06/2014

T. Bogaerts, A. Van Yperen-De Deyne, Y-Y Liu, V. Van Speybroeck, P. Van der Voort, *Design of enantioselective catalysts in MOF architectures: a combined computational and experimental approach*, Annual IAP Meeting, Ghent, Belgium, wo, 18/09/2013

T. Bogaerts, M. Vandichel, P. Van der Voort, V. Van Speybroeck, *Design of enantioselective catalysts in MOF architectures: a combined theoretical and experimental approach*, NCCC XIV, Noordwijkerhout, The Netherlands, 11/03/2013 - 13/03/2013

Y. Aelbrecht, T. Bogaerts, M. Vandichel, K. Hemelsoet, P. Van der Voort, V. Van Speybroeck, *Immobilization of a homogeneous enantioselective catalysts on a large pore Metal-Organic Framework*, NCCC XIV, Noordwijkerhout, The Netherlands, 11/03/2013 - 13/03/2013

T. Bogaerts, M. Vandichel, V. Van Speybroeck, P. Van der Voort, *Design of enantioselective catalysts in MOF architectures: a combined theoretical and experimental approach*, MOF2012, Edinburgh, UK, 16/09/2012 - 19/09/2012

K. Leus, S. Couck, T. Bogaerts, M. Vandichel, Y-Y Liu, M. Waroquier, V. Van Speybroeck, J.F.M. Denayer, P. Van der Voort, *Synthesis, characterization, adsorption and catalytic properties of an amino functionalized Metal-Organic Framework: NH₂-MIL-47*, MOF2012, Edinburgh UK, 16/09/2012 - 19/09/2012

T. Bogaerts, M. Vandichel, M. Waroquier, P. Van der Voort, V. Van Speybroeck, *Mechanistic investigation of the enantioselective titaniumtartrate catalyst*, ICTAC-14, Vlissingen, The Netherlands, 26/06/2012 - 30/06/2012

T. Bogaerts, M. Vandichel, M. Waroquier, P. Van der Voort, V. Van Speybroeck, *Molecular modeling of the Enantioselective titaniumtartrate catalyst*, XIIIth Netherlands' Catalysis and Chemistry Conference (NCCC XIII), Noordwijkerhout, The Netherlands, 05/03/2012 - 07/03/2012

T. Bogaerts, M. Vandichel, M. Waroquier, P. Van der Voort, V. Van Speybroeck, *Molecular modeling of the Enantioselective titaniumtartrate catalyst*, MolSim 2012, Amsterdam, NL, 09/01/2012 - 20/01/2012

Molecular modeling of enantioselective catalysis in chiral MOFs, T. Bogaerts, M. Vandichel, M. Waroquier, P. Van der Voort, V. Van Speybroeck, 5th Int. FEZA Conference, Valencia, Spain, 03/07/2011 - 07/07/2011

Molecular modeling of enantioselective catalysis in chiral MOFs, T. Bogaerts, M. Vandichel, M. Waroquier, P. Van der Voort, V. Van Speybroeck, XIIth Netherlands' Catalysis and Chemistry Conference (NCCC XII), Noordwijkerhout, The Netherlands, 28/02/2011 - 02/03/2011

APPENDIX B. ACKNOWLEDGEMENTS



This research was sponsored by the research programs of the European Research Council under the European Community's Seventh Framework Program FP7(2007-2013) ERC grant agreement number 240483 and Ghent university GOA grant 01G00710



Computational resources and services used in this work were provided by the Stevin Supercomputer Infrastructure of Ghent University and by the VSC (Flemish Supercomputer Center), funded by the Hercules Foundation and the Flemish Government – department EWI.

